Novel Blade Design Strategy to Control the Erosion Aggressiveness of Cavitation

Jeremy Nahon

A thesis submitted for the degree of Doctor of Philosophy in the Faculty of Engineering

Department of Mechanical Engineering
University College London

January 24, 2020

I, Jeremy Nahon confirm that the work presented in this thesis is my own. Where information has been derived from other sources, I confirm that this has been indicated in the thesis.

Abstract

With the reduction in size of turbomachinery systems, cavitation aggressiveness is intensified. Erosion, caused by the repeated collapse of gaseous bubbles in proximity to solid surfaces, occurs at rates that dramatically downgrade the life expectancy of rotating parts. As a result, the compacting strategy, meant to reduce cost and improve efficiency, fails for liquid flows. The research undertaken here proposes a novel design method aimed at controlling the erosion aggressiveness of cavitation. The underlying idea is that the cavity closure shock is a determining factor in the intensity of bubble collapse mechanisms: sharp and high amplitude shocks give rise to strong erosion, while low gradient and low amplitude recoveries reduce the erosive intensity.

The working hypothesis is tested here, first, by developing a novel inverse design algorithm capable of handling cavitating flow. The code solves the inviscid Euler equations and models blade cavitation using the Tohoku-Ebara barotropic equation of state. Bespoke preconditioning and multigrid procedures are constructed to handle the large amplitudes in flow regime (from hypersonic in the cavity to very low Mach number in the liquid phase).

The inverse solver is then used to produce a set of 2D cascade hydrofoil geometries with smoothed shock profiles at cavity closure. The blades are assessed numerically using both steady state and time-resolved approaches. Both hydrodynamic performance, given in terms of swirl, lift and drag, and cavitation dynamics are evaluated. Recently developed erosion prediction methodologies are implemented and demonstrate compelling correlations between the erosion patterns and shock profile.

Finally, experimental testing is carried out using a purposefully developed observation platform. The erosive performance of two of the geometries is measured using the paint removal technique. Results reveal a significant improvement in erosive response for the shock smoothed design, thus confirming the numerical findings as well as the validity of the design hypothesis.

Impact Statement

This research addresses one of the major challenges brought about by the miniaturisation of rotating components in liquid flows: the breakdown of life expectancy caused by cavitation erosion. It proposes and verifies a new design strategy for controlling cavitation aggressiveness on 2D cascade hydrofoils. This constitutes a substantial advancement towards the development of a comprehensive 3D methodology for containing cavitation erosion.

The implications of such a tool are significant. Its application to existing cases which suffer from excessive damage could quench the intensity of wear. The new geometries would be just as efficient and follow equivalent performance characteristics as the original but withstand far longer exposure times. This would have an immediate impact on cost thanks to reduced maintenance and largely benefit the turbomachinery user.

More generally, the inclusion of the strategy into hydraulic machinery design practices could eliminate the cavitation erosion problem. The miniaturisation effort, impeded until now by the extreme structural damage, could be resumed. This means that turbomachinery components can keep getting smaller and incur reduced production and operational costs. Repercussions would be far-reaching since all types of configurations would profit from the trend and these systems are an integral part of our technological environment. For instance, centrifugal pumps are responsible for more than 10% of global electricity consumption so any cutback in operational requirements has extensive economic impacts.

The direction taken by this work is mainly aimed at industrial optimisation. Nevertheless, two noteworthy advances contribute to scientific research of a more fundamental character. The first is the development of a robust cavitating flow solver with inverse design capabilities. It is an entirely novel achievement which opens up the range of application of the inverse technique to complex multiphase flows. The second is the comparison of two contrasting approaches to cavitation modelling with experimental data for cascade flow. Significant discrepancies put forward the need for further enhancement of prediction techniques for cavitation.

A number of planned publications will serve to disseminate the findings presented in this thesis. Collaboration and emulation either with industry or academia can only help to enhance the novel design methodology and establish its value in turbomachinery development.

Acknowledgements

First and foremost, I would like to thank Prof. Mehrdad Zangeneh. It is through his insight and expertise that this research was shaped. Under his supervision, the ideal environment for bringing this thesis to fruition was created. A special thanks to my colleagues Peng Wang and Jiangnan Zhang who were always more than happy to share their knowledge and guide me through the first stages of the PhD.

I extend my most sincere gratitude to the team at Ebara Corporation, without whom this research would not have been possible. Dr Akira Goto for driving the research forward by always keeping an eye on the big picture. Dr Hiroyoshi Watanabe who was instrumental in coordinating our collaboration. A very particular thank you is addressed to Dr Motohiko Nohmi who has been more than happy to share his encyclopaedic knowledge of cavitation. Without failure, he was the one who provided the answers. Working on the experimental platform with Tomoki Tsuneda was highly productive and great fun. Thank you to Mr Sato and his colleagues for designing an outstanding rig in astoundingly short time. Finally a special thank you to Byungjin An for taking the time to show me around Shōnan and making my stay more than pleasant.

I would like to thank Prof. Yiannis Ventikos and his research group for their scientific insight. In particular, Nikos Bempedelis, with whom discussing cavitation generally led to more questions.

Last but not least, I would like to thank my family and friends for their unflinching support. Especially Anna, in whose footsteps I followed closely, and will never stop following.

Publications and Conference Proceedings

Jeremy Nahon, and Mehrdad Zangeneh. (In Preparation) New Inverse Design Solver for Cavitating Hydrofoil Cascades. *Computers & Fluids.*

Jeremy Nahon, Mehrdad Zangeneh, Motohiko Nohmi, and Hiroyoshi Watanabe. Numerical Investigation on the Effect of Blade Loading on Unsteady Sheet Cavitation. In *AJK Fluids Meeting 2019*, 2019.

Jeremy Nahon, Mehrdad Zangeneh, Motohiko Nohmi, and Hiroyoshi Watanabe. Comparative Assessment of a Barotropic Model and a Void Fraction Transport Model for Numerically Predicting Steady Sheet Cavitation. In *Proceedings of the 10th International Symposium on Cavitation (CAV2018)*. ASME Press, 2018.

Contents

List of Figures

List of Tables

List of Symbols

Abbreviations

1D	One-dimensional formulation
2D	Two-dimensional formulation
3D	Three-dimensional formulation
AUSM	Advection Upstream Splitting Method
CFD	Computational Fluid Dynamics
CFL	Courant-Friedrichs-Lewy number
DES	Detached Eddy Simulation
DNS	Direct Numerical Simulation
DO	Dissolved Oxygen
DP	Prefix to case names indicating design by Δp algorithm
EOS	Equation of State
FAS	Full Approximation Storage
FDS	Flux Difference Splitting
FMG	Full Multigrid
fps	Frames per second
FVM	Finite Volume Method
FVS	Flux Vector Splitting
LE	Leading Edge
LES	Large Eddy Simulation
LHS	Left Hand Side
MS	Merkle & Sullivan time-derivative preconditioning
NPSH	Net Positive Suction Head
ODE	Ordinary Differential Equation
PS	Blade pressure side
RANS	Reynolds Averaged Navier-Stokes equations
Re	Reynolds number

RHS	Right Hand Side
RMS	Root Mean Square residuals
RPM	Revolutions per minute
SLAU	Simple low dissipation advection upstream method
Sr	Strouhal number
SS	Blade suction side
SST	Shear Stress Transport
TE	Tohoku-Ebara cavitation model
TE	Trailing Edge
URANS	Unsteady Reynolds Averaged Navier-Stokes equations
VOF	Volume of Fluid
VY	Prefix to case names indicating design by V_y algorithm
WS	Weiss & Smith time-derivative preconditioning
ZGB	Zwart-Gerber-Belamri cavitation model

Chapter 1

Δp_c	Non-condensable gas effect on vapour pressure	Pa
ρ	Density or mixture density for homogeneous cavitating flow	$\mathrm{kg\,m^{-3}}$
ρ_l	Density of pure liquid water at 20 °C	$\mathrm{kg\,m^{-3}}$
ρ_v	Density of pure water vapour at 20 °C	$\mathrm{kg\,m^{-3}}$
σ	Cavitation number	
σ_i	Inception cavitation number	
C	Flow speed	$\mathrm{m\,s^{-1}}$
C_p	Pressure coefficient	
$chord$	Axial chord length	m
g	Gravitational acceleration constant	$\mathrm{m\,s^{-2}}$
H	Hydraulic head	m
$NPSH$	Net Positive Suction Head	m
p	Absolute static pressure	Pa
p^0	Total pressure (absolute)	Pa
p_∞	Free stream pressure	Pa
p_v	Saturation vapour pressure at 20 °C, $p_v = 2339.2\,\mathrm{Pa}$	Pa
T	Temperature	K
U_∞	Free stream velocity	$\mathrm{m\,s^{-1}}$
x	Axial coordinate	m

Z	Elevation of reservoir free surface	m

Chapter 2

α_g	Non-condensable gas volume fraction	
α_l	Liquid water volume fraction	
α_v	Water vapour volume fraction	
α_{nuc}	Volume fraction at nucleation site	
Δp	Pressure difference between liquid and vapour	Pa
δ	Material dependent impulse threshold	$\mathrm{Pa\,s^{-1}}$
$\dot{m}^+$	Massic rate of condensation	$\mathrm{kg\,m^{-3}\,s^{-1}}$
$\dot{m}^-$	Massic rate of vaporisation	$\mathrm{kg\,m^{-3}\,s^{-1}}$
η	Aggressiveness efficiency/transmissivity coefficient	
γ	Polytropic coefficient or mass fraction	
μ	Dynamic viscosity	Pa s
ν_l	Kinematic viscosity of liquid	$\mathrm{m^2\,s^{-1}}$
Ω	Rotational speed of pump/turbine	$\mathrm{rad\,s^{-1}}$
Ω_s	Specific speed of pump/turbine	
Ω_{jet}	Volume of collapse micro-jet	$\mathrm{m^3}$
ρ	Density or mixture density for homogeneous cavitating flow	$\mathrm{kg\,m^{-3}}$
ρ_g	Density of non-condensable gas	$\mathrm{kg\,m^{-3}}$
ρ_l	Density of pure liquid water at 20 °C	$\mathrm{kg\,m^{-3}}$
ρ_v	Density of pure water vapour at 20 °C	$\mathrm{kg\,m^{-3}}$
ξ	Micro-jet constant	m
c	Speed of sound	$\mathrm{m\,s^{-1}}$
C^c	Condensation constant for *transport equation* type cavitation models	
C^v	Vaporisation constant for *transport equation* type cavitation models	
E_p	Potential energy of vapour cloud	J
I_{agr}	Erosive aggressiveness of cavitation	
K	Liquid constant in the Tammann equation for liquid water	Pa
k	Turbulent kinetic energy	J
n_B	Vapour bubble density	$\mathrm{m^{-3}}$
P	Turbine power	W
p_∞	Pressure of liquid surrounding a bubble	Pa
p_a	Radiated acoustic pressure	Pa
p_B	Pressure within cavitation bubble	Pa

p_B	Vapour bubble pressure	Pa
p_c	Critical pressure in the Tammann equation for liquid water	Pa
p_v	Saturation vapour pressure at 20 °C, $p_v = 2339.2\,\text{Pa}$	Pa
P_{agr}	Aggressiveness power of cavity from potential energy formulation	W
Q	Volume flow rate	$\text{m}^3\,\text{s}^{-1}$
R	Vapour bubble radius	m
r	Distance from bubble collapse	m
R_a	Ideal gas constant for air	$\text{J}\,\text{kg}^{-1}\,\text{K}^{-1}$
R_M	Maximum bubble radius	m
R_v	Ideal gas constant for vapour	$\text{J}\,\text{kg}^{-1}\,\text{K}^{-1}$
S	Bubble surface tension	$\text{N}\,\text{m}^{-1}$
T	Total exposure time	s
T_0	Critical temperature in the Tammann equation for liquid water	Pa
t_∞	Mean flow time scale	s
u, v, w	Flow velocity vector	$\text{m}\,\text{s}^{-1}$
U_∞	Free stream velocity	$\text{m}\,\text{s}^{-1}$
V_B	Vapour bubble volume	m^3
V_v	Total volume of vapour cloud	m^3
V_{cell}	Cell volume	m^3
v_{jet}	Micro-jet velocity of collapsing bubble	$\text{m}\,\text{s}^{-1}$
x, y	Two-dimensional coordinate system	m
Y	Mass fraction of air in mixture	

Chapter 3

$(\,)^{\pm}$	State on the left (+) or right (−) of interface
$(\,)^n$	Value at time step number n
$(\,)^{L/R}$	State on the left/right of interface
$(\,)_i$	Iterator index in x direction
$(\,)_j$	Iterator index in y direction
$(\,)_k$	Cell face index
$(\,)_{RL}$	Roe averaged quantity
α	Water vapour volume fraction
$\alpha^{\pm}$	Top and bottom blade surfaces
α_m	Multistage time stepping coefficients
$\beta^{\pm}$	Polynomial weighting in upwind flux splitting

$\boldsymbol{D}$	Dissipative term in finite volume formulation	
$\boldsymbol{F_c}$	Convective flux vector	
$\boldsymbol{F_v}$	Viscous flux vector	
$\boldsymbol{I}$	Grid to grid mapping operator	
$\boldsymbol{Q}$	Primitive variable vector	
$\boldsymbol{R}$	Residual vector in finite volume formulation	
$\boldsymbol{S_S}$	Surface source term in Navier-Stokes equation	
$\boldsymbol{S_V}$	Volumetric source term in Navier-Stokes equation	
$\boldsymbol{U}$	General vector quantity	
$\boldsymbol{W}$	Conservative variable vector	
χ	High speed flow weighting in SLAU scheme	
Δp	Blade pressure loading	Pa
Δt	Discrete time step	s
Δx	Discrete space step	m
$\dot{m}$	Mass flux through interface	
Γ	Preconditioning matrix	
γ	Polytropic coefficient	
$\hat{A}$	Linearisation Jacobian matrix	
$\hat{f}$	Target cascade camber line	
$\hat{V}_y$	Target tangential velocity distribution	$\mathrm{m\,s^{-1}}$
$\kappa_{R/P}$	Multigrid restriction (R) and prolongation (P) shock weighting coefficients	
Λ^p	Face area weighted eigenvalues	
λ^p	Eigenvalues of linearised equations	
μ	Dynamic viscosity	Pa s
ν	Pressure gradient sensor	
Ω	Cell volume	$\mathrm{m^3}$
ϕ	Generic mass flow averaged quantity	
ρ	Density or mixture density for homogeneous cavitating flow	$\mathrm{kg\,m^{-3}}$
ρ_g	Density of non-condensable gas	$\mathrm{kg\,m^{-3}}$
τ	Viscous stress tensor	
Θ	Propagation parameter in preconditioning procedure	
ε, η	Curvilinear set of coordinates	
$\varepsilon^{(2)}$	Dissipation coefficient for second order difference	
$\varepsilon^{(4)}$	Dissipation coefficient for fourth order difference	

ζ	Direction of curvilinear axis ε	
c	Speed of sound	$\mathrm{m\,s^{-1}}$
c_p	Specific heat at constant pressure	$\mathrm{J\,kg^{-1}\,K^{-1}}$
c_v	Specific heat at constant volume	$\mathrm{J\,kg^{-1}\,K^{-1}}$
d	Face specific artificial dissipation operator	
E	Total energy per unit mass	$\mathrm{J\,kg^{-1}}$
f	Cascade camber line	
f_h	Forcing function	
f_p	Supersonic expansion switch in SLAU scheme	
J	Determinant of mapping function from absolute to body-fitted coordinates	
K	Liquid constant in the Tammann equation for liquid water	Pa
M	Mach number	
m	Meridional coordinate	
N	Blade number	
p	Absolute static pressure	Pa
p_c	Critical pressure in the Tammann equation for liquid water	Pa
R	Ideal gas constant	$\mathrm{J\,kg^{-1}\,K^{-1}}$
r^p	Eigenvectors of linearised equations	
T	Blade tangential thickness	
T_0	Critical temperature in the Tammann equation for liquid water	Pa
u, v, w	Flow velocity vector	$\mathrm{m\,s^{-1}}$
V	Contravariant velocity	$\mathrm{m\,s^{-1}}$
$V_{m_{bl}}$	Average meridional velocity across blade	$\mathrm{m\,s^{-1}}$

Chapter 4

$(\,)_{in}$	Quantity assigned at inlet	
$(\,)_{out}$	Quantity assigned at outlet	
β	Cascade flow angle	$^\circ$
$\dot{m}^+$	Massic rate of condensation	$\mathrm{kg\,m^{-3}\,s^{-1}}$
$\dot{m}^-$	Massic rate of vaporisation	$\mathrm{kg\,m^{-3}\,s^{-1}}$
$\kappa_{R/P}$	Multigrid restriction (R) and prolongation (P) shock weighting coefficients	
Ω	Angular velocity of impeller in RPM	
ω	Turbulent specific dissipation rate	
σ	Cavitation number	
ε	Turbulent dissipation rate	

C_D	Drag coefficient	
C_L	Lift coefficient	
D	Drag force exerted on blade surface	N
D_{hub}	Diameter of impeller at hub	m
k	Turbulent kinetic energy	J
L	Lift force exerted on blade surface	N
N_{blades}	Number of impeller blades	
p^0	Total pressure	Pa
$pitch$	Tangential distance between camber lines	m
s	Distance from camber line to camber line; $s = pitch$	m

Chapter 5

α	Volume fraction	
Δp	Blade pressure loading	Pa
ΔV_y	Tangiential velocity difference between inlet and outlet	$\mathrm{m\,s^{-1}}$
ρ	Fluid density	$\mathrm{kg\,m^{-3}}$
σ	Cavitation number	
C_p	Pressure coefficient	
$chord$	Axial chord length	m
f	Cascade camber line	
H_y	Distance between leading and trailing edges in tangential direction	m
L	Blade length	m
s	Blade pitch	m
V_∞	Free stream velocity	$\mathrm{m\,s^{-1}}$
V_m	Average meridional velocity across blade	$\mathrm{m\,s^{-1}}$
V_y	Mass averaged tangential velocity	$\mathrm{m\,s^{-1}}$

Chapter 6

Δt	Time step	s
ΔV_y	Tangiential velocity difference between inlet and outlet	$\mathrm{m\,s^{-1}}$
δ	Material dependent impulse threshold	$\mathrm{Pa\,s^{-1}}$
η_C	Cascade efficiency	
σ	Cavitation number	
$\sigma_{3\%}$	Cavitation number at 3% head breakdown	
C_D	Drag coefficient	

C_L	Lift coefficient	
C_p	Pressure coefficient	
$chord$	Axial chord length	m
f_C	Cavity fluctuation frequency	Hz
I_{agr}	Erosive aggressiveness of cavitation	
p_v	Saturation vapour pressure	Pa
T	Total exposure time	s
T_C	Cavity cycle duration	s
V_α	Total vapour volume	m^3
v_{jet}	Micro-jet velocity of collapsing bubble	$m\,s^{-1}$

Chapter 7

Δh	Height difference between pressure sensor and tap	m
ρ	Water density	$kg\,m^{-3}$
σ	Cavitation number	
c	Dissolved oxygen mass concentration	$mg\,L^{-1}$
$chord$	Axial chord length	m
f	Cavity fluctuation frequency	Hz
g	Gravitational acceleration constant	$m\,s^{-2}$
N	Number of blades in cascade tunnel, $N = 6$	
p_v	Saturation vapour pressure	Pa
p_{sensor}	Pressure measured by sensor	Pa
p_{tap}	Fluid pressure at tap location	Pa
$pitch$	Tangential distance between camber lines	m
Q	Volume flow rate	$m^3\,s^{-1}$
$span$	Width of cascade tunnel cross-section	m
T	Water temperature	K
V_x	Axial velocity at cascade inlet	$m\,s^{-1}$
V_y	Tangential velocity at cascade inlet	$m\,s^{-1}$
x	Axial position	m

1 Introduction

To enhance the performance of turbomachinery systems, stages are getting smaller and their rotational speed is increasing. This hike in energy density has a positive impact on cost and efficiency but amplifies the potency of adverse hydrodynamic phenomena such as shocks, secondary flows, backflow or instabilities. For the liquid flow installations, employed in hydraulic power generation (turbines), maritime transport (propellers and water-jets) or across all forms of industrial processes (pumps), cavitation is one of the most problematic occurrences. It corresponds to the formation of vapour bubbles in liquid flow as the local pressure drops below the vaporisation threshold. Bubbles then develop into large scale cavity structures with deleterious effects on the system.

There are a variety of forms to the manifestations of cavitation in hydraulic machinery. As the inlet pressure goes down, vapour first appears in the low pressure cores of blade tip vortices (Figure 1.4a). Further reduction in inlet pressure leads to cavitation in the main flow path. First, under the form of individual travelling bubbles (Figure 1.4b), then as attached cavities on suction surfaces as bubbles grow large enough to coalesce (Figures 1.4c, 1.4d and 1.5). This type of attached or blade cavitation extends until the flow pressure is sufficiently high to drive collapse. It is in that particular region that cavitation damage is strongest. For pumps, backflow cavitation occurs when operating at low flow rates and often constitutes its most visible form. Figure 1.1 is an apt schematic representation of the encountered types of cavitation.

As soon as cavitation appears, *noise* levels rise due to the pressure pulsations emanating from fluctuating bubbles [2]. The noise increase is indissociable from cavitation and often

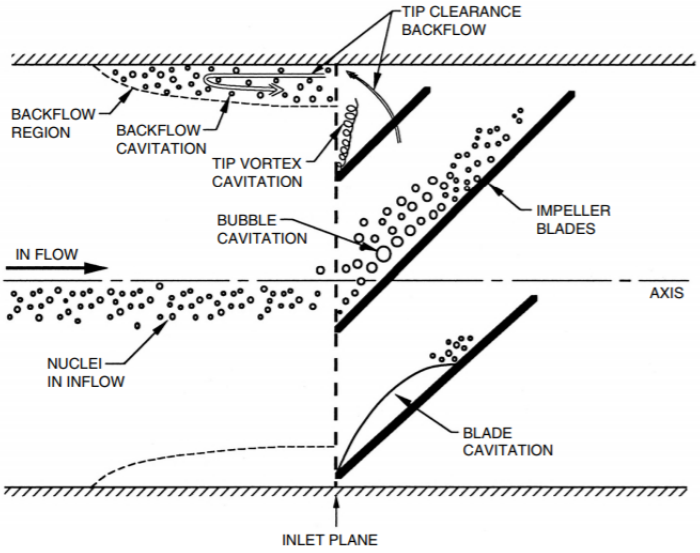

Figure 1.1: Typical forms of cavitation occurring within hydraulic turbomachinery [1]. The schematic depicts an axial flow pump but the listed phenomena, except for backflow cavitation, also appear around propellers and turbines.

constitutes a more reliable measure of inception than visual observation [1]. The problem becomes particularly severe at off-design operation.

Another issue of paramount importance is *erosion*. It is caused by the repeated collapse of bubbles in proximity to solid surfaces. The failure mechanism is that of fatigue as deformations in the solid build up until material is torn off. It is most potent on the suction surfaces around the closure region of attached cavities or where vapour clouds shed by the cavity collapse (Figure 1.7). Erosion is the most problematic of the cavitation induced phenomena because of its complexity and severe impact on component durability.

Once cavitation has reached a critical volume within the main flow path, it downgrades the amount of work transmitted by the stage. *Performance breakdown* is observed in the efficiency, transmitted power and head of hydraulic machines. The character of the drop depends on the type of configuration, on blade design and on flow rate [1, 3, 4]. The breakdown point constitutes the absolute limit of the operating range. Naturally, the lower it sits, the more versatile and economical the stage will be.

The role of the turbomachinery designer, when considering cavitation, is to ensure, for given plant conditions, that (i) the stage is consistently operated above the breakdown point, (ii) it produces minimal noise and (iii) delivers the required life expectancy. For large diameter and low rotational speed turbomachinery systems, cavitation is an issue that only crops up at the low pressure end of the operating range. Its aggressiveness is limited meaning that the designer is only concerned with delivering an adequately low breakdown point. With the increase in

compactness driven by industrial optimisation, cavitation is substantially more problematic: instead of appearing in exceptional conditions, it is a persistent phenomenon with increased damaging potential [5, 6]. In that scenario, it is erosion that turns into the critical obstacle to be addressed as the accelerated deterioration rates caused by increased RPM [7, 8] cancel out the gains in cost and efficiency delivered by the smaller stage. To make the minimisation trend viable, new solutions are needed to dampen the aggressiveness of cavitation erosion.

Experimental research on hydraulic machinery has shown that the intensity of erosion is driven by the characteristics of the cavity structure with shape, unsteadiness and noise playing important parts [7, 8, 9, 10]. One of the distinctive features of attached blade cavities is the large pressure shock at closure. It is caused by the sudden deceleration of liquid as the wall effect created by the vapour sheet vanishes. The thicker the cavity gets, the larger the shock in both amplitude and gradient (see Figure 1.2).

Here, it is advanced that the closure shock is crucial in the aggressiveness of cavitation. Firstly, it is, by definition, superimposed on the region of highest damage. Furthermore, it is understood that erosion is caused by high pressure shock waves emanating from collapsing bubbles and liquid micro-jets impinging onto solid surfaces (see Section 2.2). These mechanisms are driven, among other parameters, by the difference between ambient and bubble pressure. The closure shock means that bubbles collapse in a high pressure environment. With larger amplitudes the aggressiveness of cavitation is accentuated and with sharpness its erosive action is concentrated, accelerating material loss.

To the author's knowledge, the correlation between closure shock and erosion aggressiveness has never been directly investigated. Most characterisations focus on cavitation unsteadiness and cavity shape. This research seeks to address this gap by examining the changes in erosion brought about by changes in the shock profile. The work goes a step further by proposing an unprecedented method to control cavitation erosion on the basis of this relationship. The working philosophy is that by imposing a smooth pressure recovery at cavity closure, the violence of bubble collapse can be attenuated and erosion reduced. The idea is depicted in Figure 1.2 where the original abrupt jump along the suction surface is replaced by a low gradient rise.

To test the hypothesis, cavitating flows characterised by a sharp closure shock are to be compared to smoothed or attenuated cavitation. The inverse design method for blade geometries constitutes the ideal approach. It provides the means to generate profiles that comply to prescribed flow features such as the low gradient recovery. It has already been applied with success to suppress the shock in transonic compressors, eliminate secondary flows and

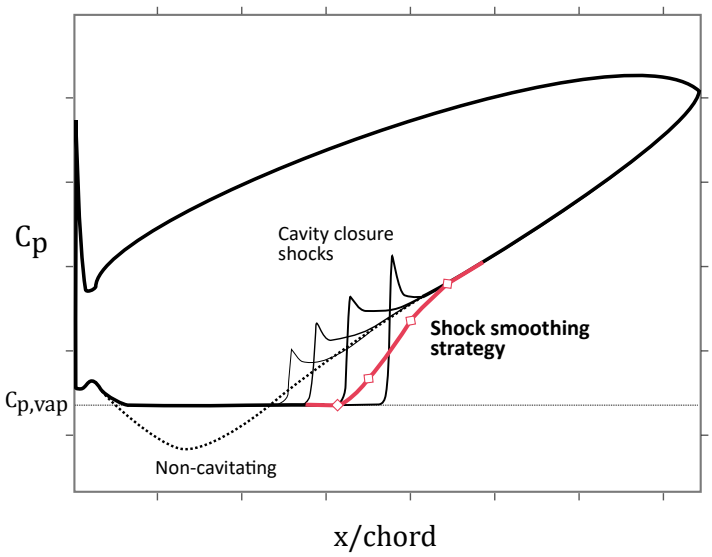

Figure 1.2: Schematic representation of the working hypothesis: a typical blade pressure profile for an impeller stage with growing leading edge cavitation. The assumption is that by smoothing the closure shock (see profile in red) the aggressiveness of erosion can be contained.

delay cavitation breakdown. The method has, however, never been used to tackle erosion or been applied to multiphase flow. A substantial part of the research work, therefore, consists in developing the first inverse design algorithm capable of running in cavitating conditions.

To assess the performance of the produced blades, both numerical and experimental assessments are carried out. The numerical CFD approach serves to characterise the pressure profile, in particular the shock region, evaluate the hydrodynamic performance and use time accurate solutions to apply recent cavitation erosion prediction methods. The computational approach offers incomparable advantages in terms of versatility and cost-effectiveness but its reliability is limited for the high complexity of erosion mechanisms. Experimental analysis is, therefore, an essential step of this research. It serves to measure the response of the designs to cavitation erosion in real conditions and delivers the verdict on the success of the approach.

The idea laid out here addresses the cavitation erosion problem from a new angle by opening the possibility of controlling its aggressiveness through surface pressure. If successful, the work can serve to augment existing design guidelines with a recipe to diminish the erosive intensity of turbomachinery cavitating flows.

1.1 Cavitation in hydraulic machinery

Taking the phase diagram of any pure substance as reference one can infer the possibility of a liquid-to-gas phase change brought about by an isothermal drop in pressure below the vapour

pressure point (see Figure 1.3). This transformation is referred to as cavitation [11, 12]. Boiling, in contrast, describes the phase change obtained by increasing temperature while maintaining constant pressure.

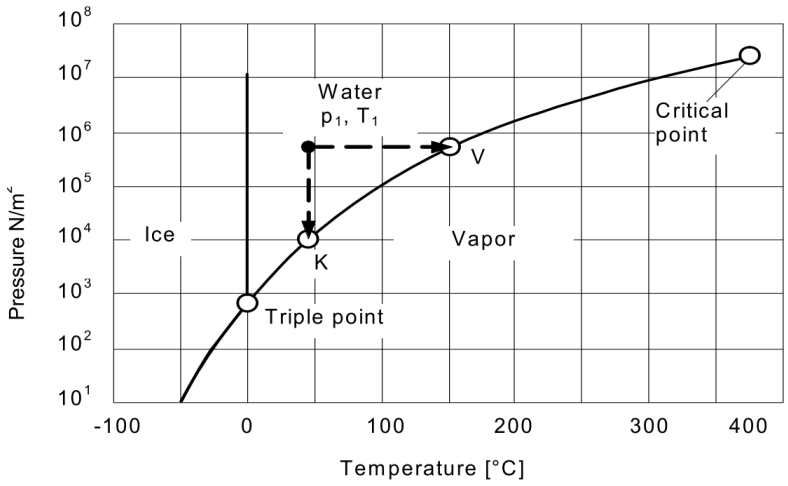

Figure 1.3: Phase diagram for water [3]. The transformation from p_1, T_1 to K corresponds to isothermal cavitation, and from p_1, T_1 to V to isobaric boiling. Purity conditions match those typically found in industrial applications.

This is a broad characterisation of cavitation. It holds for a heterogeneous static environment where the liquid and gas phases are already present and in contact. For pure liquids, on the other hand, extremely large tensions (of the order of 10 MPa) can be withstood before vaporisation [13, 14, 15]. In that scenario, vapour formation only occurs through homogeneous nucleation: an increase in molecular kinetic energy sufficiently strong to break the liquid surface tension at void spaces between molecules.

That level of purity is only attained in extremely well controlled environments. In reality, the pre-existence of microscopic bubbles suspended in the liquid or anchored to either particle impurities or crevices in solid surfaces greatly facilitates vapour formation. For this type of nucleation, termed heterogeneous nucleation, the tensile strength of the liquid-vapour interface is substantially reduced by the asperities of solid surfaces. Under these conditions, it is common to observe cavity growth at pressures along the liquid-vapour demarcation line in Figure 1.3.

This applies to hydraulic machinery, where the untreated liquid contains both solid particles and contaminant gas. Cavitation, therefore, occurs around pressures $p_v - \Delta p_c$. Pressure Δp_c incorporates provisions made for the effect of non-condensable gases and the fact that cavitation may require a minimal volume threshold before detection [11].

Assuming a liquid flowing at free-stream pressure p_∞ and velocity U_∞, one introduces the

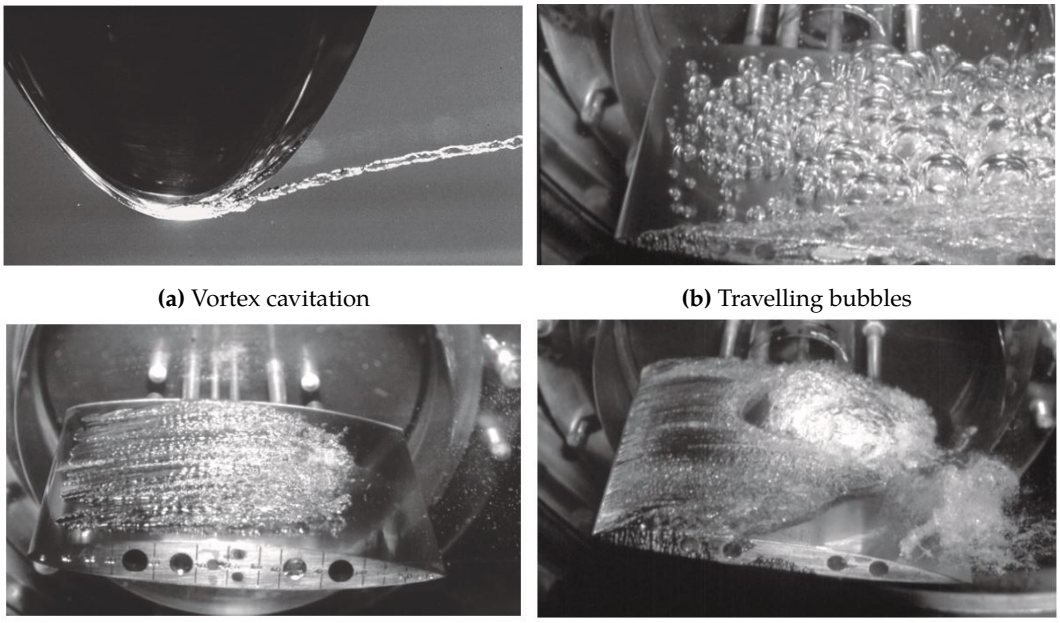

(a) Vortex cavitation

(b) Travelling bubbles

(c) Partial or steady sheet cavity

(d) Cloud cavity shedding from sheet cavity

Figure 1.4: Typical manifestations of large cavity structures in hydraulic machinery [16].

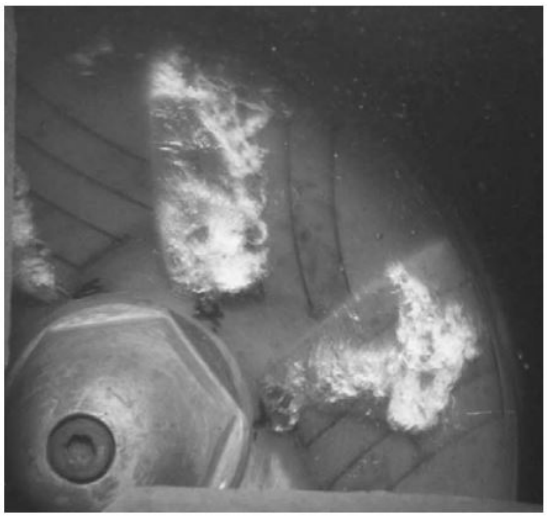

Figure 1.5: Attached cavity at the leading edge of a centrifugal pump [3].

non-dimensional cavitation number σ to characterise its cavitation potential

$$\sigma = \frac{p_\infty - p_v}{\frac{1}{2}\rho_L U_\infty^2} \tag{1.1}$$

where ρ_L is the liquid density. In its construction, it is analogous to the pressure coefficient

$$C_p = \frac{p - p_\infty}{\frac{1}{2}\rho U_\infty^2} \tag{1.2}$$

but its interpretation and purpose is inverted: while C_p produces a distribution independent of the free-stream conditions (constant under changes in p_∞ and U_∞), σ determines whether cavitation occurs for said conditions (dependent on p_∞ and U_∞). At cavitation inception, the minimal static pressure point in the flow is by definition equal to p_v. From equations 1.1 and 1.2, it transpires that

$$\sigma_i = -C_{pmin} \tag{1.3}$$

such that for a given geometry one can deduce the inception free-stream state from the non-cavitating pressure distribution.

For hydraulic machinery installations, the pressure and velocity at the intake are not readily accessible. Instead, the *Net Positive Suction Head* (*NPSH*) number is used to measure the difference between the total plant head and the vapour head:

$$\begin{aligned} NPSH &= H_p - H_v \\ &= \left[\frac{p}{\rho g} + (Z - Z_{ref}) + \frac{C^2}{2g}\right]_p - \frac{p_v}{\rho g} \end{aligned} \tag{1.4}$$

One will distinguish between the *available* $NPSH$ (or $NPSH_A$), which indicates the pressure level the plant is able to provide and the *required* $NPSH$ or ($NPSH_R$) which is specific to the machine and can vary according to the performance or durability criteria under consideration. The form given by equation 1.4 corresponds to $NPSH_A$.

The $NPSH$ range is essential to hydraulic turbomachinery design and operation because it determines the conditions, not at which cavitation appears, but when it becomes problematic (see Figure 1.6). The nuance is important as it is increasingly frequent to find high speed machines that operate at pressures below the cavitation inception condition, $NPSH_i$. Determining the $NPSH_R$ number depends on the chosen cavitation criterion. If judging performance it may correspond to a 1%, 3% or x% breakdown. Alternatively, noise or erosion can be the selected parameter. In the latter case, $NPSH_R$ is tailored to maximum material loss (measured in mass or volume) or to component life (measured in operating hours)[3].

The principal message conveyed in Figure 1.6 is that the breakdown point is significantly further down the $NPSH$ range than the inception point ($NPSH_i$ can be between two to five times $NPSH_{3\%}$). Between, $NPSH_i$ and $NPSH_{3\%}$ cavitation occurs in the form of attached or tip vortex cavitation. Increased compactness means that the noise and erosion generated by these types of manifestation reaches excessively high levels.

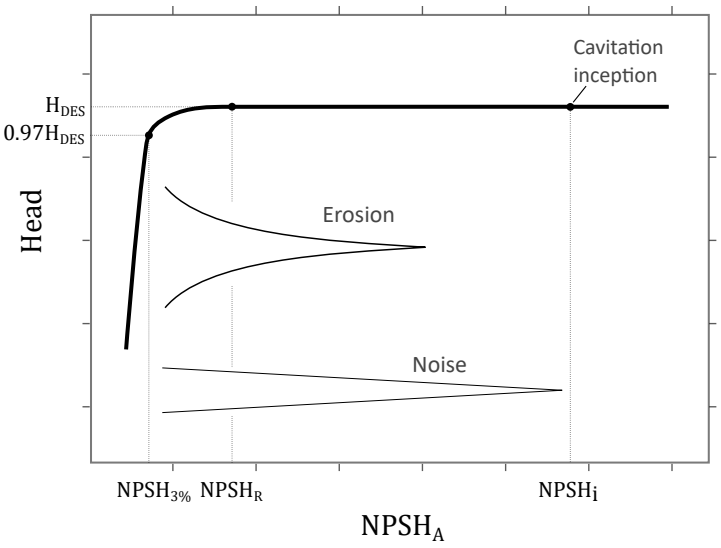

Figure 1.6: Characteristic example of the NPSH profile for an impeller stage. Despite the presence of cavitation, the head does not deviate from the designed value H_{DES} until further down the scale. Erosion and noise, on the other hand, grow in intensity with the size of the cavity.

(a) Mixed-flow pump **(b)** Francis turbine

Figure 1.7: Cavitation damage on impeller (1.7a) and runner blades (1.7b) [1].

1.2 Scope and Methodology

The development of a comprehensive numerical tool for turbomachinery design needs to incorporate a three-dimensional treatment of the flow field. It also has to take into account the variety of geometry types: radial, mixed or axial, as well as the possibility of off-design configurations. The complexity of cavitating flow in conjunction with the ambition of this research imposes a restriction as to the achievable extent of this investigation within the framework of a PhD. A frequent simplification is to consider a two-dimensional formulation for the initial venture into a novel area. So, instead of the 3D rotating blade channel, the studied flow case is a stationary two-dimensional cascade (see Section 4.1 for geometry).

One may question the validity of this translation, particularly in its ability to provide useful

insight when 3D effects are neglected. The issue arises especially at the experimental stage where 2D flow cannot be replicated exactly. This essentially boils down to determining whether or not spanwise variations are important. Put simply, the answer to this is that they are not, for the following reasons:

- considering that the cascade is a transformation of axial-flow type machines, streamwise variations in these type of mechanisms are far greater than those in the spanwise direction; the former are, therefore, the dominant agent in cavity dynamics and ensuing erosion,
- by selecting the appropriate span length and cascade height it is possible to construct an experimental rig wherein the counter-streamwise variations are negligible; this will be a key requirement of the experimental platform.

Another limitation concerns the development of the inverse design solver. The fluid flow equations it considers are the inviscid Euler equations instead of the full Navier-Stokes system. Compressibility is taken into account but viscous and turbulent effects are neglected from the computation. The issue is that reliable inverse design techniques which include turbulent treatment are not currently at maturity. Constructing such a tool is an excessively demanding endeavour in itself.

Fortunately, the absence of viscosity or RANS turbulence from the numerical method should not dramatically affect the reliability of the designs. Cavitation is indeed driven by inertial rather than viscous effects such that the inclusion of diffusive terms is of no added value. To illustrate the validity of the inviscid approach for steady state cavitation calculations, results from the *in-house* solver are compared to RANS solutions in Section 4.5.

It is worth expanding on the steps that constitute the research presented here:

- *Inverse solver development* (Chapter 3): the first step consists in constructing the numerical approach using techniques drawn or adapted from literature. The solver must be able to model cavitating flow and handle large differences in flow regime (hypersonic in the cavity region, low speed in the liquid phase), all the while providing high speed and robustness performance. A crucial component is the selection of the cavitation model. Numerical schemes are then chosen to maximise compatibility with cavitating flow in terms of accuracy and robustness.
- *Solver verification* (Chapter 4): the developed code is validated against numerical solutions obtained from industry standard CFD applications. Solver testing also serves to select the numerical techniques that perform best for the studied configuration.

- *Blade generation* (Chapter 5): geometries are produced using the inverse solver in cavitating conditions with the smooth closure shock imposition. Additional profiles are generated following global modifications of the pressure profile.
- *Numerical* (Chapter 6) *and experimental* (Chapter 7) *assessment of designs*: the performance of the produced blades is evaluated both numerically and experimentally. With the numerical CFD approach, hydrodynamic performance metrics such as lift, drag or efficiency are evaluated. Newly developed erosion prediction techniques are also put to application. The experimental analysis provides a more reliable assessment of the erosion performance in real conditions. The combined results of the analyses serve to determine the success of the hypothesis.

The work essentially divides itself into three major stages: inverse solver development, blade generation and performance assessment.

2 Literature Review

The review presented here covers the practices currently in use for modelling cavitation in CFD calculations of turbomachinery flows. It also lays out the mechanisms responsible for erosion and presents various aggressiveness prediction techniques. The design procedure for hydraulic machinery is described, with emphasis on the *inverse* approach and on the methods used to suppress the effects of cavitation.

2.1 Numerical Modelling of Cavitation

The inverse design methodology consists in wrapping a geometry generator over the core CFD solver. To apply the method in cavitating conditions the CFD part of the solver must be able to model the features of the phase changing flow. Design requirements mean that the treatment of cavitation must be fast to allow rapid iterations, and respond well to changes in geometry. Consequently, the features that are sought after are accuracy, efficiency and robustness.

Both homogeneous and non-homogeneous approaches to numerical cavitation have been developed. The multiphase (non-homogeneous) class of methods includes all the techniques that rely on two or more separate sets of properties to treat each phase or species. In this configuration, the computational domain is split into independent phase regions which grow or collapse according to the surrounding and internal flow field. Sophisticated interface models are, therefore, required to handle mass transfer and to track the changes in boundary geometry. This type of method is used extensively for individual bubble simulations. These focus on collapse or bubble interaction phenomena which occur over small scales in time and

space. Variations exist in the treatment of the interface: Osterman et al. [17] and Koukouvinis et al. [18] employ the Volume Of Fluid (VOF) method to study bubble collapse near walls and under gravity respectively, Hawker and Ventikos [19] consider front tracking techniques for bubble and wave interaction, Lauer et al. [20] use the level set approach to simulate bubbles attached and detached to the wall.

For flowing liquids, the picture is considerably different: instead of the well-defined immiscible segregation of phases, cavitation manifests itself as clusters containing a large number of bubbles moving with the liquid. True multiphase treatment where the interior and exterior of bubbles are governed by different equations is unrealistic, not to mention the difficulty current interface models face at handling coalescence. Works by Chen and Heister [21] and Deshpande et al. [22] have, however, adopted the non-homogeneous approach to simulate attached cavities. The interface is constructed around the entire cavity by assuming constant internal pressure and implementing a wake closure model. The issue with this technique is that it disregards the heterogeneity within the cluster and is incapable of following bubbles that detach from the surface [23].

The alternative homogeneous approach is a simplified interpretation of cavitating flow. It is best understood by considering an arbitrary volume of cavitating liquid. By definition, the volume contains both vapour bubbles and pure liquid. One defines the average density as the characteristic property of said volume. It varies with the internal vapour content and is naturally bounded by the pure vapour and pure liquid density values. An important assumption is the ubiquitous presence of bubbles which allows the entire flow domain to be governed, as a single continuum, by the same equations expressed in terms of the volume averaged density. Cavities automatically correspond to the flow regions where the density is lower than its pure liquid state. The homogeneous formulation was first proposed by Delannoy and Kueny [24] as a means to study unsteady cavitation. To determine the volumetric vapour content – or more simply the vapour volume fraction – the authors construct a direct law for density in terms of pressure. Concurrently, Kubota et al. [25] chose to use a surface tension free form of the Rayleigh-Plesset equation to correlate ambient pressure with bubble radius and, by extension, volume. The relation between pressure, which becomes the determinant parameter, and density variations constitutes the central mechanism of homogeneous cavitation models.

Despite the reduction of the multiphase problem to a single variable density fluid, homogeneous models are used extensively in research and in industry to predict cavitating flows around hydrofoils, nozzles, impellers, propellers or turbines. Computationally, the effort required is of the same order of magnitude as for single phase compressible flows. Furthermore,

they are not marred by coalescence or detachment issues as cavities (bubble clusters) are virtually dissolved in the liquid. The drawback is the masking of bubble dynamics which drive erosion and vibration. Nevertheless, cavitation erosion models based on homogeneous calculations are being developed. Furthermore, the vast hardware capacity needed for bubble-scale multiphase cavitation in flowing liquids nullifies any argument for the non-homogeneous approach.

The Delannoy and Kueny [24] and Kubota et al. [25] models correspond to the first instances of the two contrasting approaches to homogeneous cavitation modelling: *void fraction transport* and *pressure-density coupling*. The distinction is based on the formulation of the pressure and density/volume fraction relationship:

1. *void fraction transport equation* approaches append the Navier-Stokes governing system with an equation of the form

$$\frac{\partial \rho_l \alpha_l}{\partial t} + \frac{\partial \rho_l \alpha_l u_j}{\partial x_j} = \dot{m}^+ + \dot{m}^- \tag{2.1}$$

   designed to advect and produce liquid or vapour volume fraction, $\alpha_l = 1 - \alpha_v$, from condensation and vaporisation terms $\dot{m}^+$ and $\dot{m}^-$. The definitions of the LHS source terms differ from model to model. The rest of the governing system, i.e. the Navier-Stokes equations, holds its conventional form and is solved using the mixture density

$$\rho = \rho_l \alpha_l + \rho_v \alpha_v \tag{2.2}$$

2. *pressure-density state law* methods devise a relation that expresses the density in terms of the pressure

$$\rho = f(p) \tag{2.3}$$

   and use this relation as closure for the mixture Navier-Stokes problem. The state law is applied uniformly over the entire domain regardless of variations in flow state, earning the alternative *barotropic model* designation. For this class of approach, the density is calculated directly and the volume fraction is extracted from equations similar to 2.2.

Instances of both homogeneous model categories are detailed here.

2.1.1 Transport Equation Models

Rayleigh-Plesset source terms

The Kubota et al. [25] model, although initially expressed in the Poisson form of the Navier-Stokes equations, belongs to the *transport* type of approaches. The shortened Rayleigh-Plesset equation is used as a means to evaluate the bubble radius R

$$R\frac{d^2R}{dt^2} + \frac{3}{2}\left(\frac{dR}{dt}\right)^2 = \frac{p_v - p}{\rho_l} \tag{2.4}$$

The authors make another strong simplification which consists in assuming a constant bubble density n_B. The vapour volume fraction is then given by

$$\alpha_v = V_B n_B = \frac{4}{3}\pi R^3 n_B \tag{2.5}$$

where V_B stands for the volume of a single bubble. The rate of vaporisation $\dot{m}^-$ is deduced by combining equations 2.4 and 2.5. In the original version of the model the resulting governing equations concatenate the bubble radius differential equation into the viscous Poisson pressure formulation. In [26], Zwart et al. reduce the complexity of the model by eliminating the second order term in equation 2.4. The variation in time of the bubble radius and bubble mass become simply

$$\frac{dR}{dt} = \left[\frac{2}{3}\frac{p_v - p}{\rho_l}\right]^{\frac{1}{2}} \quad \text{and} \quad \frac{dm_B}{dt} = 4\pi R_B^2 \rho_v \left[\frac{2}{3}\frac{p_v - p}{\rho_l}\right]^{\frac{1}{2}} \tag{2.6}$$

so that the formulation of $\dot{m}^-$ is made completely explicit

$$\dot{m}^- = n_B \frac{dm_B}{dt} = \frac{3\alpha_v}{R_B}\rho_v \left[\frac{2}{3}\frac{p_v - p}{\rho_l}\right]^{\frac{1}{2}} \tag{2.7}$$

The authors adjust the vaporisation rate to take into account the coalescence of bubbles by substituting α_v for $\alpha_{nuc}(1-\alpha_v)$ in equation 2.7, where α_{nuc} is the volume fraction at nucleation. The remaining R_B is taken as the radius at nucleation. Condensation is captured by generalising 2.7 and introducing empirical constants C_v and C_c. The final vaporisation and condensation

terms of the Zwart et al. model are:

$$\begin{aligned} \dot{m}_Z^- &= -C_Z^v \frac{3\alpha_{nuc}(1-\alpha_v)\rho_v}{R_B}\left[\frac{2}{3}\frac{p_v - p}{\rho_l}\right]^{1/2} && \text{if } p < p_v \\ \dot{m}_Z^+ &= C_Z^c \frac{3\alpha_v \rho_v}{R_B}\left[\frac{2}{3}\frac{p - p_v}{\rho_l}\right]^{1/2} && \text{if } p > p_v \end{aligned} \tag{2.8}$$

Typical values of the model constants are $C_Z^v = 50$, $C_Z^c = 0.01$, $R_B = 1 \times 10^{-6}$ m and $\alpha_{nuc} = 5 \times 10^{-4}$.

In [27], Singhal et al. derive their mass transfer model from the same simplified Rayleigh-Plesset equation. The method extends the Kubota et al. technique by taking into account several supposedly influential factors. The first is the definition of the nucleation radius R_B which is given in terms of the surface tension. The relative velocity between the vapour and liquid phases is also included in the model and is correlated to the turbulent kinetic energy. It is also argued that turbulence affects the phase transition such that the critical vapour pressure is modified to

$$p_c = p_v + 0.39\frac{\rho k}{2} \tag{2.9}$$

where k is the turbulent kinetic energy. Finally, the presence of contaminant non-condensable gas is acknowledged and implemented into the volume fraction balance such that $1 = \alpha_l + \alpha_v + \alpha_g$. The complete Singhal et al. vaporisation and condensation rates are

$$\begin{aligned} \dot{m}_S^- &= -C_S^v \frac{\sqrt{k}}{S}\rho_l\rho_v\left[\frac{2}{3}\frac{p_v - p}{\rho_l}\right]^{1/2}\left(1 - \frac{\alpha_v\rho_v}{\rho} - \frac{\alpha_g\rho_g}{\rho}\right) && \text{if } p < p_c \\ \dot{m}_S^+ &= C_S^c \frac{\sqrt{k}}{S}\rho_l\rho_l\left[\frac{2}{3}\frac{p - p_v}{\rho_l}\right]^{1/2}\frac{\alpha_v\rho_v}{\rho} && \text{if } p > p_c \end{aligned} \tag{2.10}$$

where S is the surface tension of the liquid and the index g represents the non-condensable gas.

With this model, a non-trivial layer of complexity is added to the calculation of the mass transfer rates. The performance gain, however, is not evident. To begin with, the manner in which non-condensable gas is included does not align with its known effect. Instead of facilitating cavitation [11], it reduces the vaporisation rate (see equation 2.10). Furthermore, independent works by Morgut et al. [28] and Ducoin et al. [29] tasked with comparing *transport equation* cavitation models did not reveal noticeable improvements on the Zwart et al. approach.

Pressure difference source terms

The alternative approach to *transport* model development is based on the growth of global cavities rather than single bubbles. The fundamental difference is that the vaporisation and condensation rates are driven by the ambient to vapour pressure difference instead of the square root of said difference. Merkle et al. [30] are the first to propose this type of implementation. In their model, the vaporisation and condensation definitions are symmetrical

$$\begin{aligned} \dot{m}_M^- &= \frac{C_M^v \rho_l \rho_l \min(p - p_v, 0)(1 - \alpha_v)}{0.5 \rho_l U_\infty^2 \rho_v t_\infty} && \text{if } p < p_v \\ \dot{m}_M^+ &= \frac{C_M^c \rho_l \max(p - p_v, 0) \alpha_v}{0.5 \rho_l U_\infty^2 t_\infty} && \text{if } p > p_v \end{aligned} \tag{2.11}$$

where the numbers U_∞ and t_∞ are the free-stream flow velocity and mean flow time scale. For water, the model constants are taken to be $C_M^v = 1$ and $C_M^c = 80$ as recommended in [31, 30, 32].

The model developed by Kunz et al. [33] and tested in [34, 28] resembles the Merkle et al. technique except for the condensation term which is replaced by a simplified Ginzburg-Landau phase transition potential:

$$\begin{aligned} \dot{m}_K^- &= \frac{C_K^v \rho_v \alpha_l \min(p - p_v, 0)}{0.5 \rho_l U_\infty^2 t_\infty} && \text{if } p < p_v \\ \dot{m}_K^+ &= \frac{C_K^c \rho_v \left(\alpha_l - \alpha_g\right)^2 \left(1 - \alpha_l - \alpha_g\right)}{t_\infty} && \text{if } p > p_v \end{aligned} \tag{2.12}$$

Provisions are also made for non-condensable gas. In this implementation, α_g hinders condensation which automatically means that cavitation increases with larger α_g. This constitutes a more valid interpretation of the effect of contaminant gas than the model proposed by Singhal et al.. In [33], model constants are $C_K^v = 100$ and $C_K^c = 100$.

Both Rayleigh-Plesset and large scale *transport* type models are highly sensitive to the condensation and vaporisation constants C^c and C^v. A common shortcoming is the under-prediction of the cavity length when comparing to experimental data. Morgut et al. [28] show that the performance can be enhanced by applying an optimisation strategy to fine tune the constants of the Zwart, Singhal and Kunz models. The issue is that this approach is associated to individual geometries and cannot be generalised. The differences brought about by the addition of turbulent effects, surface tension or by abandoning the Rayleigh-Plesset approach are negligible for steady state computations over two-dimensional hydrofoils. Visible

differences do start to arise when simulating unsteady flows. The most notable discrepancy is the disparity in shedding frequency with improved performance delivered by the Merkle et al. model for a 2D hydrofoil [29]. However, the frequency is also dependent on the turbulence model and on proper discretisation [35].

2.1.2 Pressure-Density State Law Models

Sinusoidal barotropic state law

In [24], Delannoy and Kueny investigate the performance of a barotropic state law to calculate unsteady cavitating flow around a hydrofoil. At the time, the approaches to simulating attached cavities were based on potential flow and cavity closure models which poorly capture separation and detachment. With the increase in competitiveness of Navier-Stokes computations for unsteady compressible flow, the authors chose to abandon the conventional techniques and devise a bespoke pressure-density law. The development of barotropic laws for multiphase bubbly flows predates the work done in [24] (see [11, 36]) but is until then only applied to one-dimensional calculations or to acoustic propagation modelling.

Delannoy and Kueny construct their state equation of state by implementing the Tait law (see [37]) to model the pure liquid phase, the ideal gas law for the pure vapour phase, and use a sinusoidal law in the transition zone to join the two states (see Figure 2.1). A crucial feature of the Delannoy model is the maximum slope of the transition curve which is equal to $1/c_{min}^2$, where c is the mixture speed of sound. Its value is adjusted in accordance to fluid properties. In [38], Goncalves and Patella formulate the sinusoidal transition state in terms of the vapour volume fraction α_v

$$p = p_v + \left(\frac{\rho_l - \rho_v}{2}\right) c_{min}^2 \arcsin\left(A\left(1 - 2\alpha_v\right)\right) \tag{2.13}$$

where c_{min} is the minimum speed of sound evaluated at $p = p_v$, and the constant A serves to prevent infinite sound speeds at singularities. The authors enforce conditions on A and c_{min} to ensure continuity of the pressure and of the speed of sound across phases.

Mixture stiffened gas equation of state

Goncalves and Patella also compare the Delannoy and Kueny law to a mixture of stiffened gas equation of state (see [39]):

$$p = \left(\gamma(\alpha_v) - 1\right) \rho \left(e - q(\alpha_v)\right) - \gamma(\alpha_v) p_\infty(\alpha_v) \tag{2.14}$$

where $\gamma(\alpha_v)$ is the mixture polytropic coefficient, e is the internal energy, q is the energy at a reference state and p_∞ is a constant that represents molecular attraction. The stiffened gas formulation is the only model that takes into account the internal energy of the fluid. To meet thermodynamic consistency, i.e. entropy growth, constraints are imposed on the manner pressure, density and temperature vary with each other.

The authors show that both the Delannoy and Kueny barotropic law and the Goncalves and Patella stiffened EOS predict the steady state cavity length accurately. However, the stiffened gas method yields an excessively low pressure inside the cavity and cannot capture the re-entrant jet responsible for cavity unsteadiness.

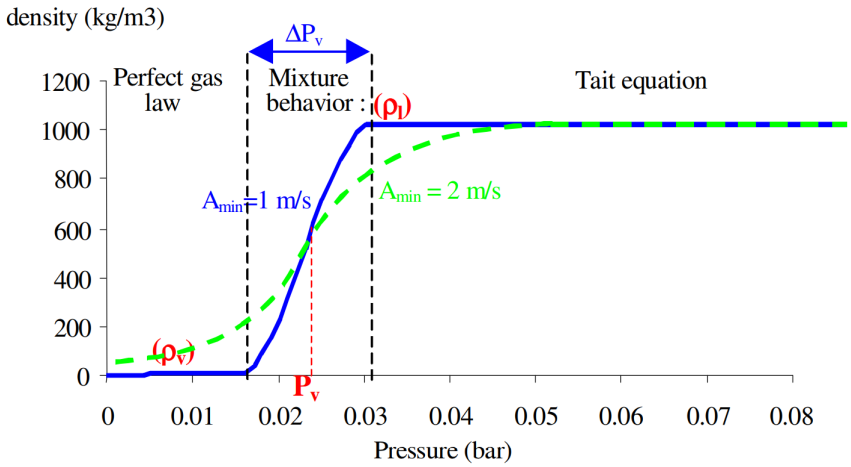

Figure 2.1: Delannoy and Kueny barotropic state law for water at 20° [40].

Blended fully compressible law

In [41], Iga et al. develop a barotropic state law which, instead of the separate liquid, transition and vapour formulations, merges the transition and pure liquid states into a single law. The liquid phase is modelled by the Tammann equation which confers compressibility to the fluid [37]:

$$p_l + p_c = \rho_l K(T_l + T_0) \tag{2.15}$$

The pressure, density and temperature of the liquid are p_l, ρ_l and T_l. Symbols p_c, T_0 and K are pressure, temperature and liquid constants of the model. It is assumed that the pure vapour phase behaves as an ideal gas

$$p_v = \rho_v R_v T_v \tag{2.16}$$

From $\rho = (1 - \alpha_v)\rho_l + \alpha_v\rho_v$ and using the mass fraction γ definitions

$$\rho(1 - \gamma) = (1 - \alpha_v)\rho_l \quad \text{and} \quad \rho\gamma = \alpha_v\rho_v \tag{2.17}$$

The final mixture state law is given by:

$$\rho = \frac{p(p + p_c)}{K(1 - \gamma)p(T + T_0) + R\gamma(p + p_c)T} \tag{2.18}$$

where it is assumed that local thermodynamic equilibrium holds, i.e. $p = p_l = p_g$ and $T = T_l = T_g$. The equation of state given by 2.18 is applied at pressures above saturation vapour pressure. Below that, the density is given by the ideal gas law for vapour (equation 2.16). Another specificity of the Iga et al. model is that it takes into account the advection of vapour by appending the Navier-Stokes equations with a transport equation of the form

$$\frac{\partial\rho\gamma}{\partial t} + \frac{\partial\rho\gamma u_j}{\partial x_j} = 0 \tag{2.19}$$

The Iga et al. model can therefore be considered a hybrid of the two schools of homogeneous models.

In [42], Nohmi et al. enhanced the model by acknowledging the presence of contaminant air in the mixture. The result is a modified barotropic state law

$$\rho = \frac{(p + p_c)(p - p_v)}{(1 - Y)(p - p_v)K(T + T_c) - Y\rho_v K(T + T_0)R_a T + Y(p + p_c)R_a T} \tag{2.20}$$

where R_a and R_v are the ideal gas constants for air and vapour respectively, and Y, the mass fraction of air in the mixture, has taken the place of γ. Its value is held constant at $Y = 1 \times 10^{-5}$. The resulting state equation is referred to as the *Tohoku-Ebara* (TE) model as it originates from the collaboration between the university and company.

The Iga et al. [41] type pressure-density coupling carry a non-negligible quality: no artificial behaviour is imposed on the transition from liquid to vapour. Instead of the sinusoidal curve inserted in [24], the density variation is deduced from volume and mass equilibrium.

2.1.3 Shortcomings and Benefits of Cavitation Modelling Techniques

It has been shown that vorticity production is a crucial feature governing the behaviour of quasi-stable cavities [29]. Its strength is dependent on the baroclinic torque

$$\frac{1}{\rho^2}\nabla\rho \times \nabla p \tag{2.21}$$

With *pressure-density coupling* cavitation models the pressure and density gradients are aligned by definition. The vorticity produced through baroclinity is therefore equal to zero. *Transport equation* models do not suffer from this limitation as the density is dependent not just on the vaporisation and condensation rates but also on the convective term.

On the other hand, *transport* models assume that the pure liquid or vapour phases are fully incompressible. This is particularly problematic as liquid compressibility in particular significantly affects cavitation inception and growth. This characteristic is taken into account in all of the *pressure-density* laws laid out here. Furthermore, one can argue that the baroclinity shortcoming is only an issue for unsteady break-off calculations. For steady-state attached cavitation, *pressure-density* models provide a level of accuracy which matches and sometimes surpasses mass transport models, as shown in [43].

To summarise, *transport* models offer the advantage of capturing unsteady cavity behaviour, whereas *pressure-density coupling* models provide higher steady state accuracy. In this study, both steady-state and time-resolved solutions will be sought after. The first serve the inverse design methodology, the second are needed to assess cavitation performance. The natural way forward consists in implementing the TE state law (equation 2.20) into the in-house inverse design solver and run the time-resolved simulations using the Zwart et al. vaporisation and condensation terms (equation 2.8).

A comparative study of the TE and Zwart et al. models is carried out by the present author in [44] on a stationary cascade (the same assessment is presented in Section 7.12c). The main difference is the offset in inception point: higher σ for TE than for Zwart. At equivalent conditions, the offset translates to an increased cavity length and closure shock amplitude for the TE solution.

2.2 Cavitation Erosion Mechanisms

2.2.1 Single Bubble Collapse

The Rayleigh-Plesset equation is commonly accepted as the fundamental mathematical model to describe the behaviour of single spherical bubbles [11, 45]. It is derived by considering the forces that drive the movement of the interface separating the gas from the liquid. These include conservation of mass and momentum, evaporation and condensation, as well as surface tension. The resulting expression is given by:

$$\frac{p_B(t) - p_\infty(t)}{\rho_L} = R\frac{d^2R}{dt^2} + \frac{3}{2}\left(\frac{dR}{dt}\right)^2 + \frac{4\nu_L}{R}\frac{dR}{dt} + \frac{2S}{\rho_L R} \tag{2.22}$$

where p_∞ and p_B are the liquid and bubble pressures respectively, ρ_L and ν_L are the liquid density and kinematic viscosity, and S is the surface tension.

Erosion occurs when bubbles collapse and rebound in proximity to solid surfaces. It has been shown that damage is caused by two mechanisms: the propagation of a pressure shock wave and the impact of a liquid micro-jets [11]. The strength of the pressure wave is determined by the internal bubble pressure p_{max} when it reaches its minimum radius. From the Rayleigh-Plesset equation, one finds that

$$p_{max} \propto (p_\infty - p_v)^k \tag{2.23}$$

where p_{max} is the pressure of the gas in the bubble, p_∞ is the pressure of the liquid, p_{vap} is the vapour pressure and k is a positive number. The computations run by Hickling and Plesset [46] addressing the flow in the vicinity of a collapsing bubble wall also provide an approximate relation for the amplitude of the pressure wave emitted at collapse and at a distance of r, with

$$p_p \approx 100 R_M p_\infty / r \tag{2.24}$$

R_M being the maximum bubble radius.

For the liquid micro-jet, the erosive potential is dependent on the speed of the moving front.

When it impacts the opposite side of the collapsing bubbles, the velocity v_{jet} is given by [11]

$$v_{jet} = \xi\sqrt{\Delta p/\rho_L} \tag{2.25}$$

where ξ is a constant (with values varying from 7 to 9 depending on the shape of the bubble and its distance from the wall [11]), and $\Delta p = p_\infty - p_v$ corresponds to the difference in environmental pressures between the equilibrium state and the collapse.

The noise due to cavitation is produced by the cyclical emission of large pressures resulting from the compression of bubble contents. Brennen [11] quantifies the radiated acoustic pressure of a single bubble in terms of the volume change, allowing us to write

$$p_a \propto \frac{d^2V}{dt^2} \tag{2.26}$$

Analysis of the Rayleigh-Plesset equation shows that the rate of change of bubble radius $\dot{R}$ during growth tends to

$$\dot{R} \rightarrow \left[\frac{2}{3}\frac{(p_{vap} - p_\infty)}{\rho_L}\right]^{1/2} \tag{2.27}$$

and that, more importantly, during collapse it can be approximated by

$$\dot{R} \propto R^{-3/2}(p_\infty - p_{vap})^{1/2} \tag{2.28}$$

The principal observation from relations 2.24 to 2.28 is that the larger the difference between environmental and vapour pressure is, the stronger the adverse cavitation effects will be. These observations are made for bubbles in static conditions but hold true for situations where pressure gradients are present. This is demonstrated by Tinguely [47], who experimentally assesses the collapse of single cavitation bubbles in water flowing around a truncated NACA0009 hydrofoil or subject to a varying hydrostatic pressure gradient. The author shows that the volume of the collapse micro-jet scales with the pressure gradient

$$\Omega_{jet} \propto \frac{\left|\nabla p\right| R_{max}}{\Delta p} \tag{2.29}$$

and that the energy imparted to the shock wave increases with the pressure difference $\Delta p =$

$p_\infty - p_v$.

These correlations support the approach adopted in this work. When a sharp shock prevails at cavity closure, the bubbles travel from a low pressure zone where $p \approx p_v$ to the high pressure region where violent collapse is triggered. By softening the gradient at closure, the gap between environmental and vapour pressure at collapse is not as large. As shown here, this positively affects the magnitude of the pressure wave, the speed and volume of the micro-jet and the production of noise.

2.2.2 Large Cavity Erosion and Aggressiveness Prediction

For the large cavity structures found in hydraulic machinery, a number of experimental assessments have been carried out to identify the processes that lead to erosion. Avellan and Dupont [7] examine the effects of cavitation unfolding within a centrifugal impeller, a Francis turbine runner and a NACA009 hydrofoil profile. Damaged regions are located at the wake of leading edge attached cavities where transient U-shaped vapour structures collapse. From Laser Doppler Anemometry (LDA) measurements carried out on the hydrofoil, the authors were able to correlate the vorticity of the shed structures to the energy produced in the closure region of the cavity. From parallel research on vortex cavitation collapse [48], it is advanced that material damage is caused by the pressure wave emanating from the collapsing vortical cavities. This means that a higher shedding frequency leads to more aggressive cavitation. The results match the experiments of Chan [8], who examines the damage caused by sheet cavitation on centrifugal impellers. From tests at varying NPSH numbers and RPM, the author demonstrates that cavities of the same volume can vary in cloud formation and shedding frequency. The implication is that erosion aggressiveness does not only depend on cavity size but also on its intrinsic dynamics.

A stochastic approach is adopted by Dular et al. [9]. Visual recordings of the attached cavity on a circular leading edge hydrofoil are taken and the unsteady regions are indicated by the image variance. To measure erosion the authors proceed by counting the pits formed on the copper surface film. The conclusion of the study is that cavitation erosion intensity and unsteadiness are correlated. In a subsequent paper, Dular et al. [49] expand on their findings by proposing a sequence of events that constitute the erosion mechanism. Their approach considers the impinging micro-jet resulting from collapsing surface bubbles to be the main cause of damage. Unlike in [7], the authors follow the findings of Brennen [11] and Shimada et al. [50] who suggest that the pressure wave is quickly attenuated but that it triggers the collapse of bubbles in proximity to the solid surface.

These attempts at identifying the mechanisms governing erosion are examples of the two opposing schools of thought:

- *micro-jet water hammer* induced deformation,
- *pressure wave* induced deformation.

Proponents of the first advance that the pressure wave is excessively dampened by the liquid and only serves to produce eroding micro-jets [49, 50, 51]. The others suggest that the pressure wave emitted by collapsing clouds is responsible for most of the damage [7, 52, 53, 54, 35, 55]. This has given rise to a variety of approaches to predict the aggressiveness of cavitation. Here, the methods of interest are those that can be coupled to CFD calculations. Earlier techniques [56, 57, 52] based on similarity laws and intended to be used in combination with prototype testing are not considered.

Micro-jet based erosion predictors

The work, already mentioned here, by Dular et al. [49] exploits the vapour volume variance correlation and proposed micro-jet formation mechanism to develop an erosion aggressiveness prediction method of the first category. It works by evaluating the intensity of each of the phenomena that lead to the formation of pits: wave emitted from cloud collapse, attenuation of the pressure wave, micro-jets forming near solid surfaces and material deformation. The amplitude of the wave is determined using the variance of the vapour fraction to indicate the frequency of collapse events and their strength. The velocity of the jet is then given by the Plesset and Chapman [58] relation

$$v_{jet} = 8.97\gamma^2\sqrt{\frac{p - p_v}{\rho}} \tag{2.30}$$

where $\gamma = H/R$ with H being the distance from the bubble centre to the surface and R its radius. The water hammer velocity is compared against the material-dependent stress needed to produce plastic deformation. Originally devised to evaluate erosion from visual sheet cavitation measurements, the technique can be adapted to CFD calculations instead. The suggested pressure wave calculation does becomes redundant since it can be readily obtained from the numerical solution.

In [51], Peters et al. implement this methodology into a URANS simulation. The authors indeed eliminate the first steps of the procedure and compute v_{jet} from the calculated pressure.

They assume that damaging bubbles are located within $\gamma = 1.1$ and consider a finite sphere of influence for each surface point. Critical events are accrued over the simulation time to deliver the erosion aggressiveness distribution. The calculations carried out for an axisymmetric nozzle show good agreement with experimental results in terms of erosion location despite the tendency to over-predict the spread. Follow-up investigations on a three-bladed propeller [59] deliver an outstanding match between predicted and measured eroded zones.

Pressure wave based erosion predictors

In [60], Fortes-Patella et al. apply a key concept in the understanding of the cavitation erosion process: the energy cascade. First introduced by Hammitt [61], the idea is to view erosion as a transformation of the potential energy carried by large cavity structures into material deformation energy. It is advanced that the translation occurs through shock-wave propagation which automatically places this approach in the second group of methods. The potential energy of the vapour cloud is given by

$$E_p = \Delta p V_v \tag{2.31}$$

where $\Delta p = p_\infty - p_v$ is the difference between the surrounding and bubble pressure and V_v is the vapour volume. In this type of approach, the erosion aggressiveness P_{agr} is taken to correspond to the transmitted cavitation power. The authors argue that the rate of pressure change over time is negligible compared to the rate of change of the vapour volume such that

$$\begin{aligned} P_{agr} = \frac{dE_p}{dt} &= \Delta p \frac{\partial V_v}{\partial t} + \frac{\partial p}{\partial t} V_v \\ &\cong \eta \int_{h_c} \Delta p \left| \frac{\partial \alpha}{\partial t} \right| V_{cell} dh \end{aligned} \tag{2.32}$$

where h_c is the height of the active zone from the solid surface (10% of cavity sheet height [54]) and η is an efficiency coefficient which depends on the geometry and unsteadiness of the cavitating flow. The derivative of the vapour volume is replaced by the derivative of the vapour volume fraction from $\alpha = V_v / V_{cell}$. Testing on a 2D NACA 65012 hydrofoil revealed good qualitative agreement with experimental results at a specific angle of attack but breaks down when the angle and unsteadiness are increased.

Li et al. [35] follow the energy cascade interpretation. In their method, it is the vapour time derivative rather than the pressure derivative that is eliminated from the definition of the cavitation potential power (equation 2.32). The choice is supported by a sensitivity study on a

hydrofoil case rather than dimensional comparison. To distinguish the non-damaging events from those that count, the authors introduce a material dependent threshold δ on the rate of change of pressure. The final expression for cavitation aggressiveness is a straightforward summation of the high intensity collapses

$$I_{agr} = \frac{1}{T}\int_0^T I dt \qquad \text{with} \qquad I = \begin{cases} \frac{\partial p}{\partial t} & \text{if } \frac{\partial p}{\partial t} \geq \delta \\ 0 & \text{if } \frac{\partial p}{\partial t} < \delta \end{cases} \tag{2.33}$$

where T is the total exposure time. Comparing the numerical results to paint removal data demonstrates the qualitative performance of the method in terms of location prediction. The weakness of the technique is its reliance on the empirical threshold. No guidelines are currently available other than using pre-existing experimental data to tune the parameter.

Ochiai et al. [55] and Nohmi et al. [62] take into account the Rayleigh-Plesset equation by implementing a one-way coupling procedure between the bubble behaviour and the homogeneous cavitating numerical solution. A finite number of bubble seed points are placed upstream and tracked through the flow using the surrounding state as boundary conditions. The advantage is that pressure waves emitted by single bubble collapses can be accurately evaluated. The issue, however, is the heavy resources needed to characterise the entire cavity. Instead Nohmi et al. propose a general formulation for cavitation aggressiveness based on the global variables α and pressure

$$\left(\frac{\partial^{N1}\alpha}{\partial t^{N1}}\right)^{N2}\left(\frac{\partial^{N3}(p_\infty - p_v)}{\partial t^{N3}}\right)^{N4} \tag{2.34}$$

with $N_{1...4}$ being positive integers. The relation was not derived from the identification of erosion mechanisms but by combining significant quantities: α scales with the number of potential collapse events, $\partial\alpha/\partial t$ determines the rate of collapse, p and $\partial p/\partial t$ drive the wave intensity. With relation 2.34, possible higher order effects and non-linearities are taken into

consideration. The author lays out four simple configurations:

$$\begin{aligned}
&\frac{1}{T}\int_0^T \alpha \max\left(\frac{\partial p}{\partial t}, 0\right) \\
&\frac{1}{T}\int_0^T \alpha \max\left(p_\infty - p_v, 0\right) \\
&\frac{1}{T}\int_0^T p_\infty \max\left(\left|\frac{\partial \alpha}{\partial t}\right|, 0\right) \\
&\frac{1}{T}\int_0^T \max\left(\left|\frac{\partial \alpha}{\partial t}\right|, 0\right)
\end{aligned} \tag{2.35}$$

One will note that the first and third formulations are equivalent to the techniques proposed by Li et al. and Fortes-Patella et al. respectively.

Recent work by Mouvanal et al. [64] introduces a procedure for detecting bubble collapse from a homogeneous cavitation URANS solution. The implosion event is characterised by three sets of conditions on the time-resolved flow state:

$$\begin{aligned}
&(i) \quad \alpha^n = 0 \quad \text{and} \quad \alpha^{n-1} = 0 \quad \text{and} \quad \alpha^{n-2} > 0 \\
&(ii) \quad p^n > p^{n-1} \\
&(iii) \quad \dot{m}^{+n} > 0
\end{aligned} \tag{2.36}$$

where exponent n indicates the current time step. This flow assessment acts as a safeguard against the risk of recording travelling cavities as collapses. This possibility is overlooked by the other aggressiveness predictors. The erosive intensity of the collapse is determined by the magnitude of the pressure wave. The authors estimate that the pressure computed by the solver in a cell where conditions 2.36 are met is equal to the emitted pressure wave. In a manner similar to the Li et al. model, one can write

$$I_{agr}^{Mouv} = \frac{1}{T}\int_0^T I dt \qquad \text{with} \qquad I = \begin{cases} p & \text{if conditions are met} \\ 0 & \text{otherwise} \end{cases} \tag{2.37}$$

Comparative assessment using the same axisymmetric nozzle as Peters et al. demonstrates a suitable performance for predicting sensitive zones. In terms of intensity, however, the results deliver an offset in peak erosion between experimental and numerical results.

Predictor selection

For the purpose of this research a selection of the predictive tools is made. These will be used in combination with time accurate CFD calculations to assess the erosion performance of the designs. Furthermore, from the experimental assessment, it will be possible to evaluate the models against each other for an identical geometry set. The chosen methods are:

- Peters et al. [51]: it constitutes the only selected *micro-jet* approach and delivers compelling, albeit dimensionless, results.
- Li et al. [35]: follows the energy cascade mechanism and provides the most straightforward implementation.
- Nohmi et al. [62]: the four reduced formulations are selected. These will deliver contrasting results from which constructive conclusions may be made.
- Mouvanal et al. [64]: the collapse detector is a unique and convincing feature which is worth comparing to competing methods.

2.3 Design Practices for Turbomachinery Components

Adverse flow features, such as separation, secondary flow and cavitation, occur within the main flow path of turbomachinery systems and are responsible for downgrading the performance of the machine. As the intensity of these adverse phenomena is largely dependent on the geometry of the hydraulic components, the design of said components is targeted at reducing their negative impact and concurrently improving the performance of the system.

2.3.1 Sizing for Hydraulic Machinery

The design cycle begins with the requirements of the installation. For hydraulic machinery, the volume flow rate Q, rotational speed Ω and head H are given as inputs. Combined, they form the non-dimensional specific speed:

$$\Omega_S^p = \frac{\Omega\sqrt{Q}}{(gH)^{3/4}} \tag{2.38}$$

The role of this number is to determine the shape of the machine that delivers the best efficiency. For pumps, a low specific speed ($\Omega_S < 0.1$) calls for displacement type mechanisms, a high

specific speed for the centrifugal type with flow configurations that range from radial to axial as Ω_S increases (see Figure 2.2). The specific speed is also used as a reference for turbine selection, but is expressed in terms of power P instead of flow rate:

$$\Omega_S^T = \frac{\Omega\sqrt{P}}{\sqrt{\rho}(g\Delta H)^{5/4}} \tag{2.39}$$

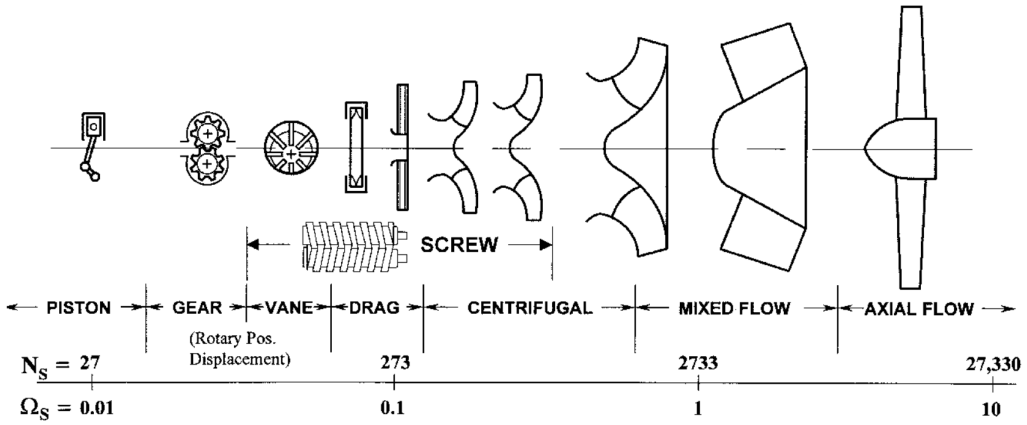

Figure 2.2: Recommended pump configuration for highest performance in terms of the specific speed Ω_S [5].

Having established the appropriate flow channel shape, the main dimensional features are determined using one-dimensional correlations which relate the inputs Q, Ω and H to:

- inlet and outlet diameters,
- leading and trailing blade angles,
- number of blades,
- meridional section.

The empirical laws are based on statistical analyses of turbomachinery parts using either numerical or experimental techniques [3, 65, 66]. These also serve to provide early approximations of the component performance.

2.3.2 Blade Design

This first set of steps constitutes the sizing procedure for rotating turbomachinery components. At this point, the blade geometry is a zero thickness surface defined only in terms of the leading

and trailing angles. The design of the internal distribution determines the behaviour of the flow as well as the performance of the stage. Two approaches are available for blade design:

1. direct
2. inverse.

The *direct* approach consists in applying modifications on the geometry. The shape is usually characterised using a grid of control points over the blade surface which the designer displaces within reasonable constraint. The geometry is then tested experimentally or numerically and compared to performance requirements. Adjustments are then made according to the measured discrepancy. This trial and error procedure is repeated until satisfied.

With the *inverse* method, it is the flow features instead of the geometry that is altered. The shape is generated indirectly using numerical strategies that take characteristics of the flow field as input to solve the geometry problem. Target distributions can include surface velocity, surface pressure or blade loading (see Section 2.3.3).

The *inverse* method offers a number of significant advantages over the *direct* procedure. First of all, it eliminates the need for experience, which is required by the *direct* strategy to anticipate the effect of changes in geometry on the flow field. Indeed, small modifications in critical locations (e.g. separation point) can have dramatic effects on performance. The design task quickly turns into a laborious problem as one cannot readily identify the correct modifications to eliminate losses and perturbations in the primary requirements such as head or power have to be taken into account. With the *inverse* procedure, adverse phenomena are tackled directly [67]. For example, the risk of separation is attenuated by imposing lower adverse pressure gradients. General requirements (H or P) are kept constant through the prescribed distributions all the while allowing large variations in flow and geometry.

Furthermore, characterising the flow path in terms of fluid features means that recipes used for suppressing a specific loss mechanism are readily transposed to other turbomachinery configurations suffering from the same problem. Despite different scales or geometries, the similarity holds as long as the flow field is comparable. The *inverse* method provides a more general approach to blade design.

Multi-Objective Optimisation (MOO) is a key step in turbomachinery design given that design objectives are usually multiple. When it comes to computational cost, the advantage of the *inverse* technique is that it requires significantly less parameters. Target flow distributions are given by Bezier or polynomial curves in 2D or surfaces in 3D, which contain the optimisation variables in their definition. By comparison, MOO using the *direct* method involves assigning

degrees of freedom to each of the control nodes on the blade surface. The computational progress is not only slowed down by the number of parameters but also by the non-linearities relating geometry (rather than blade pressure for example) to performance metrics. Preliminary optimisation routines such as Design of Experiments (DOE) have to work more to identify useful correlations.

2.3.3 Inverse Design Techniques

Building upon the foundations of aerofoil theory, Lighthill [68] proposed to use the properties of potential flow (i.e. incompressible, inviscid and irrotational) for producing geometries. His work focused on enforcing a velocity distribution at the surface to ensure a viable flow field. By transposing the external flow problem into the complex plane, the author was able to approach the coordinates definition analytically, using Poisson's equation as the central means of resolution. Although applicable in 2D, the three-dimensional extension of the method is demanding. Furthermore, its fundamental assumption of irrotationality is not suited to realistic, compressible and viscous flows. A potential flow based approach was also developed by Stanitz and D [69] for internal channel flows but suffers from the same limitations as the Lighthill method.

In [70, 71], Hawthorne et al. proposed an *inverse method* that takes marginal departure from the potential flow approach. It uses the *Clebsch* formulation, which includes a rotational term, to govern the flow field. The method is specifically designed for axial turbomachinery configurations and introduces an additional novelty by representing blades as sheets of bound vorticity. This allows the authors to connect the camber profile to the pitch-wise averaged tangential velocity and to define the blade shape by solving an ordinary differential equation. Although applicable to 3D annular cascades, the method cannot handle high thickness blades, or compressible flow.

These shortcomings were remedied by Zangeneh [72] who was able to successfully evaluate the compressibility effects and include a stream sheet thickness into the computation. This approach was applied to enhance a number of turbomachinery components: for example, suppressing boundary layer separation in a radial-inflow turbine [72], or increasing the efficiency of a centrifugal compressor [73].

Concurrently, investigations into the use of distributions other than the averaged tangential velocity were undertaken. For instance, Meauzé [74] recommends prescribing the velocity distribution over the surface, while Zannetti [75] and Léonard and Van den Braembussche [76] examine the imposition of static pressure. Abandoning control over blade thickness,

these techniques can lead to ill-posed problems and carry the risk of producing open surfaces, especially at the trailing edge. In contrast, prescribing the averaged tangential velocity and the tangential blade thickness, as in [70, 71, 72], ensures a viable geometry which satisfies the Kutta condition. It also gives direct control over the swirl and, automatically, the work transfer through the turbomachinery component. In this light, it constitutes the most robust and practical approach to relate blade geometry to flow field variables.

From that point on, enhancements of the method are concerned with improving its accuracy and efficiency. In [77], Dang and Isgro showed that the methodology can be adapted to a conservative Euler-type solver which, unlike the previous formulations, is capable of handling complex shock structures in supersonic flow regimes. Taking inspiration from Demeulenaere et al. [78], the authors enforce a pressure jump across the surfaces, the amplitude of which is proportional to the tangential velocity distribution, rather than the customary slip condition (tangential velocity), which is itself used as the basis for the blade shape update routine. The benefit of the aforementioned permeable wall boundary condition is that, instead of having to produce a converged flow field at every blade shape iteration, modifications are executed during the time marching procedure, thus reducing the method's computational demand. The authors further develop their approach to account for three-dimensional flow and non-zero thickness in [79].

The addition of viscous effects is accomplished by Tiow and Zangeneh [80, 81, 82] using the Denton [83] approximate body force approach. In their work, the authors also propose to shortcut the usual procedure by prescribing the pressure loading directly (i.e. difference between static pressures on either side of the blade), given that it favours the implementation of the advantageous permeable wall condition, all the while providing control over the specific work of the stage. Application of the procedure to the design of a 2D cascade, transonic turbine stator, compressor stator and compressor rotor proves its robustness and range.

As for hydraulic machinery, Zangeneh et al., Goto et al. [84, 85] and Goto and Zangeneh [86] successfully apply the thee-dimensional methodology oultined by Zangeneh in [72] to get rid of secondary flow in a mixed-flow impeller for the former, and improve the overall performance of a diffuser stage for the latter. Work was also carried out on a Francis turbine runner by Okamoto and Goto [87] and Daneshkah and Zangeneh [88]. In both studies, the authors show that the onset of cavitation can be delayed without downgrading the turbine efficiency by displacing the peak loading towards the high pressure region. In [89], Bonaiuti et al. combine the inverse design method with a parametric study to determine the best compromise between suction performance and efficiency for a waterjet pump. Significant gains on the baseline case

are attained by adjusting the streamwise and spanwise loading distributions. It is important to note that for these applications of the inverse method, the geometries are generated by the single phase compressible solver developed in [72] in non-cavitating conditions. The suction performance is evaluated from CFD analysis of the produced designs.

2.3.4 Design against Cavitation

Apart from the recent advances made using the inverse approach, the cavitation problem is only superficially addressed during the design stage of turbomachinery components. Provisions made against cavitation in impellers or runners conventionally follow empirical recommendations. In [3], Gulich provides a number of remedies specific to each manifestation of the cavitation phenomenon. For a suction side attached cavity leading to erosive damage, for example, it is advised to operate at a higher flow rate, reduce the blade inlet angle and the inlet diameter. Further recommendations can be found in [3]. The concept of L shaped loading was also introduced to shift the work transfer downstream of the leading edge [90]. Its effect is to smooth the pressure distribution and avoid sudden drops in the leading edge region, thus delaying the onset of cavitation and delivering an improved $NPSH_{3\%}$ requirement for the stage.

The issue with this course of action is that it is only concerned with delaying the onset of cavitation and ensuing performance breakdown. Cavitation aggressiveness is evaluated at the end of the design cycle using similarity laws of the form given by Pereira et al. [52]. These are based on the volume of cavitation and the σ or $NPSH$ value. Due to the difficulties in measuring the thickness of the cavity sheet, the volume is further approximated to be the value of the cavity length L_{cav}. As mentioned by the author himself, important factors are left out of this simplification, namely the type of cavitation, the internal dynamics of the cavitating sheet and the local pressure field affecting the collapse of vapour bubbles.

Currently, only a few efforts have been invested in understanding the effect of geometry on cavitation and its dynamics. In [91], Yu et al. investigate the effect punching holes through a hydrofoil has on the sheet cavity. The immediate result is the pressurisation of the suction side by the pressure side flow which downgrades the hydrofoil lift. Cavitation gains are not well explored or disclosed and this type of design feature is mainly inconvenient. Hofmann et al. [92] compare the behaviour of rotating cavitation for two radial flow impellers. However, the characterisation of the geometry is limited to basic dimensions such as inlet and outlet diameter, blade leading and trailing edge angles or passage width. Furthermore, the two candidates are too similar for any conclusive understanding to be drawn from the study. Sun

[93] follows an interesting approach, wherein a 2D NACA0015 profile is optimised using a Response Surface Method (RSM). The author is able to improve lift performance in both non-cavitating and cavitating conditions by proposing a leading to trailing edge modification of the profile. The drooped nose design concept is also investigated and delivers improvements in lift and in lift to drag ratio. The study, however, does not address the dynamic behaviour of the cavity or erosive aggressiveness.

2.4 Novelty of Present Research

The review carried out here brings to light the gap in research on the relation between blade geometry and cavitation aggressiveness. Engineering research in the field of cavitation focuses on developing numerical cavitation modelling techniques or erosive prediction methodologies. While, on the design side, the limited guidelines aimed at reducing the effects of cavitation in hydraulic machinery are draconian in that they significantly alter the specifications of the machine and only attempt to delay the formation of vapour.

The research undertaken here, therefore, constitutes the first attempt at controlling the intensity of cavitation erosion through blade design. A major asset of the strategy is that it is a non-disruptive approach constructed on the understanding that a low amplitude and low gradient cavity closure pressure jump can reduce the aggressiveness of cavitation. The notable additions to the state-of-the-art are:

- modifications brought to the global internal geometry rather than limited to the leading edge region, while the general size of the machine remains untouched,
- blade profiles are generated by the inverse design technique and characterised by the loading distribution which provides direct control over flow features,
- comparative assessments of the cavitation aggressiveness levels for a variety of profiles are carried out through both numerical and experimental means.

3 Development of Inverse Design Solver for Cavitating Flow

The inverse design solver is tasked with providing both a realistic representation of cavitating flow and a solution to the design problem. As such it is required that the algorithmic construction be able to accommodate the selected cavitation model. Features of particular importance are sharp shock capturing and the ability to cope with a large range of flow regimes. To boost repeatibility of design experiments, speed and robustness are favoured over demanding and sensitive turbulence models. Inverse design techniques are implemented and adjusted to cater for the specificities of cavitating flow. The solver is written from scratch using the FORTRAN95 programming language for its well documented efficiency at translating mathematical problems.

3.1 Flow Domain & Spatial Discretisation

The linear cascade is divided into single channels. An individual channel - made up of an inflow section, a blade region and an outflow sections - constitutes the computational domain (see Figure 3.1). The blade is split along its camber line with the pressure side placed at the top and the suction side at the bottom of the computational domain. Periodic boundaries enclose the inflow and outflow sections to replicate the cyclic character of the cascade. The inlet boundary is located at one chord length from the blade leading edge; the outlet boundary is positioned further downstream at three chord lengths to mitigate the flow non-uniformity formed at the wake.

Approaches to spatial discretisation can be either structured or unstructured. For complex

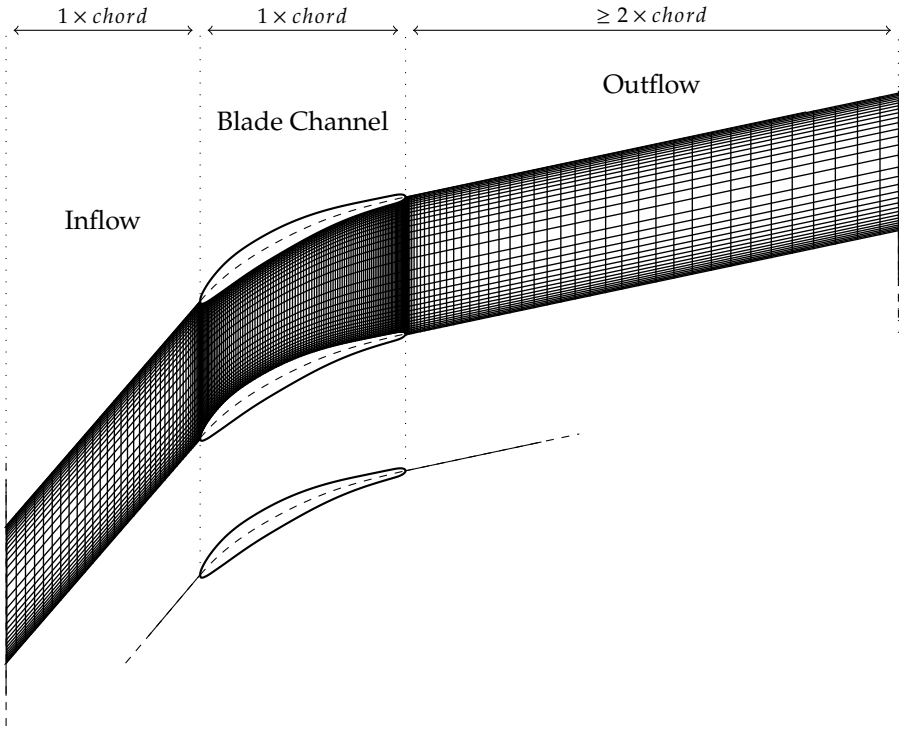

Figure 3.1: Discretisation of the cascade channel:an H-grid topology is used in conjunction with structured quadrilateral cells.

geometries, the unstructured method is more efficient at producing a high quality mesh but is harder to implement and computationally more demanding. For the case studied here, the geometry is simple enough that elementary structured techniques are capable of generating a suitable mesh. The structured approach also facilitates the calculation of tangentially averaged distributions which will be needed by the inverse design algorithm.

A single block H-mesh topology is fitted into the domain. Local refinement is achieved by controlling the distribution of nodes along the edges. Their position follows a geometric law of the form

$$H_i = \frac{1-r}{1-r^{n-1}} \sum_{j=2}^{i} r^{j-2} \tag{3.1}$$

where H_i is the distance from the starting node to node i, n is the total number of nodes along a specific segment, and r is the growth ratio. In the pitchwise direction, the domain is halved so that two independent geometric laws produce a finer grid close to the blade surfaces. In the streamwise direction, four partitions are constructed, i.e. inflow region, upstream half of the blade channel, downstream half of the blade channel, outflow region; each are characterised by a node count n and ratio r. This allows for localised control over node density and refinement levels at the leading and trailing edges.

3.2 Inviscid Euler Solver

The mathematical expressions used to describe the dynamic behaviour of fluids are constructed from the principles of conservation of mass, momentum and energy. In continuum mechanics, the total variation of a conserved quantity within an arbitrary volume is a result of either the fluxes cutting across the boundary, the internal forces and sources or the external forces. Assuming a general vector quantity $\boldsymbol{U}$, the balance between its variation and the aforementioned contributions can be expressed as

$$\frac{\partial}{\partial t}\int_{\Omega}\boldsymbol{U}d\Omega+\oint_{\partial\Omega}\left(\underline{\boldsymbol{F_C}}-\underline{\boldsymbol{F_D}}\right)\cdot\boldsymbol{n}dS=\int_{\Omega}\boldsymbol{S_V}d\Omega+\oint_{\partial\Omega}\underline{\boldsymbol{S_S}}\boldsymbol{n}dS \tag{3.2}$$

where $\underline{\boldsymbol{F_C}}$ and $\underline{\boldsymbol{F_D}}$ are the convective and diffusive flux tensors respectively, and $\underline{\boldsymbol{S_V}}$ and $\underline{\boldsymbol{S_S}}$ are the volume and surface sources. To recover the complete Navier-Stokes equations which govern fluid dynamics, we substitute $\boldsymbol{U}$ for each of the conservative quantities i.e. mass, momentum and energy, and introduce terms representing body forces (e.g. gravity, buoyancy), surface forces (e.g. pressure, shear stress) and heat exchanges. By concatenating all three conserved quantities into a single vector $\boldsymbol{W}=[\rho,\rho u,\rho v,\rho w,\rho E]^T$ we can write

$$\frac{\partial}{\partial t}\int_{\Omega}\boldsymbol{W}d\Omega+\oint_{\partial\Omega}(\boldsymbol{F_c}-\boldsymbol{F_v})dA=\int_{\Omega}\boldsymbol{S}d\Omega \tag{3.3}$$

Here, the unit normal vector $\boldsymbol{n}$ has been absorbed into the definitions of the vector of convective fluxes $\boldsymbol{F_c}$ and the vector of viscous fluxes $\boldsymbol{F_v}$ such that

$$\boldsymbol{F_c}=\begin{pmatrix}\rho V\\ \rho uV+pn_x\\ \rho vV+pn_y\\ \rho wV+pn_z\\ \rho VH\end{pmatrix}\quad\text{and}\quad\boldsymbol{F_v}=\begin{pmatrix}0\\ n_x\tau_{xx}+n_y\tau_{xy}+n_z\tau_{xz}\\ n_x\tau_{xx}+n_y\tau_{xy}+n_z\tau_{xz}\\ n_x\tau_{xx}+n_y\tau_{xy}+n_z\tau_{xz}\\ n_x\theta_z+n_y\theta_y+n_z\theta_z\end{pmatrix} \tag{3.4}$$

Quantities ρ, p, E, H and V are respectively the density, pressure, total energy per unit mass, total enthalpy per unit mass with $H = E + p/\rho$, and *contravariant velocity* defined as $V = n_x u + n_y v + n_z w$. The components of $\boldsymbol{F}_v$ depend on the viscous stress tensor $\underline{\boldsymbol{\tau}}$ and on $\boldsymbol{\theta}$ which contains the rate of work exerted by $\underline{\boldsymbol{\tau}}$ and thermal diffusivity. Their definition is not essential here and can be found in literature (see [94]). The source term $\boldsymbol{Q}$ encapsulates body forces and heat sources.

In this form, the Navier-Stokes equations are valid for compressible flows. Often the thermodynamic properties of a fluid are related by an equation of state which can be used to build an expression that closes the system. By taking, for example, the ideal gas law

$$\frac{p}{\rho} = RT \tag{3.5}$$

and combining it with the definitions for enthalpy $H = E + p/\rho = c_p T$, the gas constant $R = c_p - c_v$ and $\gamma = c_p/c_v$ we obtain an expression for p in terms of the conservative variables:

$$p = (\gamma - 1)\rho \left(E - \frac{u^2 + v^2 + w^2}{2} \right) \tag{3.6}$$

Given the form of 3.3 and 3.4, isolating the pressure comes as a natural choice for system closure. This approach is similar to the implementation of the cavitation model, described in more detail in section 3.3.

For high Reynolds number flows, the viscous forces are far smaller than the convective forces. By neglecting the vector of viscous fluxes in the Navier-Stokes equations we arrive at a set of hyperbolic conservation equations known as the Euler equations.

$$\frac{\partial}{\partial t} \int_\Omega \boldsymbol{W} d\Omega + \oint_{\partial\Omega} \boldsymbol{F}_c dA = 0 \tag{3.7}$$

The numerical treatment of said equations constitutes the first layer of our solver's architecture. What this means, practically, is that equation 3.7 is applied to cells individually. Fluxes are evaluated at the interfaces using information from the surrounding elements and the state vector $\boldsymbol{W}$ is adjusted according to the balance of fluxes. Numerous techniques have been developed to perform these two steps. Those that have been selected are laid out in detail in this chapter. The numerical approximation is realistic once the conservation principles

expressed by equation 3.7 hold true for all the subdivisions of our domain.

This solver's target is to arrive at a steady state solution. This implies that the first term on the LHS of equation 3.7 has to eventually cancel out. Two approaches are possible:

- *explicit time marching schemes*, wherein the first term is transformed into a pseudo-time derivative which can be integrated and is used to update variables,
- *implicit schemes* which gets rid of the temporal derivative in 3.7 to solve the linearised system using iterative methods for linear systems.

In both cases, the solution is deemed acceptable when the relative difference between successive updates is below a user-defined threshold. With explicit schemes, the convergence rate is limited by the physical properties of the flow. Implicit schemes, on the other hand, allow for larger time steps and improved robustness by virtue of the linearisation of the system.In this work however, we chose to use an explicit time marching method because (i) the addition of acceleration techniques such as preconditioning or multigrid can entirely compensate the gap in convergence rates (see Section 3.5), (ii) by preserving the physical formulation of the time-dependent problem, explicit schemes are able to pick up unsteady or cyclic behaviour. Furthermore, its implementation is more straightforward, and it can easily be parallelised.

For spatial discretisation, we chose to implement the widely used cell-centred Finite Volume Method (FVM) which, because it is based on the integral formulation, ensures conservation of variables. Its core principle is to approach the surface integral in Equation 3.7 by evaluating and summing the fluxes across each cell face. Combining the explicit and FVM treatments of time derivative and flux terms respectively, the Euler equations can be rewritten in their discretised form:

$$\frac{\Omega}{\Delta t}\Delta \boldsymbol{W}^n + \sum_k \boldsymbol{F}_{c_k}^n A_k = 0 \tag{3.8}$$

where k stands for the cell face index and Ω represents the volume of a single cell, which, assuming a static (independent in time) division of the domain, can be taken out of the time derivative. For clarity, cell indices are omitted.

Applying the simplest time integration technique, i.e. Euler's first order forward difference method, one can write Equation 3.8 as

$$\boldsymbol{W}^{n+1} = \boldsymbol{W}^n - \frac{\Delta t}{\Omega}\boldsymbol{R}^n \tag{3.9}$$

which plainly illustrates the time marching procedure and incorporates all time independent

terms into the *residual* $\boldsymbol{R}^n$. For steady state solutions, temporal discretisation techniques determine only the speed of the computation. The manners in which this is optimised in our code are presented in Section 3.5. The accuracy of the solution is therefore entirely dependent on the evaluation of the fluxes. The difficulty that props up at this stage, and which has been the focus of a large portion of past and ongoing research in CFD, is due to the discontinuous nature of variables across cell faces. A variety of techniques have therefore been developed to compute interface fluxes in a more physically realistic or flexible manner. All fall in either one of the two categories:

- *central schemes* which average the values of the convective flux vectors on either sides of an interface. Artificial dissipation is added to suppress odd-even decoupling.
- *upwind schemes* which take into account the wave propagation directions to build a physically representative flux.

Our solver is implemented with techniques from both groups as detailed in sections 3.4.1, 3.4.2. The idea is to be able to compare the performance of each approach under cavitating conditions.

3.3 *Tohoku-Ebara* Cavitating Fluid

It seems natural to start by laying out the properties of the working fluid and the laws that govern its behaviour. The selected cavitation model is the Tohoku-Ebara (TE) barotropic state equation [42]. It treats the multiphase character of cavitating flow as a homogeneous medium of density

$$\rho = (1 - \alpha)\rho_l + \alpha\rho_v \tag{3.10}$$

where α is the vapour volume fraction. The flow is considered isoenergetic and, so, the conservation of energy equation is dismissed from the problem to be solved. The conservative variable vector and convective flux vector (see equation 3.3 and 3.4), which are contained in the inviscid formulation of the governing equations as given by equation 3.7, are simplified to:

$$\boldsymbol{W} = \begin{pmatrix} \rho \\ \rho u \\ \rho v \end{pmatrix}, \qquad \boldsymbol{F_c} = \begin{pmatrix} \rho V \\ \rho V u + p n_x \\ \rho V v + p n_y \end{pmatrix} \tag{3.11}$$

The state law for density is pressure dependent and is produced by blending the two independent equations of state for liquid water and vapour respectively. The liquid phase is modeled using the Tammann equation which confers compressibility to the fluid [95]:

$$p_l + p_c = \rho_l K(T_l + T_0) \tag{3.12}$$

The pressure, density and temperature of the liquid are p_l, ρ_l and T_l. Numbers p_c, T_0 and K are pressure, temperature and liquid constants of the model. It is assumed that the vapour phase behaves as an ideal gas

$$p_g = \rho_g R T_g \tag{3.13}$$

where subscript g is used for the vapour phase. Using the definition of density for a homogeneous mixture (Equation 3.10) and assuming local equilibrium i.e. $p = p_l = p_g$ and $T = T_l = T_g$, the state laws are combined into

$$\rho = (1-\alpha)\frac{p + p_c}{K(T + T_0)} + \alpha\frac{p}{RT} \tag{3.14}$$

The mass fraction of the vapour phase γ is related to the vapour volume fraction and to density by

$$\rho(1-\gamma) = (1-\alpha)\rho_l \quad \text{and} \quad \rho\gamma = \alpha\rho_g \tag{3.15}$$

By inserting relations 3.15 into 3.14, the equation of state that determines the mixture density in terms of the pressure is easily deduced:

$$\rho = \frac{p(p + p_c)}{K(1-\gamma)p(T + T_0) + R\gamma(p + p_c)T} \tag{3.16}$$

Nohmi et al. [42] enhanced the model by acknowledging the presence of entrained air in the liquid. The pressure of the pure gas phase is therefore no longer given by equation 3.13 but by

$$p_g = \rho_g \left(Y R_a + (1-Y) R_v\right) T_g \tag{3.17}$$

where Y is the mass fraction of air in the mixture, R_a and R_v are the ideal gas constants for air and vapour respectively. Substituting ρ_v in equation 3.10 for ρ_g in 3.17 yields the applied version of the *TE* mixture state law. It is valid as long as the pressure is above the saturation threshold. Below the vapour pressure p_v, the fluid obeys the ideal gas law for the air and vapour gas mixture. The complete equation of state used in the TE model for cavitating water therefore reads as

$$\rho = \begin{cases} \dfrac{(p+p_c)(p-p_v)}{(1-Y)(p-p_v)K(T+T_c) - Y\rho_v K(T+T_0)R_aT + Y(p+p_c)R_aT} & \text{if } p > p_v \\ \dfrac{p}{(YR_a + (1-Y)R_v)T} & \text{otherwise} \end{cases} \tag{3.18}$$

For the studied cases, temperature is assumed constant at $T = 293.15\,\text{k}$ and the corresponding saturation vapour pressure is $p_v = 2339.2\,\text{Pa}$. Additional variables are model constants; the function and value for each is given in Table 3.1.

To determine the speed of sound of the cavitating mixture, one applies the formal definition for continuous media i.e. $c^2 = \partial p/\partial\rho$. Owing to the full dependency of density on pressure and vice-versa, it is possible to write

$$c^2 = \frac{\partial p}{\partial \rho} = \left[\frac{d\rho}{dp}\right]^{-1} \tag{3.19}$$

Numerically, a value for the speed of sound is easily computed by isolating the numerators and denominators in 3.18. For molecular viscosity, the approximation

$$\mu = (1-\alpha)(1+2.5\alpha)\mu_l + \alpha\mu_v \tag{3.20}$$

is used with $\mu_l = 1.002 \times 10^{-3}\,\text{Pa s}$ and $\mu_v = 9.72 \times 10^{-6}\,\text{Pa s}$.

The TE equation is formulated such that density is determined for a given pressure. Because it cannot be readily inverted, it is imperative that pressure be used as an updated variable. The Euler equations are therefore expressed in terms of the primitive variable set $\boldsymbol{Q} = [p, u, v]^T$. A space change matrix $\partial \boldsymbol{W}/\partial \boldsymbol{Q}$ is introduced and constitutes the fist step in the time derivative preconditioning approach detailed in section 3.5.2

$$\frac{\partial \boldsymbol{W}}{\partial \boldsymbol{Q}} \frac{\partial}{\partial t} \int_\Omega \boldsymbol{Q} d\Omega + \oint_{\partial\Omega} \boldsymbol{F}_c dS = 0 \tag{3.21}$$

The evaluation of density is the last step of each iteration, once the continuity and momentum equations have been balanced.

Table 3.1: Model constants for the TE Equation of State

Coefficients	Definition	Value
P_c	TE pressure coefficient	1.945×10^9 Pa
P_v	Saturation vapour pressure	2339.2 Pa
Y	Mass fraction of air	1×10^{-5}
K	Liquid constant	472.3 $m^2\,s^{-2}\,K^{-1}$
T	Mixture Temperature	293.15 K
T_c	TE temperature coefficient	3.837×10^3 K
ρ_v	Saturation vapour density	0.0173 $kg\,m^{-3}$
R_a	Ideal gas constant for air	287.1 $m^2\,s^{-2}\,K^{-1}$
R_v	Ideal gas constant for vapour	461.0 $m^2\,s^{-2}\,K^{-1}$

3.4 Approaches to Flux Discretisation

As explained in Section 3.2, the solver has been implemented with several techniques for flux evaluation belonging to both the *central* and *upwind* groups. Characterisation is achieved by considering the flux through a generalised interface between two cells. Here, a structured grid is assumed with cells marked by indices i (x direction) and j (y direction). By convention, the states on either side of the interface are marked as $\boldsymbol{W_L}$ and $\boldsymbol{W_R}$ on the left and right respectively. The relations laid out for one face are transposed exactly around the cell, allowing for component changes in the x or y directions.

3.4.1 Jameson's Central Method

For the central method, the approach constructed by Jameson et al. [96] is the most prominently used. Values at cell faces are obtained from an arithmetic average of the states on both sides. Additionally, and because the averaging induces non-physical behaviour such as non entropy preserving overshoots, the method is improved using *artificial dissipation*. The magnitude of the dissipative terms is calculated from second and fourth derivatives of the flow variables and adjusted to take local characteristics into account through the pressure gradient. The

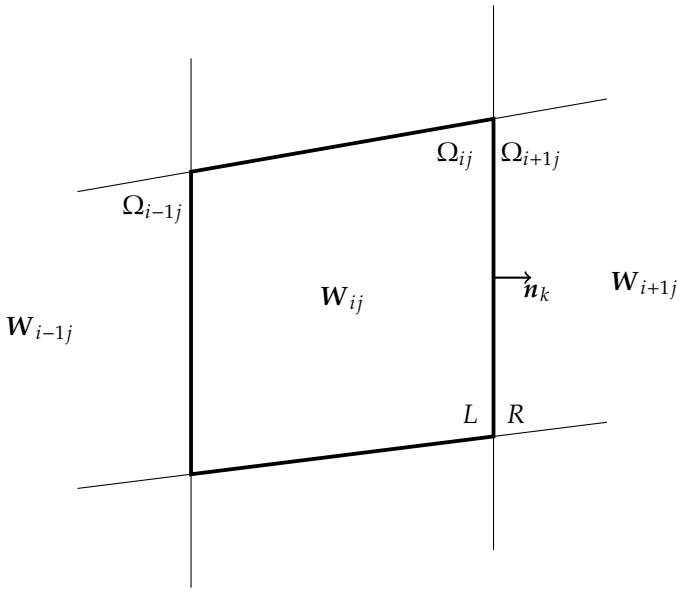

Figure 3.2: Single quadrilateral cell with interfaces and neighbours. The unit normal vector $\boldsymbol{n}_k$ points outwards by definition.

mathematical expression of Jameson's scheme for a single control volume is as follows

$$\boldsymbol{R}^n = \sum_k \boldsymbol{F}_k(\boldsymbol{W}^n) A_k - \boldsymbol{D}(\boldsymbol{W}^n) \tag{3.22}$$

where $\boldsymbol{F}_k(\boldsymbol{W}^n)$ is the convective flux across the face and $\boldsymbol{D}(\boldsymbol{W}^n)$ the cell specific dissipative term. For each cell face $k$vas shown in Figure 3.2,

$$\boldsymbol{F}_k(\boldsymbol{W}^n) = \frac{1}{2}\boldsymbol{F}_c(\boldsymbol{W}_L^n) + \frac{1}{2}\boldsymbol{F}_c(\boldsymbol{W}_R^n) \tag{3.23}$$

$\boldsymbol{W}_L^n$ and $\boldsymbol{W}_R^n$ being the states on the left and right side of face k. In 2D, the dissipative term $\mathcal{D}(\boldsymbol{W}^n)$ is a combination of the contributions in both directions

$$\boldsymbol{D}(\boldsymbol{W}^n) = \boldsymbol{D}_x(\boldsymbol{W}^n) + \boldsymbol{D}_y(\boldsymbol{W}^n) \tag{3.24}$$

It follows that,

$$\begin{aligned} \boldsymbol{D}_x(\boldsymbol{W}^n) &= d_{i+\frac{1}{2},j} - d_{i-\frac{1}{2},j} \\ \boldsymbol{D}_y(\boldsymbol{W}^n) &= d_{i,j+\frac{1}{2}} - d_{i,j-\frac{1}{2}} \end{aligned} \tag{3.25}$$

with

$$d_{i+\frac{1}{2},j} = \frac{\Omega_{i+\frac{1}{2},j}}{2\Delta t}\left[\epsilon^{(2)}_{i+\frac{1}{2},j}(w_{i+1,j} - w_{i,j}) - \epsilon^{(4)}_{i+\frac{1}{2},j}(w_{i+2,j} - 3w_{i+1,j} + 3w_{i,j} - w_{i-1,j})\right] \tag{3.26}$$

where w corresponds to a single component of the conservative variable vector $\boldsymbol{W}^n$ and $\Omega_{i+\frac{1}{2},j} = (\Omega_{i,j} + \Omega_{i+1,j})/2$. The coefficients $\epsilon^{(2)}$ and $\epsilon^{(4)}$ are responsible for adjusting the intensity of artificial dissipation and are functions of the local pressure gradient. To that intent, the sensor $\nu_{i,j}$ is defined

$$\nu_{i,j} = \frac{|p_{i+1,j} - 2p_{i,j} + p_{i-1,j}|}{|p_{i+1,j}| + 2|p_{i,j}| + |p_{i-1,j}|} \tag{3.27}$$

and used to determine the value of the coefficients according to

$$\begin{aligned} \epsilon^{(2)}_{i+\frac{1}{2},j} &= \kappa^{(2)} \max\left(\nu_{i+1,j}, \nu_{i,j}\right) \\ \epsilon^{(4)}_{i+\frac{1}{2},j} &= \max\left(0, \kappa^{(4)} - \epsilon^{(2)}_{i+\frac{1}{2},j}\right) \end{aligned} \tag{3.28}$$

Numbers $\kappa^{(2)}$ and $\kappa^{(4)}$ are tunable constants. The default values are $\kappa^{(2)} = 1/4$ and $\kappa^{(4)} = 1/256$.

3.4.2 Riemann Analogy and Flux Upwinding

For upwind schemes, the fluxes are determined using only information propagating towards the interface. The characteristic wave speeds and directions are therefore fundamental elements in upwind construction. The advantage over central schemes is that the method is more consistent with fluid physics. Assuming a simple one dimensional linear advection equation of the form

$$\frac{\partial w}{\partial t} + u\frac{\partial w}{\partial x} = 0 \tag{3.29}$$

the rate and direction of propagation is u. Numerically updating w_i^n to w_i^{n+1} is achieved by carrying the state at a neighbouring point located against flow direction into cell i. So if $u > 0$

$$w_i^{n+1} = w_i^n - \frac{u\Delta t}{\Delta x}\left(w_i^n - w_{i-1}^n\right) \tag{3.30}$$

For the finite volume approach, it is practical to express the spatial discretisation in terms of face fluxes

$$\begin{aligned} w_i^{n+1} &= w_i^n - \frac{\Delta t}{\Delta x}\left(F_{i+1/2} - F_{i-1/2}\right) \\ \text{with} \quad F_{i-1/2} &= u w_{i-1}^n \quad \text{and} \quad F_{i+1/2} = u w_i^n \end{aligned} \tag{3.31}$$

When studying the set of conservation principles expressed by the Euler equations additional complexity is introduced because information propagation is governed not by a single but by a number of waves. Their specific speed and direction is not readily available from equations 3.3 or 3.7 but can be identified by linearising the system into the form

$$\boldsymbol{W}_t + \hat{A}\boldsymbol{W}_x = 0 \tag{3.32}$$

and isolating the eigenvalues and eigenvectors of matrix $\hat{A}$. At this point, the Riemann initial value problem is introduced as a surrogate for the cell interface. The states on the left and right are determined by the evolution in time and space of the wave characteristics. Numerically, the updated cell state is given by the combination of right-going waves from $x_{i-1/2}$ and left-going waves from $x_{i+1/2}$:

$$\boldsymbol{W}_i^{n+1} = \boldsymbol{W}_i^n - \frac{\Delta t}{\Delta x}\left[\sum_{p=1}^{m}(\lambda^p)^+ \alpha_{i-1/2}^p r^p + \sum_{p=1}^{m}(\lambda^p)^- \alpha_{i+1/2}^p r^p\right] \tag{3.33}$$

Taken term by term, the positive eigenvalue λ^+ which corresponds to the speed of its associated wave carries the Rankine-Hugoniot jump condition equal to $\alpha_{i-1/2} r$ through the interface. At the other side of the cell the same process plays out but it is only the backward moving waves (negative eigenvalues) that are taken into account. This is repeated for each of the p components of the system. If using the flux notation as in equation 3.33, it can be shown that

$$\mathrm{F}_{\mathrm{i-1/2}}^{\mathrm{n}} = \boldsymbol{F_c}(\boldsymbol{W_i^n}) - \underbrace{\hat{A}^+\Delta\boldsymbol{W_{i-1/2}^n}}_{\text{right going}} = \boldsymbol{F_c}(\boldsymbol{W_{i-1}^n}) + \underbrace{\hat{A}^-\Delta\boldsymbol{W_{i+1/2}^n}}_{\text{left going}} \tag{3.34}$$

where $\hat{A}^+\Delta\boldsymbol{W_{i-1/2}^n} = \sum_{p=1}^{m}(\lambda^p)^+\alpha_{i-1/2}^p r^p$. Here, careful attention is drawn to the notation:

- F denotes the appropriate upwind flux which is used – in this form or another – to numerically update $\boldsymbol{W_i}$,

- $\boldsymbol{F_c}$ is the conservative inviscid flux function as given in equation 3.3.

For a non-linear system such as the Euler equations, the difficulty lies in applying a valid linearisation approach. A number of techniques have been developed to produce a flux formula that appropriately captures the wave structure at the interface. All fall into either the *flux difference splitting* (FDS) or *flux vector splitting* (FVS) categories. The difference between the two is contained within the application of the linearisation. Equation 3.34 corresponds to the FDS formulation. The flux at the interface is made up of the conservative flux function and of a correction term used to compensate for the discrepancy between $\boldsymbol{F_c}(\boldsymbol{W_i})$ and $\boldsymbol{F_c}(\boldsymbol{W_{i-1}})$. The correction term is either the left moving fluctuation for $\boldsymbol{W_{i-1}}$ or the right moving fluctuation for $\boldsymbol{W_i}$.

Alternatively, using the identity $\boldsymbol{F_c}(\boldsymbol{W_i}) = \hat{A}\boldsymbol{W_i}$ in equation 3.34 one can arrive at the flux vector splitting formulation

$$\begin{aligned} \mathrm{F}^{\mathrm{n}}_{\mathrm{i}-1/2} &= (\hat{A}^+ + \hat{A}^-)\boldsymbol{W_i} - \hat{A}^+(\boldsymbol{W_i} - \boldsymbol{W_{i-1}}) \\ &= \hat{A}^-\boldsymbol{W_i} + \hat{A}^+\boldsymbol{W_{i-1}} \end{aligned} \tag{3.35}$$

The implication is that, instead of using an arithmetic average of the fluxes on both sides of the interface, as is done in central schemes, a more elaborate averaging where the left going and right going parts are separated produces a stable upwind method. Generally, FVS methods are more prone to diffusion across contact discontinuities and shear layers than FDS schemes. Hybrid schemes have, however, been rather successful at combining the simplicity of the former with the accuracy of the latter.

Our solver has been implemented with both a Roe based FDS approach and instances from the hybrid *Advection Upstream Splitting Method* (AUSM) family schemes. The selection pool for upwind fluxing scheme is limited by the specificity of our equation of state since many of the linearisation methods are given for ideal gases and cannot readily be generalised to arbitrary fluids. The aim in using multiple techniques is to identify which is most apt at picking up the features of cavitating flow.

3.4.3 Roe Flux Difference Splitting Scheme

The novelty introduced by Roe [97] is to impose a number of conditions on the linearisation matrix $\hat{A}$, of which the most important are:

- for any $\boldsymbol{W^L}$ and $\boldsymbol{W^R}$, $\hat{A}(\boldsymbol{W^R} - \boldsymbol{W^L}) = \boldsymbol{F_C^R} - \boldsymbol{F_C^L}$,

- the eigenvectors of $\hat{A}$ are linearly independent,

- as $\boldsymbol{W^R} \to \boldsymbol{W^L} \to \boldsymbol{W}$, $\hat{A} \to \partial F/\partial \boldsymbol{W}$.

This enables the method to capture shock waves accurately. The eigenvalues and eigenvectors of $\hat{A}$ are

$$\lambda^1 = u_{RL} \qquad \lambda^2 = u_{RL} + c_{RL} \qquad \lambda^3 = u_{RL} - c_{RL} \tag{3.36}$$

and

$$r^1 = \begin{pmatrix} 1 \\ u_{RL} \\ \frac{1}{2}u_{RL}^2 \end{pmatrix} \quad r^2 = \frac{\rho_{RL}}{2c_{RL}} \begin{pmatrix} 1 \\ u_{RL} + c_{RL} \\ H_{RL} + u_{RL}c_{RL} \end{pmatrix} \quad r^3 = -\frac{\rho_{RL}}{2c_{RL}} \begin{pmatrix} 1 \\ u_{RL} - c_{RL} \\ H_{RL} - u_{RL}c_{RL} \end{pmatrix}. \tag{3.37}$$

The components of $\hat{A}$, λ^p and r^p are calculated using a weighted average of the left and right states; it is selected such that the linearisation conditions are met:

$$\begin{aligned} u_{RL} &= \frac{\sqrt{\rho_L}u_L + \sqrt{\rho_R}u_R}{\sqrt{\rho_L} + \sqrt{\rho_R}} \\ H_{RL} &= \frac{\sqrt{\rho_L}H_L + \sqrt{\rho_R}H_R}{\sqrt{\rho_L} + \sqrt{\rho_R}} \\ \rho_{RL} &= \sqrt{\rho_L \rho_R} \\ c_{RL} &= \sqrt{(\gamma - 1)\left(H_{RL} - \frac{1}{2}u_{RL}^2\right)} \end{aligned} \tag{3.38}$$

In order to produce a symmetric scheme, the flux as given in equation 3.34 is modified by summing the second and third parts of the equation

$$\mathrm{F}^{\mathrm{n}}_{\mathrm{i}-1/2} = \frac{1}{2}\left(\boldsymbol{F_c}(\boldsymbol{W^R}) + \boldsymbol{F_c}(\boldsymbol{W^L})\right) - \frac{1}{2}|\hat{A}|\Delta \boldsymbol{W_{i-1/2}} \tag{3.39}$$

The second term on the RHS of 3.39 is expanded using the relation $|\hat{A}|\Delta\boldsymbol{W_{i-1/2}} = \sum_{p=1}^{m} |\lambda^p|\alpha^p r^p$ which yields the complete Roe flux formulation expressed in terms of state variables only:

$$|\hat{A}|\Delta\boldsymbol{W_{i-1/2}} = |V| \begin{pmatrix} \Delta\rho \\ \Delta(\rho u) \\ \Delta(\rho v) \\ \Delta(\rho E) \end{pmatrix} + \delta V \begin{pmatrix} \rho \\ \rho u \\ \rho v \\ \rho H \end{pmatrix} + \delta p \begin{pmatrix} 0 \\ n_x \\ n_y \\ \sqrt{u^2 + v^2} \end{pmatrix} \tag{3.40}$$

where

$$\begin{aligned} \delta u &= M^* \Delta V + (c^* - |V|)\frac{\Delta p}{\rho c^2} \\ \delta p &= M^* \Delta p + (c^* - |V|)\rho \Delta V \\ c^* &= \frac{|V + c| + |V - c|}{2} \\ M^* &= \frac{|V + c| - |V - c|}{2c} \end{aligned} \tag{3.41}$$

It is important to note that all intermediate variables are Roe averaged. Here, some liberty has been taken as to the one dimensional to two dimensional transition since the contravariant velocity $V = un_x + vn_y$ is included in equations 3.40 and 3.41. In practice, extension to multidimensional flow is achieved by applying the Riemann analogy to each dimension or cell face individually. Although consistent, this strategy brushes over the fact that discontinuities oblique to grid faces do not match the initial conditions of the Riemann problem. It is therefore crucial to ensure that cell faces are aligned with shocks so that diffusion is minimal.

The derivation presented here works for an ideal gas. In our case, the fluid is isothermal and obeys a bespoke equation of state of the type $\rho = \rho(p)$. Ideally, the procedure carried out to arrive at the approximate Roe solver should be repeated using the appropriate system of equations and properties. Work has been undertaken by others for specific cases but the derivations can not be smoothly transposed to the TE EOS. To avoid investing serious effort into arduous mathematical developments, simplifying assumptions were made:

- the form of the eigenvalues and eigenvectors remains unchanged when working with the TE model,
- Roe averages still hold true,
- the energy equation can be decoupled and discarded.

One notable difference is in the determination of the intermediate speed of sound c_{RL}. Under the assumptions associated to the TE fluid it is determined by equation 3.19 with p as the single dependent variable. Because p_{RL} is not defined and finding its value from ρ_{RL} is too demanding, the arithmetic average is used instead:

$$c_{RL}^{TE} = \frac{1}{2}(c_R + c_L) \tag{3.42}$$

where c_R and c_L are easily deduced from p_R and p_L.

3.4.4 Hybrid *AUSM* Scheme

The development of the AUSM scheme by Liou and Steffen [98] was motivated by the need for improved accuracy at a lower computational cost. Specifically, the authors were looking for: sharp shock resolution, flux calculation requiring $O(n)$ operations (instead of $O(n^2)$ for the Roe scheme), and robustness i.e. the ability to solve a wide range of flow regimes. The mechanism at the core of the AUSM approach is to separate the purely convective and pressure (acoustic) terms in the inviscid flux vector

$$\boldsymbol{F_c} = V \underbrace{\begin{pmatrix} \rho \\ \rho u \\ \rho v \\ \rho H \end{pmatrix}}_{convective} + \underbrace{\begin{pmatrix} 0 \\ p n_x \\ p n_y \\ 0 \end{pmatrix}}_{acoustic} \tag{3.43}$$

Knowing that the convective terms are advected by a velocity V and that the pressure term is propagated according to acoustic wave speeds, individual treatments are proposed to define i/ a suitable velocity V and values for $(\rho, \rho u, \rho v, \rho H)^T$ which incorporate the jump at the interface, ii/ the appropriate intermediate pressure $\tilde{p}$.

Assuming an interface at $i - 1/2$ and two states on the left (L) and right (R), the purely

convective flux is given by

$$\mathbf{F}^{\text{conv}}_{i-1/2} = V_{1/2} \begin{pmatrix} \rho \\ \rho u \\ \rho v \\ \rho H \end{pmatrix}_{L/R} \tag{3.44}$$

where

$$()_{L/R} = \begin{cases} ()_L & \text{if } V_{1/2} > 0 \\ ()_R & \text{otherwise} \end{cases} \tag{3.45}$$

From the Riemann analogy it is understood that the advection velocity $V_{1/2}$ sits between the wave speeds $V + c$ propagating from the left and $V - c$ propagating from the right. If V is supersonic, $V - c > 0$ and only the state on the left is passed through the interface. The opposite is true when $V < -c$ ($M < -1$). For subsonic flow, an easy choice is to take the arithmetic average of V_L and V_R but it fails to reflect the wave structure. However, the splitting proposed by van Leer [99] has been shown to capture shock features accurately. It is introduced here as a weighting procedure applied to the intermediate Mach number $M_{1/2}$ with

$$\begin{aligned} V_{1/2} &= c_{L/R} M_{1/2} \\ M_{1/2} &= M^+_L + M^-_R \end{aligned} \tag{3.46}$$

and

$$M^{\pm} = \begin{cases} \frac{1}{2}(M \pm |M|) & \text{if } |M| > 1 \\ \pm\frac{1}{4}(M \pm 1)^2 & \text{otherwise} \end{cases} \tag{3.47}$$

For the pressure term, the splitting is weighted using a polynomial expansion expressed in terms of the wave speeds in non-dimensional form $M \pm 1$:

$$p_{1/2} = (\beta^+ p)_L + (\beta^- p)_R \tag{3.48}$$

and

$$\beta^{\pm} = \begin{cases} \frac{1}{2}(1 \pm \text{sign}(M)), & \text{if } |M| > 1 \\ \frac{1}{4}(M \pm 1)^2(2 \mp M), & \text{otherwise} \end{cases} \tag{3.49}$$

The complete AUSM flux at interface $i - 1/2$ is given by

$$\mathbf{F}^{n}_{i-1/2} = \frac{M_{1/2}}{2}\left(\begin{pmatrix} \rho c \\ \rho c u \\ \rho c v \\ \rho c H \end{pmatrix}_L + \begin{pmatrix} \rho c \\ \rho c u \\ \rho c v \\ \rho c H \end{pmatrix}_R\right) - \frac{|M_{1/2}|}{2}\left(\begin{pmatrix} \rho c \\ \rho c u \\ \rho c v \\ \rho c H \end{pmatrix}_R - \begin{pmatrix} \rho c \\ \rho c u \\ \rho c v \\ \rho c H \end{pmatrix}_L\right) + p_{1/2}\begin{pmatrix} 0 \\ n_x \\ n_y \\ 0 \end{pmatrix} \tag{3.50}$$

Leaving out the pressure part, this form resembles the flux averaging and dissipation correction of the Roe FDS scheme (see equation 3.39). At the same time, the FVS form (see equation 3.35) can easily be recovered by isolating the left and right states:

$$\mathbf{F}^{n}_{i-1/2} = \frac{M_{1/2} + |M_{i/2}|}{2}\begin{pmatrix} \rho c \\ \rho c u \\ \rho c v \\ \rho c H \end{pmatrix}_L + \frac{M_{1/2} - |M_{1/2}|}{2}\begin{pmatrix} \rho c \\ \rho c u \\ \rho c v \\ \rho c H \end{pmatrix}_R + p_{1/2}\begin{pmatrix} 0 \\ n_x \\ n_y \\ 0 \end{pmatrix} \tag{3.51}$$

In this manner, the hybrid character of the AUSM scheme is evident. One advantage of the AUSM approach is that its construction is not dependent on the equation of state. It is therefore applied to the *TE* fluid without modification other than the decoupling of the energy conservation equation.

3.4.5 Parameter-Free SLAU Scheme

Successive improvements of the original method have been endowed with more sophisticated splitting techniques in order to expand the regime capability to low Mach numbers and to enhance the shock capturing performance. A way of achieving this has been to add case specific parameters to the algorithm. In the SLAU version however, Shima and Kitamura [100] succeed

in providing a parameter-free approach which maintains and increases the aforementioned benefits.

The FVS form of the AUSM flux (equation 3.51) is written in terms of the mass flow $\dot{m}$ rather than the Mach number

$$\mathrm{F}^{\mathrm{n}}_{\mathrm{i}-1/2} = \frac{\dot{m} + |\dot{m}|}{2} \begin{pmatrix} 1 \\ u \\ v \\ H \end{pmatrix}_L + \frac{\dot{m} - |\dot{m}|}{2} \begin{pmatrix} 1 \\ u \\ v \\ H \end{pmatrix}_R + \tilde{p}_{1/2} \begin{pmatrix} 0 \\ n_x \\ n_y \\ 0 \end{pmatrix} \tag{3.52}$$

The definition of the SLAU mass flux takes its origin in the Roe mass flux (first row in vector equations 3.39 and 3.40)

$$\begin{aligned} \dot{m}_{Roe} = & \overbrace{\frac{1}{2}\left((\rho V)_L + (\rho V)_R\right)}^{①} - \overbrace{\frac{1}{2}|V|\Delta\rho}^{②} \\ & \underbrace{- \left(\frac{|V+c| - |V-c|}{4c}\right)\rho\Delta V}_{③} \underbrace{- \left(\frac{|V+c| + |V+c| - 2|V|}{4c^2}\right)\Delta p}_{④} \end{aligned} \tag{3.53}$$

In [100], the authors analyse the effect of each of the four terms and either eliminate those that prove detrimental or bring modifications to others in order to extend the scheme to low speed flow regime. For instance, it is found that

- the ΔV term counteracts the diffusivity of the $\Delta\rho$ term and so is discarded (term ② is kept, ③ eliminated),

- the Δp term is essential for producing non-oscillatory features in the direction normal to a shock, especially for low speed flow, but leads to instabilities in the parallel direction. Its effect needs to be controlled (term ④ is modified).

The SLAU mass flux therefore combines terms ①, ② and ④ and introduces specific weighting functions to correct the shortcomings that appear in certain conditions. It is found that the flux leads to negative internal energy in the case of asymmetric supersonic expansion. The first

adjustment therefore involves multiplying the first two terms by f_p designed such that

$$f_p = \begin{cases} \approx 1 & \text{if no expansion} \\ \\ = 0 & \text{if strong supersonic expansion} \end{cases} \tag{3.54}$$

To achieve the behaviour described in relation 3.54, the authors use

$$f_p = 1 - g \tag{3.55}$$

with

$$g = -\max[\min(M_L, 0), -1] \cdot \min[\max(M_R, 0), 1] \tag{3.56}$$

When it comes to the Δp term, its effect is unfavourable for any transonic multidimensional problem. Nevertheless, for low speed flows, it contributes to producing stable and smooth flow fields. So the idea is to multiply Δp by a function χ such that its effect is eliminated for high speed flows

$$\chi = \left(1 - \hat{M}\right)^2 \tag{3.57}$$

and

$$\hat{M} = \min\left(1.0, \frac{1}{\overline{c}}\sqrt{\frac{u_L^2 + v_L^2 + u_R^2 + v_R^2}{2}}\right) \tag{3.58}$$

Putting together the preserved terms and their appropriate correction yields the complete SLAU mass flux:

$$\dot{m} = \frac{1}{2}\left[(\rho V)_L + (\rho V)_R - |\overline{V}|\Delta\rho\right](1 - g) - \frac{\chi}{2\overline{c}}\Delta p \tag{3.59}$$

For the pressure flux, equation 3.48 of the original AUSM method is remodelled without loss to

$$p_{1/2} = \frac{p_L + p_R}{2} + \frac{\beta_L^+ + \beta_R^-}{2}(p_L - p_R) + (\beta_L^+ + \beta_R^- - 1)\frac{p_L + p_R}{2} \tag{3.60}$$

The diffusivity brought in by the third term is essential as the pressure averaging (first term) produces unwanted oscillations. The problem is that its magnitude scales with the speed of sound and becomes exceedingly large for low speed flows. To alter this behaviour weighting

f_p is introduced such that scaling is in tune with the convective velocity i.e.

$$\tilde{p}_{1/2} = \frac{p_L + p_R}{2} + \frac{\beta_L^+ + \beta_R^-}{2}(p_L - p_R) + f_p(\beta_L^+ + \beta_R^- - 1)\frac{p_L + p_R}{2} \tag{3.61}$$

with

$$f_p \begin{cases} \propto |M| & \text{if } |M| \ll 1 \\ = 1 & \text{if } |M| > 1 \end{cases} \tag{3.62}$$

The function selected to replicate the high speed/low speed switch is

$$f_p = 1 - \chi \tag{3.63}$$

where χ is as defined in equations 3.57 and 3.58. In comparison to previous attempts at extending the inviscid flux of AUSM family schemes to low speed flows, the approach described here carries a number of advantages:

- there is no prescribed cut-off Mach number M_∞ and f_p asymptotes to zero with M,
- the preservation of the contact discontinuity is maintained,
- it avoids introducing problem dependent parameters allowing the scheme to be applied to a wide range of cases.

3.5 Acceleration Techniques

A primordial property demanded of our code is that it arrives at the steady state solution in an efficient manner. Under this notion, the specific features sought after are :

- minimal computational load,
- robustness i.e. likelihood of converging to a solution.

This is motivated by the design needs of the scheme as well as the desire to enhance its applicability to industrial problems and schedules.

There are a number of ways to attain this objective. First of all, as stated in Section 3.2, explicit time marching methods rely on the discretisation of the time dependent terms to advance to a solution. It is, thus, understood that an appropriate treatment of these terms will result

in a gain in the efficiency of the code. Such techniques include *local time stepping*, *multistage schemes* and *preconditioning*. Other approaches take inspiration from implicit methods: *residual smoothing*; or use the relation between the division of space and the error frequency: *multigrid*, in order to improve the computational performance. The implementation and adaptation of these techniques to our specific case are detailed here.

3.5.1 Multistage Local Time Stepping

For steady state problems, time accuracy is irrelevant. It is therefore common practice to take away the physical significance from the definition of timestep Δt to focus, instead, on applying the maximal numerically stable step size. The stability of a computation is conditioned by the CFL number and the maximum wave speed. For an explicit scheme, the amplitude of the timestep must be equal or smaller than the time it takes for information to propagate through the control volume. For 1D Euler,

$$\Delta t \leq CFL \frac{\Delta x}{\Lambda_c} \tag{3.64}$$

where Λ_c is the propagation wave speed and corresponds to the maximum eigenvalue of the flux Jacobian which, for the 1D Euler equations, is equal to $u + c$.

For the 2D (or 3D) Euler equations, the non-linearity and multidimensional propagation mean that only an approximation of the maximum time step can be obtained. On structured grids, the method first described by Rizzi and Inouye [101] provides a straightforward and robust relation:

$$\Delta t \leq CFL \frac{\Omega}{\Lambda_c^i + \Lambda_c^j} \tag{3.65}$$

The speeds Λ_c^i and Λ_c^j represent the approximate convective waves in the x and y direction respectively and are given by:

$$\begin{aligned} \Lambda_c^i &= (\|\boldsymbol{v}\| \cdot \boldsymbol{n}^i + c)\hat{A}^i \\ \Lambda_c^j &= (\|\boldsymbol{v}\| \cdot \boldsymbol{n}^j + c)\hat{A}^j \end{aligned} \tag{3.66}$$

where $\boldsymbol{n}^{()}$ and $A^{()}$ are the average of the two unit normal face vectors and face lengths respectively in the directions of interest. It is clear that the time step magnitude will differ from cell to cell due to changes in volume and wave speeds. This constitutes the asset of *local time stepping*, which exploits the largest possible time step universally.

The value of the *CFL* number depends on the type of time discretisation. For an explicit first order finite difference approach, it is imperative that $CFL \leq 1$. More sophisticated strategies

have successfully enhanced the CFL number: Jameson et al. [96] applied a fourth order Runge-Kutta method to solve the Euler equations. Later studies produced the *multistage* scheme which decomposes time integration into a number of sub-steps with the purpose of broadening the stability region of a computation. For an m-stage scheme, the conventional time marching, given by Equation 3.9, turns into

$$\begin{aligned}
\boldsymbol{W}^{(0)} &= \boldsymbol{W}^{n} \\
\boldsymbol{W}^{(1)} &= \boldsymbol{W}^{0} - \alpha_1 \frac{\Delta t}{\Omega} \boldsymbol{R}^{(0)} \\
\boldsymbol{W}^{(2)} &= \boldsymbol{W}^{0} - \alpha_2 \frac{\Delta t}{\Omega} \boldsymbol{R}^{(1)} \\
&\vdots \\
\boldsymbol{W}^{n+1} &= \boldsymbol{W}^{(m)} = \boldsymbol{W}^{0} - \alpha_m \frac{\Delta t}{\Omega} \boldsymbol{R}^{(m-1)}
\end{aligned} \tag{3.67}$$

Stability analysis carried out by Tai et al. [102] provides us with the values for coefficients α_m and the corresponding *CFL* number in terms of the number of stages (see Table 3.2). In this study, it was found that using $m = 5$ stages produces the most efficient computational load to solution advancement compromise.

Table 3.2: Explicit multisatge α_m coefficients and *CFL* number for first order upwind schemes [102].

Stages m	*CFL*	α_1	α_2	α_3	α_4	α_5	α_6
2	1.0	0.3333	1.0				
3	1.5	0.1481	0.4000	1.0			
4	2.0	0.0834	0.2071	0.4267	1.0		
5	2.5	0.0533	0.1263	0.2375	0.4414	1.0	
6	3.0	0.0370	0.0851	0.1521	0.2562	0.4512	1.0

3.5.2 Preconditioning for Low Mach Regime

As seen in section 3.5.1, the time step is limited by the largest eigenvalue ($u+c$ in one dimension). It is also that the propagation of information is governed by not one but multiple waves moving in specific directions at specific speeds $u+c$, u and $u-c$. The slower the flow regime, the bigger the discrepancy between the large acoustic eigenvalues and the small convective ones. This has a direct detrimental effect on the rate at which a solution is obtained, otherwise known as the stiffness of the system. To illustrate this, one should consider a single cell and its associated timestep, defined using the maximum wave speed (Equation 3.65). A single pseudo-time

iteration will allow the information carried by the acoustic wave to be properly passed into the control volume. For the convective waves, on the other hand, only a small portion of the flux is advected. Thus, the number of operations required to reach convergence is significantly higher.

The issue is particularly important for cavitating flow where incompressible, high sound-speed liquid coexists with compressible, low sound-speed vapour. In the liquid region, the large discrepancies between eigenvalues will naturally slow down convergence.

To relieve stiffness, *preconditioning* is applied to the equations. Its purpose is to cluster the system's eigenvalues by multiplying the time derivative term by a matrix Γ. Time accuracy being of no concern, Γ can be populated by coefficients which control propagation speeds. The method also involves a change of set of variables from conservative $\boldsymbol{W}$ to primitive $\boldsymbol{Q} = [p, u, v]^T$. This modification carries with it a number of advantages: the viscous variables that appear in the diffusion operator are defined directly [103], $\boldsymbol{Q}$ is more practical for building higher order interpolation, and using pressure means that the acoustic waves can be isolated [104]. Moreover, in our case, application of the TE Equation makes the setting of pressure as an update variable not just beneficial but essential.

Having detailed the aim and background for preconditioning, we outline here the implementation of the method into our code. The preconditioned Euler equations, in their integral form, are given by

$$\Gamma \frac{\partial}{\partial t} \int_{\Omega} \boldsymbol{Q} d\Omega + \oint_{\partial\Omega} \boldsymbol{F}_{inv} dA = 0 \tag{3.68}$$

When discretised, the residual $\boldsymbol{R}^n$ is multiplied by the inverse of the preconditioning matrix and the primitive variable set is updated using the multistage time stepping scheme described in Section 3.5.1. It is worth noting that, in our implementation, Γ is only defined at principal time steps rather that at every sub-stage.

For the construction of Γ, our approach takes its inspiration from the method proposed by Weiss and Smith [104] compatible with the conservative flux formulation and with arbitrary EOS. Discarding the energy equation, the expression for the preconditioning matrix is

$$\Gamma = \begin{pmatrix} \Theta & 0 & 0 \\ \Theta u & \rho & 0 \\ \Theta v & 0 & \rho \end{pmatrix} \tag{3.69}$$

Here, Θ is a tunable parameter used to control propagation speeds. Defining the optimal θ is achieved by adjusting the preconditioned system's eigenvalues such that the condition number is close to unity. In [104], the authors proceed by calculating the Jacobian of the one-dimensional Euler equations and extrapolate to multi-dimensional flow by replacing u by $||u|| = \sqrt{u^2 + v^2 + w^2}$. Turkel [105], on the other hand, proposes an approach more consistent with multi-dimensional stability which seeks to derive the eigenvalues of the two-dimensional preconditioned system. In our study, the optimal value for θ is derived in a similar manner with, however, one notable difference in that the equations are expressed in their conservative form rather than the local strong form.

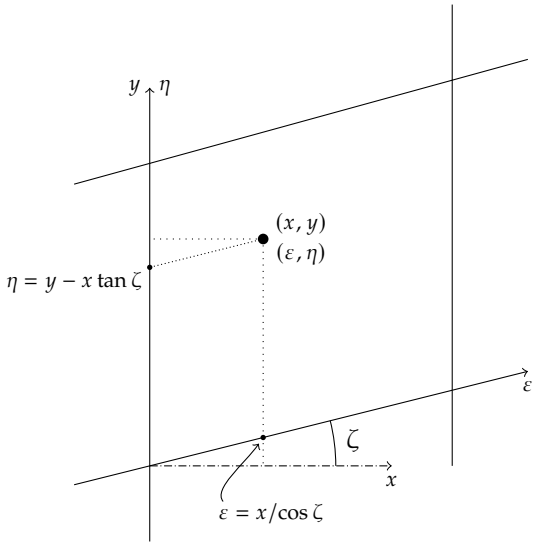

Figure 3.3: Cartesian to curvilinear transformation for the selected grid topology. The direction ζ of the curvilinear axis ε can be different at the south and north cell faces. To get a uniform cell transformation ζ is the arithmetic average of the two.

First, a set of curvilinear coordinates $\varepsilon = \varepsilon(x, y)$ and $\eta = \eta(x, y)$ is introduced to split the horizontal and vertical contributions in a manner consistent with grid topology (see Figure 3.3). By simple geometric analysis it can be shown that the mapping of (x, y) onto the (ε, η) set and vice versa is

$$\begin{pmatrix} \varepsilon \\ \eta \end{pmatrix} = \begin{pmatrix} \frac{1}{\cos\zeta} & 0 \\ -\tan\zeta & 1 \end{pmatrix} \begin{pmatrix} x \\ y \end{pmatrix} \quad \text{and} \quad \begin{pmatrix} x \\ y \end{pmatrix} = \begin{pmatrix} \cos\zeta & 0 \\ \sin\zeta & 1 \end{pmatrix} \begin{pmatrix} \varepsilon \\ \eta \end{pmatrix} \tag{3.70}$$

The conservative two-dimensional Euler equation in curvilinear space is given by

$$J^{-1}\Gamma\frac{\partial \boldsymbol{Q}}{\partial t} + \frac{\partial \boldsymbol{F}_{c,\varepsilon}}{\partial \varepsilon} + \frac{\partial \boldsymbol{F}_{c,\eta}}{\partial \eta} = 0 \tag{3.71}$$

with

$$\boldsymbol{F}_{c,\varepsilon} = J^{-1}\begin{pmatrix} \rho V_\varepsilon \\ \rho V_\varepsilon u + \varepsilon_x p \\ \rho V_\varepsilon v + \varepsilon_y p \end{pmatrix} \quad \text{and} \quad \boldsymbol{F}_{c,\eta} = J^{-1}\begin{pmatrix} \rho V_\eta \\ \rho V_\eta u + \eta_x p \\ \rho V_\eta v + \eta_y p \end{pmatrix} \tag{3.72}$$

Here, J^{-1} is the determinant of the mapping function from (ε, η) to (x, y) such that $J^{-1} = \cos\zeta$. The advection speeds V_ε and V_η are the contravariant velocities in the curvilinear plane i.e.

$$\begin{aligned} V_\varepsilon &= \varepsilon_x u + \varepsilon_y v = \frac{1}{\cos\zeta}u \\ V_\eta &= \eta_x u + \eta_y v = -\tan\zeta u + v \end{aligned} \tag{3.73}$$

A simplification is made here by taking the arithmetic average of the ζ angle at the top and bottom interfaces such that a single set of contravariant velocities exists for the whole cell rather than for each face. Notice that when V_ε and V_η are multiplied by J^{-1}, we recover the contravariant velocity vectors in the physical space.

Our procedure then follows that of Turkel [105] who transforms the convective flux vectors into their Jacobian form and multiplies by the inverse of the preconditioning matrix such that the differential system looks like the canonical hyperbolic equation

$$J^{-1}\frac{\partial \boldsymbol{Q}}{\partial t} + A\frac{\partial \boldsymbol{Q}}{\partial \varepsilon} + B\frac{\partial \boldsymbol{Q}}{\partial \eta} = 0 \tag{3.74}$$

with

$$\begin{aligned} A &= \Gamma^{-1}\frac{\partial \boldsymbol{F}_{c,\varepsilon}}{\partial \boldsymbol{Q}} \\ B &= \Gamma^{-1}\frac{\partial \boldsymbol{F}_{c,\eta}}{\partial \boldsymbol{Q}} \end{aligned} \tag{3.75}$$

By transforming the field into Fourier space, matrices A and B can be combined to form

$$D = \omega_1 A + \omega_2 B \tag{3.76}$$

where ω_1 and ω_2 are the ε and η components of the Fourier transform variable. The eigenvalues of matrix D are the Fourier equivalent of the eigenvalues of the preconditioned system. After derivation it is found that

$$\begin{aligned}
\lambda_0^D &= q \\
\lambda_\pm^D &= \frac{1}{2}\left(\left(1+\frac{1}{\Theta c^2}\right)q \pm \sqrt{\left(1+\frac{1}{\Theta c^2}\right)^2 q^2 + 4\left(l_1^2 + l_2^2 - \frac{q^2}{c^2}\right)\frac{1}{\Theta}}\right)
\end{aligned} \tag{3.77}$$

Parameters q, l_1 and l_2, which arise from the Fourier transformation, are given by

$$\begin{aligned}
q &= J^{-1}\left(V_\varepsilon \omega_1 + V_\eta \omega_2\right) \\
l_1 &= y_\eta \omega_1 - y_\varepsilon \omega_2 \\
l_2 &= -x_\eta \omega_1 + x_\varepsilon \omega_2
\end{aligned} \tag{3.78}$$

To optimise Θ, the ratio between the largest and smallest eigenvalue is to be minimised. Using the knowledge that, for low speed flows, $q^2/c^2 \ll 1$ and $1/(\Theta c^2) \ll 1$, the analysis is simplified and it transpires that

$$\frac{l_1^2 + l_2^2}{\Theta q^2} = 2 \tag{3.79}$$

To retrieve a useful value for Θ in the physical space, we substitute q for

$$q^2 = u^2 + v^2 \tag{3.80}$$

and it can be shown that

$$\begin{aligned}
l_1^2 + l_2^2 \leq L^2 &= x_\varepsilon^2 + x_\eta^2 + y_\varepsilon^2 + y_\eta^2 + 2|x_\varepsilon x_\eta + y_\varepsilon y_\eta| \\
&= 2\left(1 + |\sin\zeta|\right)
\end{aligned} \tag{3.81}$$

which finally yields

$$\frac{1}{\Theta} = \frac{u^2 + v^2}{1 + |\sin \zeta|} \tag{3.82}$$

Special care is necessary in the vicinity of stagnation points, where the low velocity will stall convergence. As a safeguard, the value for $1/\Theta$ is bounded at the low end so that any singularity is avoided. Experience has shown that using the minimum Mach number within the flow field as a global threshold produces smooth and robust convergence. At high speeds, the preconditioning mechanism is turned off by returning the system to its original primitive variable form. This is achieved by bounding $1/\Theta$ at the higher end this time and replacing its value by c^2. Put together, the complete definition of Θ is

$$\frac{1}{\Theta} = \begin{cases} M_{min}^2 c^2 & \text{if } u^2 + v^2 < M_{min}^2 c^2 \\ \dfrac{u^2 + v^2}{1 + |\sin \zeta|} & \text{if } M_{min}^2 c^2 < u^2 + v^2 < c^2 \\ c^2 & \text{if } c^2 < u^2 + v^2 \end{cases} \tag{3.83}$$

With a new set of eigenvalues comes a new time step definition. The maximum wave speed is given by λ_+ in Equation 3.77 where numbers q^2, $l_1^2 + l_2^2$ and $1/\theta$ are replaced by the expressions given in Equations 3.80, 3.81 and 3.83. Because the eigenvalue derivation is based on the 2D Euler system, the preconditioned time step takes the form

$$\Delta t = \frac{CFL\Delta_{min}}{\lambda^+} \tag{3.84}$$

rather than the method by Rizzi and Inouye which separated the wave speed for each components (see Equation 3.65 The geometric parameter Δ_{min} is the cell minimum edge length.

3.5.3 Multigrid for Cavitating Flow

The notion at the core of the multigrid technique is to construct a number of successively coarser grids to hasten convergence to steady state. The idea was developed by Brandt [106] for elliptic problems and applied to the Euler equations by Jameson [107]. Two beneficial mechanisms come into play [94]:

1. An increased stable timestep amplitude on the coarser grids, due to larger control volumes, helps to surge the computation forward and bypass the majority of the work.

2. Single grid computation is weighed down by a significant numerical defect: it can quickly cancel out residuals of the frequency that matches the spatial discretisation but is inept at handling those at lower frequencies. Mesh coarsening will balance the discrepancy between the frequency of the error and that of the spatial discretisation, thus, leading to a faster damping of residuals.

The present architecture of the multigrid algorithm follows the conventional recommendations formulated by Brandt [108] for the Euler or Navier-Stokes equations. It has however been adapted to the specificity of our studied medium, i.e. cavitating flow characterised by the TE Equation of State. A number of operations have therefore been modified, most notably in the transfer of information from grid to grid (both in the coarsening - *restriction* - and refining -*prolongation* - directions), and will be detailed below.

As a reminder, the system of equation being solved is

$$\Gamma^h \frac{\Omega^h}{\Delta t^h} \Delta \boldsymbol{W}^h + \sum_k \boldsymbol{F}_{\boldsymbol{c}_k^n} S_k = 0 \tag{3.85}$$

For steady state problems, it can be reduced to computing the generalised linear form

$$\boldsymbol{R}_h(\boldsymbol{Q}_h) = \boldsymbol{f}_h \tag{3.86}$$

where R_h contains the residuals and f_h is a source or forcing function. In the case of the Euler equations the source terms are null such that $f_h = 0$. Index h indicates the fine grid solution; coarse grids are denoted as base 2 multiples of h.

FMG Architecture

The global strategy is based on the Full Multigrid (FMG) method, wherein the computation is initiated on the coarsest grid and runs for a number μ of iterations. The temporary solution is then mapped onto the second coarsest grid where the same number μ of iterations is performed. This process is repeated until the finest level is attained. From there, the calculation will continue until convergence (see Figure 3.4). The rationale of this approach is to reduce the amount of work required at the beginning of the simulation, as the initialisation is likely to be far off the final solution.

Within the FMG framework, individual multigrid cycles advance the computation to steady

state using all available grids (or activated grids depending on the position along the FMG routine). *Brandt*'s Full Approximation Storage (FAS) method was developed for non-linear equations. It incorporates the fine grid residuals into the specially built *forcing function* of the coarser layers in order to smooth the low frequency error components while maintaining fine grid accuracy. The algorithmic programme for a single multigrid cycle is detailed here. Assuming a fine grid approximation $\boldsymbol{Q}_h^n$, the linear problem given by Equation 3.86 is modified on the next coarse grid to

$$\begin{aligned} \boldsymbol{R}_{2h}(\boldsymbol{Q}_{2h}) &= \boldsymbol{f}_{2h} \\ &= \boldsymbol{R}_{2h}\left(\boldsymbol{Q}_{2h}^{(0)}\right) - \hat{I}_h^{2h}\left(\boldsymbol{R}_h(\boldsymbol{Q}_h^n) - \boldsymbol{f}_h\right) \end{aligned} \tag{3.87}$$

Vector $\boldsymbol{Q}_{2h}^{(0)}$ is the initial guess on grid $2h$. For simplicity and robustness, it is calculated using a volume average of the states in the subset of fine grid cells. Function $\hat{I}_h^{2h}$ is the residual mapping operator. It proceeds by summing the residuals in the same subset. After a user-defined number of iterations, the coarse grid approximation $\boldsymbol{Q}_{2h}^m$ is used to correct the fine grid solution through

$$\boldsymbol{Q}_h^{n+1} = \boldsymbol{Q}_h^n + I_{2h}^h\left(\boldsymbol{Q}_{2h}^m - \boldsymbol{Q}_{2h}^{(0)}\right) \tag{3.88}$$

Here, I_{2h}^h is the reverse mapping function from coarse to fine. Depending on the interpolation technique, I_{2h}^h can be of order 0, piecewise constant, order 1, linear (bi-linear in 2D), or more using polynomial functions.

The FAS cycle is repeated until satisfactory convergence. Its algorithm can be broken down into the following steps:

- *Restriction* : the current solution is mapped onto the next coarser level and the associated fine grid residuals are brought into the coarse grid forcing function.
- Explicit time integration: the same multistage iteration and flux techniques are used on fine and coarse grids; the only difference being the presence of the forcing function on coarse levels. Time iterations can be carried out before restriction and/or after prolongation, thus, two parameters γ_1 and γ_2 are introduced and defined by the user according to the problem to be solved.
- *Prolongation* : the coarse grid correction is added to the solution on the next finer grid.

In their conventional symmetrical construction, the restriction and prolongation operators

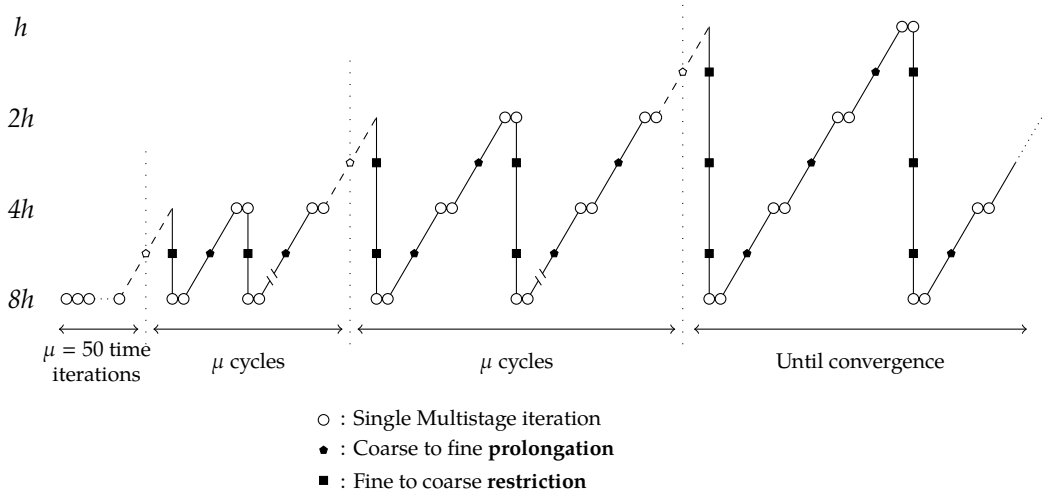

Figure 3.4: Four-grid FMG routine used to accelerate the calculation of steady state cavitating flow solutions. Note that no time-marching is carried out during restriction (from fine to coarse).

perform poorly for special flow cases such as hypersonic regimes or strong shocks. Specific treatments can be introduced to handle the upwinded propagation. The ideal value for parameters μ, γ_1 and γ_2 is obtained by trial and error. It was found that 2 post prolongation iterations and none before restriction, i.e. $\gamma_1 = 0$ and $\gamma_2 = 2$, provide the highest convergence and robustness performance. The number of initialisation cycles μ is set to 50. This specific FMG architecture is given schematically in Figure 3.4.

Cavitation Compatible *Restriction* & *Prolongation* Operators

The *restriction* and *prolongation* steps demand additional attention as specific procedures need to be implemented to handle cavitating flow and in particular the cavitation closure shock. Indeed, such conditions bring on serious difficulties for multigrid acceleration: i/ the mixture of hypersonic ($M > 10$) and low speed ($M \approx 0.1$) lead to large differences in acoustic and convective propagation in promiscuous regions, ii/ at the cavitation closure shock, density differences of several orders of magnitude are found on each side. These large gradients are smeared when transferred using central restriction or prolongation operators, leading to erroneous propagation of information and halted convergence.

The approaches chosen to remedy the aforementioned issues take inspiration from multigrid techniques for hypersonic flow problems. These introduce upwinding attributes into multigrid operators. Two procedures are of particular interest:

- the upwinded residual smoothing technique suggested by Grasso and Marini [109] or Blazek et al. [110],

- the Radespiel and Swanson [111] shock weighting operator.

The former, **upwinded residual smoothing technique**, relies on the same logic as the central residual smoothing approach i.e. enhancing the high frequency damping properties of an explicit scheme. The difference being that the smoothing coefficients are switched on or off according to local propagation speeds. We have opted for a straightforward implementation based on Mach number values. For a one-dimensional case, the smoothed residual vector $\overline{\boldsymbol{R}}_i$ is given by

$$\overline{\boldsymbol{R}}_i = [1 + \epsilon(a_i\Delta_+ - b_i\Delta_-)]\boldsymbol{R}_i \tag{3.89}$$

where Δ_+ and Δ_- correspond to the forward and backward (first order) finite difference operators. Upwinding is taken into account by coefficients a_i and b_i, defined such that

$$\begin{aligned} a_i &= 0 \quad b_i = 1 \quad \text{if} \quad M_i > 1 \\ a_i &= 1 \quad b_i = 0 \quad \text{if} \quad M_i < -1 \\ a_i &= 1 \quad b_i = 1 \quad \text{if} \quad |M_i| \leq 1 \end{aligned} \tag{3.90}$$

where M is the local Mach number obtained using contravariant velocities at the face depending on the smoothing direction. In the multigrid implementation, this procedure is carried out within the *prolongation* step only: instead of the residual vector $\boldsymbol{R}_i$, it is on the coarse grid correction vector $\delta\boldsymbol{Q}_{2h} = \left(\boldsymbol{Q}_{2h}^m - \boldsymbol{Q}_{2h}^{(0)}\right)$ that Equations 3.89 and 3.90 are applied.

The latter **shock weighting procedure** evaluates the pressure characteristic of the flow in order to locate supersonic shocks. Physically, information cannot propagate through shocks in the upstream direction. However, with conventional grid transfer operators, there is no safeguard against the averaging of cells or application of the same coarse grid correction on different sides of a shock. *Radespiel et al.* therefore introduce a damping procedure of the form

$$\tilde{\boldsymbol{R}}_i = \max(1 - \varepsilon, 0)\boldsymbol{R}_i \tag{3.91}$$

with

$$\varepsilon = \kappa_{R/P} \max(\nu_{i-1}, \nu_i, \nu_{i+1}) \tag{3.92}$$

and

$$\nu_i = \left| \frac{p_{i-1} - 2p_i + p_{i+1}}{p_{i-1} + 2p_i + p_{i+1}} \right| \tag{3.93}$$

$\kappa_{R/P}$ being a tunable parameter applied to either the restriction (index R) or prolongation (index P) steps that can vary with the coarseness and convergence levels. The shock weighting method is included in both restriction and prolongation steps, and therefore, takes on either the residual $\boldsymbol{R}_i$ or correction $\delta \boldsymbol{Q}_{2\boldsymbol{h}}$ as argument.

In the implementation presented here, the search for shocks and ensuing weighting is applied in the streamwise direction only. Computational load is cut down without downgrading the convergence rate as verified numerically. For the prolongation procedure, the value for κ_P is set at $\kappa_p = 2.1$ throughout the multigrid cycle. For the restriction operator, it was found that the shock weighting strategy is only required when mapping from h (finest) to $2h$. So parameter κ_R is switched on or off following

$$\kappa_R = \begin{cases} 2.1 & \text{if } h \rightarrow 2h \\ 0 & \text{otherwise} \end{cases} \tag{3.94}$$

With these two techniques, the amount of information passed up and down the grid tree is controlled in highly sensitive pressure shock zone. In that region, most of the numerical work is relinquished to the fine grid. This increases the computational cost but the limited size of the sensitive region means that the convergence gains are comparable to those obtained for subsonic cases. The manner in which these two amendments are built into the restriction and prolongation steps is detailed in Table 3.3.

3.6 Inverse Design Algorithms

Having detailed the techniques implemented to meet the requirements of the CFD solver, the *Inverse Design* part of the code is addressed here. Several strategies have been developed but many lack the robustness required for industrial design. The issue is the absence of a formal mathematical definition for expressing the blade geometry. This implementation follows the formulation given by Hawthorne et al. [70]. The blade surfaces $\alpha^{\pm}$ (superscript + for the pressure side, superscript − for the suction side) are expressed in terms of the camber line $f(x)$ and thickness distribution T :

$$\alpha^{\pm} =: y - (f(x) \pm T/2) = ns \tag{3.95}$$

Table 3.3: Algorithmic operations carried out by the restriction and prolongation routines.

Grid Level	Algorithmic Operation	Expression
Restriction		
h	Evaluate fine grid (preconditioned) residuals.	$\boldsymbol{R}_h = \Gamma_h^{-1}\boldsymbol{R}(\boldsymbol{Q}_h)$
h	Apply residual shock weighting.	$\tilde{\boldsymbol{R}}_h = \max(1-\varepsilon, 0)\boldsymbol{R}_h$
$h \rightarrow 2h$	Initialise coarse grid.	$\boldsymbol{Q}_{2h}^{(0)} = I_h^{2h}\boldsymbol{Q}_h^{(n)}$
$2h$	Calculate initial coarse grid residuals.	$\boldsymbol{R}_{2h}^{(0)} = \Gamma_{2h}^{-1}\boldsymbol{R}(\boldsymbol{Q}_{2h}^{(0)})$
$2h$	Assemble coarse grid forcing function.	$f_{2h} = \boldsymbol{R}_{2h}^{(0)} - I_h^{2h}(\tilde{\boldsymbol{R}}_h - f_h)$
Prolongation		
$2h$	Evaluate coarse grid correction.	$\delta\boldsymbol{Q}_{2h} = \boldsymbol{Q}_{2h}^{(*)} - \boldsymbol{Q}_{2h}^{(0)}$
$2h$	Smooth correction using upwind strategy.	$\overline{\delta\boldsymbol{Q}}_{2h} = f(\epsilon, \delta\boldsymbol{Q}_{2h})$
$2h$	Apply shock weighting to correction.	$\delta\tilde{\boldsymbol{Q}}_{2h} = \max(1-\varepsilon, 0)\overline{\delta\boldsymbol{Q}}_{2h}$
$2h \rightarrow h$	Add correction to fine grid using bi-linear interpolation.	$\boldsymbol{Q}_h^{corrected} = \boldsymbol{Q}_h^{(n)} + I_{2h}^h\delta\tilde{\boldsymbol{Q}}_{2h}$

The modifications are applied to the camber line only. The thickness distribution remains unaltered throughout the computation, thus ensuring the blade is always closed. Under this inverse design formulation, two approaches to the problem are available and vary according to the prescribed quantity:

- Mass averaged tangential velocity
- Blade static pressure loading

The former relies on iterative computations of the steady state solution interspersed with geometrical updates to arrive at the target geometry, the latter makes uses of a permeable wall boundary condition to modify blade shape during the transient phase of the simulation. Here, only the numerical mechanism is presented and the choices made for the target distribution are explained in Chapter 5.

3.6.1 Tangential Velocity Loading

Tan et al. [71] have shown that for two-dimensional turbomachinery cascades the camber line

is connected to the mass flow averaged velocity distribution between the pressure and suction sides of a blade through the relation

$$\frac{\partial f}{\partial x} = \frac{\overline{V_y}}{\overline{V_x}} \tag{3.96}$$

where f is the camber line coordinate. The mass averaged quantities are given by

$$\overline{\phi} = \frac{\int_{PS}^{SS} \phi \rho V_m dy}{\int_{PS}^{SS} \rho V_m dy} \tag{3.97}$$

where ϕ is replaced by V_x or V_y and V_m is the meridional velocity. Expression 3.96 allows the prescription of a target distribution $\hat{V}_y$, offering control over the swirl evolution. It has been shown by Hawthorne et al. [70] that the meridional derivative of the mass averaged tangential velocity is related to the pressure difference across the blade $\Delta p = p_{PS} - p_{SS}$

$$\Delta p = \frac{2\pi}{N} \rho V_{m_{bl}} \frac{\partial \overline{V_y}}{\partial m} \tag{3.98}$$

where N is the number of blades and $V_{m_{bl}}$ is the averaged meridional velocity across the blade. For the infinite cascade configuration studied here, equation 3.98 is non-defined but the proportionality relation still holds

$$\Delta p \propto \frac{\partial \overline{V_y}}{\partial m} \tag{3.99}$$

meaning that prescribing $\overline{V_y}$ not only determines the amount of work produced through the channel but also grants control over the pressure on the blade surfaces.

Given an initial baseline geometry and its associated flow field, one can derive an iterative procedure to advance to the desired geometry by combining the camber line relations for the current and target distributions:

$$\begin{aligned} \text{Current:} \quad & \frac{\partial f}{\partial x} = \frac{\overline{V_y}}{\overline{V_x}} \\ \text{Target:} \quad & \frac{\partial \hat{f}}{\partial x} = \frac{\hat{V}_y}{\hat{V}_x} \end{aligned} \tag{3.100}$$

It is assumed that the changes operated on f only marginally affect the meridional/axial

velocity so that $\overline{V_x} \approx \hat{V}_x$, which allows the approximation

$$\frac{\partial \hat{f}}{\partial x} - \frac{\partial f}{\partial x} = \frac{\hat{V}_y - \overline{V_y}}{\overline{V_x}} \tag{3.101}$$

Equation 3.101 is a first order ODE which can easily be integrated to provide the solution of $\hat{f}$ in terms of $\Delta\hat{V}_y = \hat{V}_y - \overline{V_y}$. Flow field variables $\overline{V_x}$ and $\overline{V_y}$ are obtained from the steady state solution of the current geometry. The update procedure is therefore iterative and consists of:

1. CFD computation of the steady state solution associated to the baseline or intermediate geometry

2. Numerical integration of 3.101, i.e.

$$\frac{\hat{f}_{i+1} - \hat{f}_i}{x_{i+1} - x_i} - \frac{f_{i+1} - f_i}{x_{i+1} - x_i} = \frac{\Delta\hat{V}_{y_{i+1}}}{\overline{V_x}_{i+1}} \tag{3.102}$$

   to obtain $\hat{f}$ using $\overline{V_x}$ and $\overline{V_y}$ from the CFD solution.

Convergence is attained when the change in camber line profile and the maximum absolute difference $|\Delta\hat{V}_y|$ are below a specified tolerance.

An issue that crops up for cavitating flow is the transmission of the amplitude and sharpness of the pressure shock into the $\Delta\hat{V}_y$ distribution. The result is a camber line that may undergo large nodal variations, with neighbouring points potentially shifted in opposite directions. Given the sensitivity of the shock location and pattern, a negative feedback loop is thus initiated, preventing convergence of the Inverse Design problem. As a countermeasure, smoothing is introduced into the resolution approach of Equation 3.101. It is applied to the RHS using a weighted moving average to soften the irregularities in the $\Delta\hat{V}_y$ profile:

$$\psi_i^* = \frac{1}{\sum_{k=i-s}^{i+s} w_k} \sum_{k=i-s}^{i+s} w_k \psi_k \tag{3.103}$$

where ψ stands as any arbitrary function and is replaced by the RHS of 3.101 in the design iteration, s is an integral number that limits the left and right reach of the moving average, and

w_k are the distance weighting coefficients given by:

$$w_k = 1 - \frac{|x_k - x_i|}{|x_{i+s} - x_{i-s}|} \tag{3.104}$$

3.6.2 Pressure Loading Approach

The alternative family of inverse design techniques exploits the pressure distribution over the blade and allows geometry changes during the transient computation. The methods assume a permeable boundary at the wall and allow the displacement of the blade surfaces during the transient computation. Mathematically, the problem remains well-posed as an additional boundary condition balances the new degree of freedom granted to the blade. The gain is a substantial reduction in computational demand as the amount of work required for producing a new geometry is of the same order of magnitude as a pure analysis run.

Algorithm Construction

When the target pressure is prescribed over the blade surfaces, a change in the direction of velocity at the wall is expected. Because the flow tangency condition has to be satisfied, the new velocity vectors guide the blade update procedure. On the blade surfaces the free slip wall condition is formulated as:

$$\mathbf{V}^{\pm} \cdot \nabla \alpha^{\pm} = 0 \tag{3.105}$$

where $\mathbf{V} = (V_x, V_y)$ is the velocity vector at the wall. From equation 3.105, the relation between camber line and velocity vector can be extracted and used as the update procedure. The conditions on both surfaces are combined

$$\mathbf{V}^{+} \cdot \nabla \alpha^{+} + \mathbf{V}^{-} \cdot \nabla \alpha^{-} = 0 \tag{3.106}$$

and the blade definition 3.95 is introduced into 3.106. After expansion it is found that

$$\langle V_x \rangle \frac{\partial f}{\partial x} = \langle V_y \rangle - \frac{1}{4} \Delta V_x \frac{\partial T}{\partial x} \tag{3.107}$$

noting the operators

$$\langle () \rangle = \frac{1}{2} \left(()^{+} + ()^{-} \right) \qquad \Delta() = ()^{+} - ()^{-} \tag{3.108}$$

Equation 3.107 provides an expression for integrating the camber line, dependent only on the velocity vectors at the blade surfaces. Blade stacking (i.e. the position of the immobile camber node) is imposed at the leading edge and serves as the boundary condition for the numerical integration process. The blade update is repeated periodically until the computation converges, yielding tangential flow along the blade and the desired pressure distribution. For multigrid computations, the geometry is modified on the fine grid after each cycle.

Because the fluid computation and the design procedure are amalgamated into one single problem, no additional convergence control mechanism is necessary other than the residual values i.e. the average residuals for p,V_x,V_y need to be below 10^{-6}.

Permeable Wall Boundary

The prescribed quantity is the pressure loading $\Delta p = p^+ - p^-$ rather than the surface values directly. This is motivated by robustness and by alignment with industrial practice. The pressure on the blade surfaces is given by

$$p^{\pm} = \langle p^n \rangle \pm \frac{\Delta p}{2} \tag{3.109}$$

where $\langle p^n \rangle$ is the average of the current suction side and pressure side pressures.

In analysis mode, the solver models the free slip wall condition using a reflecting boundary. Ghost cells are created on the other side of the wall with equal density and pressure but with a symmetrical image of the velocity vector. As with all other internal cells, the contribution of the ghost cell is determined by solving the Riemann problem at the interface. This type of boundary implementation already possesses the properties of a permeable wall.

Therfore, the approach for prescribing the pressure over the blade is a straightforward modification of the existing reflecting boundary. Instead of assigning the same pressure on the outside (gost cell) and inside of the boundary, it is the target pressure value that is given to the exterior ghost cell. The other flow quantities (density, velocity, temperature) follow the classical reflecting boundary condition. The prescribed pressure is therefore transmitted into the computational domain by a purely acoustic wave originating at the wall. At convergence, the amplitude of the wave is too small to disturb the computed flow field.

This constitutes a significantly different procedure than the ones described by Tiow and Zangeneh [80] and Dang et al. [79]. In both, the velocity components at the wall are corrected using terms derived solver the tangency condition 3.105. For this flow configuration, it was

found that forcing the wall velocity had deleterious effect on stability. The simple adaptation of the reflecting boundary proved much more effective.

For the multigrid procedure, no special treatment is implemented. The one-dimensional target distribution is mapped onto the next coarse level by averaging the Δp points in pairs. Of course, it is essential that the mesh be constructed such that grid coarsening does not create cells overlapping both the blade region and the inflow/outflow regions around the leading and trailing edges. Such cells would be corrupted due to a non-homogeneous definition of one of the faces i.e. half periodic boundary and half reflecting/permeable boundary. Considering the mesh topology, it is recommended to split the domain into three blocks (inflow, blade channel, outflow) which can be fully discretised independently from the finest to the coarsest level.

Leading and Trailing Edge Treatment

There are regions along the blade where the tangency condition is only poorly satisfied even at full convergence. This phenomenon is due to mesh topology and to high velocity gradients. Regions most affected are located in proximity to the stagnation points at the leading and trailing edges even in the absence of separation. The effect is amplified for thicker blades as velocity gradients tend to be stronger.

For the studied cascade configuration, prescribing a target pressure and applying the update procedure (equation 3.107) in these sensitive zones systematically causes either a cyclical flapping of the blade, caused by transient vortices forming at the trailing edge and feeding into the inverse procedure, or the breakdown of the computation. To mitigate these instabilities the freedom of movement is limited to the region ranging from 10% to 95% of blade chord. For the purposes of this research, this approach does not significantly hinder the capability of the design method as it is the flow behaviour in the central part of the blade, namely at the cavitation closure shock that is most valuable.

In the leading edge region ($x/chord \leq 0.1$), the camber line keeps its original shape i.e. that of the baseline geometry. Any differences between the target and baseline loadings are ignored. The starting point of the integration process (equation 3.107) corresponds to the first node i which satisfies $x_i/chord \geq 0.1$. At the trailing edge, the nodal positions after $0.9 \leq x_i/chord \leq 1$ are constructed from the updated upstream points using linear extrapolation. A smooth transition is ensured to maintain numerical robustness and structural integrity.

3.7 Concluding remarks

In this chapter, we have laid out the algorithmic construction of our inverse design solver. Implementation choices were motivated by the need for robustness and speed. In this regard, the preconditioning and multigrid techniques are key elements of the numerical structure and have been enhanced with unique features put in place to answer the specificities of cavitating flow. The inverse design capacity is met through two approaches: the mass averaged $\overline{V}_y$ and Δp techniques.

For the fluxing scheme, the question is left open. Four approaches have been implemented: the central JST method, the upwind flux-difference-splitting Roe method, and the upwind hybrid AUSM and its evolution SLAU methods. The best candidate will be determined in the next chapter based on the capturing of the cavity closure region. Other numerical settings will also be examined in the next chapter, which will detail the work accomplished to verify our solver's efficacy. These include multigrid parameters, grid independence, and the effects of viscous or RANS turbulence modelling.

4 Verification of Solver Performance

Here, a number of numerical experiments are carried out to demonstrate the accuracy and efficiency of the developed solver. The solutions obtained are compared against tried-and-tested commercial software. ANSYS Fluent is selected as reference because it accepts purely 2D computations and offers the user substantial control over solver parameters. Calculations are run for the Baseline problem in cavitating and non-cavitating conditions.

The runs also serve to fine tune the solver's settings. Components to be assigned are (i) flux discretisation schemes: Jameson central, Roe FDS, AUSM or SLAU, (ii) minimal grid resolution, (iii) multigrid parameters: residual smoothing ε and shock weighting κ. The impact of RANS turbulence modelling on the character of cavitation is examined to determine whether its implementation is necessary.

4.1 Baseline Profile

The Baseline blade serves two purposes: (i) as a test specimen for the development of the *inverse design* solver, (ii) as the baseline geometry against which improved designs will be measured. As such, it must meet specific requirements. Primarily, it should present flow characteristics, i.e. meridional velocity, swirl and static pressure distribution, similar to those found within impeller or runner wheels. To start blade construction, an arbitrary impeller is designed. An important condition is that the produced flow field have minimal 3D effects given the two-dimensional character of the research. This eliminates radial and mixed flow type impellers from the possible options. The result is a high diameter and high blade number axial flow

impeller (see Table 4.1).

The 2D profile is extracted from the hub location by unfolding the cylindrical coordinates onto the Cartesian transverse plane, such that $X = z$ and $Y = r\theta$. The resulting blade is as shown in Figure 4.1. With these values of $chord$ and $pitch$, the solidity ratio, given as the ratio of the former over the latter ($chord/pitch$), is equal to 0.259. At this value the interaction between blades is close to negligible and the case study resembles more that of a single hydrofoil case than that of hydraulic turbomachinery components which tend to have solidity ratios close to 1.5. The pitch is therefore shrunk to match the desired solidity value ($pitch = chord/1.5 = 0.090\,53\,\text{m}$).

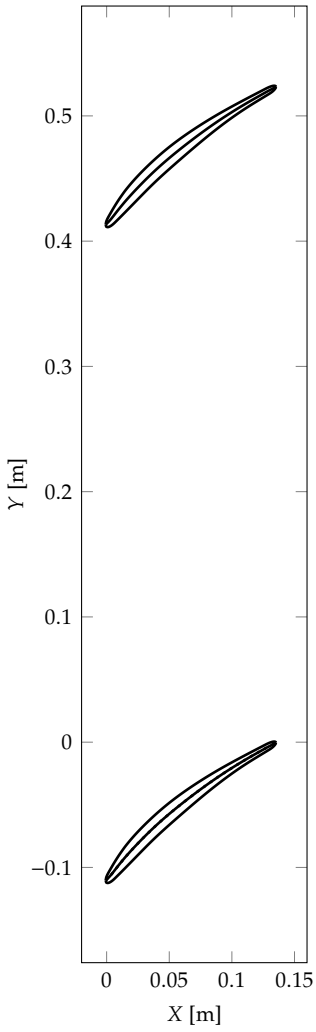

Figure 4.1: Blade profile taken from the hub of the arbitrary pump impeller design.

This modification does not come without its repercussions on the flow. Examining blade pressure for both wide and narrow pitches for identical boundary conditions (see Figure 4.2b) shows a dramatic change in both the general pattern and incidence level: whereas, with the

Table 4.1: Designed impeller characteristics and conversion to the 2D stationary cascade.

3D Axial Impeller	
D_{hub}	20 m
N_{blades}	120
Ω	10 RPM
$U_{meridional}$	10.0 m/s
Chord	0.1358 m

Hub Cascade	
U_{inflow}	10.0 m s^{-1}
V_{inflow}	10.472 m s^{-1}
Inflow Angle β	46.321°
Pitch	0.5236 m
Chord	0.1358 m

wide pitch setting, a workable distribution was produced, the character of the new distribution is evidently not conducive to a proper study of cavitation, the principal issue being the low pressure drop in the leading edge region.

To recover a satisfactory profile, a redesign of the case is undertaken. The final blade shape is shown in Figure 4.2a and its specific pressure profile at cavitation numbers $\sigma = 1.167$ and $\sigma = 0.667$ is given in Figure 4.2b. Incidence is absent and it exhibits a constant increase in pressure throughout the channel. At low σ number, sheet cavitation is limited to the blade's suction side and the sharp closure shock is a clear feature of the flow.

Table 4.2: Baseline cascade characteristics. Other than the pitch, none of the values have changed from the preliminary hub cascade (Table 4.1).

Baseline Stationary Cascade	
U_{inflow}	10.0 m s^{-1}
V_{inflow}	10.472 m s^{-1}
Inflow Angle β	46.321°
Pitch	0.090 53 m
Chord	0.1358 m

4.2 Fluxing Scheme Analysis

A primordial question to be answered concerns the discretisation of the inviscid fluxes. Being solely interested in the steady state solution for design purposes, the accuracy of our code is fully dependent on the numerical interpretation of the spatial derivative terms. As explained in Section 3.2, both upwind and central approaches have been implemented, namely Jameson's central, Roe FDS, original AUSM and SLAU schemes. To determine the most capable technique, the static pressure distribution over the blade, as well as the water vapour volume fraction con-

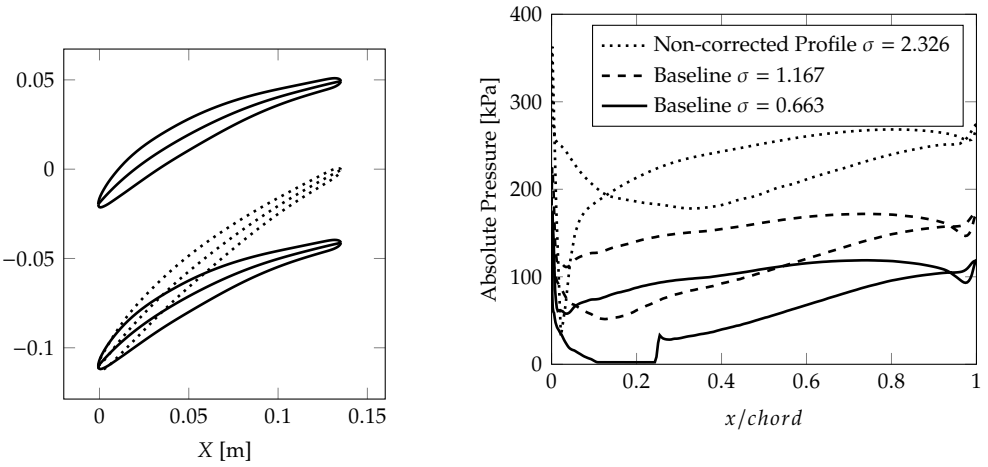

(a) Blade Geometry **(b)** Pressure Distribution

Figure 4.2: Baseline geometry and surface pressure after the redesign of the prelimnary hub profile. Pressure data is obtained from ANSYS Fluent solutions.

tours are monitored. In cavitating conditions, the features specifically sought after are: sharp shock capturing and clear demarcation of the cavitating region. Because fluxing techniques also affect computational stability, the convergence rate is another assessment criterion.

All four schemes are run for the *Baseline* geometry (see Section 4.1) on three grids of increasing resolution with respectively 5120, 6656 and 15360 cells (see levels 4, 5 and 6 in Table 4.4). The inflow angle and mass flow match the configuration detailed in Table 4.1. For a comprehensive assessment, computations are run under both non-cavitating and cavitating conditions. The cavitation number and corresponding boundary conditions are given in Table 4.3.

Table 4.3: Boundary conditions applied for the performance assessment of the *in-house* solver on *TE Equation-of-State* governed flow. Both non-cavitating (σ = 1.369) and cavitating (σ = 0.651) pressure levels are considered.

Cavitation number σ	Inlet		Outlet
	Total pressure [kPa]	Inflow angle	Mass flow rate [kg s^{-1}]
1.369	P^0_{in} = 250	β = 46.321°	$\dot{m}_{out} = \rho_{in} u_\infty pitch$
0.700	P^0_{in} = 180		

The solutions produced by the in-house solver are compared to those provided by Fluent. To isolate the effect of the fluxing schemes, the fluid properties and discretisation parameters are copied from the *In-house* code to the commercial solver: the flow is assumed compressible,

inviscid and isothermal, cell face values are first order accurate and cavitation is modelled using the TE equation of state (see Section 3.3). The standard cavitation model in Fluent is the Zwart-Gerber-Belamri *transport* type approach. To override it, the multiphase option is switched off. Instead, a new compressible fluid is created with a density that varies according to the TE equation. The state law is defined by coupling user-defined subroutines written using the C language Fluent library to the solver. They serve to calculate the density and the speed of sound from the pressure computed by the core algorithm. The Fluent calculation is run for grids 5 and 6 (respectively 6656 and 15360 cells see Table 4.4). At the inlet, total pressure is imposed as is done for the In-house solver. At the outlet, the target mass flow rate is prescribed through static pressure adjustment. Its value is such that the axial velocity at inlet is $u_\infty = 10\,\mathrm{m\,s^{-1}}$.

At $\sigma = 1.369$, the differences in static pressure over the blade are marginal (see FIgure 4.3). Wriggles are picked up when using the hybrid P-Roe and SLAU schemes in zones where the aspect ratio of the cells at the blade is poorest. Moreover, at the trailing edge, the pressure and suction side distributions either intersect for the Fluent, Jameson, and AUSM solutions, or don't for the P-Roe and SLAU technique. The latter two are based on a similar low dissipation treatment of the mass flow and appear to be more sensitive to grid alignment and to the direction of the wall. Deviations are more significant when cavitation occurs at $\sigma = 0.700$ (Figure 4.3b). Differences are found around the closure shock which varies in terms of location, gradient and amplitude. The Jameson central scheme delivers the smoothest pressure increase illustrating the method's excessive diffusivity. Its amplitude, on the other hand, is less than half of the other four solutions. For P-Roe, the amplitude sits in between the AUSM and Fluent results. The P-Roe shock is also initiated further downstream. Generally, the Roe FDS method is known to perform well in the presence of shocks. Here, it has been altered to take preconditioning into consideration. The simplifications made to adapt the scheme, in particular abandoning the Roe averaging, may be responsible for downgrading the method. Out of the tested approaches, the SLAU scheme agrees best with the Fluent result. Shock location and amplitude are identical, while sharpness is enhanced in the SLAU distribution. In the trailing edge region, a discrepancy of the same nature as in non-cavitating conditions is visible.

The effect of grid resolution on the closure shock is shown in Figure 4.4. For the Fluent runs, mesh refinement has no significant effect on the character of the shock: same amplitude, gradient and location for grids 5 and 6. For the four fluxing schemes implemented into the in-house solver, the results are more or less sensitive to grid resolution. For the Jameson central

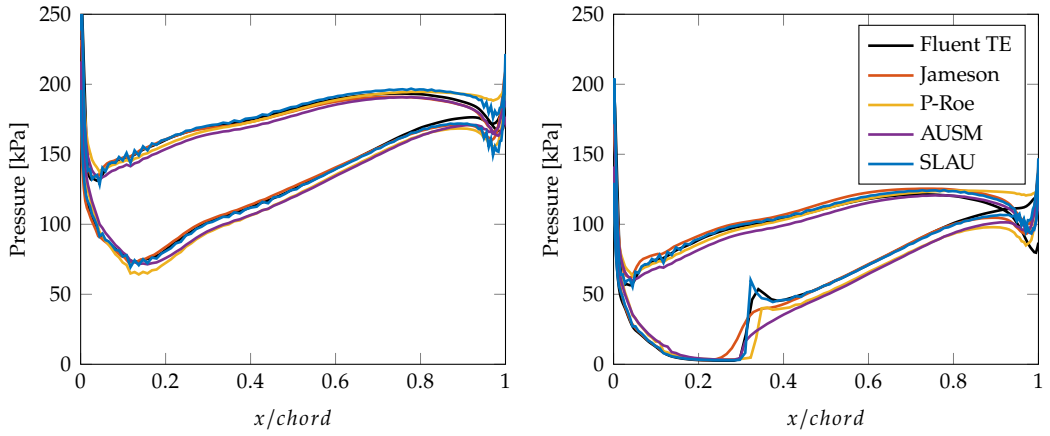

(a) Non-Cavitating $\sigma = 1.369$ **(b)** Cavitating $\sigma = 0.700$

Figure 4.3: Blade static pressure distribution obtained from the *Central*, *Original AUSM* and *SLAU* flux discretisation methods. The Fluent, with built-in *TE Equation-of-State*, solution is used as reference.

scheme (Figure 4.4a), the shock increases in sharpness from grid 4 to grid 5. Beyond this refinement level, the variations are negligible as suggested by the grid 5 and grid 6 solutions which perfectly overlap. Compared to the Fluent data, the Jameson solution still lacks the adequate sharpness. The preconditioned Roe FDS technique appears much more sensitive to the tested resolution levels (Figure 4.4b). Discrepancies are observed in the location and amplitude of the shock, even from grid 5 to grid 6. Another defect is that the solution still produces a non negligible offset in shock location and in the computed pressure along the suction side when compared to the Fluent reference. The same can be said of the AUSM scheme (Figure 4.4c) except that changes are more linear: shock gradient, shock amplitude and closure position increase with the number of cells. At the finest grid, the pressure jump does not carry the sharpness of the Fluent distribution and the closure position is too far downstream. By contrast, the SLAU scheme (Figure 4.4d) delivers both a consistent distribution regardless of grid size and one that matches the Fluent result. Discrepancies are limited to the extent of the shock overshoot while gradient and location remain fixed.

Observation of the contour maps for each solution (Figures 4.6 to 4.10) leads to the same conclusion. The *central* and *AUSM* schemes yield a smooth pressure field and a reduced cavity size; whereas the *SLAU* solution delivers a clearly defined closure region at which the pressure contours converge to mark the shock.

In terms of convergence rate, the upwind methods (P-Roe, AUSM and SLAU) reach steady state in a comparable number of iterations. The residual decrease curves plotted in Figures 4.5a and 4.5b come from 4 grid FMG computations at $\sigma = 0.700$. The Jameson central scheme

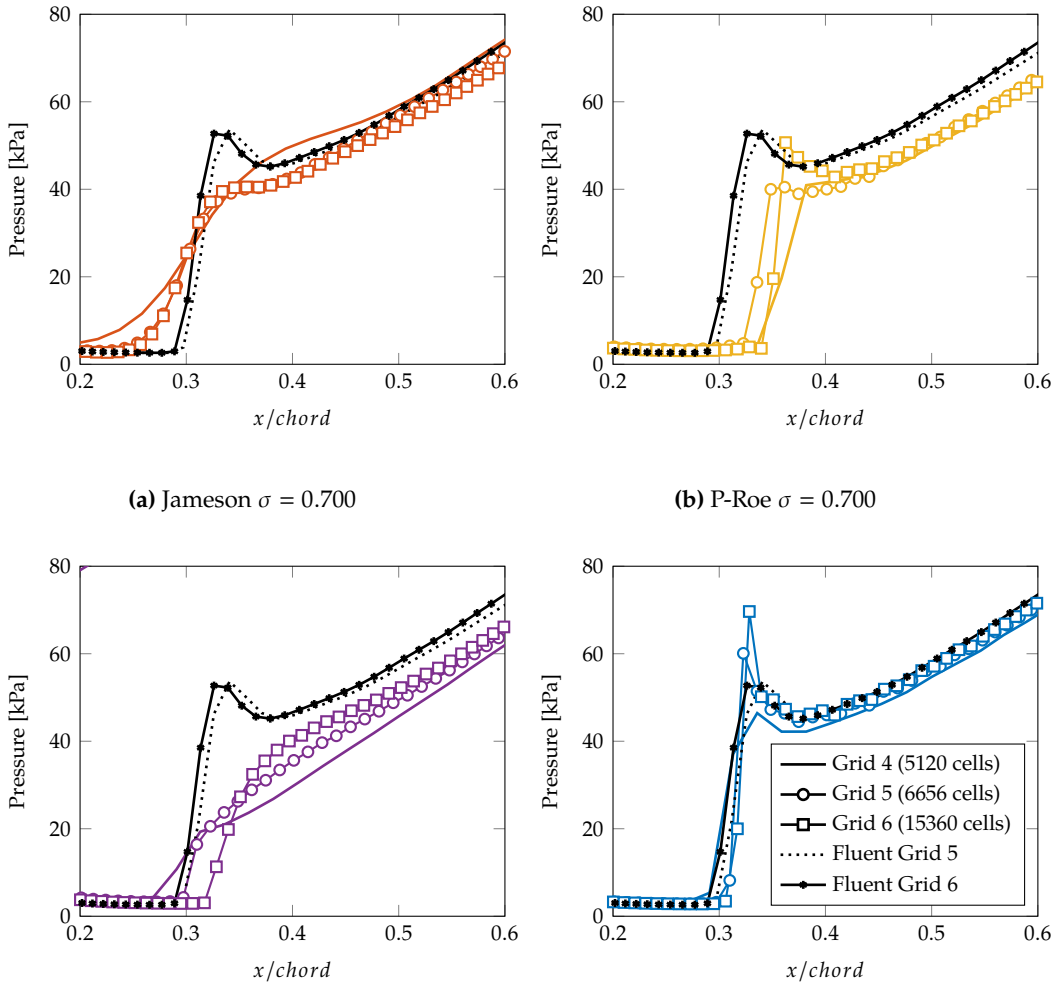

(a) Jameson $\sigma = 0.700$

(b) P-Roe $\sigma = 0.700$

(c) AUSM $\sigma = 0.700$

(d) SLAU $\sigma = 0.700$

Figure 4.4: Closure shock captured by the four tested fluxing schemes: Jameson, P-Roe, AUSM and SLAU, and by Fluent with the TE model for increasing grid resolutions at $\sigma = 0.700$.

was not implemented into the FMG enhanced solver. Its single grid convergence history is shown in Figure 4.5 against the single grid SLAU computation. Ideally, the preconditioned Jameson flux should receive special treatment to enable artificial dissipation on the primitive rather conservative state vector. This task was not undertaken here because (i) the upwind methods already constitute a robust and accurate approach, (ii) ready-to-use forms for artificial dissipation are available for ideal gas flow, but none exist for the TE Equation of State. Out of the three upwind schemes, the SLAU convergence rate is the lowest. However, its robustness surpasses the other two which are sensitive to boundary changes and fail to arrive at a solution at cavitation numbers below $\sigma = 0.700$.

From the results presented here, the choice of the SLAU scheme comes as natural. Its low dissipation construction delivers the sharpest shock at a location that matches the benchmark

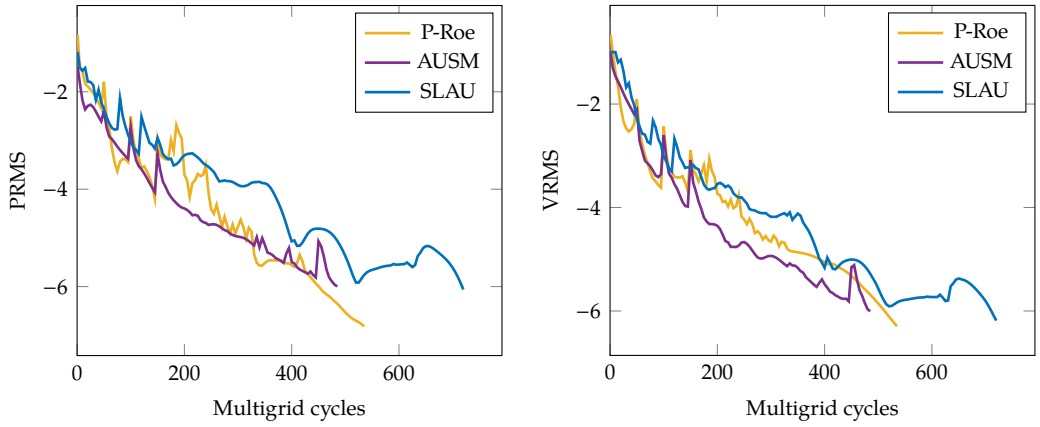

(a) Pressure residual

(b) v_y residual

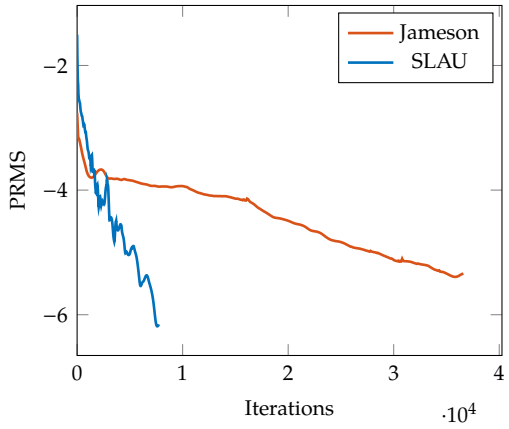

(c) Single grid pressure residual

Figure 4.5: Comparison of residual decrease for central (Jameson) and upwind (P-Roe, AUSM and SLAU) fluxing schemes at $\sigma = 0.700$.

solver. On top of that, the applicability over a wide range of flow regimes ensures the calculation converges in a stable manner and, of utmost importance for design, can cope with changing conditions. The data in the following paragraphs and chapters is calculated using the SLAU fluxing scheme.

4.3 Grid Dependence Analysis

A grid independence study is carried out to ensure that the flow features of the 2D cascade, particularly those pertaining to cavitation, are constant regardless of mesh refinement. In this work, cavitation closure shock and cascade hydrodynamic performance are the primary points of interest. For the former, the assessment criteria are shock location, amplitude and gradient. In terms of hydrodynamic performance, metrics such as swirl, lift and drag are evaluated. In

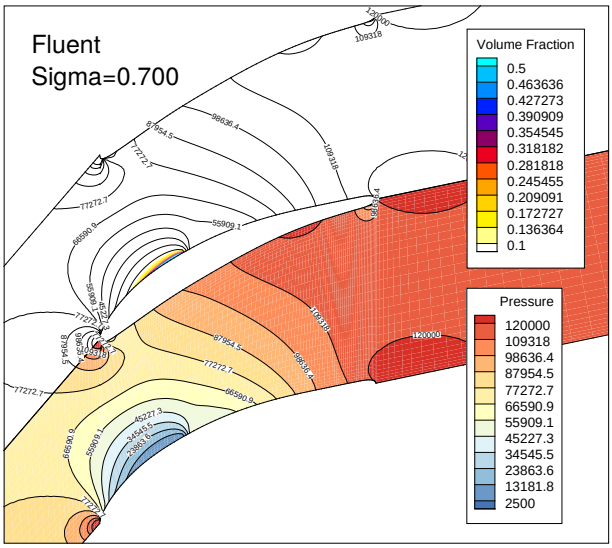

Figure 4.6: Pressure and volume fraction contours from Fluent with *TE* model

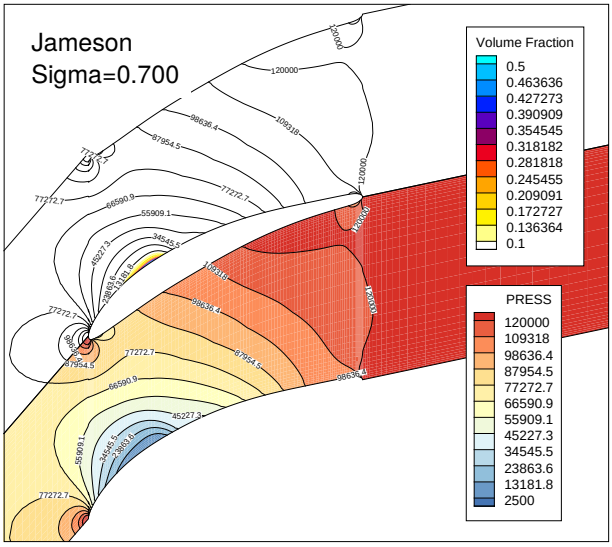

Figure 4.7: Pressure and volume fraction contours from the Jameson Central scheme

the case of single hydrofoils the lift and drag are equal to the forces exerted in the directions normal and parallel to the free stream flow. For cascade problems, the directions of lift and drag are case specific. By convention, a new coordinate system is introduced by rotating the Cartesian (x, y) frame by β_m. The angle β_m is dependent on the amount of swirl performed by the cascade and is defined as

$$\tan \beta_m = \frac{1}{2} \left(\tan \beta_1 + \tan \beta_2 \right) \tag{4.1}$$

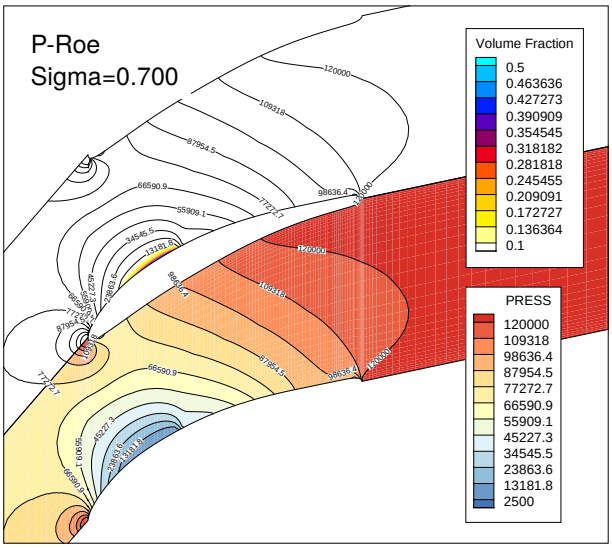

Figure 4.8: Pressure and volume fraction contours from the P-Roe scheme

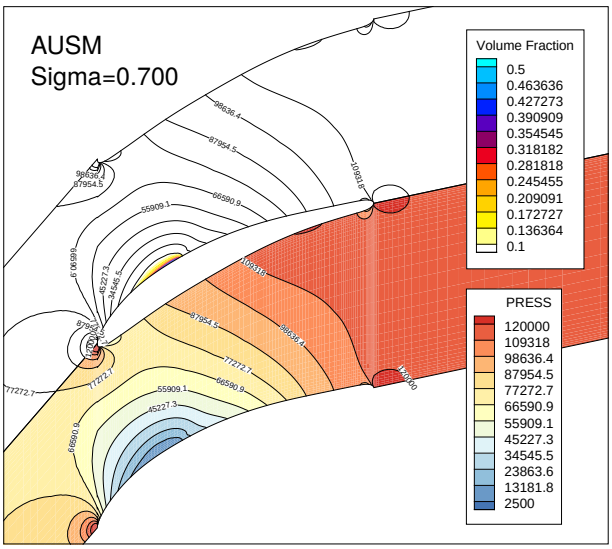

Figure 4.9: Pressure and volume fraction contours from the AUSM scheme

where β_1 and β_2 are the inflow and outflow angles respectively. The values for lift and drag can be obtained by calculating the force vector resulting from the pressure exerted on blade surfaces and projecting it onto the rotated axes. Alternatively, by balancing the momentum equation across the control volume surrounding a single channel, lift and drag can be expressed in terms of total pressure loss:

$$\begin{aligned} D &= s\Delta p_0 \cos\beta_m \\ L &= \rho s V_x^2 \left(\tan\beta_1 - \tan\beta_2\right) \sec\beta_m - s\Delta p_0 \sin\beta_m \end{aligned} \tag{4.2}$$

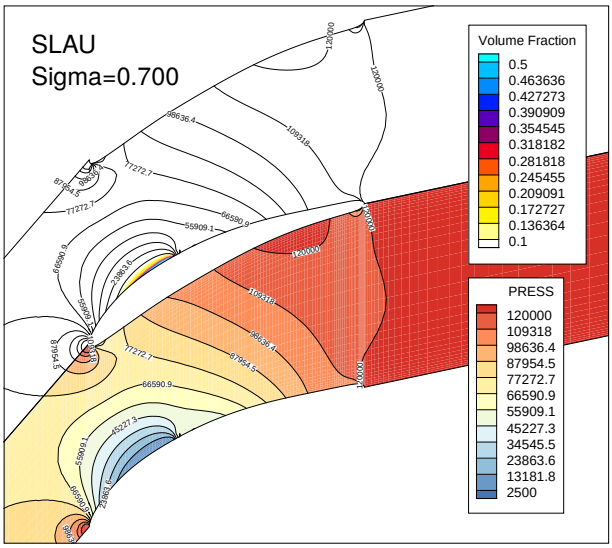

Figure 4.10: Pressure and volume fraction contours from the SLAU scheme

The advantage of the control volume approach is that it directly takes into account viscous and turbulent losses. Under the inviscid assumption, as is the case here, Δp measures the numerical dissipation produced by the solver. The analysis carried out here will serve to determine the minimal mesh dimensions for obtaining a reliable flow field and carrying out design runs.

Six grids of increasing resolution are constructed and listed in Table 4.4. The flow conditions are those used for the flux discretisation comparison i.e. $\sigma = 1.369$ and $\sigma = 0.700$. Convergence is attained when residuals for both mass and momentum conservation equations have decreased by at least 6 orders of magnitude.

Table 4.4: Grid dimensions for each resolution level. In the streamwise direction, the domain is divided into three sections: inflow region, blade channel and outflow region.

Grid	Streamwise				Tangential	Total Cells
	Full length	(In	Blade Channel	Out)		
1	40	12	16	12	10	400
2	80	24	32	24	16	1280
3	112	32	48	32	24	2688
4*	160	48	64	48	32	5120
5*	192	48	112	48	32	6656
6*	236	56	128	56	64	15360

* Grids used for fluxing scheme assessment (Section 4.2).

The pressure distribution results are presented in Figure 4.11 for both non-cavitating and

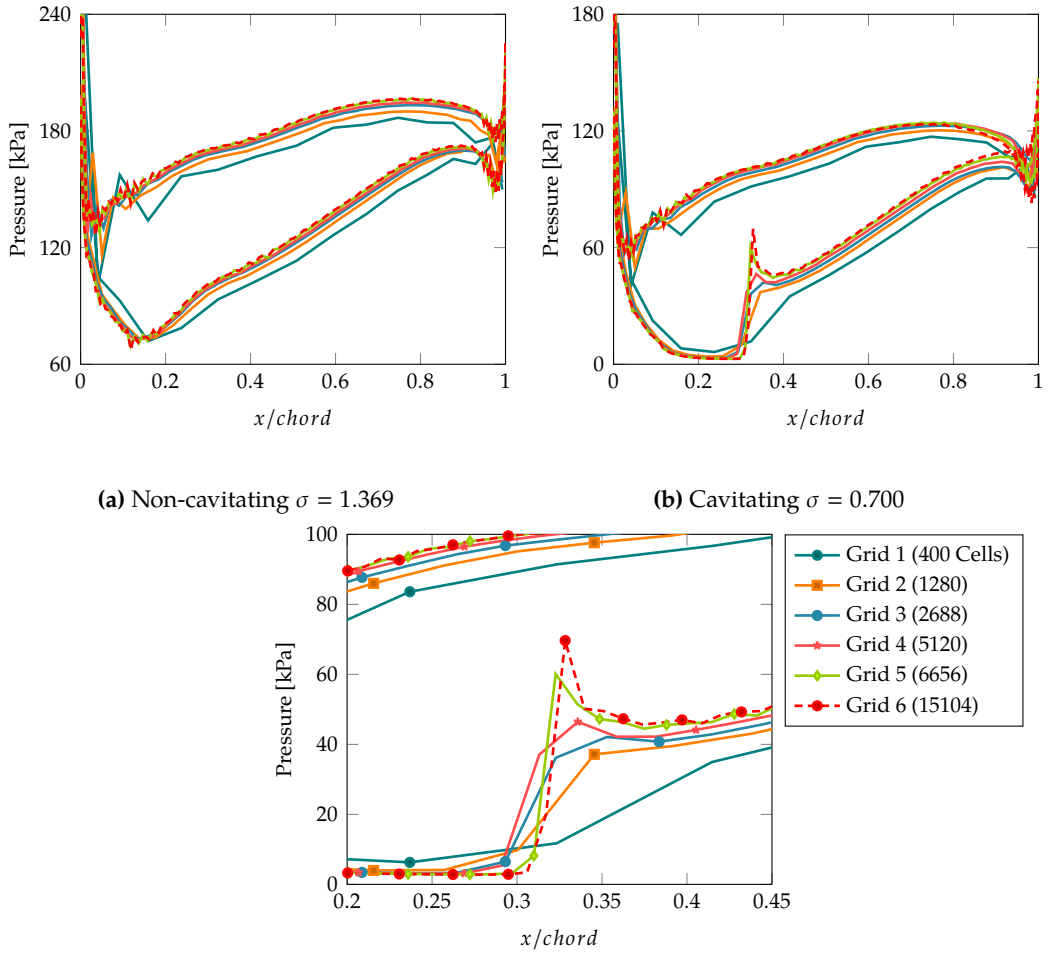

(a) Non-cavitating $\sigma = 1.369$

(b) Cavitating $\sigma = 0.700$

(c) Close-up $\sigma = 0.700$

Figure 4.11: Comparison of blade static pressure for increasing resolution levels at $\sigma = 1.369$ and $\sigma = 0.700$. All solutions are obtained using the SLAU flux discretisation method.

cavitating conditions. At $\sigma = 1.369$, discrepancies are noticeable for grids 1 to 3, which show a general negative offset on both suction and pressure sides when compared to the finer distributions. The more refined solutions overlap well, especially grids 5 and 6 which are perfectly aligned. The cavitating pressure profiles at $\sigma = 0.700$ are more telling. The pressure jump consistently stretches over a single cell interface such that shock gradient is limited by the cell size and shock location is determined by the first node position. Variations in shock amplitude are observed for the different refinement levels. Grids 4 and above present a recovery overshoot of increasing strength as the mesh is refined. For consistency, the amplitude is measured as the pressure difference between the pre-shock and post-overshoot drop at $x/chord \approx 0.4$. Figure 4.12 shows the shock growth in terms of the streamwise node count in the blade channel section. For the resolution levels computed here, the increase is root graph shaped. Additional refinements in the shock region may asymptotically lead to a fixed value.

Numerical oscillations appear along the pressure solutions of grids 5 and 6 for both non-cavitating and cavitating cases because of aspect ratio downgrade as laid out in Section 4.2. The distributions for the coarser grids are smooth.

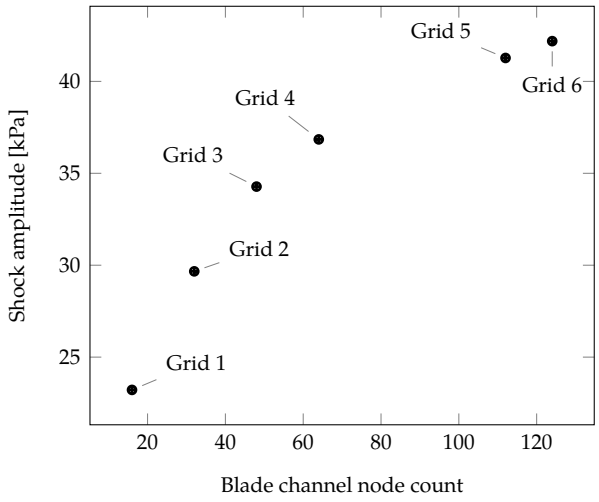

Figure 4.12: Amplitude of closure shock captured by the SLAU scheme for the six refinement levels.

The changes in swirl, lift and drag are reported in Figure 4.13. In non-cavitating conditions ($\sigma = 1.369$), the ΔV_y and C_L values start to plateau at grid 3. The two metrics evolve in a similar manner, demonstrating their equivalence for quantifying cascade work output. In cavitating conditions ($\sigma = 0.700$), the generated work keeps decreasing as the grid is refined. The deviations in the cavitation region being marginal, the drop comes from the trailing edge behaviour where the pressure side and suction side distributions intersect and locally invert the loading direction. The effect is only picked up by the finest grids (5 and 6). In reality, both the stark pressure gradient on the suction side and the flow acceleration on the pressure side are softened by viscous and turbulent diffusivity, which stall the intensity of the negative loading. In the inviscid solver tested here, the absence of boundary layer treatment means that the flow field captured at the trailing edge is not entirely accurate. Additional refinements aimed at stabilising the inversion would therefore bring no added value.

The drag coefficient C_D decreases asymptotically with grid refinement regardless of flow conditions. By definition (see Equation 4.2), its value is proportional to total pressure loss. For inviscid flow, the Bernoulli equation holds such that $\Delta p_0 = 0$. As the grid is refined, numerical losses become negligible and the solver's approximation converges towards the exact solution

to the Euler equations. One can therefore write

$$C_D \propto \Delta p_0 \xrightarrow{h \to 0} 0 \tag{4.3}$$

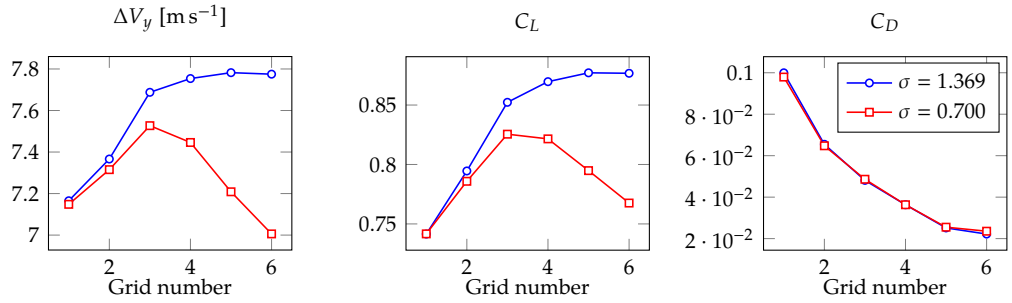

(a) ΔV_y **(b)** Lift coefficient **(c)** Drag coefficient

Figure 4.13: Amount of turning, $w = |\overline{V_y}^{TE} - \overline{V_y}^{LE}|$, lift C_L and drag C_D computed by the *SLAU* scheme in terms of grid resolution.

Having eliminated ΔV_y and C_L in cavitating conditions, as well as C_D in all conditons, as measures of grid independence, the selection is based on i/ the non-cavitating ΔV_y and C_L, ii/ on cavitation closure shock features. From Figure 4.13, it is observed that starting from grid 4 steady values for both ΔV_y and C_L are obtained. In terms of shock amplitude, grid 4 yields a substantial jump, in excess of 35 kPa. It is also the coarsest grid to successfully pick up the pressure overshoot. Grids 1 through 3 are eliminated as sub-standard resolution candidates. Grid 6, when compared to grid 5, does not present significant differences despite the large increase in cell number. Therefore, considering computational efficiency, grids 4 and 5 are selected for further numerical experiments. For design runs that use the V_y distribution algorithm, calculations are carried out on the coarser grid number 4 because of the heavier computational load. The Δp method, given its ability to update geometry during the time marching process, allows the finer grid number 5.

4.4 Performance of Acceleration Techniques

As pointed out in Section 3.5, computational efficiency is a key axis of code development. The methods employed and adapted to fulfil this obligation include:

- Multistage and local time-stepping,
- Preconditioning for low speed flow,

- Multigrid.

The precise manner in which these have been built into our code is detailed in Section 3.5. Here, the aim is to demonstrate the gains obtained using *preconditioning* and *multigrid*. Multistage and local time-stepping are taken as standard. For this analysis, the equations are kept inviscid. Cavitating flow at $\sigma = 0.700$ is considered because it requires that the scheme be able to accommodate a wide range of wave speeds, as well as strong flow gradients.

4.4.1 Preconditioning

The potency of *preconditioning* techniques over the conventional conservative formulation has been repeatedly proven for low speed flows, and it would be pointless to repeat an analysis of that sort. The purpose of this section is to show that the *preconditioning* technique developed for the solver presented here is superior to existing formulations found in literature and applicable to arbitrary fluids. To that intent, the *Weiss & Smith* (WS) [104] and the *Merkle & Sullivan* (MS) [112] approaches have been implemented using the exact expressions provided by the authors. All are constructed with the primitive set $\boldsymbol{Q} = [p, u, v]^T$ as the update variable vector.

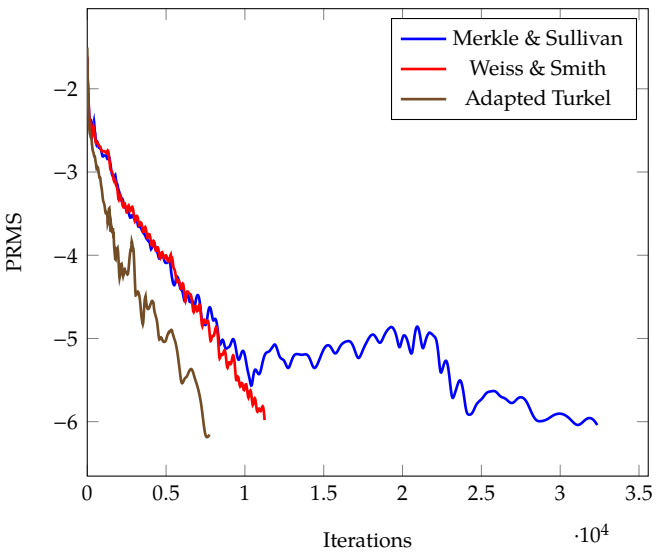

Figure 4.14: Comparison of the residual decrease for the *x-momentum* conservation equation using different preconditioning techniques at $\sigma = 0.700$.

The convergence histories obtained for a cavitating run at $\sigma = 0.700$ using each of the preconditioning techniques are presented in Figure 4.14. Evidently, the performances of the original WS and MS methods are far poorer than the *in-house* approach. Both are constructed for non iso-energetic flow. The derivation of the eigenvalue control techniques therefore

originates from a different differential problem and does not provide the same level of eigenvalue clustering. Furthermore, the *in-house* preconditioning's multidimensional framework for eigenvalue optimisation brings even stronger stability enhancements. Indeed, ad-hoc testing involving reverting to one-dimensional linearisation applied to cell faces regardless of direction, as prescribed by the WS and MS methods, lead to significantly reduced differences between convergence results. The discrepancy between the WS and MS convergence is due to the bounding of the reference velocity used to scale the acoustic propagation: speed of sound for the former, local cell Reynolds number for the latter.

4.4.2 Multigrid Performance

The routines introduced into the multigrid procedure, i.e. *upwinded residual smoothing* and *shock weighting* (see Section 3.5.3), are designed to rectify the transfer operators in the vicinity of the cavitation pressure shock. Their effectiveness is evaluated here against the untreated multigrid approach. Beforehand, the convergence gain obtained using the multigrid acceleration for the non-cavitating case is presented. This will serve to demonstrate the successful implementation of the technique for the preconditioned Euler equations.

From Figure 4.15, it is clear that the multigrid technique drastically reduces the number of time steps needed to reach convergence. In non-cavitating conditions, the computation presents a clear correlation between acceleration performance and grid coarseness levels. At $\sigma = 0.700$, however, the success of convergence improvement w.r.t. coarseness level is dependent on the application of the enhanced prolongation and restriction procedures. The value of the *shock weighting* parameter κ is set by trial and error. The prolongation step, interpolates from the coarse solution to correct the fine grid data. Its smoothing action is, by construction, stronger than for the restriction step which sums up fine grid residuals. Therefore, a non-symmetric configuration, differentiating between κ_P for prolongation and κ_R for restriction delivers the highest robustness and efficiency. To speed up convergence, both κ_P and κ_R are weakened on coarser grids. The selected values are

$$\kappa_P = \begin{cases} 2.1 & \text{for } 4h \rightarrow 2h \rightarrow h \\ 1.7 & \text{for } 8h \rightarrow 4h \end{cases} \quad \text{and} \quad \kappa_R = \begin{cases} 2.1 & \text{for } h \rightarrow 2h \\ 0 & \text{for } 2h \rightarrow 4h \rightarrow 8h \end{cases} \tag{4.4}$$

Below this threshold, the computation either diverges or stagnates (see residual curves for $\kappa = 1.5$ on Figure 4.15b). The *upwind residual smoothing* coefficient ϵ was found to perform best

in combination with *shock weighting* at a value of $\epsilon = 0.2$.

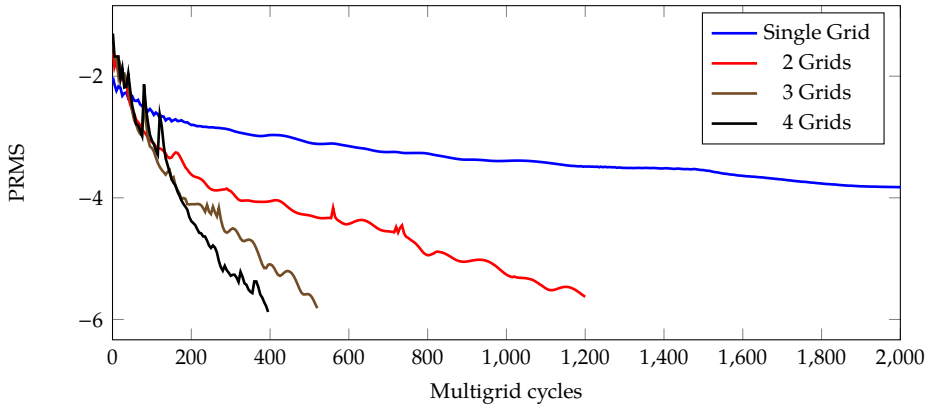

(a) Non-cavitating $\sigma = 1.369$

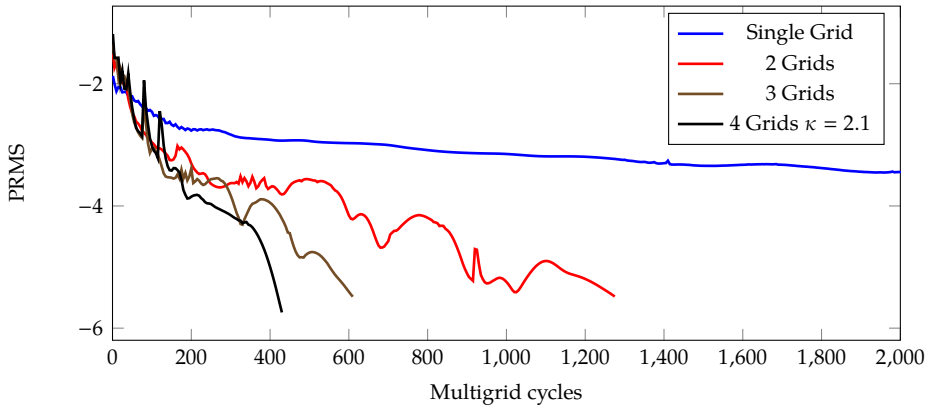

(b) Cavitating $\sigma = 0.700$

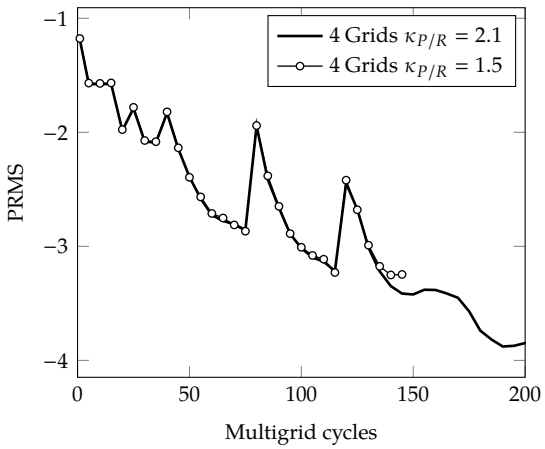

(c) κ comparison $\sigma = 0.700$. The $\kappa_{P/R} = 1.5$ run ends due to negative pressure.

Figure 4.15: Convergence performance comparison in terms of multigrid coarsening levels.

It is imperative to note that, for the multigrid results presented here, one time iteration equates to a single multigrid cycle, which itself encompasses multiple integration steps carried out on several grids. For reliable comparison one should consider the amount of actual computational work corresponding to the singling out of the individual processes executed from time step to time step. The chosen reference unit lumps together the flux evaluation and multistage time-stepping over a single control volume. By isolating individual cells, the measure takes grid coarseness levels into account.

The resulting numbers are given in Table 4.5. Rather than the ~ 20 times reduction in time steps, a more realistic, yet extremely favourable, tenfold decrease in work units is observed from single grid to 4 level FMG. A convergence improvement of such an order of magnitude matches the wall clock time gains measured during the computational runs.

Table 4.5: Total computational work units required to reach convergence (RMS < -6) for single grid and multigrid runs in both non-cavitating and cavitating conditions.

	Grid number	**Multigrid cycles**	**Approximate work units**
$\sigma = 1.369$	Single Grid	12200 (iterations)	80×10^6
	2 Level FMG	1200	20×10^6
	3 Level FMG	550	10×10^6
	4 Level FMG	400	7×10^6
$\sigma = 0.700$	Single Grid	22600 (iterations)	150×10^6
	2 Level FMG	1300	21×10^6
	3 Level FMG	600	10×10^6
	4 Level FMG	410	7.2×10^6

4.4.3 Fluent Benchmark

Comparison of convergence rates between the in-house solver and Fluent is largely to the advantage of the former. For inviscid flow under non-cavitating conditions, the Fluent relaxation factors have to be reduced from 0.5, 0.5 and 1 for pressure, momentum and density respectively to 0.2 for all. On the same machine, the in-house solver is able to deliver a steady state solution (6 orders residual decrease) in approximately 1.5 min against 6 min for Fluent. Furthermore, the calculations carried out by Fluent are parallelised over 10 cores, while the *In-house* algorithm is single threaded and relies on compiler optimisation.

Differences are amplified when the liquid starts to cavitate. At $\sigma = 0.700$, the Fluent calculation systematically diverges within a dozen iterations unless initialised from a solution at a marginally higher σ value. This means that running a cavitating case in Fluent involves a protracted repetition of steady state calculations at successively smaller σ values. On top of that, it was found necessary to further reduce the relaxation factors to 0.1. The accumulated time needed to arrive at a solution, at $\sigma = 0.700$ for instance, is in excess of 30 min. By contrast, the robustness of the in-house solver is such that cavitation has no effect on convergence rate as shown in Table 4.5 for the 4 level FMG. Furthermore, its range of applicability extends to $\sigma = 0.642$, whereas none of the Fluent runs for $\sigma < 0.700$ converged.

4.5 RANS Turbulence Effects

The aim here is to identify the effects of turbulence on the cavitating pressure distribution. For exhaustiveness, multiple RANS models of varying complexity are applied to the Baseline case :

- *Zero Equation*: it requires no additional transport equation but cannot properly take into account the convection and diffusion of turbulent energy.
- *Standard k-ε*: the two transport equations for the turbulent kinetic energy k and dissipation ε are capable of evaluating history effects and deliver high robustness for internal flows as long as no large adverse pressure gradients are present. Unlike *zero equation* models, near-wall treatment is necessary.
- *Shear Stress Transport* (SST): blends the k-ϵ approach in the free stream with the k-ω formulation in the boundary layer. As a result, the model can be used without supplementary near-wall treatment and corrects the $k - \omega$ free stream sensitivity. It behaves well in the context of large pressure gradients and separation.

All three models have been run using the default Fluent parameters to compute steady state solutions in cavitating conditions.

For the RANS models to provide accurate turbulence predictions, the mesh needs to be adequately refined in the boundary layer. A high resolution unstructured quadrilateral mesh is therefore generated separately. For the *zero equation* and *SST*, the absence of near wall treatment imposes $y^+ < 1$. The *Standard* $k - \varepsilon$ works in combination with a wall function so that the first layer mesh is further from the wall at $y^+ < 30$.

The pressure distribution resulting from each run is compared in Figure 4.16. It is clear that the effect of the aforementioned turbulence models is only marginal. The shock amplitude remains unchanged and its location is consistent regardless of the turbulence closure method. It is important to note that this does not signify that turbulence is inconsequential. On the contrary, it has been shown that the closure region is characterised by strong turbulent mixing [11]. Nevertheless, at $\sigma = 0.700$, cavitation is limited to a region where the boundary layer is thin and flow is governed by inertial rather than viscous or turbulent forces. Furthermore, the reliability of current RANS models for predicting cavitation closure remains a debated topic. The outcome of this analysis is that RANS turbulence modelling is not a decisive component in the prediction of the steady state cavitation and pressure patterns in the current conditions and using the TE equation of state. The solver is kept inviscid, ensuring high robustness, efficiency, as well as satisfactory accuracy.

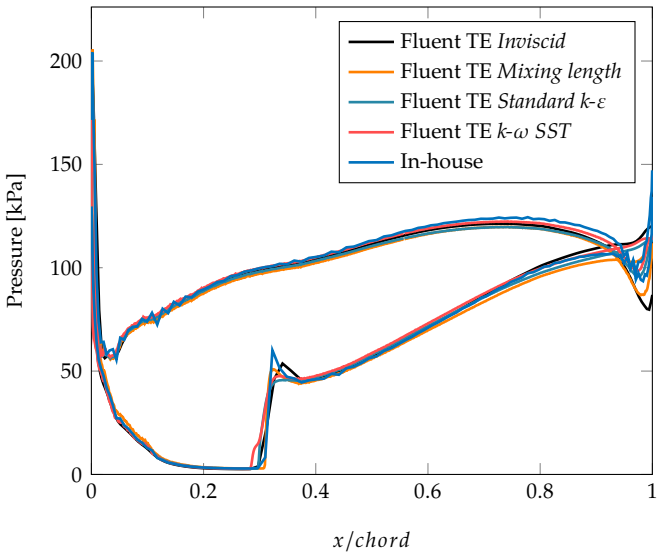

Figure 4.16: Blade pressure distributions at $\sigma = 0.700$ resulting from the solution of the RANS formulation using three turbulence models: *Zero Equation*, *Standard k-ε*, and *SST*. Fluent was used to acquire all three solutions.

4.6 Comparison to Transport Equation Modelling

The TE cavitation model is evaluated against the more prevalent transport equation type approach. In Fluent, the default model is the Zwart-Gerber-Belamri technique. Its evaporation

and condensation terms are given by

$$\begin{aligned} \dot{m}^- &= -C_e \frac{3\alpha_{nuc}\,(1-\alpha_v)\,\rho_v}{R_B}\left[\frac{2}{3}\frac{p_v - p}{\rho_l}\right]^{-1/2} && \text{if } p < p_v \\ \dot{m}^+ &= C_c \frac{3\alpha_v \rho_v}{R_B}\left[\frac{2}{3}\frac{p - p_v}{\rho_l}\right]^{-1/2} && \text{if } p > p_v \end{aligned} \tag{4.5}$$

In this study, the values recommended by Zwart et al. are chosen because they have been shown to perform well for a variety of cases: $\alpha_{nuc} = 5 \times 10^{-4}$, $R_B = 10^{-6}$ m, $C_e = 50$, $C_c = 0.01$. The treatment of the pure liquid phase is significantly different: in the case of the TE State Law, applied for all $p > p_v$, the density is variable producing an inherently compressible fluid; for the method proposed by Zwart et al., on the other hand, mixture density is constant at $\rho = \rho_l$ as $\alpha_v \longrightarrow 0$.

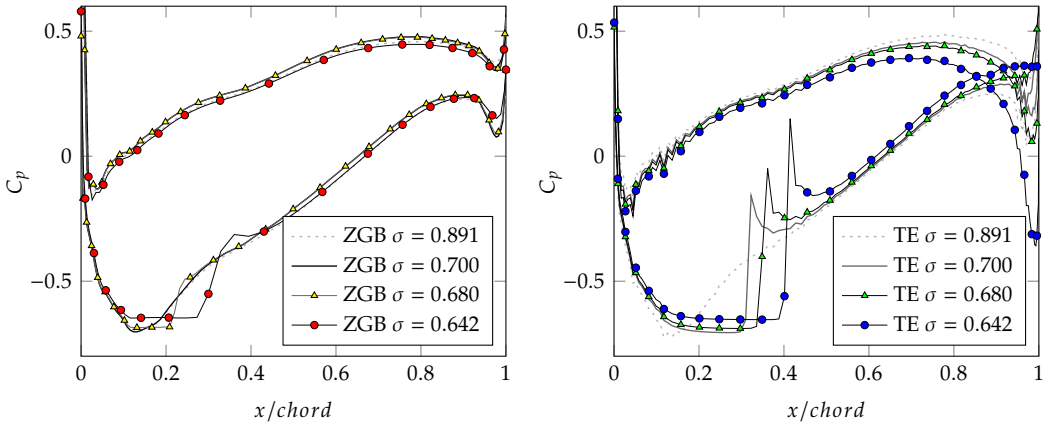

(a) Fluent ZGB **(b)** *In-house* TE

Figure 4.17: Comparison of pressure coefficient distributions for the Fluent-ZGB and in-house TE solutions at equivalent cavitation numbers.

Numerical experiments are carried out assuming inviscid flow for both TE (*In-house code*) and Zwart models (Fluent). To assess the cavitation prediction performance, the hydrofoil cascade is run for gradually decreasing inlet pressure values. The lowest pressure corresponds to the transition point between steady sheet cavitation and the onset of vapour break-off phenomena which cannot be accurately computed without unsteady analysis. Pressure coefficient results are shown in Figure 4.17. In the solutions produced by both models, the cavitation region is characterised by the flattening of the suction side pressure curve and a sharp rise at closure. There are, however, significant differences. For instance, the gradient at closure shock is higher in the case of the TE model than the Zwart model. The cause for this is the

larger counter-streamwise spread of the cavity predicted by the TE State Law. As a result, the deceleration at closure is stronger giving rise to a more pronounced static pressure gain.

More importantly, there is a clear discrepancy in the onset of cavitation: for the Zwart model results, water vapour starts to appear around $0.68 > \sigma > 0.66$, whereas with the TE model cavitation inception is observed at $\sigma = 0.75$. The disparity also affects cavity size, e.g. at $\sigma = 0.642$ the location of the closure shock is at $x/chord \approx 0.3$ for the Zwart results and at $x/chord \approx 0.4$ for the TE results.

The hydrodynamic performance of the cascade is assessed by evaluating the lift coefficient. Lift is directly related to blade pressure so, naturally, the effect of cavitation appears in the downgrading of the C_L output (see Figure 4.18). The mechanism responsible for breakdown is the expansion of the low velocity wake region as the cavity grows in thickness. As expected, the early onset of vapour formation predicted by the TE model is replicated in the C_L curve with a decrease initiated at $\sigma = 0.75$ instead of $\sigma = 0.66$ for the Zwart model.

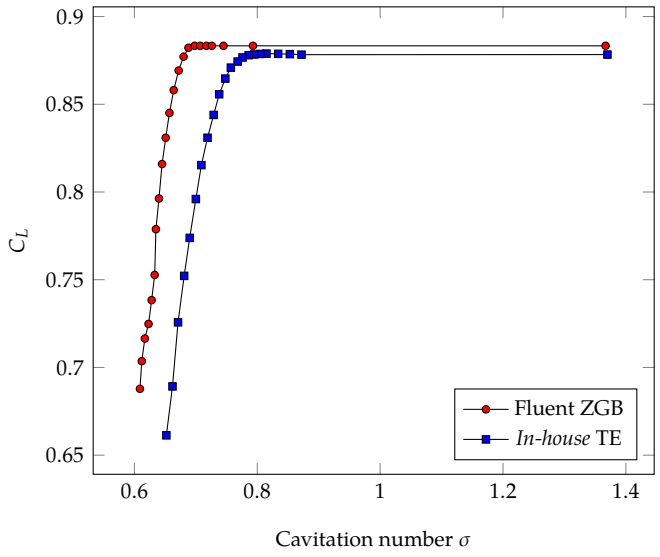

Figure 4.18: Breakdown of cascade lift from Fluent-ZGB and *In-house*-TE solutions.

The significant discrepancy in inception prediction between the two cavitation models has to be taken into account when carrying out cross-model assessments. This is the case in the numerical analysis (Chapter 6) where new geometries designed by the in-house algorithm are evaluated using the Fluent solver. To enable comparison , it is the position of the closure shock rather than σ that serves as reference. To identify the most accurate solution, the results need to be evaluated against experimental data. This is investigated and described in detail in Chapter 7 for the same Baseline geometry.

4.7 Concluding remarks

The tasks set out here were to verify the solver's performance. We notably measured the gains in convergence brought about by the preconditioning and multigrid techniques after parameter tuning. The grid dependence study indicated a minimal grid size of $160x32$ cells (64 in blade region) to reliably capture the cavity closure pressure jump. Analysis of the fluxing schemes put the SLAU approach as the clear winner with highest sharpness and robustness for cavitating flow.

The numerical experiments carried out with RANS turbulence modelling delivered a positive outcome as they showed its effects were negligible, thus confirming the validity of the inviscid assumption as a modelling choice for cavitation. Finally, an ad hoc comparison of the TE law and popular ZGB transport equation for homogeneous cavitation modelling was conducted. It put to light the discrepancy in inception condition and closure position between the two approaches (i.e. early onset and larger cavity for TE model).

Having verified our solver's capacity to produce reliable predictions of cascade flow under cavitating conditions, the next stage of the work consists in designing the set of improved blades. These will be used to test our working hypothesis: smaller closure jump means reduced aggressiveness.

5 Inverse Design Strategy and Generated Geometries

The hypothesis tested in this work is that by reducing the shock strength at cavitation closure the erosive intensity can be softened. The aim here is to generate a family of designs that can serve to assess the validity of our working hypothesis. The design strategy is therefore tasked, not with getting rid of cavitation which is an unrealistic project in itself, but with altering the closure characteristics of the cavity sheet. To answer the question posed in this work, the produced geometries should either comply to the shock reduction concept, or, alternatively, amplify the shock in order to test the hypothesis by contradiction.

5.1 Loading Concepts

Both design approaches, V_y distribution and Δp loading, are put to use. Each design is characterised by a specific loading profile given as a V_y or Δp distribution depending on the selected design method. It is possible to correlate the two distributions through

$$\Delta p = s \rho V_m \frac{\partial V_y}{\partial x} \tag{5.1}$$

where s is the pitch and V_m is the meridional velocity at the blade. The proportionality relation

$$\Delta p \propto \frac{\partial V_y}{\partial x} \tag{5.2}$$

is easily deduced. The performance of each approach is evaluated in terms of design success and computational cost. For the latter, it is the total number of iterations to arrive at a converged geometry that is considered. Design success is evaluated by comparing the prescribed and result distributions, as well as the stability of the geometry. Shock strength is measured in terms of both amplitude and gradient.

To test the closure shock adjustment hypothesis, two design routes are possible:

1. *tip to tail* which looks at a global revision of the loading profile,

2. *shock focused*, wherein modifications are limited to the shock region.

The first approach is inspired by previous work aimed at improving the suction performance of pumps and turbines using the inverse design method (see [87, 88, 89]). The rationale is to shift the loading peak in the high pressure region of the channel. This has two effects: it delays the onset of cavitation (decreased σ_i) and, when sheet cavitation occurs, it reduces the amplitude of the closure shock. Here, the method is replicated to investigate the repercussions on cavitation aggressiveness. Because it is the loading rather than the closure shock that is addressed, the *tip to tail* design approach can be carried out in non-cavitating conditions. The effect on the cavitating profile is evaluated after the design procedure.

The second *shock focused* approach uses the specifically developed in-house solver to design in cavitating conditions. Here, the closure shock is directly targeted by the prescribed loadings. This constitutes the first attempt at controlling its intensity. Modifications across other regions of the blade are kept minimal so that the suction performance remains equal to Baseline.

5.2 *Tip to Tail* Design Approach

With the *tip to tail* approach, it is changes in the overall loading character that are responsible for altering the closure shock strength. As explained earlier in Section 5.1, shock strength is defined in terms of amplitude and gradient. It is understood that when cavitation occurs, the suction side pressure stagnates at p_v and extends downstream to the closure point. From there, the shock – caused by the sudden increase in throat cross section – connects p_v to the "ideal" non-cavitating pressure. This is made especially clear when comparing pressure coefficients with and without cavitation as in Figure 5.1, where the high σ curve follows the "ideal" pressure path. The amplitude of the shock can therefore be controlled by reducing the gradient of the suction side pressure distribution: the flatter, the smaller the gap between p_v and p_{ideal} or, reversely, the steeper, the larger the amplitude will be.

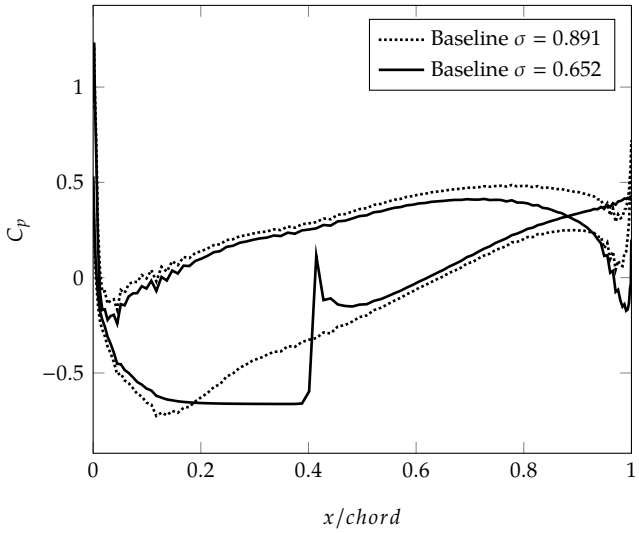

Figure 5.1: Surface pressure coefficient for the Baseline case in non-cavitating (σ = 0.891) and cavitating (σ = 0.652) conditions.

5.2.1 *Tip to Tail* Prescribed Loading Profiles

Three loading cases are proposed: VY 3, VY 7 and VY 8. All are defined in terms of V_y distribution as shown in Figure 5.2. The choice in design algorithm was made by default as the Δp approach had not been successfully validated at that point. In fact, the three cases could as easily have been produced using the Δp loading. Cases VY 3 and VY 7 are aft-loaded designs, meaning that swirl is generated mainly by the downstream half of the blade (see Figure 5.2b). The aft-loading intensity is moderate for VY 3 and strong for VY 7. For these two cases, the suction side pressure is expected to be a low gradient rise. The effect on the closure shock should be a reduction in amplitude. Design profile VY 8, on the other hand, is strongly fore-loaded with a maximum $\partial V_y/\partial m$ in the upstream half. An increase in shock amplitude is therefore targeted. The intent for case VY 8 is to use its strong shock features to verify the working hypothesis by contradiction. The design runs are summarised and categorised in Table 5.1. All three cases are run at a high cavitation number σ = 1.367. The performance under cavitation is assessed once the geometries are successfully produced.

5.2.2 Convergence and Loading Alignment : *Tip to Tail* Cases

Two convergence indicators are formulated to measure the progress of the design solution. Each address one side of Equation 3.101 i.e. camber line and tangential velocity. The maximum change in camber f and the maximum offset $V_y^{Target} - V_y$ along the blade are evaluated at every iteration. Both are scaled by the leading to trailing edge amplitudes for the Baseline geometry

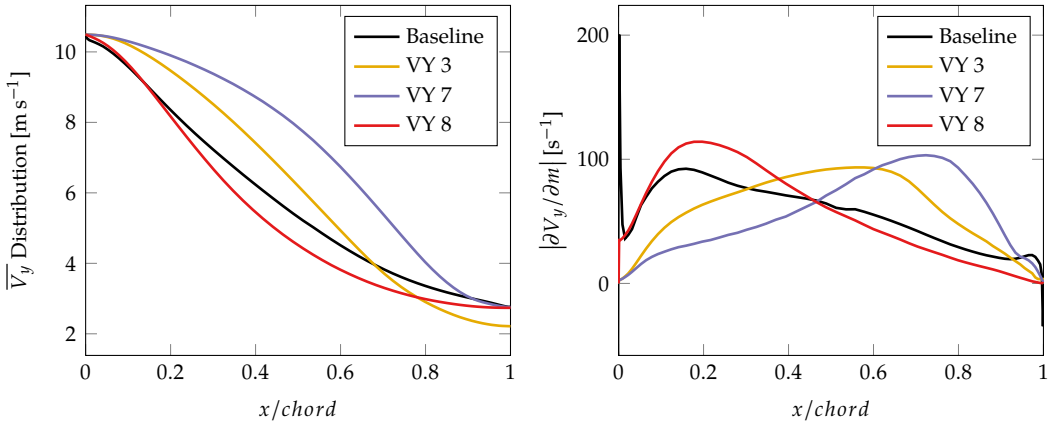

(a) V_y Distribution **(b)** $\partial V_y/\partial m$ Loading

Figure 5.2: Target $\overline{V_y}$ loadings and meridional derivative $\frac{\partial \overline{V_y}}{\partial m}$ for test cases VY 3, VY 7 and VY 8 (non-cavitating conditions). The meridional derivative distributions serve to characterise the loading type: fore-loaded for VY 8, mid/aft-load for VY 3 and aft-loaded for VY 7.

Table 5.1: Details of the *tip to tail* design cases. The runs are categorised in terms of strategy, inverse algorithm, cavitation condition and mesh.

Design Case	Design strategy		Inverse algorithm		Cavitation number σ			Blade channel cells	
	Shock focused	Tip to tail	V_y	Δp	0.652	0.680	1.367	64 × 32⋆	112×32⋆⋆
VY 3		Aft-loading	•				•	•	
VY 7		Strong aft-loading	•				•	•	
VY 8		Fore-loading	•				•	•	

⋆ Grid number 4 in Table 4.4.
⋆⋆ Grid number 5 in Table 4.4.

indicated by the exponent $()^B$:

$$R_{\hat{f}} = \frac{\max\left|f_i^{n+1} - f_i^n\right|}{\left|f_{TE}^B - f_{LE}^B\right|}$$
$$R_{\hat{V_y}} = \frac{\max\left|{V_y}_i^{Target} - \overline{V_{y_i}}^n\right|}{\left|\overline{V_{y_{TE}}}^B - \overline{V_{y_{LE}}}^B\right|} \tag{5.3}$$

where index i iterates along the blade nodes.

The advantage of the *tip to tail* design strategy is that cases are run in non-cavitating conditions. Not only is the convergence of the fluid computation facilitated, the geometric

changes are less prone to instabilities caused by the closure shock shifts. As shown in Figure 5.3, the advancement of R_f and $R_{\hat{V}_y}$ is monotonous. A rapid decrease is observed down to 10^{-3} for R_f and 10^{-2} for $R_{\hat{V}_y}$ in approximately 15 iterations. It is followed by a stagnation, made especially evident by the V_y offset history which levels out at 10^{-2} (Figure 5.3b). In these cases, the maximum is found at the trailing edge. In this region, the changes in f lose their capacity to impact the V_y distribution causing the stiffening of the design problem. This effect can be linked to the assumption of irrotational flow used to derive the camber line relation 3.96. Its validity breaks down in the trailing edge region where vorticity is non zero.

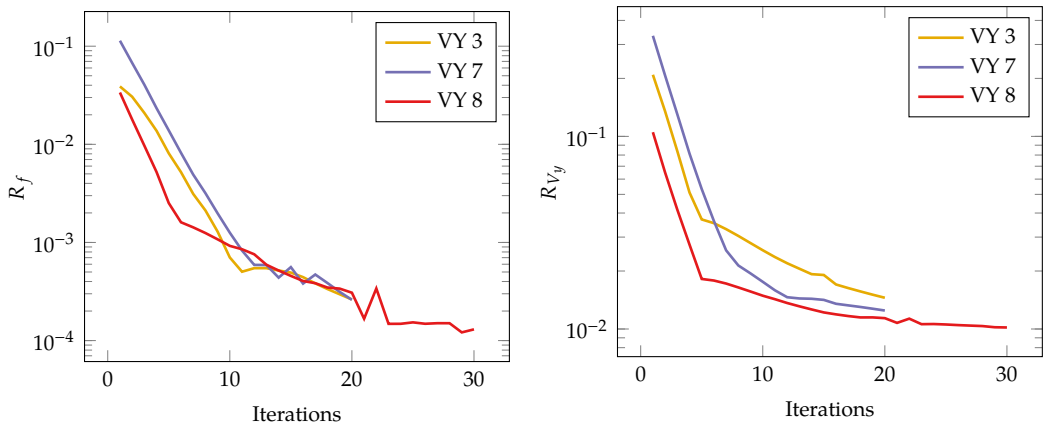

(a) Camber line residual R_f

(b) $R_{\hat{V}_y}$ offset

Figure 5.3: Design convergence for *tip-to-tail* cases VY 3, VY 7 and VY 8 ($\sigma = 1.367$). Convergence is determined by the camber line stability (through R_f) and by the difference between target and computed $\overline{V_y}$ distribution (through $R_{\hat{V}_y}$).

In terms of alignment to target distributions, the results are consistently satisfactory (see Figure 5.4). The modifications in the general loading character, i.e. aft-loading for VY 3, strong aft-loading for VY 7 and fore-loading for VY 8, are achieved as desired.

5.2.3 Generated Camber Lines : *Tip to Tail* Cases

For this two-dimensional configuration, geometric modifications consist in changes in the tangential position of the camber line nodes. The blade thickness and axial position of the nodes are fixed. To highlight the differences in our designs, the blade surfaces are ignored.

The result camber lines for *tip to tail* cases VY 3, VY 7 and VY 8 are shown in Figure 5.5. All three show substantial differences with the Baseline camber. The fore- or aft-loading can be determined by the height of the trailing edge: if below baseline the blade is fore-loaded, if above it is aft-loaded. The offset results from the location of highest curvature, which matches

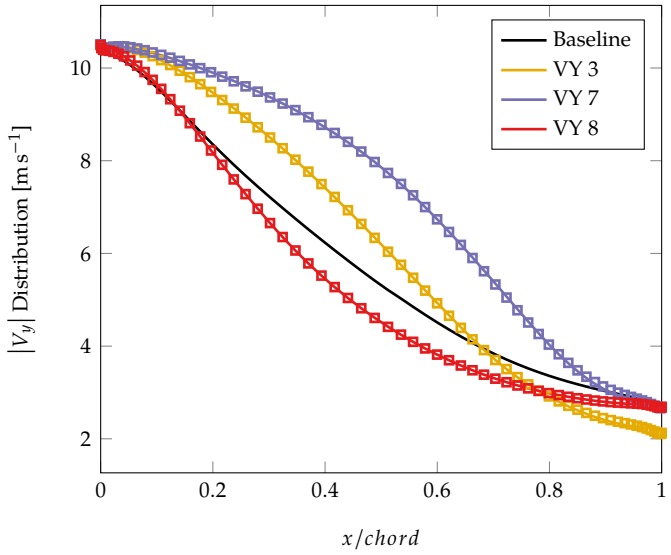

(a) V_y distribution

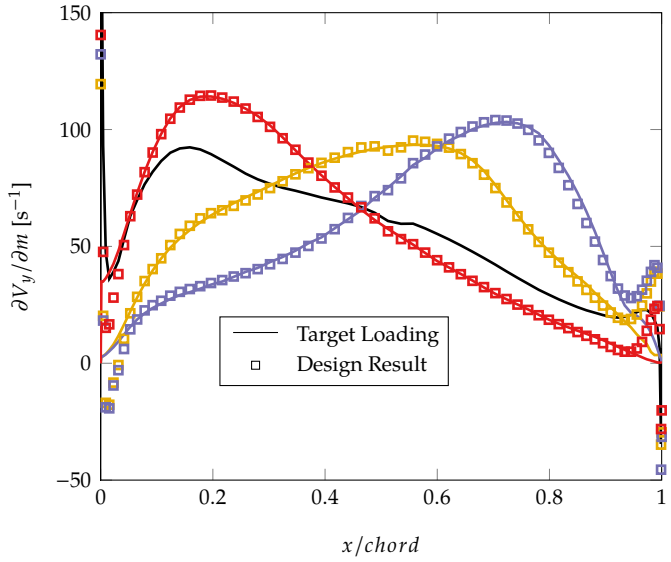

(b) $\partial V_y/\partial m$ Loading

Figure 5.4: Comparison of target versus result $\overline{V_y}$ and $\frac{\partial V_y}{\partial m}$ loading distributions for *tip to tail* cases VY 3, VY 7 and VY 8 ($\sigma = 1.367$).

the point of maximum loading. For cases VY 3 and VY 7, the upstream part of the camber is straighter than the downstream half. This is especially clear for the VY 7 camber, which bends at $x/chord = 0.7$. Case VY 8 behaves in the opposite manner with bending in the upstream half, such that its camber intersects with the Baseline. These large scale alterations also affect

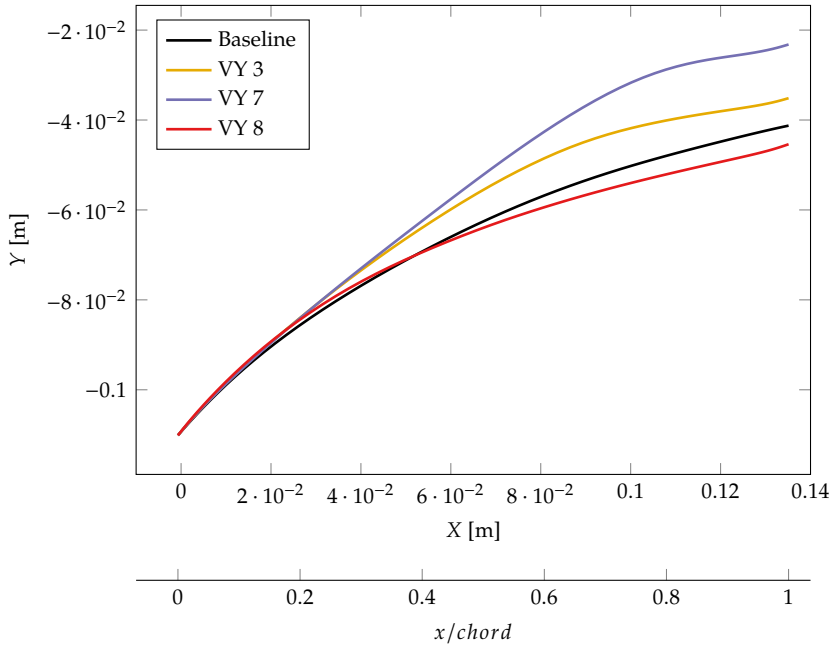

Figure 5.5: Camber line comparison for the *tip to tail* cases VY 3, VY 7 and VY 8.

the effective length of the blades i.e.

$$L = \sqrt{chord^2 + \left(H_y\right)^2} \tag{5.4}$$

where $H_y = y^{TE} - y^{LE}$. The chord being constant, it is changes in H_y that alter L. It is clear that the more the blade is fore-loaded, the shorter it will be.

5.2.4 Cavitation Performance : *Tip to Tail* Cases

To identify the success of the design candidates an assessment of their performance in cavitating conditions is undertaken. Of most interest is the behaviour around the cavity, in particular at closure. Here blade pressure and cavity size are of primary interest. The features sought after are reduced amplitude closure shocks and thin cavities for shock reducing designs (VY 3 and VY y), or the opposite for intensifying cases (VY 8).

For the three *tip to tail* cases VY 3, VY 7 and VY 8, the global profile has been substantially modified such that the flow conditions that produce cavitation do not correspond to those for the Baseline case. To arrive at cavitating flow, the cavitation number is gradually decreased by modifying the inlet total pressure. The inception point is lower for aft-loaded designs VY 3 and VY 7, and higher for fore-loaded case VY 8. In Figure 5.6 the C_p distribution is presented for all three cases under non-cavitating and cavitating conditions. The target when constructing

the loading profiles for VY 3 and VY 7 was to generate a flat suction side distribution with pressure increase concentrated in the downstream region. The point being, as explained in Section 5.2.1, that it is the gradient of the cavitation-free suction side pressure distribution that determines shock amplitude. Observation of Figures 5.6a and 5.6b confirms the success of VY 3 and VY 7: for non-cavitating flow the gradient of the suction side pressure is substantially lowered and the amplitude of the cavitation closure shock is more than halved. Both VY 3 and VY 7 produce comparable shock amplitude. Differences are found in (i) the length of the flat pressure region : $x/chord = 0.2$ to $x/chord = 0.6$ for VY 3, $x/chord = 0.2$ to $x/chord = 0.8$ for VY 7;, (ii) the cavitation number at which the cavity sizes match i.e. $\sigma = 0.585$ for VY 3 and $\sigma = 0.537$ for VY 7. This suggests that design VY 7 can sustain low amplitude closure shock at lower cavitation numbers.

With the VY 8 loading profile, the aim consisted in increasing the gradient on the suction side such that the amplitude of the shock could be enhanced. This is well attained as illustrated in Figure 5.6c. The difference in shock strength is not as pronounced as for VY 3 and VY 7 with an increase by a factor between 1.1 and 1.2. For all cases, the choice of plotting $C_p = (p - p_\infty)/\frac{1}{2}\rho V_\infty^2$ rather than static pressure is to highlight the relation between the shock and the suction side pressure in non-cavitating conditions. It does not affect amplitude as all data is scaled by the same dynamic pressure $q = \frac{1}{2}\rho V_\infty^2$.

The pressure and volume fraction contours are shown for all three cases in Figures 5.7 to 5.9 at their respective cavitation numbers. They also serve to depict the complete blade shape including suction and pressure surfaces. The observations made from the surface distributions match the two-dimensional contours: low pressure flow spreads across the majority of the blade for VY 3 and VY 7 forcing higher gradients to occur near the trailing edge while pressure rapidly increases in the upstream part of the channel for VY 8. As for water vapour, the cavity volume fraction is higher for VY 8 than for the aft-loaded cases. Indeed, the maximum volume fraction for VY 3 and VY 7 is $\alpha = 0.36$. With the VY 8 profile, there is a discernible zone within which $\alpha \geq 0.5$, reaching $\alpha = 0.75$ at its maximum (see Figure 5.9). At the same time, the VY 8 cavity is smaller with a better boundary demarcation. This is proof that the new designs alter not only the streamwise pressure gradient at the blade but the entire two-dimensional field, such that in the tangential direction the pressure rises slowly for VY 3 and VY 7, quickly for VY 8. With the TE equation of state, which assumes liquid compressibility, this results in a larger low density region for aft-loaded cases. Note that this is a specificity of the TE cavitation model. With transport equation type approaches, the liquid is incompressible and the cavity is bound to a zone where the pressure marginally deviates from p_v.

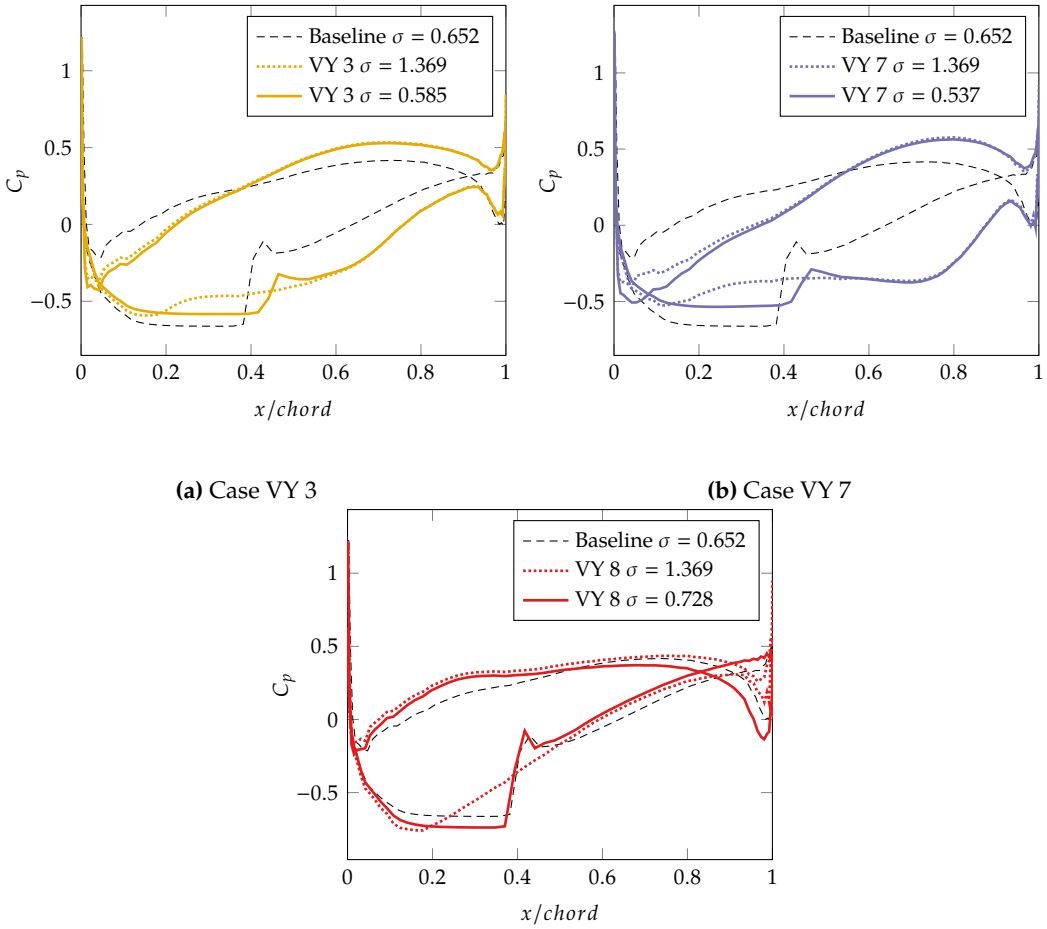

(a) Case VY 3 **(b)** Case VY 7

(c) Case VY 8

Figure 5.6: Surface pressure coefficients for *tip to tail* designs. Differences in suction side gradient are clear with aft-loaded cases (VY 3 and VY 7) delivering a flatter distribution that the fore-loaded case (VY 8). The results come from analysing the designs using the *In-house-TE* solver.

5.2.5 Correction for Non-Cavitating Output : *Tip to Tail* Cases

It was shown in Section 4.5, that RANS models have a negligible effect on the steady state location of the closure shock when using the TE equation of state. However, the effect is significant when it comes to predicting the ΔV_y output. Preliminary numerical evaluation of the new blades using Fluent with the Standard $k-\varepsilon$ model showed significant discrepancies in non-cavitating conditions. Results obtained at $\sigma = 1.0$ are shown in Table 5.2. For all three designs the relative difference is superior to ±3%. The prescribed profiles are constructed to generate the same amount of work under the inviscid assumption, but differences in velocity gradients and strain rates between geometries lead to variations in turbulence production. For example, case VY 7 is characterised by a strong adverse pressure gradient on the suction side in the downstream half of the blade. With proper boundary layer modelling separation is picked

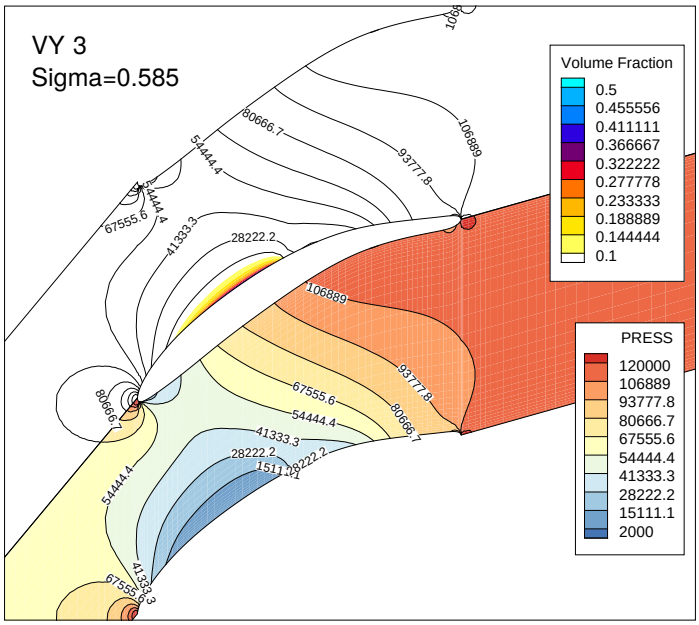

Figure 5.7: Pressure and volume fraction contours for VY 3 at $\sigma = 0.585$.

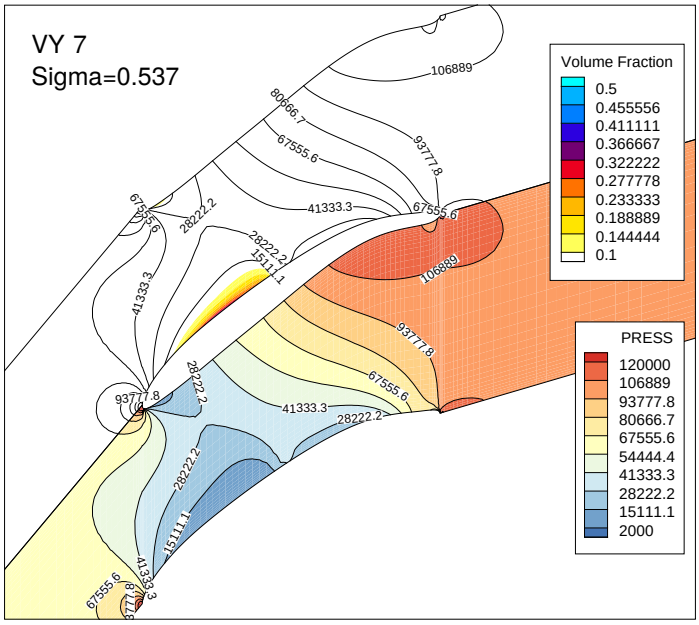

Figure 5.8: Pressure and volume fraction contours for VY 7 at $\sigma = 0.537$.

up and causes a significant downgrade in output. These non-cavitating offsets are far from superficial because they introduce an additional performance parameter. It is of no interest to this work since non-related to cavitation and damages the similarity between design cases.

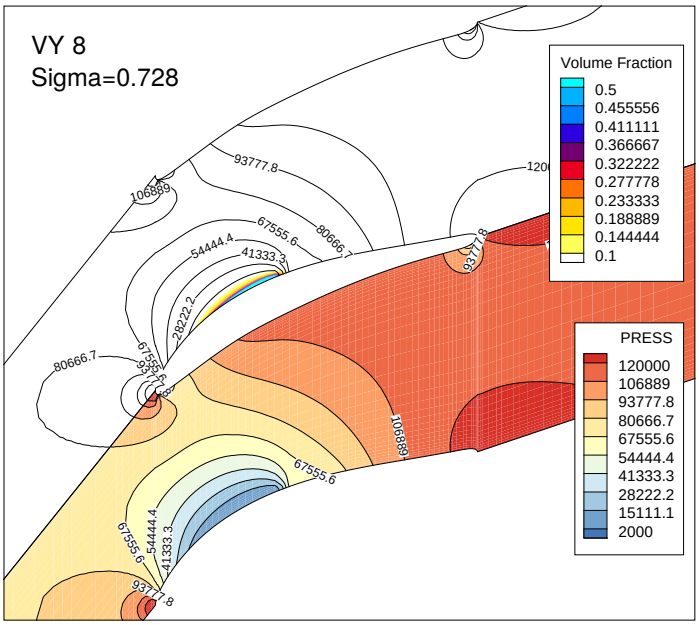

Figure 5.9: Pressure and volume fraction contours for VY 8 at $\sigma = 0.728$.

Table 5.2: Cascade hydrodynamic performance in non-cavitating conditions.

Design Case	ΔV_y [m s^{-1}] (Rel. Diff. to Baseline)
Baseline	7.0656
VY 3	7.3884 (+4.6%)
VY 7	6.5145 (-7.8%)
VY 8	7.3142 (+3.5%)

Updated Procedure

Ideally, the in-house solver should model the full NS equations so that discrepancies due to viscous or turbulent losses are compensated in the design process. This, however, constitutes an entirely new endeavour by itself. Instead, a correction process is appended to the existing design procedure. Its objective is to cancel out the discrepancy in output between the selected designs in non-cavitating conditions. The Fluent data is used to provide information on the magnitude and sign of the discrepancy. As there is no linearity between the gap obtained from turbulent calculations and the compensation needed by the inviscid design process to close it, the procedure is iterative. The designs are satisfactory once all lie within a ±2% margin from the Baseline output.

It is essential that the adjustment does not affect the chosen loading characteristics. To avoid perturbing the existing profile, modifications are applied to the downstream section of

the blade at $x/chord \geq 0.75$ away from the cavitation region. The discrepancies being small, correcting the aft-part part of the blade is sufficient to recover the desired output. The only exception is VY 8: its heavy fore-loading makes changes operated on the aft region ineffective. Instead, modifications are allowed to occur over the entire chord length while ensuring that fore-loading remains the main characteristic.

Corrected *Tip to Tail* Candidates

The adjustment procedure is carried out for all three geometries independently using the same algorithm and in the same conditions as the principal design run. The final V_y loading curves obtained after successive iterations are given in Figure 5.10 against the original target distributions and the baseline profile. The first observation is that the V_y values at the trailing edge are not necessarily equal. This is to be expected given that the aim is for equivalence with turbulent losses included, not in the case of inviscid flow. In most cases, the difference between the new and old V_y at the trailing edge does not exceed 10 % of the total difference ΔV_y. For VY 7, however, the updated loading is substantially changed. In the correction process, the output is increased by amplifying the downstream loading. This has a double sided effect: it boosts flow turning but extends the separation region such that the performance is only marginally improved. This explains the need for the large gap, which produces the desired ΔV_y but also strong separation and unsteadiness.

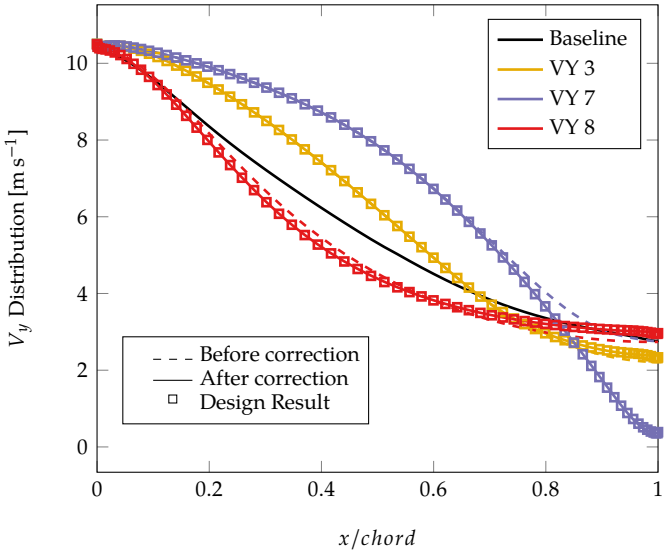

Figure 5.10: Loadings after the non-cavitating correction for the *tip to tail* VY 3, VY 7 and VY 8 cases.

The new ΔV_y breakdown values computed using ANSYS Fluent with the Standard $k-\varepsilon$ model are listed in Table 5.6. All the corrected non-cavitating ΔV_y values are well within

the ±2% range from Baseline. In terms of blade pressure (Figure 5.11), the extent of the modifications changes from case to case. As advocated by the ΔV_y discrepancies, case VY 7 undergoes the largest alterations: the aft-loading character is further accentuated. The in-house results show the lowest pressure point to be in the trailing edge region rather than the upstream part of the blade (see Figure 5.11b). This type of behaviour is the product of the inviscid treatment of the flow field. In reality, the sharp gradients in the downstream region are diffused by viscous and turbulent effects (see Section 6.1.2). The other corrected cases are only marginally different to their pre-correction profiles.

Because the corrections are contained within the downstream region of the blades, cavitation performance is as prescribed by the principal loading profiles. The same observations can be made: reduced shock amplitude but rapid cavity growth in the streamwise direction for aft-loaded designs VY 3 and VY 7; early cavitation and large amplitude at closure for fore-loaded design VY 8. Special attention is brought to VY 7, which cavitates at both upstream and downstream locations. Further analysis using turbulent CFD will determine the validity of the current result.

Table 5.3: Cascade hydrodynamic performance in non-cavitating conditions after the correction procedure.

Design Case	Old ΔV_y [m s^{-1}] (Rel. Diff. to Baseline)	Corrected ΔV_y [m s^{-1}] (Rel. Diff. to Baseline)
Baseline	7.0656	
VY 3	7.3884 (+4.6%)	7.0491 (-0.2%)
VY 7	6.5145 (-7.8%)	7.0667 (0.01%)
VY 8	7.3142 (+3.5%)	6.9828 (-1.2%)

The final geometries emerging from the correction procedure are shown in Figures 5.12 with the Baseline as well as the initial pre-correction geometries as reference. The geometrical specificities that came out of the principal design stage are maintained, i.e. high surface curvature in the aft region for VY 3 & VY 7 and in the forward region for VY 8. As planned the alterations brought about by the correction process are limited to the downstream portion except for VY 8. The updated shape for VY 7 possesses a noticeable hooked trailing edge. It is where the majority of flow turning is generated since the slope of the camber line in the upstream range $0 \leq x/chord \leq 0.6$ is mainly parallel to the inflow angle.

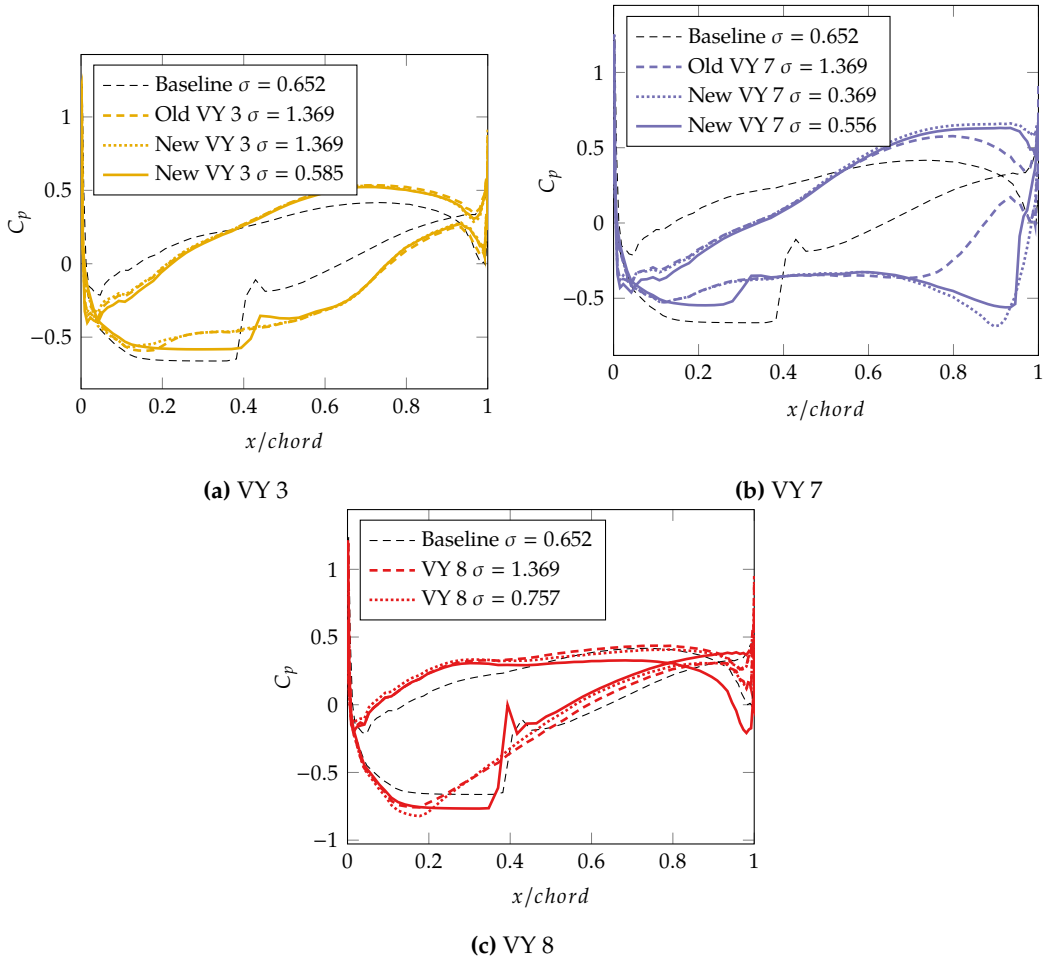

(a) VY 3 **(b)** VY 7

(c) VY 8

Figure 5.11: Surface pressure coefficients after the non-cavitating correction for the *tip to tail* cases. VY 7 suffers the most drastic modification.

5.3 *Shock Focused* Design Approach

For the *shock focused* strategy, the rationale is to impose a smooth closure recovery without altering the rest of the loading profile. In this case, the Baseline geometry not only serves as the initial condition to the design computation but also provides the reference profile. In cavitating conditions, the closure shock transpires into the loading distribution whether expressed in terms of V_y or Δp (see Figure 5.13). To enforce a smooth recovery, low gradient splines are inserted to supplant the original profile in the shock region. The recovery curves are third or fourth order polynomials controlled using two or three nodes in the closure region. The aim being to soften the pressure recovery at cavitation closure, it is crucial that the design runs be performed in the same cavitating condition as the reference Baseline case. Both design $\overline{V_y}$ and Δp algorithms are employed for the *shock focused* approach.

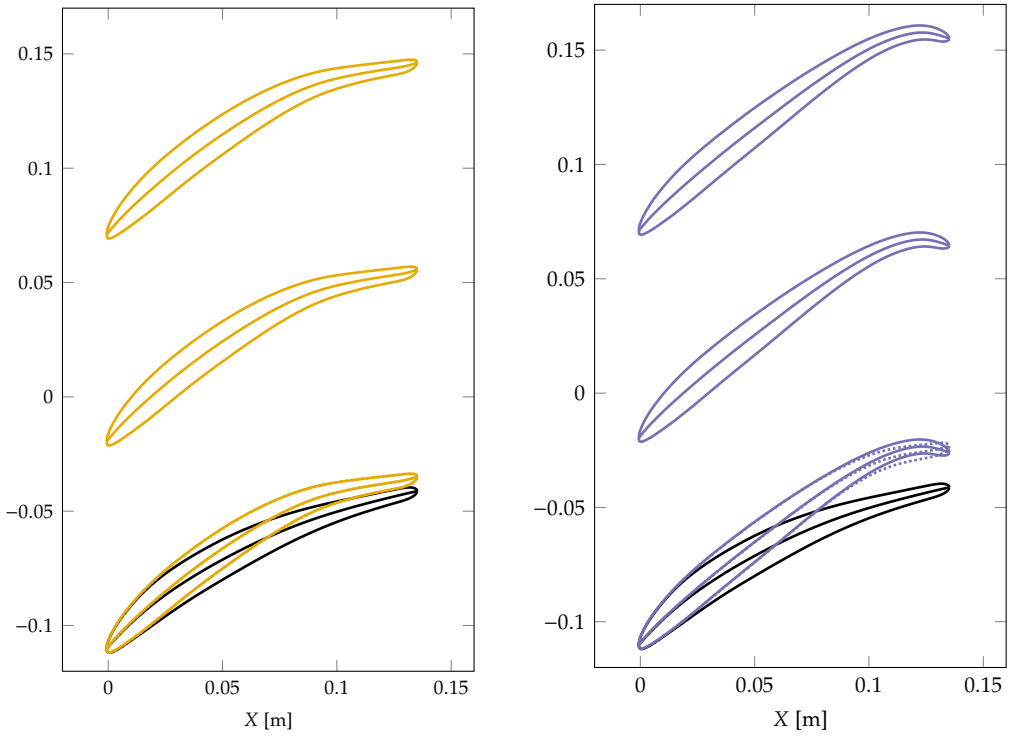

(a) VY 3

(b) VY 7

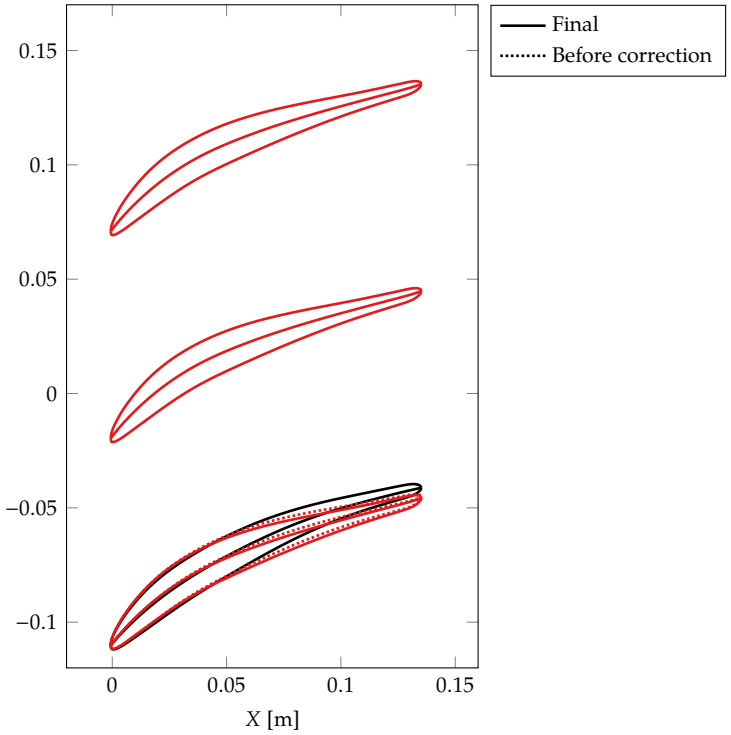

(c) VY 8

Figure 5.12: Final blade geometries for the *tip to tail* cases VY 3, VY 7 and VY 8.

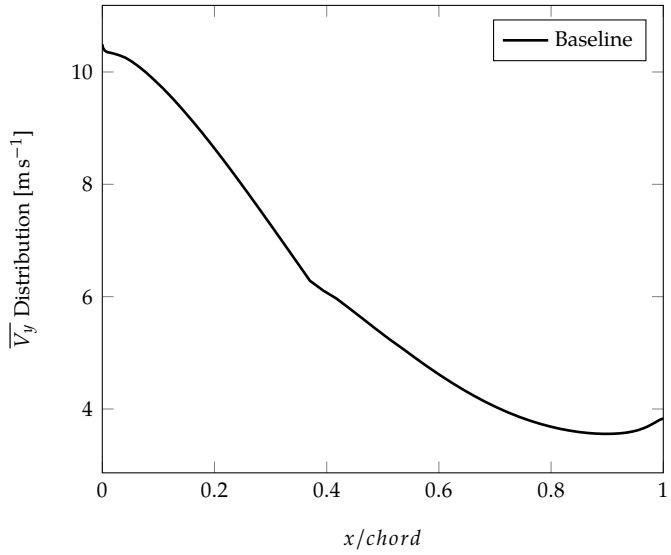

(a) V_y Distribution

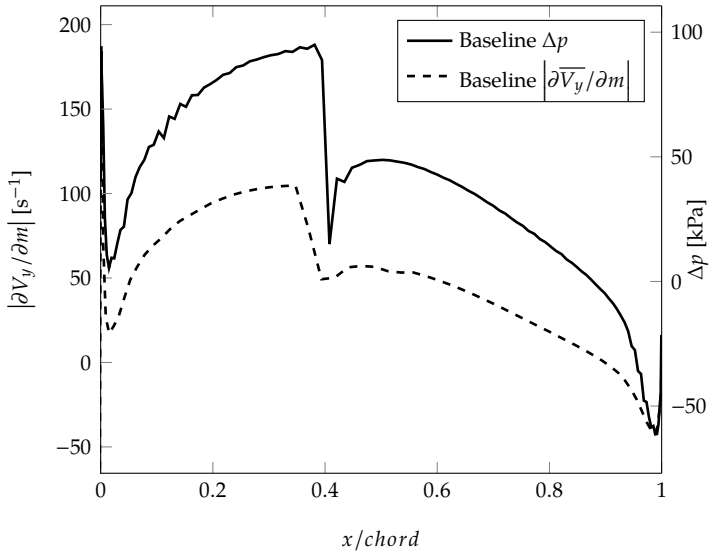

(b) Δp Loading

Figure 5.13: Baseline $\overline{V_y}$ distribution and loadings ($\partial_m \overline{V_y}$ and Δp) for cavitating flow at $\sigma = 0.652$.

5.3.1 V_y Target Loadings for *Shock Focused* Design

If the V_y approach is selected, the recovery splines are constructed from the derivative $\partial V_y/\partial m$ profile since it provides a clearer representation of the shock. The prescribed V_y distribution is then recovered by integrating the target loading. Two profiles have been tested with the V_y inverse design method: VY 4 and VY 9. The target distributions, constructed from the Baseline profile at $\sigma = 0.652$, are presented in Figure 5.14 in terms of both V_y and $\partial V_y/\partial m$.

In both cases, the target loading overlaps the Baseline profile in the upstream region.

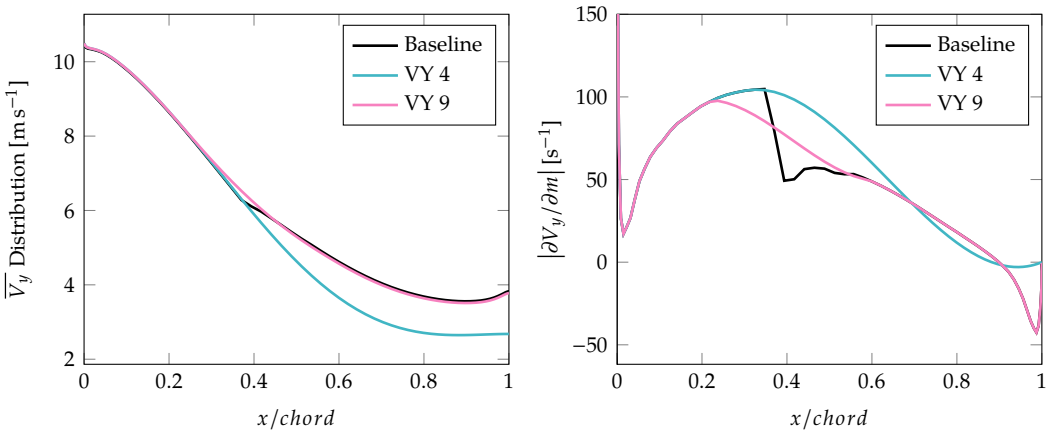

(a) V_y Distribution **(b)** $\partial V_y/\partial m$ Loading

Figure 5.14: Target $\overline{V_y}$ loadings and meridional derivative $\frac{\partial \overline{V_y}}{\partial m}$ for test cases VY 4 and VY 9 at $\sigma = 0.652$. Here, the target loadings focus on reducing the loading gradient at cavity closure while minimally affecting the rest of the blade.

Deviations start to appear at $x/chord = 0.24$ where the VY 9 recovery curve begins while VY 4 remains in perfect alignment until $x/chord \approx 0.35$. For VY 4, the idea is to initiate the smooth recovery at the start of the shock, such that no alteration is administered to the upstream section. Case VY 9, on the other hand, is an attempt at creating an early low gradient recovery which intersects with the existing Baseline shock at approximately mid-amplitude. The recovery curve for case VY 9 reconnects with the Baseline profile at $x/chord = 0.6$; in the case of VY 4 it is extended to the trailing edge. At the connection points between target and baseline loadings ($x/chord = 0.24$ and $x/chord = 0.58$ for VY 9, $x/chord = 0.35$ for VY 4) the curvature of the new splines is adjusted such that C^1 continuity is obtained. This ensures a smooth transition between the intact and updated flow regions.

5.3.2 Δp Target Loadings for *Shock Focused* Design

The advantage of the Δp method is that it provides direct control over the pressure distribution. It is therefore an enhanced approach for testing the shock smoothing design strategy. For this set of design experiments, the mesh is refined in the streamwise direction, going from 64×32 to 112×32 cells in the blade channel section. The increase in grid points not only improves the resolution of the solution, it also helps to move blade nodes in a smooth and precise manner. This is particularly important given the sensitivity of the cavitation closure region.

The grid refinement unfortunately also leads to a downgrade in numerical stability under cavitating conditions, such that the cavitation number has to be slightly increased to $\sigma = 0.680$.

Nevertheless, the adjustment does not affect the validity of the approach as the features of cavitation are still present: drop in mixture density, flattening of suction side pressure and sharp shock at closure (located at $x/chord = 0.35$ instead of $x/chord = 0.4$ at $\sigma = 0.652$).

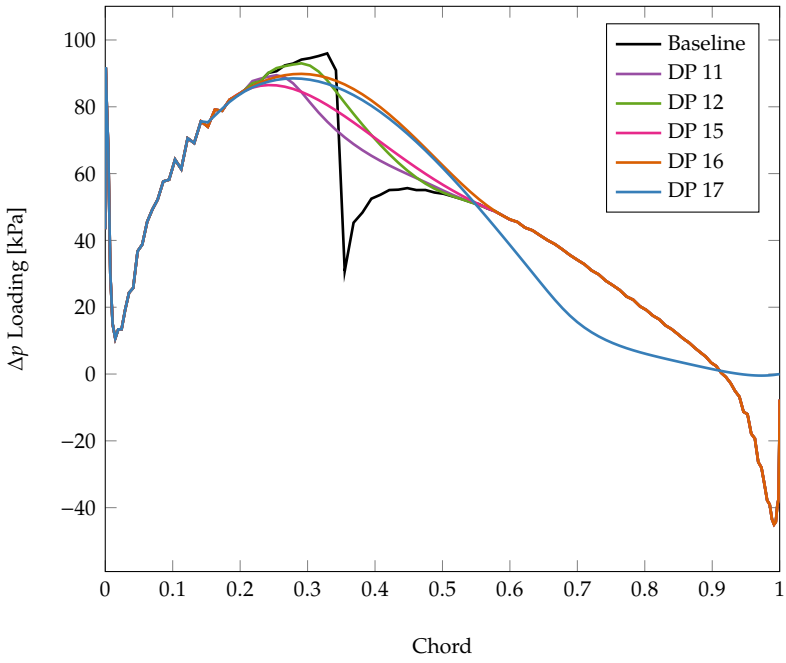

Figure 5.15: Target Δp loadings for test cases DP 11, DP 12, DP 15, DP 16 and DP 17 at $\sigma = 0.680$. For all, the rationale consists in producing a low gradient recovery. Targets vary in starting point and curvature characteristics.

In Figure 5.15, five target loadings are presented. They are constructed in the same manner as the distributions for VY 4 and VY 9 ensuring C^1 continuity at the connection points. The cases differ according to the curvature of the recovery i.e. concave (DP 16 and DP 17), convex (DP 11 and DP 12) or pseudo-linear (DP 15). The inserted splines all start at $x/chord \approx 0.25$ and end at $x/chord \approx 0.55$, except for DP 17 which never realigns with the Baseline profile. The characteristics of all *shock focused* design targets are detailed in Table 5.4.

5.3.3 Convergence and Loading Alignment : *Shock Focused* Cases

As laid out in Section 3.6 on the development of the inverse design algorithms, the V_y and Δp methods advance in different manners. For the former, geometry changes are performed once a converged solution is obtained. A number of successive steady state computations are necessary to obtain a satisfactory geometry. The Δp method operates by executing camber line changes as the solution evolves to steady state. Convergence of the flow quantities and of the geometry is coupled such that a single run is sufficient. Analysis of the design runs is therefore

Table 5.4: Summary of design test cases. The specimens are categorised in terms of strategy, inverse algorithm, cavitation condition and mesh.

Design Case	Design strategy		Inverse algorithm		Cavitation number σ			Blade channel cells	
	Shock focused	Tip to tail	V_y	Δp	0.652	0.680	1.367	$64 \times 32^{\star}$	$112 \times 32^{\star\star}$
VY 4	•		•		•			•	
VY 9	•		•		•			•	
DP 11	•			•		•			•
DP 12	•			•		•			•
DP 15	•			•		•			•
DP 16	•			•		•			•
DP 17	•			•		•			•

* Grid number 4 in Table 4.4.
** Grid number 5 in Table 4.4.

carried out separately for the V_y algorithm with cases VY 4, VY 9 (*shock focused*), and for the Δp algorithm with cases DP 11, DP 12, DP 15, DP 16 and DP 17 (all *shock focused*).

Iterative V_y Runs: VY 4 and VY 9

The convergence history for cases VY 4 and VY 9 is shown in Figure 5.16. Both are run in cavitating conditions at $\sigma = 0.652$ and attempt to smooth the discontinuity in the V_y distribution located at cavitation closure (see Figure 5.14a). The special smoothing procedure introduced in the algorithm (see Section 3.6.1) is essential to prevent divergence. Observation of Figure 5.16 is proof of the design strategy's volatility. The decrease in camber line residual R_f is non monotonous for both VY 4 and VY 9 and the maximum camber shift is consistently located in the closure region. Despite its jerky character, the residual decrease in maximum camber line shift exceeds 4 orders of magnitude (see Figure 5.16a). The normalised velocity offset $R_{\hat{V}_y}$ goes down to 2×10^{-3} for VY 4 and 1×10^{-2} for VY 9. In both cases, the maximum discrepancy is located within the closure region, where the recovery splines are imposed. It results from the difficulty to completely smooth the shock. There is approximately one order of magnitude difference between VY 4 and VY 9, suggesting that VY 4 is a more successful design concept. Mapping the $\partial V_y / \partial m$ result loadings for the new geometries as in Figure 5.17 confirms the success gap as VY 9 sill presents a shock at $x/chord = 0.35$. With the VY 4 loading, the shock is successfully reduced to a small amplitude fluctuation. In the other regions, the alignment of target and result distributions is well met.

It requires approximately 50 iterations of the steady state computation to reach $R_f < 10^{-4}$. The total computational load is extensive as each run to convergence consists of 200 to 500

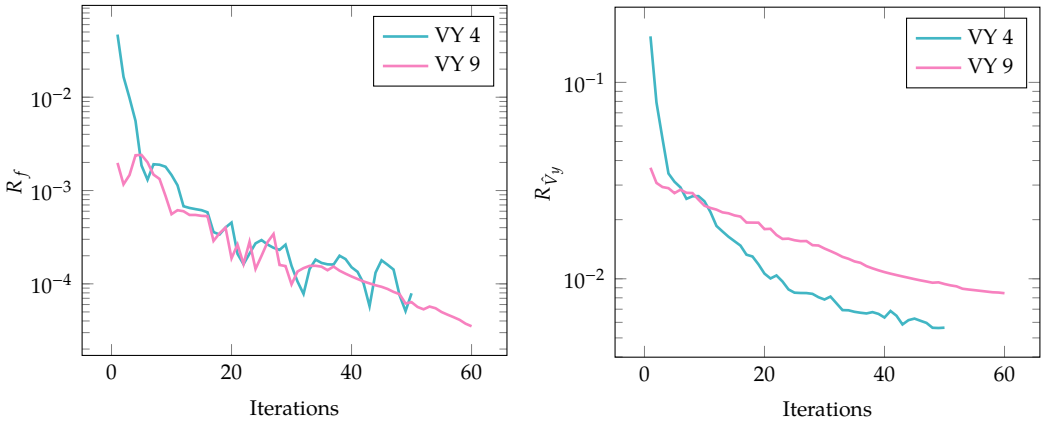

(a) Camber line residual R_f **(b)** V_y offset

Figure 5.16: Design convergence for *shock focused* cases VY 4 and VY 9 in terms of camber line and $\overline{V_y}$ offset ($\sigma - 0.652$). The design algorithm is based on the $\overline{V_y}$ method.

multigrid cycles. In Figure 5.18, the pressure residual history for the complete VY 4 design calculation from Baseline to final geometry is presented. In its entirety, close to 25 000 multigrid cycles are necessary.

Direct Δp Runs

For the Δp runs the fluid and design problems are coupled, so it is sufficient to measure convergence using the conventional root mean square residuals for flow quantities, i.e. pressure and velocity. In Figure 5.19, the camber line residuals R_f and flow RMS are given in terms of the number of multigrid cycles for cases DP 12 and DP 16. For the camber line residual, the decrease strongly fluctuates at two frequencies: a high frequency corresponding to every single geometry update and a lower frequency that matches the cyclical behaviour of the flow residuals. Attempts were made at updating the geometry at enlarged intervals but consistently caused solution divergence. Further investigation is recommended on this matter as it can enhance convergence as well as reduce computational load.

This being said, the mean R_f exhibits a monotonous decrease to 10^{-6}, as required of the flow RMS. With the Δp method, camber line stabilisation is superior to what was obtained using the V_y algorithm. Th rate of convergence is dependent on the character of the imposed loading. It takes approximately 800 cycles for DP 12 against close to 1300 for DP 16. For a completely analytical run in cavitating conditions, the number of multigrid cycles is of approximately 700. An important observation is that switching on the design algorithm does not significantly impact the rate of convergence.

The target and result Δp distributions are shown in Figure 5.20. Overlapping between the

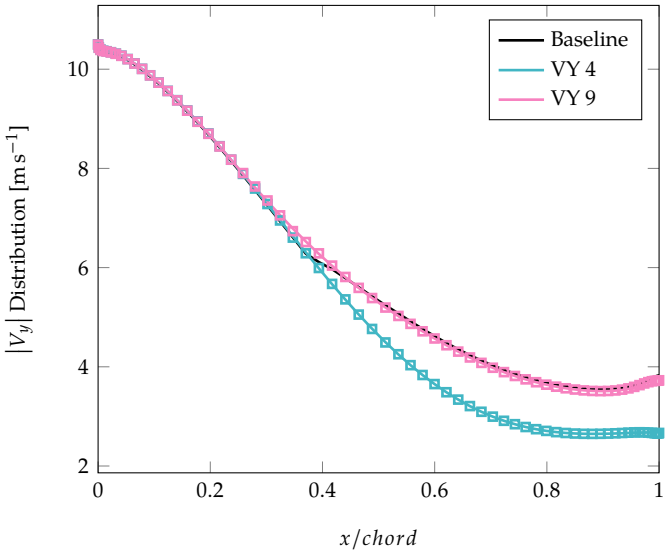

(a) V_y distribution

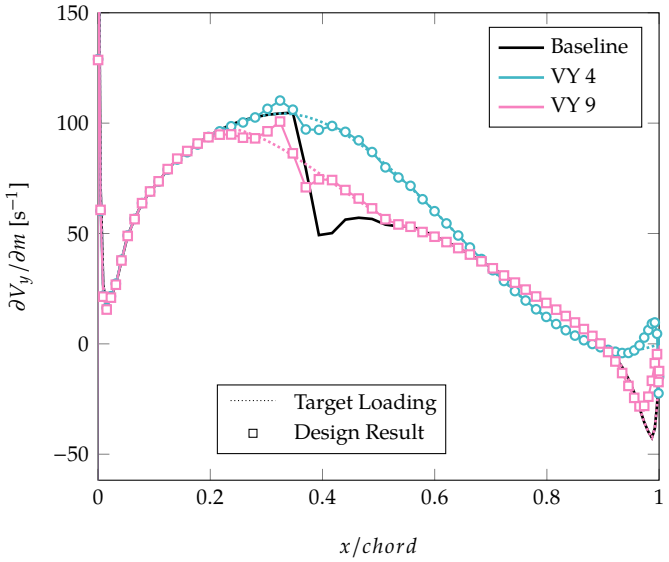

(b) $\partial V_y/\partial m$ Loading

Figure 5.17: Comparison of target versus result $\overline{V_y}$ and $\frac{\partial V_y}{\partial m}$ loading distributions for *tip to tail* cases VY 4 and VY 9 ($\sigma = 0.652$).

two is generally satisfactory. Two zones of discrepancy are picked up: the cavitation closure region and the trailing edge. For the latter, the difference is caused by the special treatment at the tail which switches off the Δp algorithm. In this situation, the flow follows its natural course. It is interesting to note that smoothing around the shock cannot be applied without affecting the downstream distribution. To maintain the loading profile it has to be actively imposed as demonstrated by cases DP 11, DP 12, DP 15 and DP 16.

The discrepancies located in the closure region correspond to small amplitude shocks.

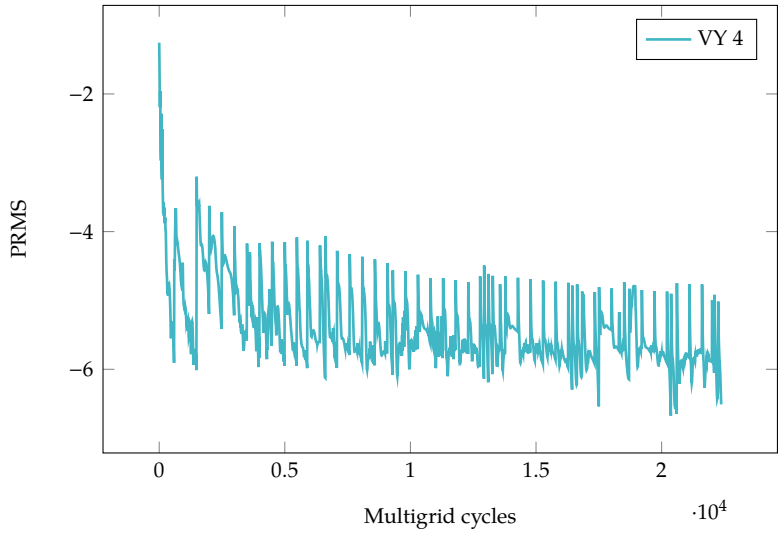

Figure 5.18: Full design run using the $\overline{V_y}$ algorithm: 50 steady state computations resulting in close to 2.5×10^4 multigrid cycles (case VY 4 example).

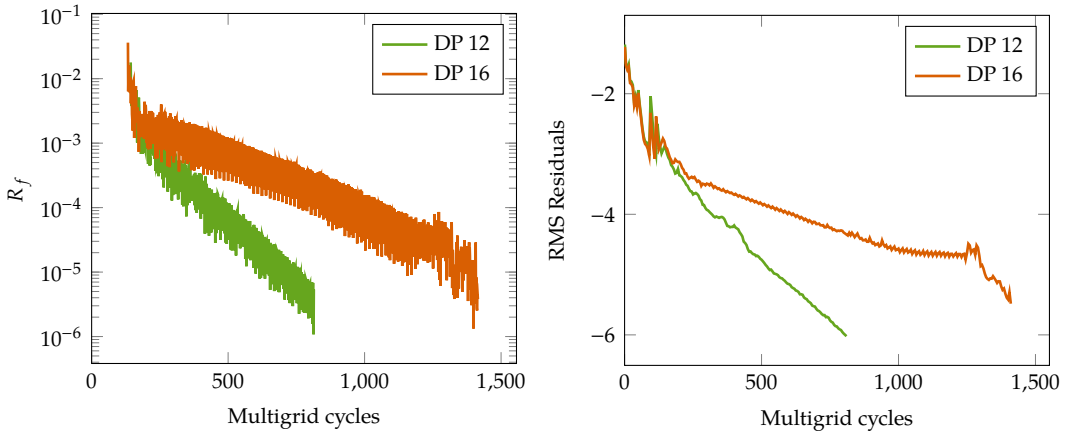

(a) Camber line residual R_f **(b)** Fluid RMS

Figure 5.19: Convergence of design procedure using the Δp algorithm: single steady state computation necessitating approximately 700 and 1500 mutligrid cycles for example cases DP 12 and DP 16.

These can be more or less pronounced depending on the loading profile. Cases DP 11 and DP 15 are the worst performers in terms of amplitude reduction. For both, the decrease in loading is initiated further upstream than DP 12, DP 16 and the Baseline shock onset. This observation correlates to the results for cases VY 4 and VY 9, where the latter was constructed using a more upstream recovery which led to poor smoothing performance. Nevertheless, the design strategy's capacity to smooth the closure is well demonstrated here.

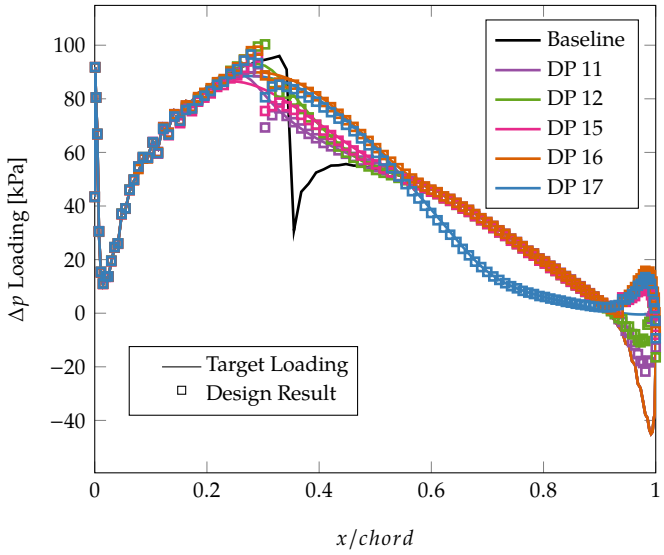

(a) Full blade

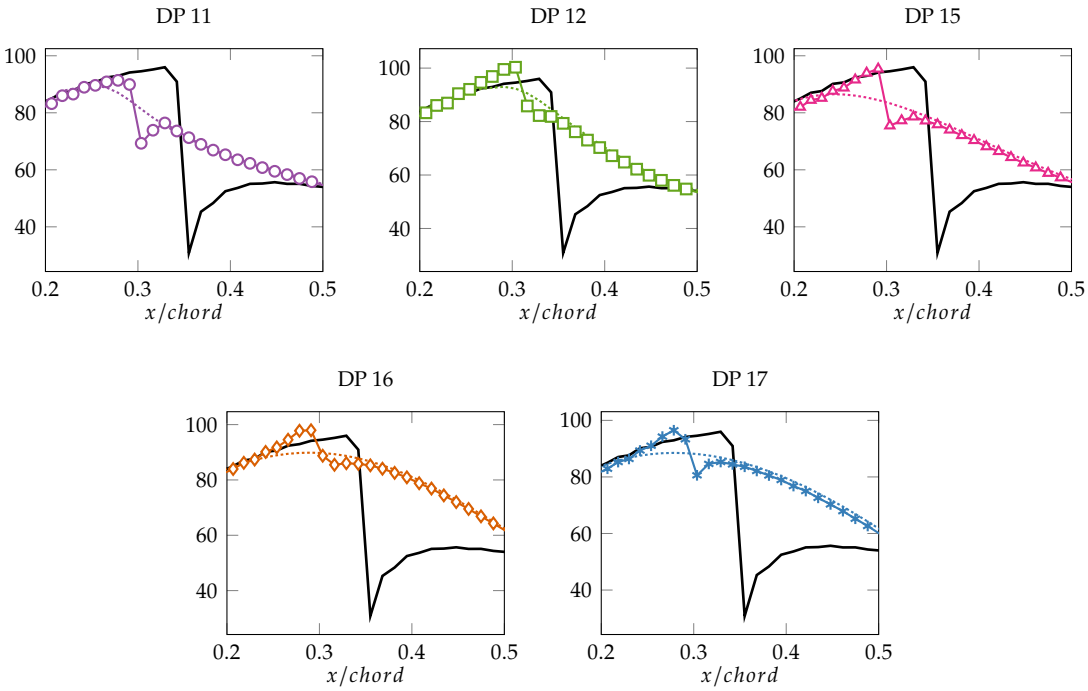

(b) Close-up on closure region

Figure 5.20: Comparison of target versus result ΔP loading for the *shock focused* cases designed using the Δp algorithm. The agreement is largely satisfactory; the only discrepancies are located upstream of the Baseline shock where the change in loading instigates an early closure.

5.3.4 Generated Camber Lines : *Shock Focused* Cases

The camber lines for blades designed using the $\overline{V_y}$ and Δp algorithms are presented separately. In Figure 5.21, cases VY 4 and VY 9 are shown. Differences to Baseline are far weaker than

for the *tip to tail* designs. The product of the smoothness imposition is the kink in the positive Y direction in the closure region. It is marginally larger for the VY 4 case. In the prescribed loadings, differences appear at $x/chord = 0.2$ between VY 9 and VY 4. However, observation of the result loadings as given in Figure 5.17b showed that VY 9 failed to match the target between $x/chord = 0.2$ and $x/chord = 0.3$, following instead the Baseline profile. The camber line comparison confirms this as no differences are found until $x/chord = 0.3$ or $x \approx 4 \times 10^{-2}$ m.

After the closure shock, the loading for VY 4 remains high before dropping at a higher gradient than Baseline. This translates to increased camber curvature after the kink, followed by a low curvature trailing edge section. These features resemble those of the fore-loaded case VY 8. Indeed, both are designed using loading profiles of a similar shape, the main distinction being the position of the maximum: $x/chord = 0.3$ for VY 4, $x/chord = 0.2$ for VY 8 (see Figures 5.14b and 5.2b) and the fact that VY 4 is imposed under cavitating conditions. The camber line for case VY 9 generally matches Baseline except at the kink and trailing edge.

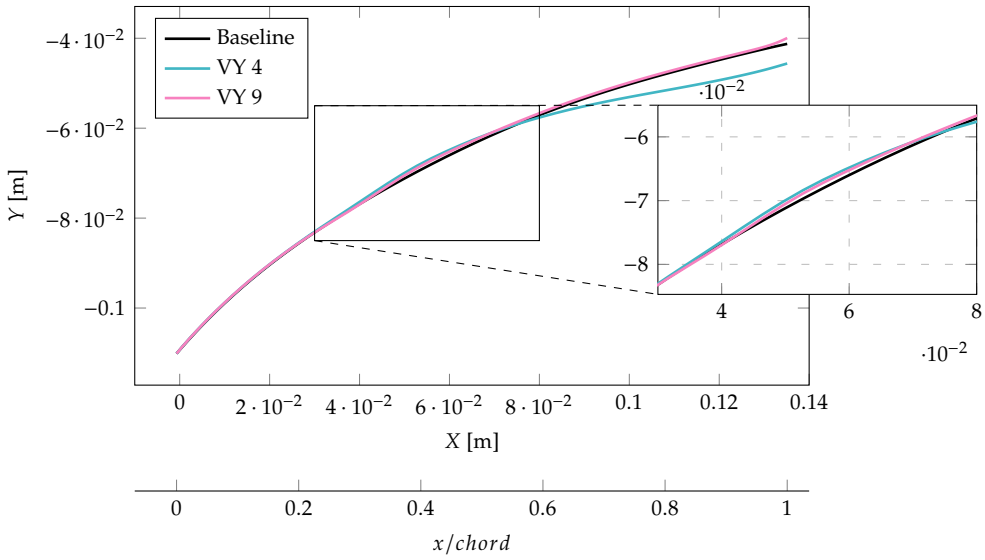

Figure 5.21: Camber line comparison for the *shock focused* cases VY 4 and VY 9 ($\overline{V_y}$ algorithm).

With the Δp algorithm, the effect of shock smoothing on the camber line echoes the results from the V_y method: a kink in the positive tangential direction is sculpted in at closure. Here, the disparities between cases are of smaller scale than those found for VY 4 and VY 9 as illustrated in Figure 5.22 where the close-up is not sufficient to identify gaps. To ease readability, the camber angle is plotted in Figure 5.23. The closure kink is easily identifiable from $x/chord = 0.2$ to $x/chord = 0.3$. By comparing to Figure 5.20, it appears that the downward bending at $x/chord = 0.3$ is what triggers cavity closure. The governing mechanism is the deviation of the surface from the flow direction which causes an increase in pressure

sufficiently strong to block the spread of cavitation. The amplitude and gradient of the recovery shock is then controlled by the surface curvature. It is interesting to note that cases DP 11 and DP 15, which perform least well, deliver similar blade angle characteristics. Most notable are the sharper changes before and after the kink ($x/chord = 0.3$) which downgrades the smoothness of the pressure distribution.

For all Δp designs, the trailing edge angle is greater than the Baseline. This is mainly a numerical artefact originating from the design algorithm. Indeed, in this region the blade thickness quickly goes to zero meaning that camber modifications cannot affect the pressure distribution. The algorithm naturally compensates by imposing larger changes. These are negligible in both the camber distributions (see Figure 5.22) and in the effect on the pressure distribution (see Figure 5.26). The flattening of the camber angle, mainly visible for DP 15, DP 16 and DP 17 after $x/chord = 0.9$, comes from the axial bounding of the Δp procedure to ensure robustness (see Section 3.6.2). The threshold is set at $x/chord = 0.98$ for DP 11, DP 12 and $x/chord = 0.95$ for DP 15, DP 16 and DP 17.

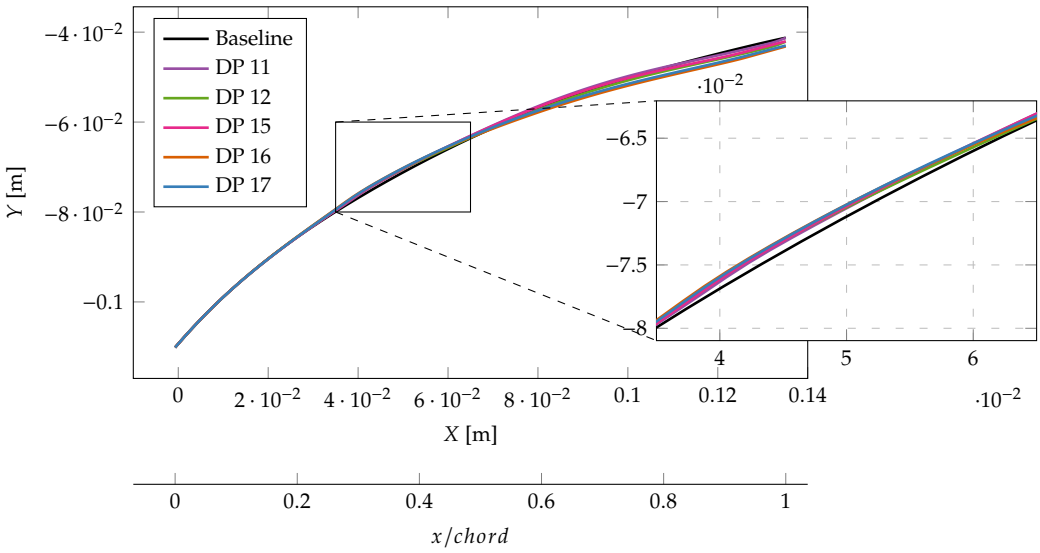

Figure 5.22: Camber line comparison for the *shock focused* cases designed using the Δp algorithm.

5.3.5 Cavitation Performance : *Shock Focused* Cases

Figures 5.24 and 5.26 present the C_p distribution for V_y and Δp cases respectively. In non-cavitating conditions, the closure kink produces a wavy pressure distribution on the suction side. For example, VY 4 and VY 9's suction side pressures rise at $x/chord = 0.2$ to 0.3, drop at $x/chord = 0.3$ to 0.4, and rise again until the trailing edge point (see Figure 5.24). The

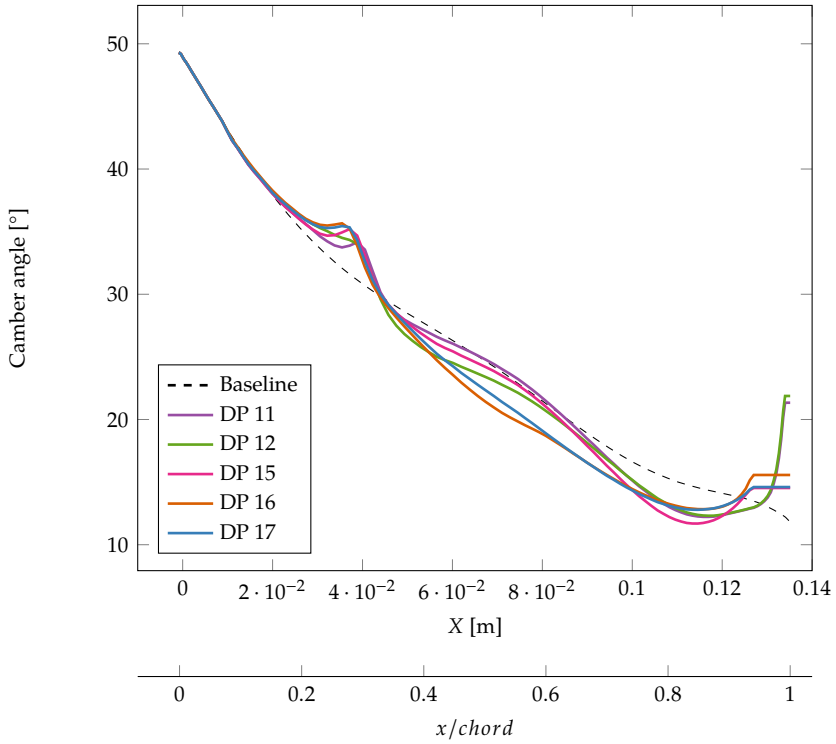

Figure 5.23: Blade angles for the *shock focused* cases designed using the Δp algorithm. The closure kink is a clear product of the shock smoothing strategy.

progression of the undulation is connected to the camber angle around the kink. The position of the kink inflection point matches the location of the pressure extremum. Plotting the camber angle highlights differences in the closure kink between cases. For instance, case VY 9, despite a smaller size bend when compared to VY 4, presents larger angle changes which downgrade the smoothness of the surfaces. As a result, the wave amplitude and gradients of the suction side pressure are greater than for VY 4. For the Δp cases, the wavy pressure distribution on the suction side is also picked up (see Figure 5.26). Differences are found in the amplitude of the undulations. A significant advantage of the ΔP designs is the reduced gradient of the pressure rise, which avoids an unnecessarily large second. This contributes to narrowing the spread of the disruption caused by the kink.

The smoothing performance of the *shock focused* designs is understood by considering the mechanism laid out in Section 5.2: the shock amplitude is equal to the gap between p_v and the "ideal" pressure if cavitation were not to occur. For all *shock focused* cases, the enforced bending is such that the position of the second pressure minimum matches cavitation closure. As a result, the shock connects pressure levels that are only marginally separated. It is essentially the difference between the first and second pressure minima, noted Δp^{WAVE}, that governs the effectiveness of the smooth recovery. This principle is illustrated by comparing cases VY 4 and

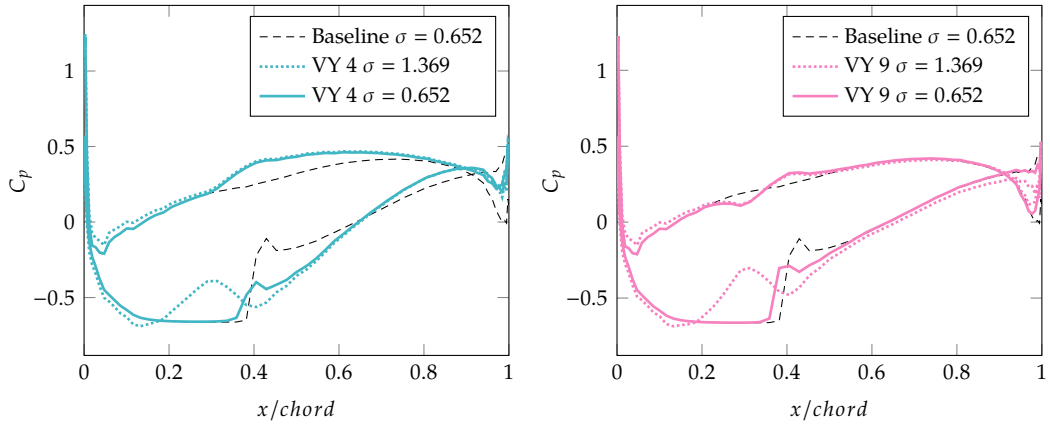

(a) VY 4 C_p distribution

(b) VY 9 C_p distribution

Figure 5.24: Surface pressure coefficients for *shock focused* designs VY 4 and VY 9. At design point $\sigma = 0.652$, the cavity closure shock is softened, most particularly for VY 4. The non-cavitating distribution reveals the suction side wave which causes the shock smoothing characteristic.

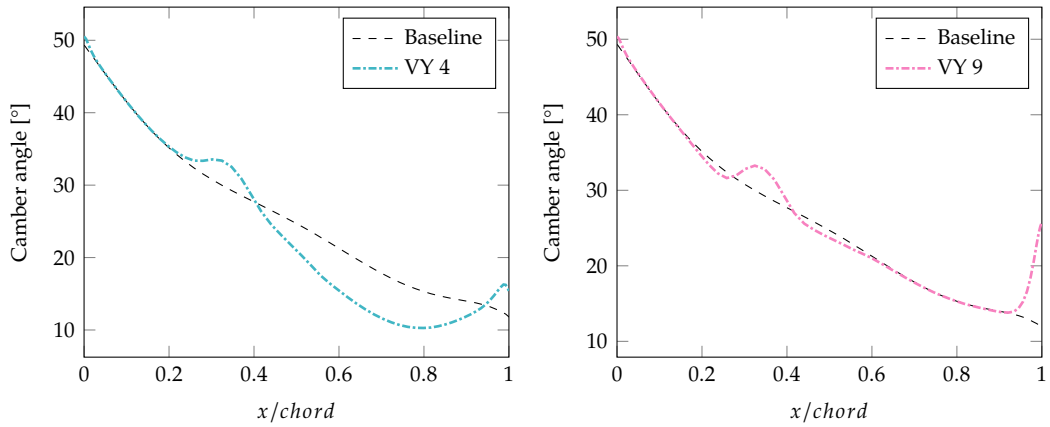

(a) VY 4

(b) VY 9

Figure 5.25: Camber angles for shock focused designs VY 4 and VY 9. The differences in the cavity closure kink ($0.35 < x/chord < 0.4$) drive the differences in the suction side distributions of cases VY 4 (small angle change) and VY 9 (larger angle change).

VY 9 (Figure 5.24) or DP 11 and DP 12 (Figure 5.26). In Figure 5.27 the shock amplitude is plotted against the Δp^{WAVE} values for each of the *shock focused cases*. The trend is positive as illustrated by the linear regression fit. One should note that given the small data sample, the regression is of poor quality with $R^2 = 0.5225$. Despite the weak correlation, the causality is understood and illustrated here.

The critical drawback of the *shock focused* strategy is that recovery smoothing is only effective if the cavity closure matches its location in design conditions. At higher cavitation numbers ($\sigma > 0.652$ for VY 4 and VY 9, $\sigma > 0.680$ for DP 11, DP 12, DP 15, DP 16 and DP 17), the closure slides upstream into the pressure rise section. In such a scenario, it is likely that

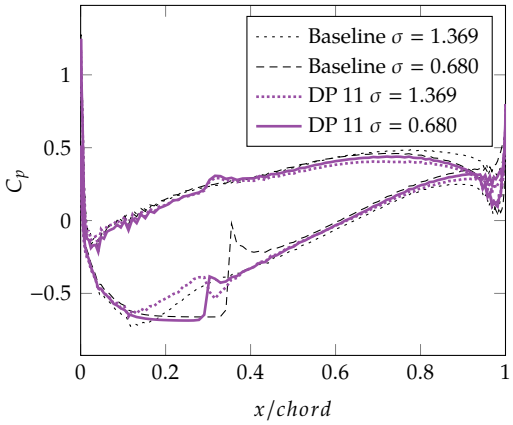

(a) Case DP 11

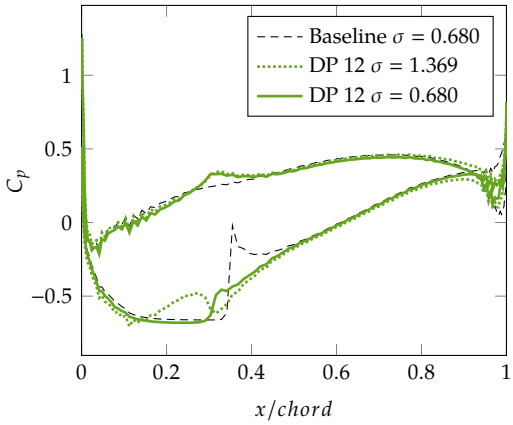

(b) Case DP 12

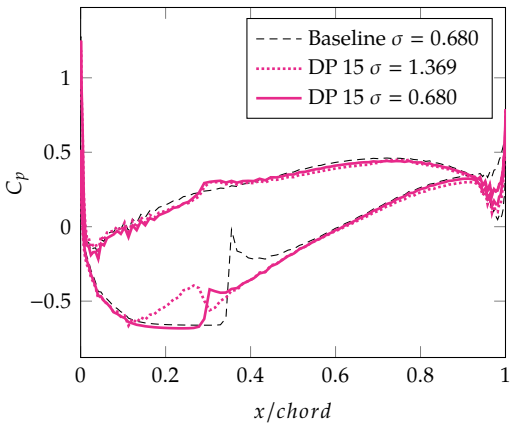

(c) Case DP 15

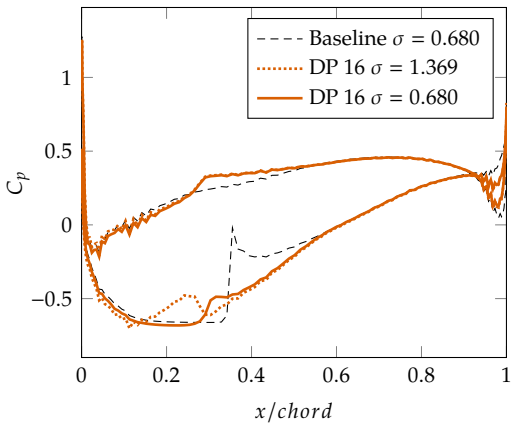

(d) Case DP 16

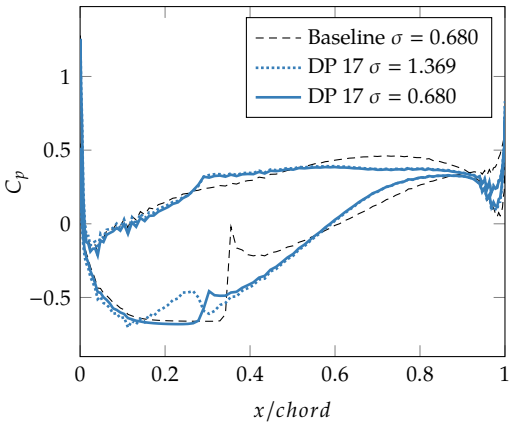

(e) Case DP 17

Figure 5.26: Surface pressure coefficients for *shock focused* cases designed using the Δp method. The first four blades produce very similar profiles with disparities focused around the closure shock region. For case DP 17,the downstream pressure profile does not follow the Baseline profile but matches the prescribed loading (Figure 5.15).

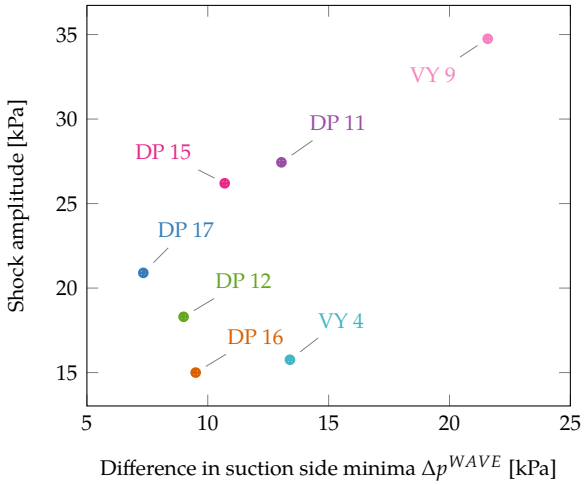

Figure 5.27: Cavitaty closure shock amplitude for the *shock focused* cases in terms of the difference Δp^{WAVE} between the first and second troughs.

the shock for the new blade exceeds in amplitude the Baseline shock. Cases VY 4 and VY 9 are particularly prone to suffer from this defect given their steeper gradients in the wavy distribution region. Furthermore, the non-monotonous pressure on both sides of the blade in non-cavitating conditions may be detrimental to flow stability. Further numerical investigations that incorporate turbulence are to be undertaken to evaluate the hydrodynamic performance.

The seven geometries generated from the *shock focused* strategy share many features. Analysing every single one numerically or experimentally would be a counter-productive effort. Instead, the designs that deliver the largest shock diminution are selected for further analysis. Based on the numbers presented in Figure 5.27, the most successful geometries are VY 4, DP 12 and DP 16. The pressure and volume fraction contours for each are found in Figures 5.28, 5.29 and 5.30. At these scales, the closure bend is only noticeable for VY 4. All three share similar two-dimensional distributions: short cavity length and absence of sharp gradients. A characteristic of interest concerns the behaviour of pressure around the closure region. A sharp change of direction in the pressure contour from normal to parallel to the surface is consistently observed. In Figure 5.30b, the close up view of the closure region indicates that the direction change emanates from the surface kink. The geometric discontinuity is essentially propagated into the flow field until fully diffused.

5.3.6 Correction for Non Cavitating Output : *Shock Focused* Cases

Like for the *tip to tail* cases, differences are found in the non-cavitating output when evaluating cases VY 4 and DP 12 using Fluent with the $k-\varepsilon$ turbulence model. Design DP 16 sits within a tolerable ±1% margin. The same correction process, which consists in adjustments on the

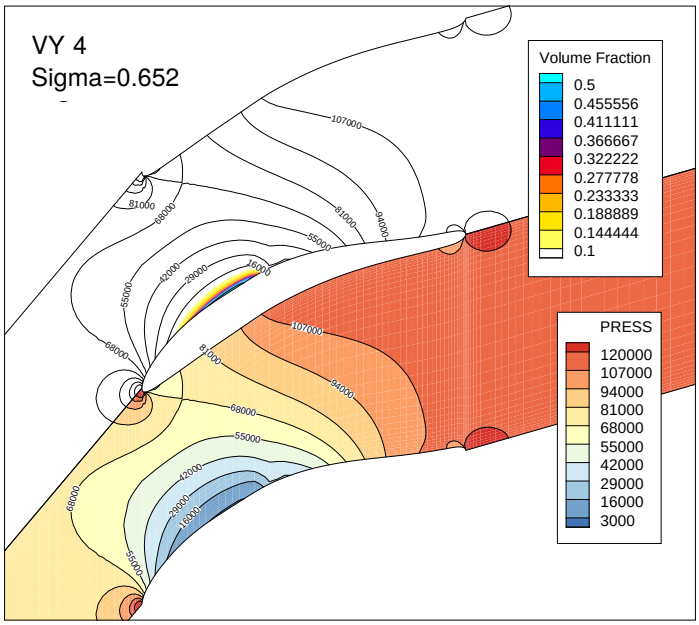

Figure 5.28: Pressure and volume fraction contours for VY 4 at $\sigma = 0.652$.

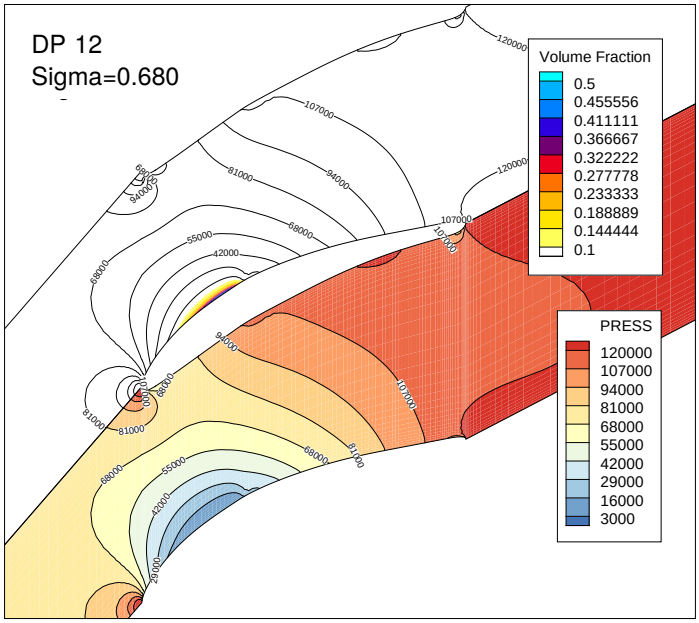

Figure 5.29: Pressure and volume fraction contours for DP 12 at $\sigma = 0.680$.

downstream section, is carried out.

The adjustment is carried out in the same conditions as the principal design run: VY 4 ($\sigma = 0.652$) and DP 12 ($\sigma = 0.680$). The final V_y and Δp loading curves obtained after successive iterations are given in Figure 5.31 against the original target distributions and the baseline profile.

The new ΔV_y breakdown values computed using ANSYS Fluent with the Standard $k - \varepsilon$

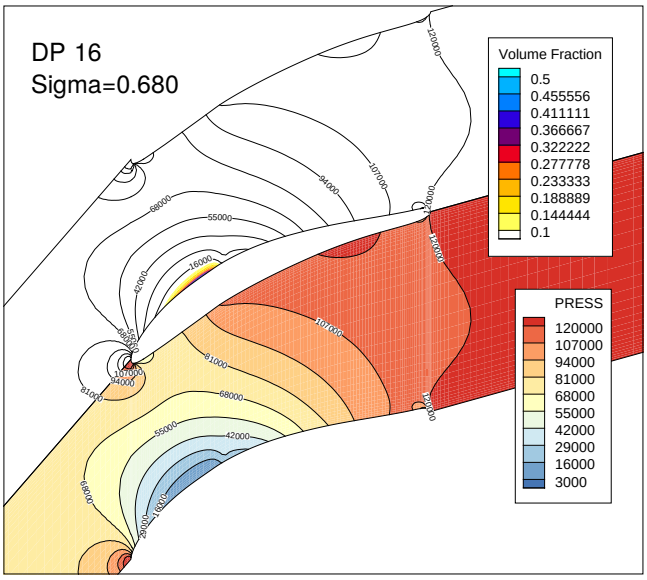

(a) Full blade view

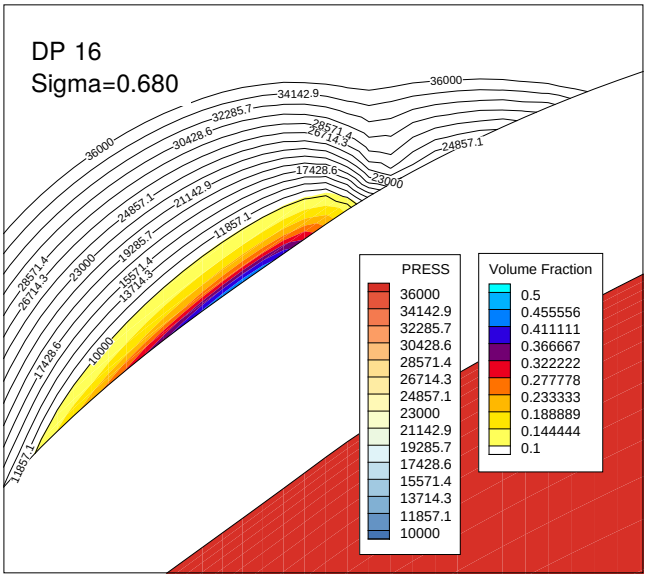

(b) Close-up on closure

Figure 5.30: Pressure and volume fraction contours for DP 16 at $\sigma = 0.680$.

model are listed in Table 5.6. All the corrected non-cavitating ΔV_y values are well within the ±2% range from Baseline. The largest alterations are performed on case VY 4 (Figure 5.31a). The loading in the downstream region is forced to zero such that the pressure side and suction side distributions meet. The corrected distribution imposed on DP 12 is only marginally different to the pre-correction profile. As shown in Figure 5.31, the corrections, limited to the downstream portion of the blades, do not affect the cavitation performance of the designs.

Table 5.5: Cascade hydrodynamic performance in non-cavitating conditions.

Design Case	ΔV_y [m s^{-1}] (Rel. Diff. to Baseline)
Baseline	7.0656
VY 4	7.6355 (+8.1%)
DP 12	6.9720 (-1.3%)
DP 16	7.0333 (-0.46%)

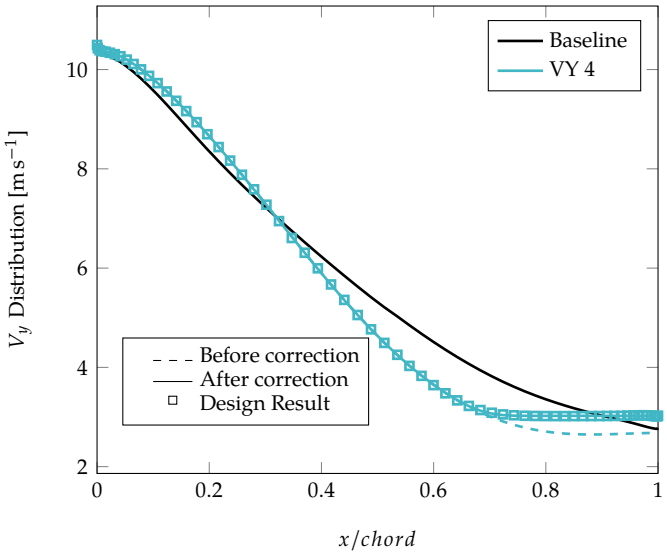

(a) Corrected V_y loadings

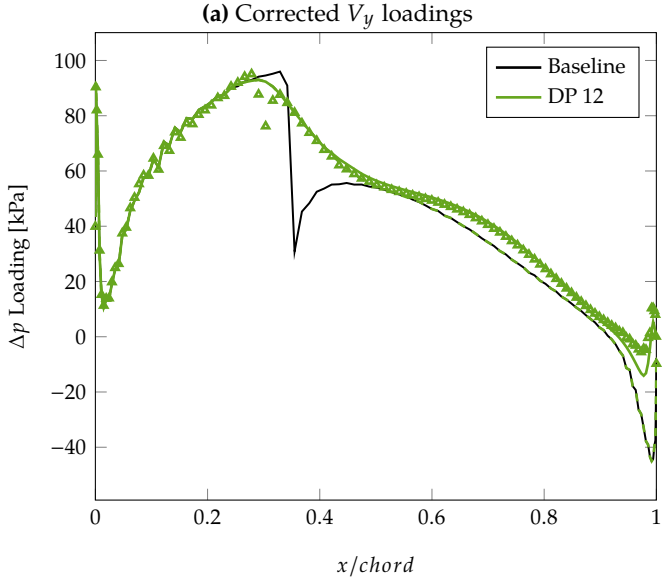

(b) Corrected Δp loading

Figure 5.31: Loadings after the non-cavitating correction for the selected *shock focused* cases (except DP 16 which is already within the tolerable margin).

Table 5.6: Cascade hydrodynamic performance in non-cavitating conditions.

Design Case	Old ΔV_y [m s^{-1}] (Rel. Diff. to Baseline)	Corrected ΔV_y [m s^{-1}] (Rel. Diff. to Baseline)
Baseline	7.0656	
VY 4	7.6355 (+8.1%)	6.9712 (-1.3%)
DP 12	6.9720 (-1.3%)	7.0722 (+0.1%)
DP 16	7.0333 (-0.46%)	-

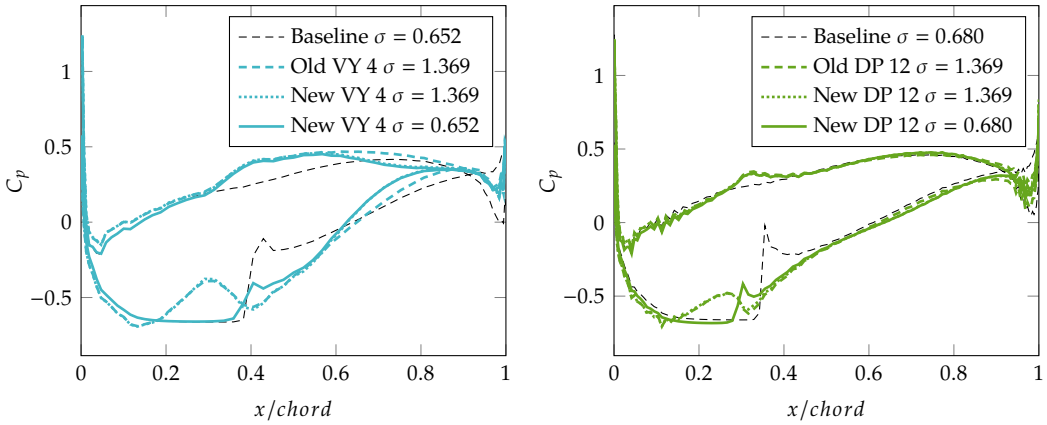

(a) VY 4

(b) DP 12

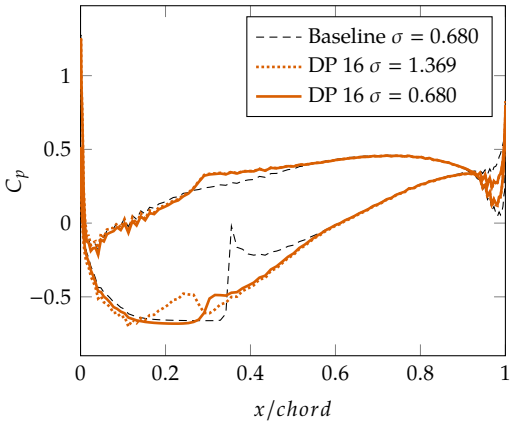

(c) DP 16

Figure 5.32: Surface pressure coefficients after the non-cavitating correction for the *shock focused* cases.

5.4 Final Designs

The final geometries emerging from the inverse design procedure are shown in Figures 5.12 and 5.33. Out of the ten generated designs, the three *tip to tail* cases and the three best *shock focused*

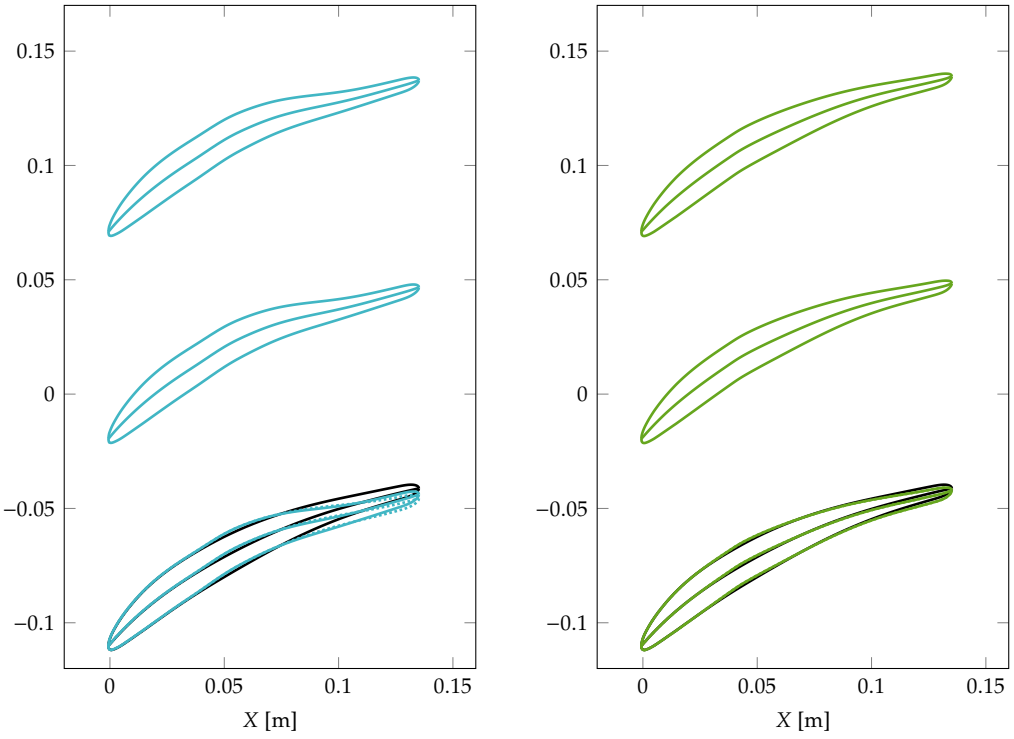

(a) VY 4

(b) DP 12

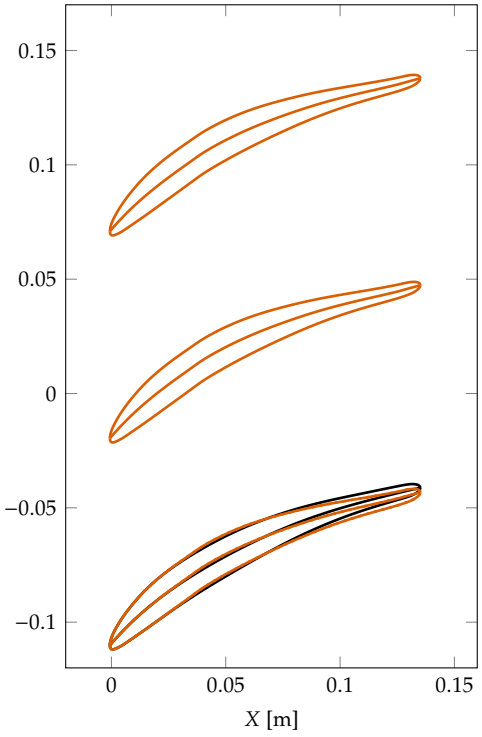

(c) DP 16

Figure 5.33: Final blade geometries for the *shock focused* cases VY 4, DP 12 and DP 16. The common feature is the kink on the suction surface created by the shock smoothing design procedure.

designs are selected for further analysis (see Table 5.7). The total of seven blades (including Baseline) constitute a set of sufficiently diverse profiles to arrive at a comprehensive characterisation of the relationship between cavitation closure shock, blade pressure and erosion. The relations between geometry and flow characteristics that came out of the design process are:

- reduced, respectively increased, suction side pressure gradient for aft-loaded, respectively fore-loaded, loading types. This affects the amplitude of the shock in cavitating conditions: small for aft-loaded blades, large for fore-loaded blades.
- the kink in the camber line is responsible for smoothing the closure shock by creating a non monotonous pressure distribution. Further analysis is needed to determine the effect on the hydrodynamic performance.

Table 5.7: Summary of design cases highlighting the selected and discarded designs.

Design Case	Design strategy		Inverse algorithm		Cavitation number at design σ			Blade channel cells at design	
	Shock focused	Tip to tail	V_y	Δp	0.652	0.680	1.367	64×32	112×32
Selected designs									
VY 3		Aft-loading	•				•	•	
VY 7		Strong aft-loading	•				•	•	
VY 8		Fore-loading	•				•	•	
VY 4	•		•		•			•	
DP 12	•			•		•			•
DP 16	•			•		•			•
Discarded designs									
VY 9	•		•		•			•	
DP 11	•			•		•			•
DP 15	•			•		•			•
DP 17	•			•		•			•

6 Analysis of Design Candidates by Computational Fluid Dynamics

The post-design CFD assessment presented here is aimed at confirming the cavitation improvements and evaluating the performance of each design for viscous and turbulent flows. The analysis is in two parts: steady state and time resolved. The first study examines cavity shape, pressure profile and suction performance. It adds to the inverse design runs by including RANS turbulence modelling. With the time resolved analysis, predictions of the dynamic behaviour of cavitation are sought after. From this data, an anticipated evaluation of the erosive intensity for each design is provided.

6.1 Steady State Analysis

As summarised in Table 5.7, seven geometries, including Baseline, have been selected for further investigation. All have been corrected for ΔV_y discrepancies in non-cavitating conditions (see Sections 5.2.5 and 5.3.6). The point of running a steady-state analysis for these geometries when results have already been delivered by the in-house solver is (i) to provide solutions that take viscous and turbulent effects into account, (ii) confirm the smoothed shock profile using a different cavitation model.

6.1.1 Computational Setup

Fluent runs use the default Zwart-Gerber-Belamri transport equation approach to model cavitating flow. It has been shown (see Section 4.6) that the ZGB technique predicts a delayed inception of cavitation and a shock offset in the upstream direction when compared to the

TE solution. The objective of the analysis is to validate the reduction in shock amplitude and gradient for each of the designs. The implication is that the discrepancy between models is not an issue for geometry to geometry comparisons. To identify the condition that matches the design point for the ZGB runs, it is the shock location instead of the cavitation number that is used as reference.

The Fluent solver is pressure-based with pressure and velocity calculated simultaneously (coupled rather than segregated algorithm) for efficiency. The ZGB model treats cavitating flow as a homogeneous mixture. The aforementioned coupled approach, reserved to single phase flow, can therefore be readily applied. ZGB parameters are set at default value ($\alpha_{nuc} = 5\times10^{-4}$, $R_B = 10^{-6}$ m, $C_e = 50$, $C_c = 0.01$) with vaporisation pressure $p_v = 2339.2$ Pa for water at 20 °C. The QUICK scheme, which calculates face values by blending second order upwind and central interpolations with a solution dependent limiter to avoid under or overshoots, is selected for its robustness. The two equation *Standard* $k-\varepsilon$ model is used for turbulence closure because of its high convergence rate. All steady state solver settings are summarised in Table 6.1.

Table 6.1: Numerical configuration for steady state cavitating simulations.

Computational modules	Selected models and details		
Solver schemes	Navier-Stokes discretisation	Pressure based	Coupled momentum and continuity equations, QUICK face interpolation
Spatial Discretisation	Unstructured Quad-dominant	Max edge length $= 4\times10^{-3}$ m	20 nodes in the boundary layer
Cavitation	Homogeneous mixture	Transport Equation	Zwart-Gerber-Belamri in default configuration, $p_v = 2339.2$ Pa
Turbulence	RANS	Standard $k-\varepsilon$	Scalable wall functions, $y^+ < 30$

Each geometry is run for a range of cavitation numbers higher and lower than the design condition. For each solution the pressure distribution, volume fraction contours and hydrodynamic performance (ΔV_y, lift, drag) are extracted. Design success is validated if the Fluent flow results replicate the data obtained from the *In-house* solver. The target features differ from case to case depending on the character of the design strategy. All desired attributes are made explicit in Table 6.2. Three categories can be distinguished: aft-loaded cases VY 3 and VY 7, fore-loaded case VY 8, shock smoothing cases VY 4, DP 12 and DP 16. Larger differences are expected for the first three *tip to tail* designs, especially in terms of suction performance with a late drop in breakdown for VY 3 and VY 7, and an early one for VY 8. Being shock focused, the

other three designs should resemble the Baseline case, except in the shock region. For these cases, it is anticipated that the effects on cavity shape and suction breakdown will be subtle. Otherwise, for all cases, except VY 8, the closure shock is expected to weaken at the design condition.

Table 6.2: Flow attributes for the selected geometries as introduced at the design stage. Analysis using the Fluent RANS & ZGB solver should recover similar features to confirm design success.

Design Case	Design strategy		Target attributes			
	Shock focused	Tip to tail	Non-cavitating suction side pressure	Cavity shape	Suction performance	Closure recovery
VY 3		Aft-loading	Flat (high gradient only in downstream region)	Streamwise elongated	Late cavitation inception, enhanced suction range	Low amplitude shock
VY 7		Strong aft-loading				
VY 8		Fore-loading	Steep gradient	Short streamwise length, thick tangentially	Early cavitation, minimised suction range	High amplitude shock
VY 4	•		Wavy distribution (high amplitude)	Baseline length, attached closure region	Matching with Baseline breakdown, kinked decrease	Smooth gradient, low amplitude
DP 12	•		Wavy distribution (low amplitude)			
DP 16	•		Wavy distribution (low amplitude)			

6.1.2 Results from the Steady State Analysis

Tip to Tail Cases

The pressure distributions for cases VY 3, VY 7 and VY 8 are plotted in Figure 6.1 with the Baseline distribution. As expected, the suction side pressure gradient is low in the upstream half of the blade for the aft-loaded cases VY 3 and VY 7, and high for the fore-loaded case VY 8. This affects the streamwise cavity length which increases in a quicker manner for VY 3 and VY 7 (see Figure 6.2b). The non-cavitating minimum C_p value for each blade determines the starting condition for cavitation. It is highest for VY 7 at $C_p^{min} = -0.5$ and lowest for VY 8 at $C_p^{min} = -0.8$. The differences in the inception cavitation number are substantial: for VY 8 the cavity reaches $x/chord = 0.4$ at $\sigma = 0.676$, whereas VY 7 doesn't cavitate until $\sigma < 0.5$.

For VY 7, the low pressure point picked up by the *In-house* solver in the downstream

region of the suction side is smoothed out here (see Section 5.2.5). By modelling the boundary layer, the fluid response to changes in surface geometry is attenuated by viscous and turbulent diffusion. Especially, towards the trailing edge, where the boundary layer is at its largest. As explained in Section 5.2.5, the large adverse pressure gradient at the trailing edge for VY 7 leads to separation. This can be observed at $x/chord = 0.9$ in Figure 6.1b where the suction side C_p curve gradient goes to zero.

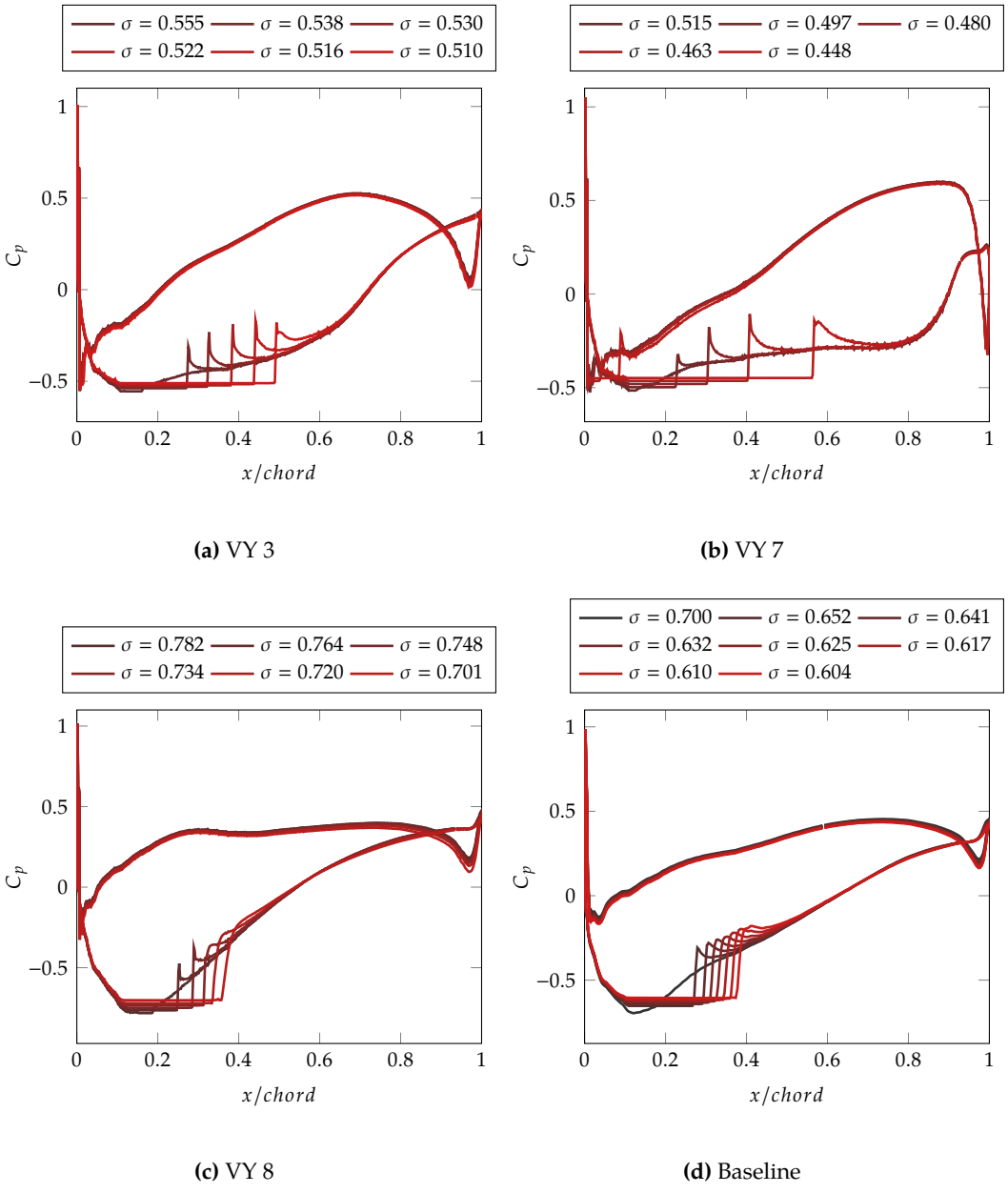

(a) VY 3

(b) VY 7

(c) VY 8

(d) Baseline

Figure 6.1: Surface pressure coefficients at descending cavitation numbers for the *tip to tail* geometries.

The closure shock delivered by the ZGB model consistently overshoots the high σ pressure coefficient line before decreasing smoothly to reconnect with it. This makes identifying shock

amplitude reduction more difficult than with the *In-house* results (see Section 5.2.4). To refine the observation, a study of the shock growth is carried out. The jump amplitudes are evaluated by measuring the pressure difference between the base and the tip of the jump for each case. Amplitude values are shown in Figure 6.2a in terms of the cavitation number. The data shows a consistent rate of increase for all cases. This suggests that the dependency of the closure shock on the suction side pressure distribution is not as strong as expected or the increase would have been slower for the aft-loaded cases. Nevertheless, the maximum shock amplitude for VY 3 and VY 7 stagnates at 40 kPa, as opposed to Baseline and VY 8 with closure amplitudes that continue to increase. It is worth noting that Case VY 8 exceeds 30 kPa as soon as cavitation appears.

The shock is caused by the flow slowing down at the closure where the channel narrowing effect of the cavity abruptly disappears. Its strength is dependent on the amount of narrowing caused by cavitation. In Figure 6.3, the vapour volume contours are shown for cavity closure locations at approximately $x/chord = 0.4$. This corresponds to cavitation numbers $\sigma = 0.522$ for VY 3, $\sigma = 0.465$ for VY 7, $\sigma = 0.690$ for VY 8 and $\sigma = 0.591$ for Baseline. The correlation between cavity thickness and shock amplitude is made evident as aft-loaded cases VY 3 and VY 7 produce a much narrower vapour volume region than the VY 8 case. As a side note, it is interesting to mention the difference between the ZGB and TE cavitation models in the size of the cavity. With the former, density variations occur within a small pressure margin around $p_v = 2339.2$ Pa. Below and above, the density is equal to that of either water vapour or liquid water respectively. By contrast, the TE model takes into account the compressibility of the mixture meaning that (i) the density drop is more gradual and (ii) the cavity region appears larger with smoother boundaries (see Section 5.2.4).

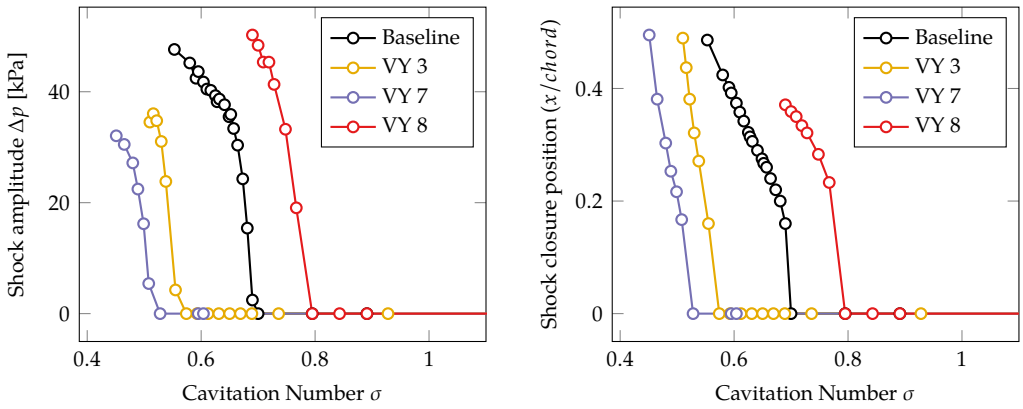

(a) Amplitude of closure shock

(b) Location of closure shock

Figure 6.2: Closure shock evolution in terms of amplitude (6.2a) and location (6.2b) for the *tip to tail* cases.

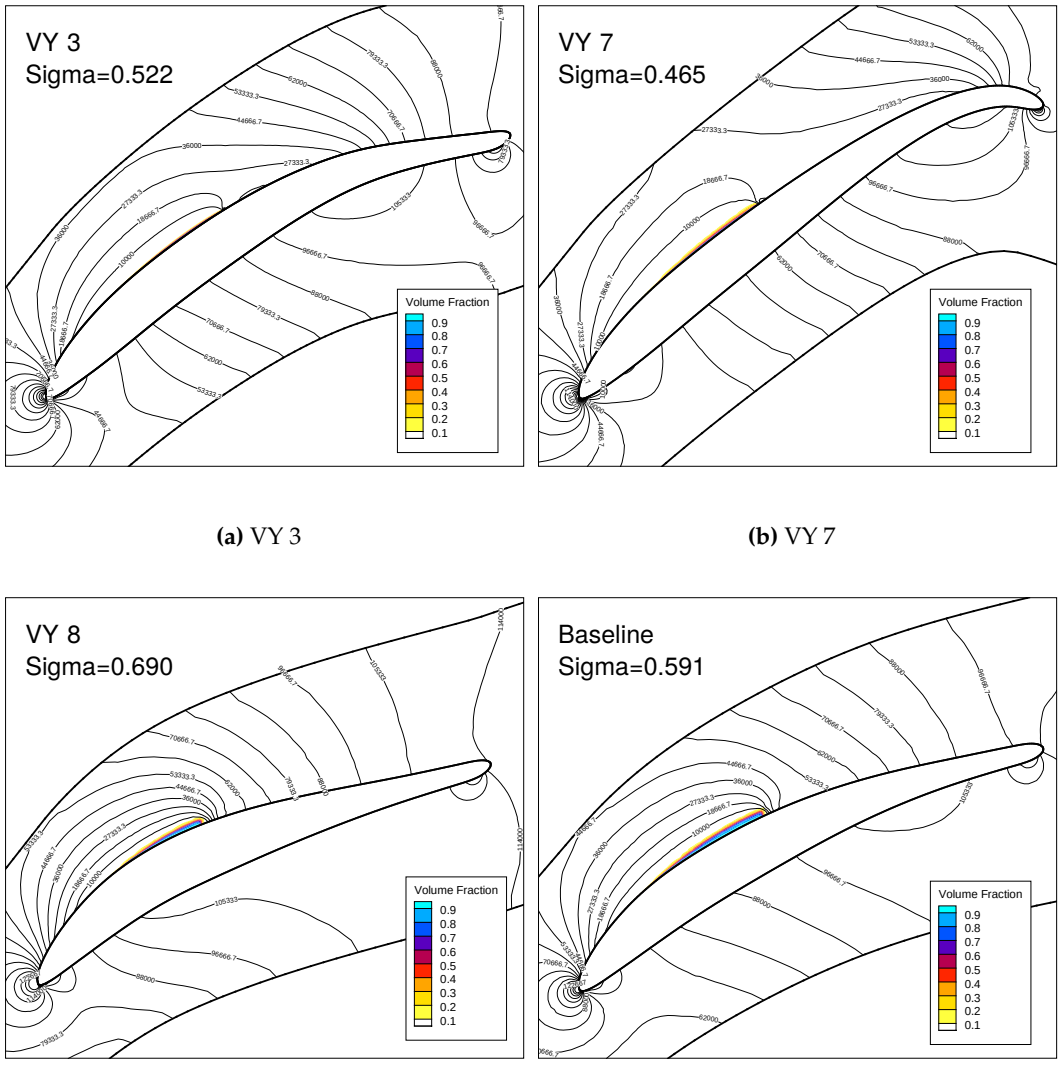

(a) VY 3 **(b)** VY 7

(c) VY 8 **(d)** Baseline

Figure 6.3: Fluent-ZGB pressure and volume fraction contours for the *tip to tail* cases at matching cavity closure location $x/chord = 0.4$ ($\sigma_{VY3} = 0.522$, $\sigma_{VY7} = 0.465$, $\sigma_{VY8} = 0.690$, $\sigma_B = 0.591$).

Differences in suction performance are shown in Figure 6.4 where the V_y breakdown is plotted for all *tip to tail* design cases. As expected, the aft-loaded designs VY 3 and VY 7 start to drop at lower cavitation numbers ($\sigma < 0.6$), than fore-loaded design VY 8, which starts to descend at $\sigma \approx 0.78$. For all cases, the drop is monotonous and progresses at equivalent rates.

Shock Focused Cases

For the *shock focused* cases, design runs were carried out at $\sigma = 0.652$ for VY 4 and at $\sigma = 0.680$ for DP 12 and DP 16 using the TE cavitation model. In terms of the Baseline closure location, these flow conditions yield a recovery at $x/chord = 0.4$ and $x/chord = 0.35$ respectively. In

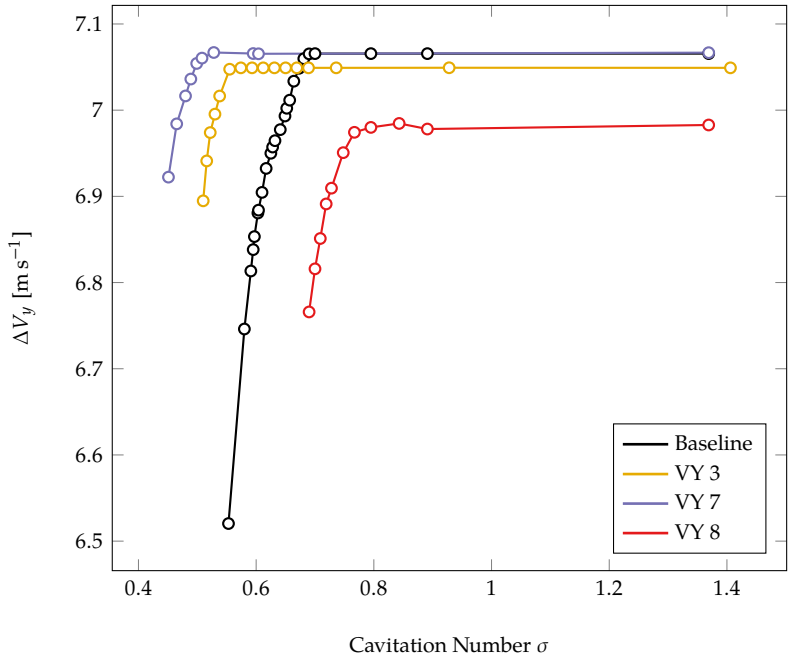

Figure 6.4: ΔV_y breakdown for the *tip to tail* cases. Differences in suction performance are directly related to the loading type: fore-loading reduces range, aft-loaded widens it.

non-cavitating conditions, it is clear that the troughs on the suction side match the design closure locations (see Figure 6.5). The difference in the streamwise extent of the wavy region (large for VY 4, small for DP 12 and DP 16) is also visible and is brought about by the change in design algorithm and mesh refinement (see Section 5.3.2). At design conditions however, the size of the cavity produced by the ZGB model does not correspond to the TE result, as illustrated in Section 4.6: the cavity is thinner and ends at a more upstream location. To determine the appropriate condition it is the position of the cavity closure rather than the cavitation number that is assessed. The inflow total pressure is gradually decreased until the closure shock location matches the one found at the end of the design procedure (see Section 5.3.5). The corresponding σ values are shown in Table 6.3 for each case.

Table 6.3: Cavitation number correspondence table between the *In-house*-TE and Fluent-ZGB solvers using the closure location as reference.

Design case	Closure location ($x/chord$)	Cavitation number	
		In-house solver with TE model	Fluent solver with ZGB model
VY 4	0.38	0.652	0.599
DP 12	0.31	0.680	0.616
DP 16	0.3	0.680	0.618

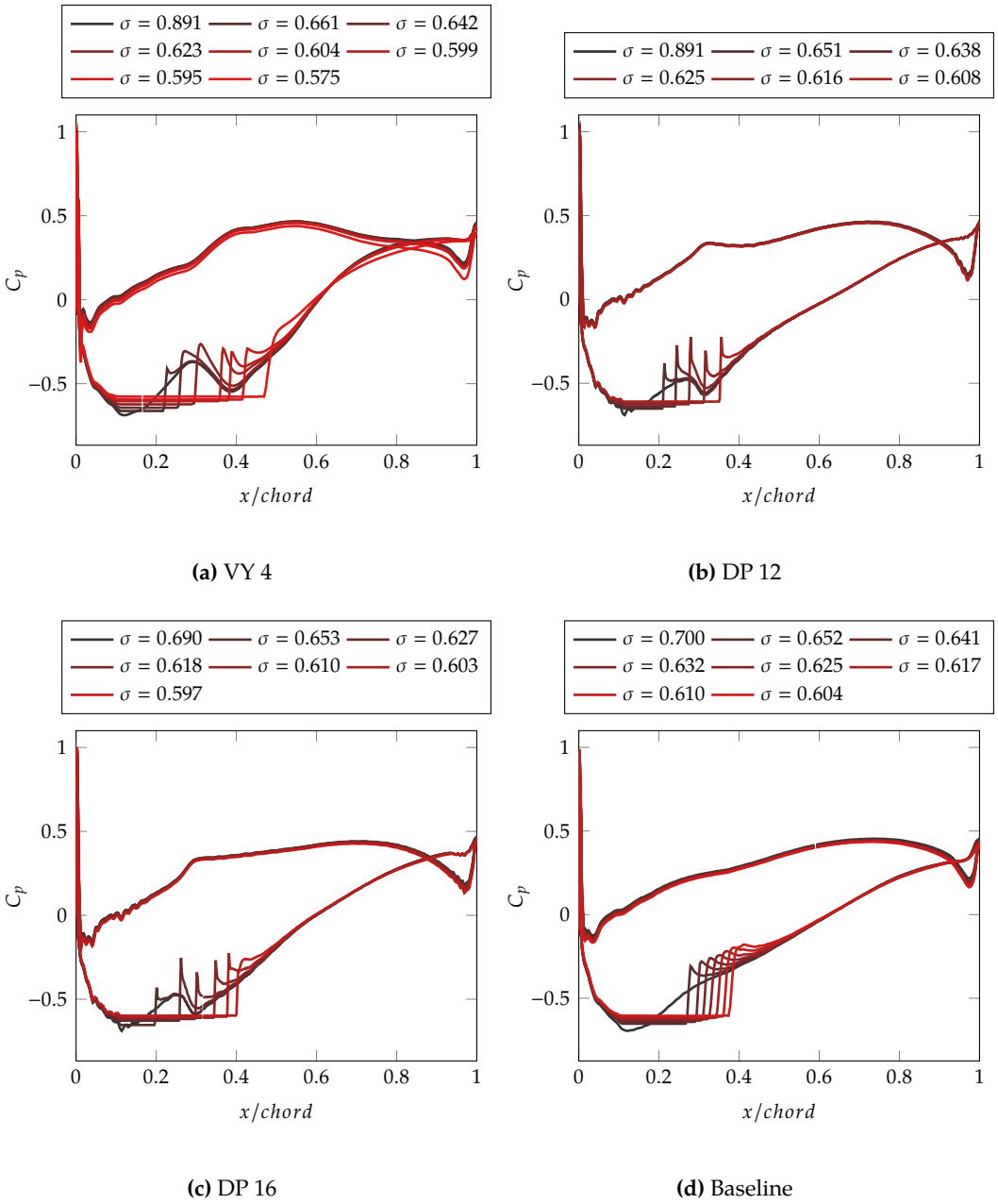

(a) VY 4

(b) DP 12

(c) DP 16

(d) Baseline

Figure 6.5: Surface pressure coefficients for the *shock focused* cases at descending cavitation numbers.

The closure shock study is repeated here. Unlike the *tip to tail* cases, amplitude growth is non monotonous as the suction side trough affects closure behaviour. Drops in amplitude are observed in Figures 6.5 and 6.6 for $\sigma = 0.599$, $\sigma = 0.616$ and $\sigma = 0.618$ for VY 4, DP 12 and DP 16 respectively. However, a negative consequence of the wavy distribution is that, at cavitation numbers higher than the design condition, the shock amplitude can exceed the Baseline case. This is true for case DP 12 at $\sigma = 0.625$ where the amplitude reaches 42 kPa against 39 kPa for the Baseline.

In terms of cavity shape and size, the vapour volume contours for the *shock focused* designs

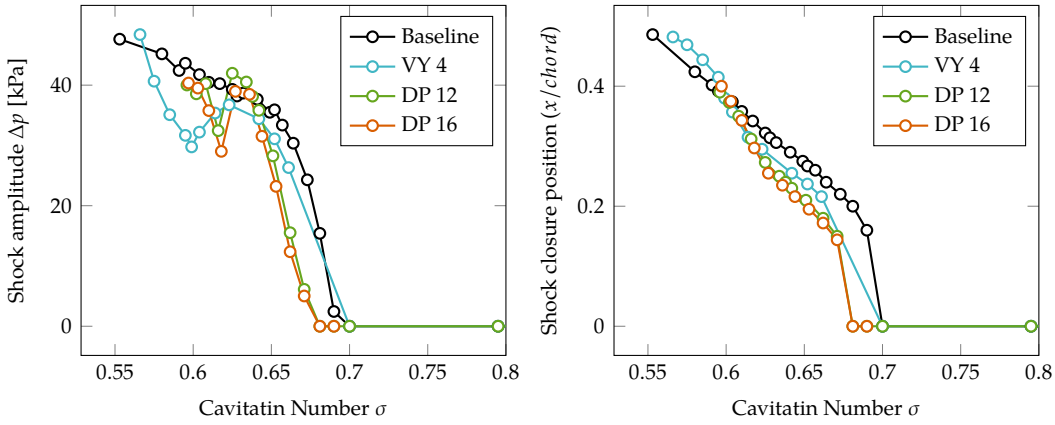

(a) Amplitude of closure shock **(b)** Location of closure shock

Figure 6.6: Closure shock evolution in terms of amplitude (6.6a) and location (6.6b) for the *shock focused* cases.

are presented in Figures 6.7 (VY 4) and 6.8 (DP 12 and DP 16) with the Baseline results at the corresponding design cavitation numbers (see Table 6.3). Instead of the wedge shaped cavity observed on the Baseline surface, the new designs produce a narrow sheet that terminates smoothly at closure. As a result, the slowing down of the flow is not as sharp and the jump in static pressure is softened.

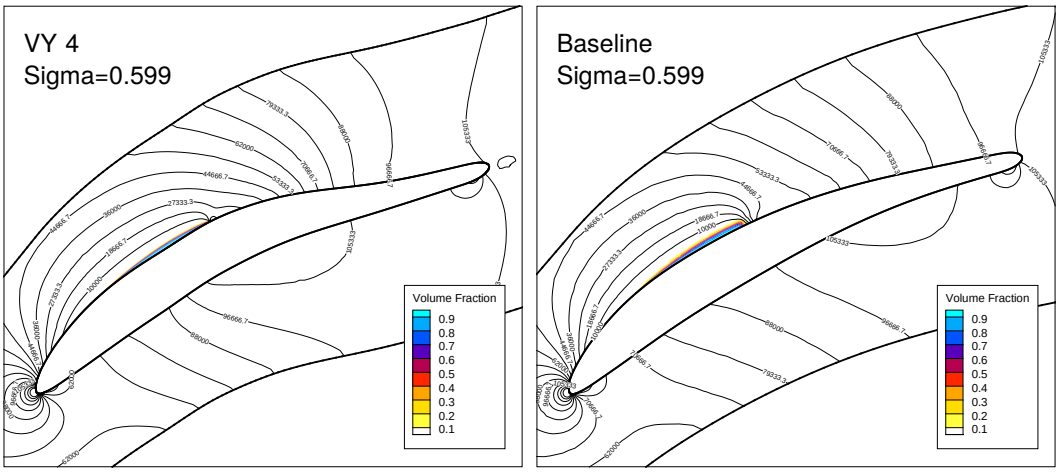

(a) VY 4 **(b)** Baseline

Figure 6.7: Pressure and volume fraction contours for the *shock focused* VY 4 case at $\sigma = 0.599$.

The breakdown point for the *shock focused* cases matches the Baseline drop (see Figure 6.9). The fluctuation in shock amplitude translates to a stepped descent as the rate of decrease slows down when it aligns with the design condition. For DP 12 and DP 16, other than the non-cavitating offset, the breakdown curves are identical. With case VY 4, the drop in ΔV_y is

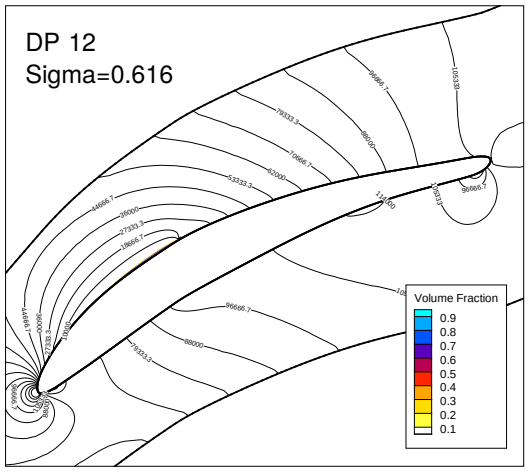

(a) DP 12

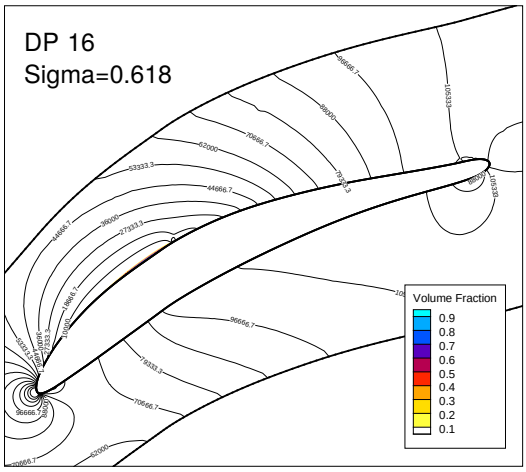

(b) DP 16

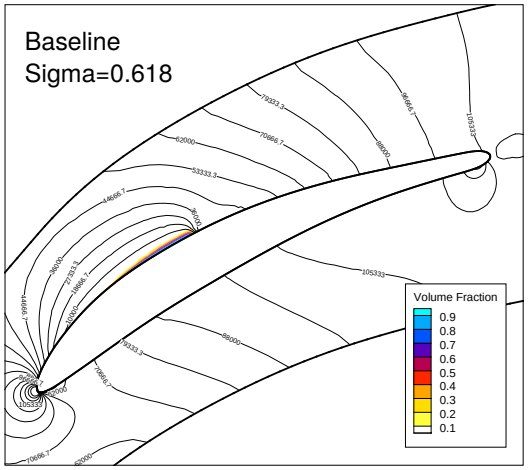

(c) Baseline

Figure 6.8: Pressure and volume fraction contours for *shock focused* cases DP 12 and DP 16 at $\sigma = 0.616$ (DP 12) and $\sigma = 0.618$ (DP 16 and Baseline).

more strongly slowed down around the design condition (i.e. shock at $x/chord = 0.4$). The reason is the streamwise length of the trough where the shock amplitude is pushed down.

Overall, referring back to the targets listed in Table 6.2, the results obtained from the steady state analysis detailed here confirm the qualitative success of the design strategies. The majority of the differences in features between designs produced by the *In-house* design solver are mirrored by the Fluent solution:

- flat, steep and wavy suction side pressure distributions for aft-loaded, fore-loaded and *shock focused* design cases respectively,
- low amplitude shocks for aft-loaded, high amplitude for fore-loaded cases,

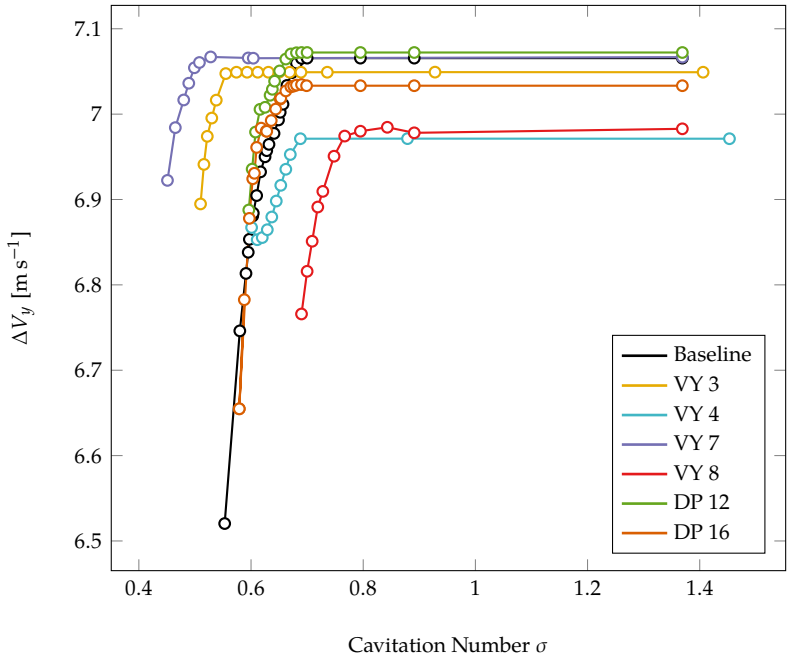

Figure 6.9: ΔV_y breakdown for all *tip to tail* and *shock focused* cases.

- enlarged, reduced and maintained suction ranges for aft-loaded, fore-loaded and *shock focused* cases respectively.

Discrepancies between solver solutions appear in the rendering of the closure shock and the cavity shape. Indeed, the consistent shock overshoot means that smoothing effects are not as evident as with the *In-house* solver. Nevertheless, it has been shown that the desired effects on shock amplitude are recovered albeit without the low gradient pressure rise. In terms of cavity shape, the disagreement relates to the pitchwise width of the vapour region for aft-loaded cases which appear thin with the ZGB solver versus thick with the TE solver. The discrepancy is, however, mitigated by the fact that the TE vapour volume fractions are negligible further from the surface and high values are contained within the same narrow and long region.

6.2 Time Resolved Simulations

The role of the post-design steady state CFD analysis was to confirm the success of the selected design cases in non-inviscid conditions. Assessment of the hydrodynamic and suction performance was carried out but no evaluation was provided on the erosive risk which constitutes the primary target of the research.

The erosive phenomena are inherently dynamic because i/ sheet cavities are sensitive to transient features occurring in the boundary layer and are never frozen in space as portrayed

by steady state solutions, ii/ the erosion mechanisms are connected to bubble collapse rates with respect to time. To numerically evaluate the erosive performance of the selected blades time accurate data is necessary. Unsteady simulations are, therefore, run for all six designs and the Baseline geometry at a variety of flow conditions.

The data of interest is similar to the information acquired from steady state i.e. pressure distribution, volume fraction distribution and breakdown performance. However, it carries additional dynamic data such as rate of change and variance. The complete set of unsteady output provides the means to quantify the erosive intensity and identify the risk zones. To achieve this, numerical methods developed to predict cavitation erosion using the current understanding of bubble/cluster collapse mechanisms are used. These tools are limited by the underlying assumptions, the resolution of the solution and the accuracy of the models. Nevertheless they provide crucial evaluation metrics which will be compared to experimental findings.

6.2.1 Unsteady Setup

ANSYS Fluent is chosen because, as for steady state calculations, it allows pure 2D setups and provides extensive control over simulation parameters. The solver is pressure-based with pressure and velocity calculated simultaneously (coupled rather than segregated algorithm) for robustness and efficiency. The Zwart-Gerber-Belamri model is maintained for evaluating the source and sink terms, as well as the QUICK scheme for face values. Time integration is achieved through a second order implicit scheme.

In terms of turbulence, the URANS approach is selected over DES, LES or DNS mainly for feasibility reasons. For cavitating flows, the $k-\omega$ SST model is often recommended as a reliable technique. It is notably commended for its treatment of adverse pressure gradients and separated flows, which are both features of the cavitation closure region. All modelling choices are summarised in Table 6.4.

At the inlet, the velocity magnitude and direction are fixed at $\|V\| = 14.48\,\mathrm{m\,s^{-1}}$ and $\gamma = 46.321°$. The outlet boundary condition is static pressure which is adjusted according to the cavitation number to analyse (see Table 6.5). For the turbulence equations, the turbulent intensity and turbulent viscosity ratio are set at the inlet with values $I = 5\,\%$ and $\mu_t/\mu = 10$. The flow is assumed isothermal so no other characteristic relations need a boundary definition.

Inlet and outlet boundaries are respectively placed at $1 \times chord$ and $4 \times chord$ from the leading edge. The angles of the inflow and outflow regions are equal to the camber line angles at the leading and trailing edges. The mesh is unstructured and highly quadrilateral dominant

(one single tetrahedral cell at the bottom acute angle of the inlet boundary). Maximum edge length is 2×10^{-3} m. To attain the desired accuracy, the viscous sub-layer is resolved, such that $y^+ \leq 1$ (or $y \approx 1 \times 10^{-6}$ m for the present flow conditions and geometry) with 75 cells in the boundary layer. The total cell count exceeds 100 000.

Table 6.4: Numerical configuration for unsteady cavitating simulations.

Computational modules	Selected models and details		
Solver schemes	Time discretisation	Second order implicit	$CFL = 0.3$, $\Delta t = 5 \times 10^{-5}$ s
	Navier-Stokes discretisation	Pressure based	Coupled momentum and continuity equations, QUICK face interpolation
Spatial Discretisation	Unstructured Quad-dominant	Max edge length $= 2 \times 10^{-3}$ m	75 nodes in the boundary layer
Cavitation	Homogeneous mixture	Transport Equation	Zwart-Gerber-Belamri in default configuration, $p_v = 2339.2$ Pa
Turbulence	RANS	$k - \omega$ SST	Resolved boundary layer, $y^+ \leq 1$

The time step is $\Delta t = 5 \times 10^{-5}$ s for a Courant number at $CFL \approx 0.3$. All calculations are run for a minimal physical duration of 0.5 s or until the monitored quantities are either stable or fluctuate at a consistent frequency. The quantities observed during calculation are:

- inlet total pressure,
- outlet total pressure,
- V_y velocity component at outlet,
- global vapour volume,
- volume averaged turbulence intensity.

Each give an indication of the case's unsteadiness level and of the stability of the computation. Quantities evaluated at the boundary surfaces i.e. inlet/outlet total pressures and outlet V_y, are mass flow averaged. The two other monitored values, total vapour volume and turbulence intensity, concern the entire domain. For the former, the vapour fraction is volume integrated to give the total vapour volume, while turbulence intensity is volume averaged over the entire solution. The surface values provide information on output and losses through ΔV_y, lift and drag. Fluctuations found in those distributions can be caused by either changes in cavity

size or turbulent instabilities. Monitoring the total vapour volume history therefore serves to determine which of the two is causing the fluctuations.

The outlet pressure conditions listed in Table 6.5 are applied progressively. The solution and boundary values of the steady state computation in non-cavitating conditions (taking the highest possible σ) are used as initial conditions. The next value for the outlet pressure is determined by observing cavity size, performance losses and unsteadiness. The corresponding cavitation number σ for each of the values in Table 6.5 is evaluated once the calculation is complete using the solution data at the inlet.

Table 6.5: Outlet pressure values for all time resolved runs for all design cases.

Design Case	Outlet Pressure Values [kPa]	Design Case	Outlet Pressure Values [kPa]
Baseline	140, 120, 112, 110, 109, 108, 107, 106, 105, 104, 100, 95	VY 8	140, 130, 126, 124, 122, 120, 110, 100, 95
VY 3	110, 105, 102, 101, 100, 99, 98, 96, 95, 92.5	DP 12	118, 114, 111, 110, 109, 108, 107, 106
VY 4	115, 109, 108, 107, 106, 105, 104, 102, 100	DP 16	118, 116, 114, 110, 108, 106
VY 7	110, 100, 96, 95, 94, 93, 92, 91, 90		

6.2.2 Transient Results

Non Cavitating Conditions ($\sigma \geq 0.8$)

All seven geometries are run at the highest outlet pressures (see Table 6.5). At these conditions, the minimal pressure is well above vapour pressure $p_v = 2339.2\,\text{Pa}$ such that the total vapour volume is negligible.

Figure 6.10 presents the total pressure and V_y histories at inlet and outlet or just at the outlet for V_y. The stabilisation phase lasts no more than 0.1 s. All geometries produce a stable flow field except for VY 7. Indeed, the trailing edge curvature (see Figure 6.11) leads to flow separation which in turn produces vortex shedding. Spectral analysis applied to either the

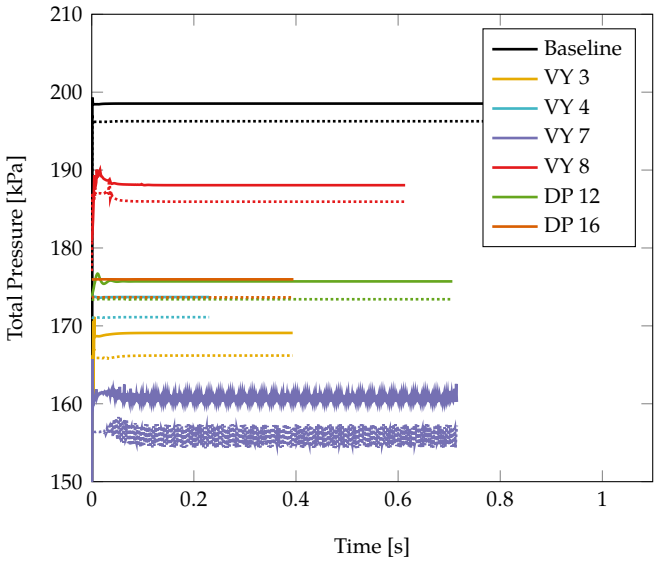

(a) Total Pressure

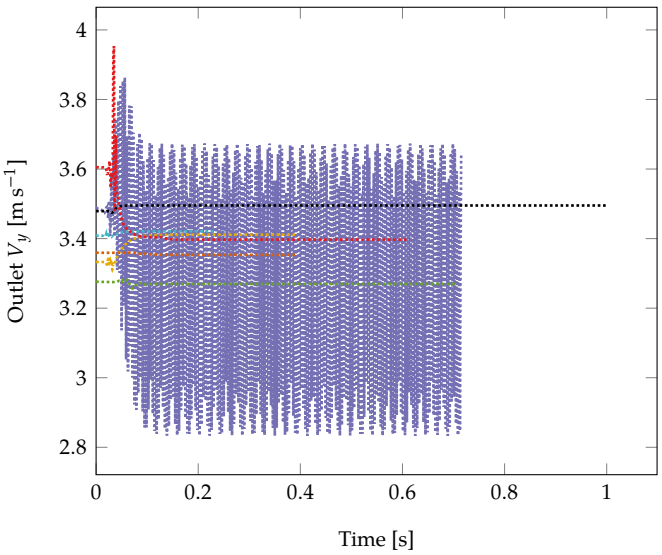

(b) Outlet V_y

Figure 6.10: Boundary monitoring points in non-cavitating conditions.

total pressure or V_y histories informs us on the frequency of the phenomenon. The main peak is located at $f_s = 250\,\text{Hz}$, which corresponds to a Strouhal number $Sr = f_s L/V_\infty = 2.5$. Considering our flow's Reynolds number at $Re \approx 2.5 \times 10^6$, the frequency is greater than what is expected for a cylindrical body in similar conditions ($0.2 \leq Sr \leq 0.5$ at $Re \approx 2.5 \times 10^6$). In terms of cascade performance, the presence of vortex shedding means increased losses, vibration and noise. Comparison of the time averaged lift and drag coefficients indeed confirm the downgrade in output (see Figure 6.16). The main conclusion from the unsteady analysis

of VY 7 in non-cavitating conditions is that its aft-loaded V_y distribution is too extreme to constitute a viable design choice.

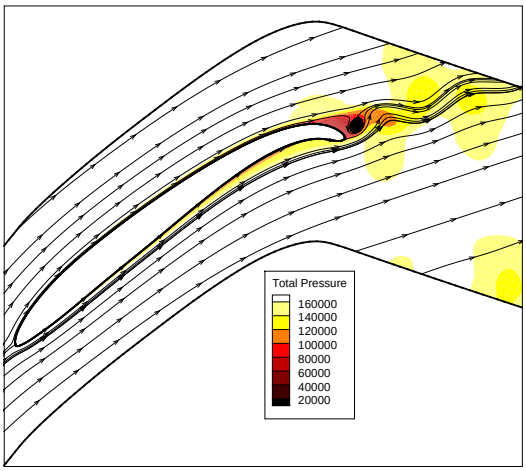

(a) Time $t = 0.1$ s

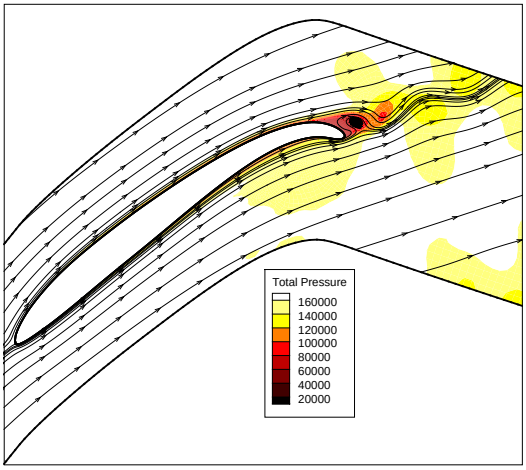

(b) Time $t = 0.11$ s

Figure 6.11: VY 7 trailing separation and vortex shedding in non-cavitating conditions.

All other designs produce satisfactory stable results. The range of values is due to the differences in the outlet static pressure condition (see Table 6.5). The numbers for $\Delta p_0 = p_0^{IN} - p_0^{OUT}$ and $\Delta V_y = V_y^{IN} - V_y^{OUT}$ are listed in Table 6.6. It is worth noting that ΔV_y is consistent for all designs with a relative difference to Baseline that does not exceed +3% (DP 12). The discrepancy is higher than the ±2% margin imposed during design but comes as an expected effect of the modelling differences i.e. steady vs transient, standard $k-\varepsilon$ vs $k-\omega$ SST. Taking these into consideration, the offset is well within an acceptable range.

In terms of total pressure loss Δp_0, the variability is far higher (see Table 6.6). The only designs that produce a value similar to Baseline are DP 12 and DP 16 constructed using a

loading profile that targets the shock location only. Design VY 4 is also focused on the closure shock but the amplitude and spread of its geometrical modifications are greater. The numbers in Table 6.6 indicate a correlation between loading configuration and loss: stronger aft-loading means higher losses, stronger fore-loading means lower losses. This is illustrated by looking at the three *tip to tail* cases VY 3, VY 7 and VY 8. Indeed, VY 8 improves on the Baseline with a 150 Pa (-7%) reduction in losses. It is characterised by high pressure gradients in the leading edge region where the boundary layer is thin and laminar. For the aft-loaded designs VY 3 and VY 7, turning occurs in the trailing edge region beyond the transition to turbulence and contributes to either expanding the boundary layer or to producing flow separation.

Total pressure loss is a measure of the friction force resisting against the flow such that a higher value incurs a drop in cascade efficiency. From V_y and Δp_0, the cascade efficiency can be evaluated through

$$\eta_C = 1 - \frac{\Delta p_0}{\frac{1}{2}\rho\left(V_y^{IN\,2} - V_y^{OUT\,2}\right)} \tag{6.1}$$

Values were calculated for each case and are given in Table 6.6. VY 8 has the lowest loss and so the highest efficiency. However, it has been shown that its suction performance is the poorest (see Figure 6.9). The opposite can be said of VY 3 and VY 7 which show high suction performance for low efficiency. These observations lead to a significant conclusion: a trade-off exists between cascade efficiency and suction performance.

Table 6.6: Cascade hydrodynamic performance in non-cavitating conditions.

Design Case	Δp_0 [Pa] (Rel. Diff. to Baseline)	ΔV_y [m s^{-1}] (Rel. Diff. to Baseline)	Cascade efficiency η_C
Baseline	2267.6	6.9932	0.9534
VY 3	2905 (+28%)	7.0609 (+1%)	0.9406
VY 4	2580.5 (+14%)	7.0511 (+1%)	0.9472
VY 7	3030 (+34%)	7.211 (+3%)	0.9383
VY 8	2117.4 (-7%)	7.075 (+1%)	0.9567
DP 12	2292 (+1%)	7.2026 (+3%)	0.9535
DP 16	2314 (+2%)	7.1189 (+2%)	0.9528

Cavitating Conditons ($\sigma < 0.8$)

As cavitation appears, an evolution in the fluctuation of the monitored variables occurs. The flow is stable at first (except for VY 7) but start to oscillate as the cavity increases in size. As an example, the total vapour volume histories at different cavitation numbers are shown in Figure 6.12 for the Baseline and VY 3 cases. There is a clear growth in he fluctuation amplitudes with the mean cavity size and a gradual departure from the perfectly sinusoidal character of the fluctuations.

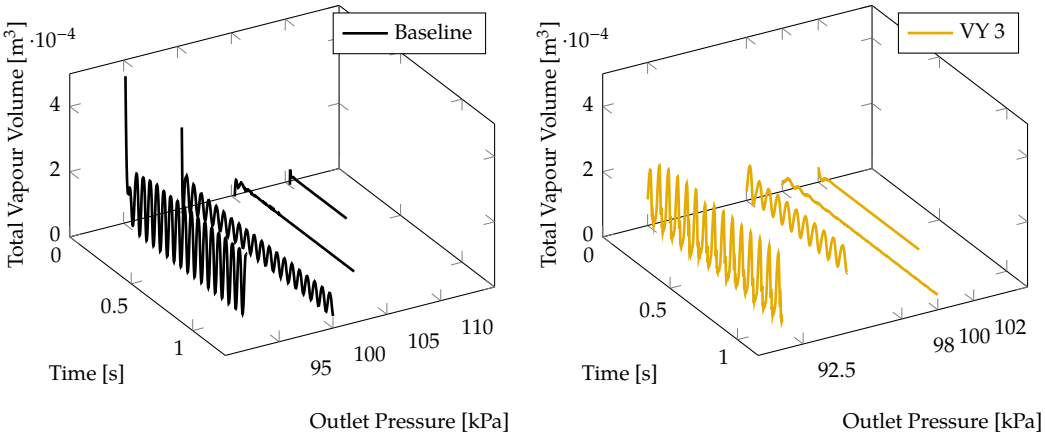

(a) Baseline **(b)** VY 3

Figure 6.12: Time history for total vapour volume at different outlet conditions.

The amplitude and frequency are dependent on the geometry and flow conditions. As an example, the time histories for total pressure, outlet V_y, vapour volume and turbulent intensity are presented in Figure 6.13 for the three cases Baseline, VY 3 and DP 16 in cavitating conditions at outlet static pressures $p_{out} = 100$ kPa, $p_{out} = 98$ kPa and $p_{out} = 106$ kPa respectively. Cyclical oscillations are consistently observed. For the inlet total pressure, total vapour volume and turbulent intensity, the distributions are sinusoidal. Perturbations are visible at the outlet monitoring points, i.e. V_y and total pressure, which are affected by the downstream transport of vorticity.

The first step in the transient data post-processing consists in carrying out a power spectral density analysis on the vapour volume history. The aim is to measure the cyclical behaviour of the cavitating flow by identifying the peak frequency f_C and the duration of a single cycle $T_C = f_C^{-1}$. Monitored values and performance metrics such as total pressure difference, ΔV_y, lift and drag are then time averaged over a finite number of cycles. As shown in Figure 6.12 the dynamic behaviour varies according to the flow condition meaning that the spectral analysis

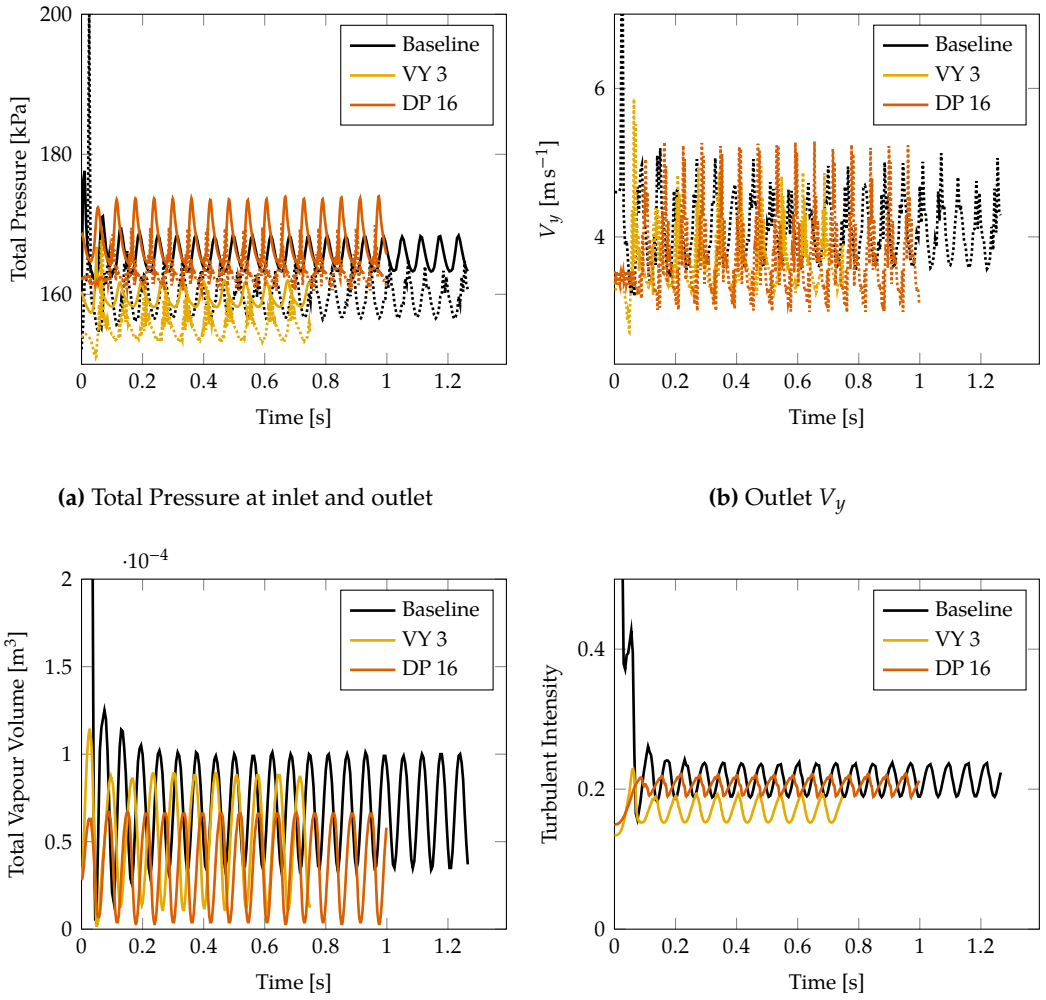

(a) Total Pressure at inlet and outlet

(b) Outlet V_y

(c) Vapour Volume

(d) Turbulent Intensity

Figure 6.13: Time histories of monitored data for cases Baseline, VY 3 and DP 16 at respectively 100, 98 and 106 kPa for outlet pressure.

needs to be carried out for all runs independently, as well as the averaging step which uses the solution specific frequency. Figure 6.14 presents the frequencies f_C resulting from the spectral analysis. An interesting observation is the dual grouping of the measured frequencies. Here, they are categorised as: high frequency ($f_C > 100\,\text{Hz}$) and low frequency ($10\,\text{Hz} < f_C < 30\,\text{Hz}$) unsteadiness. For the first type of unsteadiness, the variations, located either at cavity closure or at the trailing edge for VY 7, correspond to small scale vortical structures at separation points. The second type of frequencies corresponds to large variations in the size of the sheet cavity. These arise when the re-entrant jet is sufficiently strong to affect the location of the closure region.

Time averaged flow quantities are computed using the measured cavitation cycle frequencies and durations. Calculating the inlet pressure serves to associate the outlet static pressures

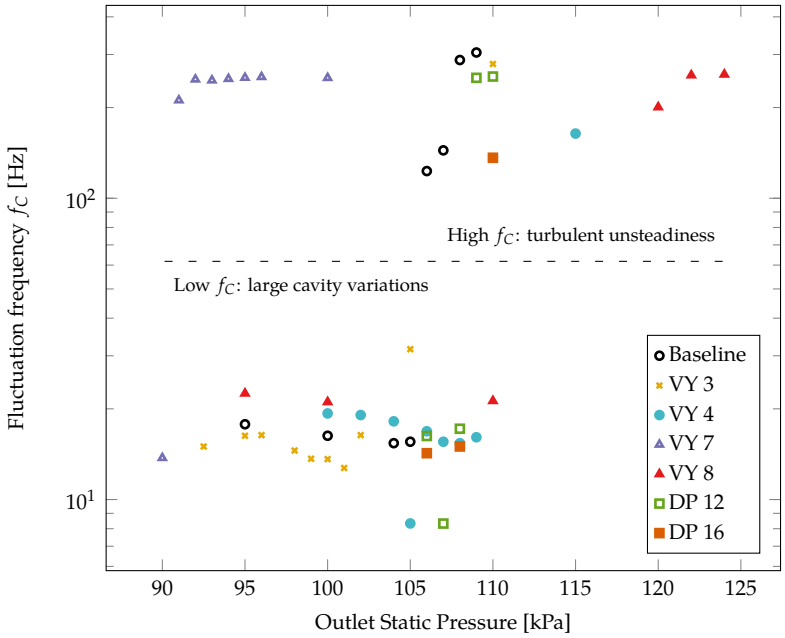

Figure 6.14: Peak frequencies from the spectral analysis carried out on the time accurate cavitating solutions for each geometry. The non-cavitating configurations are left out of the analysis. Two frequency groups are identified: high f_C where cavity variations are small, and low f_C where cavity movement is more pronounced.

listed in Table 6.5 with a cavitation number σ using the definition $\sigma = (p_\infty - p_v)/0.5\rho V_\infty^2$. Figure 6.15 shows the resulting numbers and is used to correlate the appropriate cavitation number for each run. At high outlet pressures (non-cavitating), the losses incurred between inflow and outflow are generally equivalent from blade to blade. This is picked up by the time averaged inlet pressure as case specific curves are similar for high σ (see Figure 6.15). Marginal differences are present with fore-loaded case VY 8 generating the least and aft-loaded case VY 7 the most losses (see Table 6.6). These discrepancies translate to differences in the height of the curves: VY 7 sits above VY 8 (higher pressure difference between inlet and outlet). The increase in losses caused by the onset of cavitation shows up in the change of angle of the curves in Figure 6.15. This equates to a drop in efficiency and constitutes the first indication of performance breakdown brought about by cavitation.

The advantage of unsteady over steady solutions is that they provide information on the variability of each value, which is of particular importance for assessing erosion aggressiveness. Indeed, it is understood that material damage mechanisms are related to the number and rate of bubble collapses [9]. For sheet cavitation, the collapse of vapour bubbles corresponds to reductions in the cavity size: the larger the variations, the larger the number of such events. For the present data set, spread is measured using quartiles rather than standard deviation because the data is not necessarily normally distributed. Quartiles therefore constitute a more

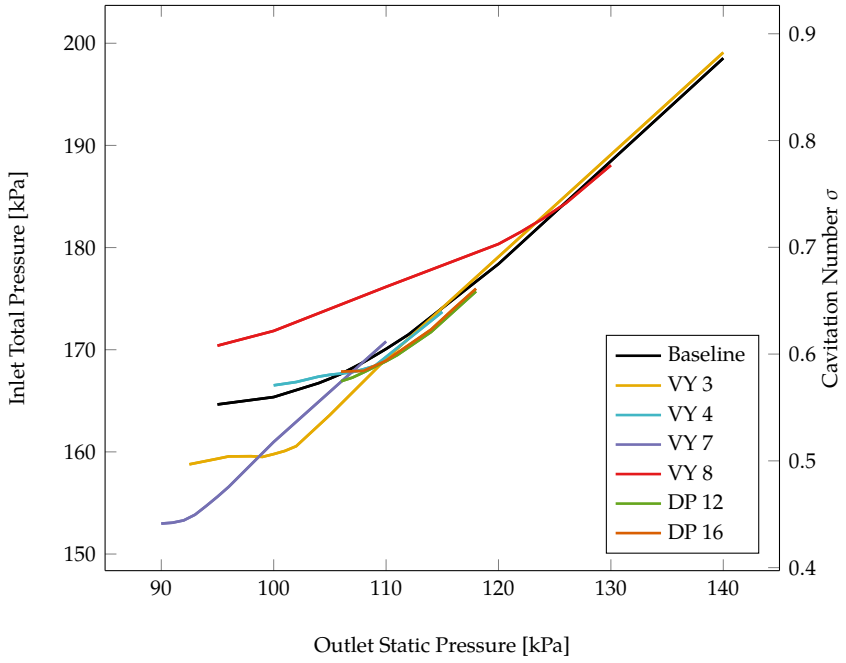

Figure 6.15: Time cycle averaged inlet total pressure (left y-axis) and cavitation number (right y-axis).

reliable statistical quantity. Cascade performance is evaluated using the same metrics as for the steady state analysis i.e. ΔV_y, C_L and C_D. All are calculated from the raw time-dependent data using the computed cycle durations $T_C = f_C^{-1}$ to average over a finite number of cycles. The results are presented in Figure 6.16. The breakdown profiles for the time averaged quantities match the steady state data in terms of drop initiation position, and confirm the superiority of aft-loaded blades for suction performance. Two distinctive features captured by the steady state analysis are recovered: the gain in ΔV_y output at cavitation inception for VY 7, and the stepped decrease for shock smoothing designs VY 4, DP 12 and DP 16. These effects are, however, significantly attenuated by the time averaging procedure.

The top and bottom limits of the spread correspond to the first and fifth quartiles, which cover a range that contains 90% of the time resolved data. It yields a new criterion to assess cavitation performance in terms of variability, which can correlate to erosion aggressiveness. The spread data in Figures 6.16 and 6.17 therefore gives insight into the erosive potential of each blade. Figure 6.17 is particularly informative because it singles out the growth and unsteadiness of the cavity.

The first observation is that the upper and lower bounds of the spread do not immediately deviate from the mean distribution at the cavitation inception point. There seem to be two dynamic regimes:

- a stable sheet cavity which occurs from the inception σ to the transition point, noted as

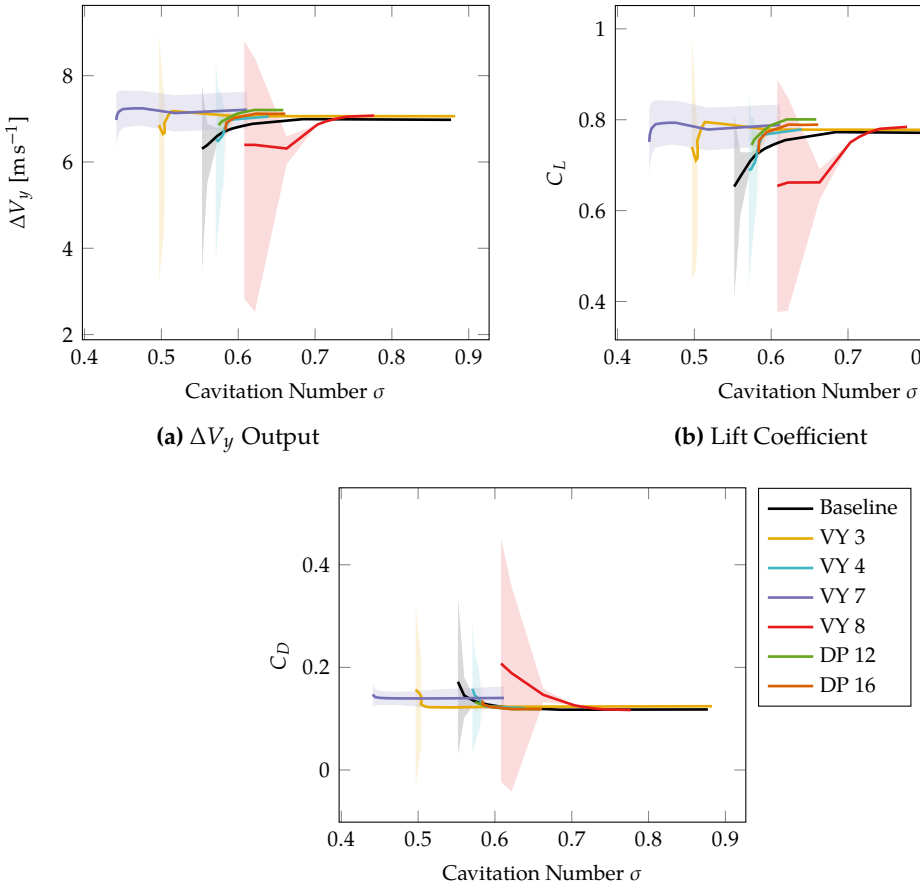

(a) ΔV_y Output

(b) Lift Coefficient

(c) Drag Coefficient

Figure 6.16: Unsteady aerodynamic performance. Curves are time cycle averaged quantities and coloured regions represent the interquartile range (contains 95% of data).

σ_T,

- followed by cyclical growth and collapse along the suction surface for $\sigma < \sigma_T$.

This distinction correlates to the two frequency groups at $f_C > 100\,\text{Hz}$ and $10\,\text{Hz} < f_C < 30\,\text{Hz}$ (see Figure 6.14). The transition condition σ_T varies from blade to blade. The volume of vapour is not a determining factor as fluctuations start at different heights in Figure 6.17. It does however provide a lower bound at $V_\alpha > 3.5 \times 10^{-5}\,\text{m}^3$ below which stability is consistently observed. This also concurs with the observation made from the vapour volume history distributions (see Figure 6.12). In Figure 6.18, the two cavitation states are illustrated by capturing the volume fraction contours for the Baseline case at two time points separated by $\Delta = 0.02\,\text{s}$ at $\sigma = 0.577$ (stable regime) and $\sigma = 0.552$ (fluctuating regime). For the former (Figure 6.18a), the variations are small and focused in the closure region where part of the cavity detaches due to separation and collapses immediately after. In the second case (Figure 6.18b), substantial shrinking from $t = 0.8\,\text{s}$ to $t = 0.82\,\text{s}$ is picked up. The size changes by a

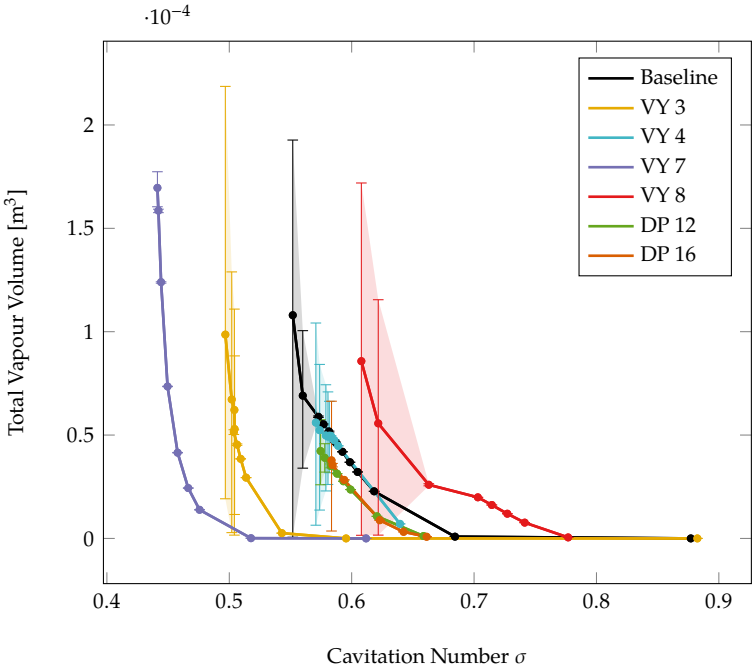

Figure 6.17: Unsteady vapour volume growth. Curves are time cycle averaged quantities and coloured regions represent the interquartile range (contains 95% of data).

factor of approximately 4. The snapshot at $t = 0.8\,\text{s}$ corresponds to the maximum cavity size; at, $t = 0.82\,\text{s}$, the vapour sheet has already passed its minimal size and is back in its growth phase. At its lowest, the total vapour volume can reach close to $0\,\text{m}^3$, at which point the closure and surface inception point coincide.

The widest spread is recorded for VY 8 (see Figures 6.16 and 6.17) with a higher amplitude between first and fifth quartiles and variations initiated for a smaller cavity size. Aft-loaded designs VY 3 and VY 7 are able to sustain the stable regime for larger cavity sheets. VY 7 is, however, a special case: the stability of the vapour volume is outstanding, but the hydrodynamic performance metrics (Figure 6.16) show constant amplitude unsteadiness regardless of the presence of cavitation. The phenomenon at the origin of the unsteadiness is the vortices shed from the separation point (see Figure 6.11). It is, however, interesting to note that, because of its downstream position, the separation has no effect on the stability of the sheet cavity. For the shock smoothing cases VY 4, DP 12 and DP 16, there is no clear consistency in spread. The data suggests an earlier onset of unsteadiness for all three cases when compared to Baseline. This does not bode well for the hypothesised erosion aggressiveness improvement but has to be weighed against the effectiveness of data spread as an erosion risk predictor.

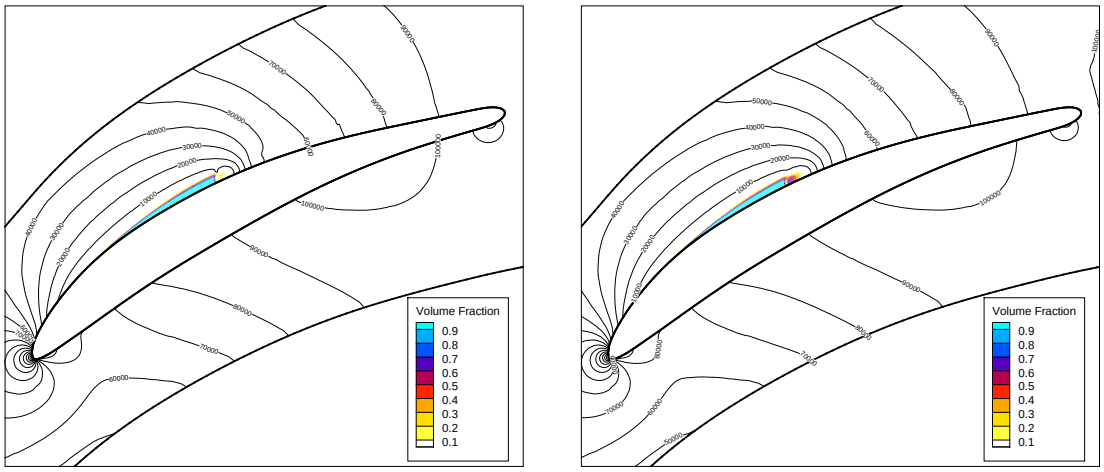

(a) $\sigma = 0.577$ at $t = 0.3\,\text{s}$ (left) and $t = 0.32\,\text{s}$ (right)

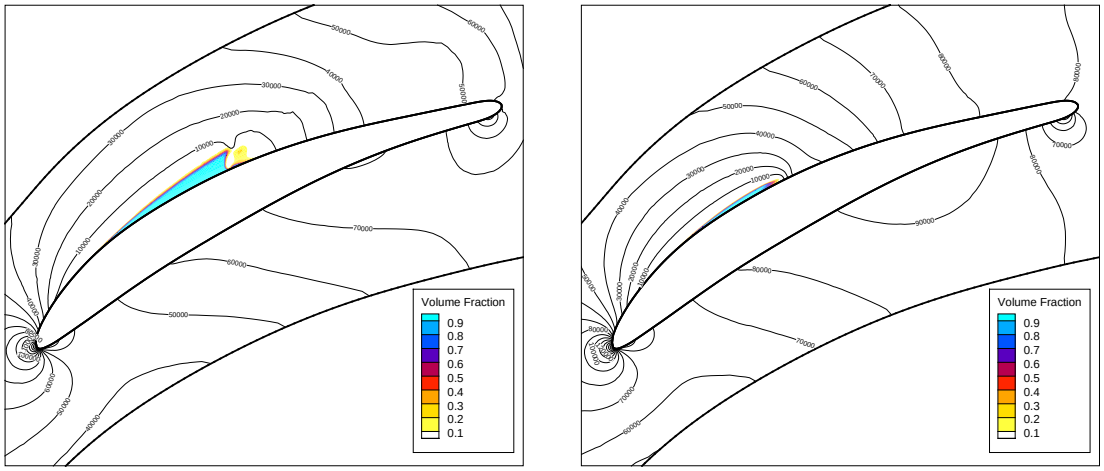

(b) $\sigma = 0.552$ at $t = 0.8\,\text{s}$ (left) and $t = 0.82\,\text{s}$ (right)

Figure 6.18: Volume fraction contour snapshots for the Baseline case at cavitation numbers $\sigma = 0.577$ and $\sigma = 0.552$. The left and right maps are separated by $\Delta t = 0.02\,\text{s}$.

6.3 Erosion Prediction

Techniques have been developed to evaluate the intensity of cavitation erosion from numerical time accurate results. Their derivation is based on the collapse mechanisms that cause material damage: pressure wave propagation and impinging micro-jet (see Section 2.2.2). In this study, four approaches are taken into consideration:

- Li et al. [35] who use the potential energy of the cavity structure to predict the intensity of the pressure wave:

$$I_{agr}^{Li} = \frac{1}{T}\int_0^T I\,dt \qquad \text{with} \qquad I = \begin{cases} \frac{\partial p}{\partial t} & \text{if } \frac{\partial p}{\partial t} \geq \delta \\ 0 & \text{if } \frac{\partial p}{\partial t} < \delta \end{cases} \tag{6.2}$$

- Mouvanal et al. [64]'s detector for critical bubble collapse:

$$I_{agr}^{Mouv} = \frac{1}{T}\int_0^T I dt \qquad \text{with} \qquad I = \begin{cases} p & \text{if conditions are met} \\ 0 & \text{otherwise} \end{cases} \tag{6.3}$$

- Peters et al. [51] who consider that erosion is caused by the micro-jet velocity at bubble collapse:

$$v_{jet} = 8.97\gamma^2\sqrt{\frac{p - p_v}{\rho}} \tag{6.4}$$

- Nohmi et al. [62]'s techniques which combine the pressure and volume fraction and their time derivatives in:

$$\begin{aligned} &\frac{1}{T}\int_0^T \alpha \max\left(\frac{\partial p}{\partial t}, 0\right) \\ &\frac{1}{T}\int_0^T \alpha \max\left(p_\infty - p_v, 0\right) \\ &\frac{1}{T}\int_0^T p_\infty \max\left(\left|\frac{\partial \alpha}{\partial t}\right|, 0\right) \\ &\frac{1}{T}\int_0^T \max\left(\left|\frac{\partial \alpha}{\partial t}\right|, 0\right) \end{aligned} \tag{6.5}$$

The four listed metrics are evaluated using the time accurate pressure, volume fraction and mass transfer rates provided by the computation. Following the technique laid out in [62], the transient values are taken at the blade surface. The calculation is carried out by running ad-hoc routines at the post-processing stage. The algorithm interprets the recipes provided by the authors (see [35, 62, 51, 64]) and accrues the recorded erosive events over the effective duration of the simulation (eliminating the initial ramping up). The results are normalised over time to get the geometry dependent erosion rate distribution.

Given the variety of behaviours, comparing the geometries for a single cavitation number does not make sense: the cavity may be large for some (e.g. VY 8) and absent for others (e.g. VY 7). To have a solid basis for comparing erosion performance, it is the breakdown in ΔV_y output that is considered. In the same way that $NPSH_{3\%}$ is a key number in pumping systems (see Section 1.1), the $\sigma_{3\%}$ point is selected here. It corresponds to the condition at which the ΔV_y output has dropped by 3%. In Figure 6.19, the data presented in Figure 6.16a is normalised by the respective ΔV_y^{nocav} in non cavitating conditions for each case. The σ values which deliver the data point closest to the $\Delta\tilde{V}_y = \Delta V_y/\Delta V_y^{nocav} = 0.97$ are listed in Table 6.7.

In Figure 6.20, the pressure and volume fraction distributions on the blade surfaces are

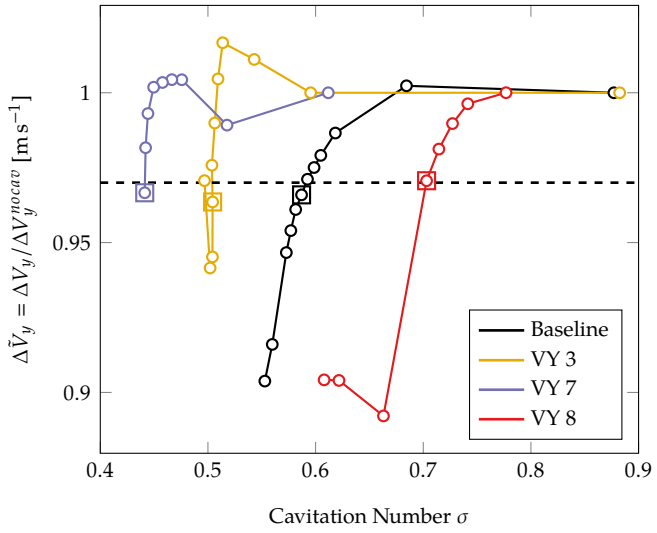

(a) *Tip to tail* designs

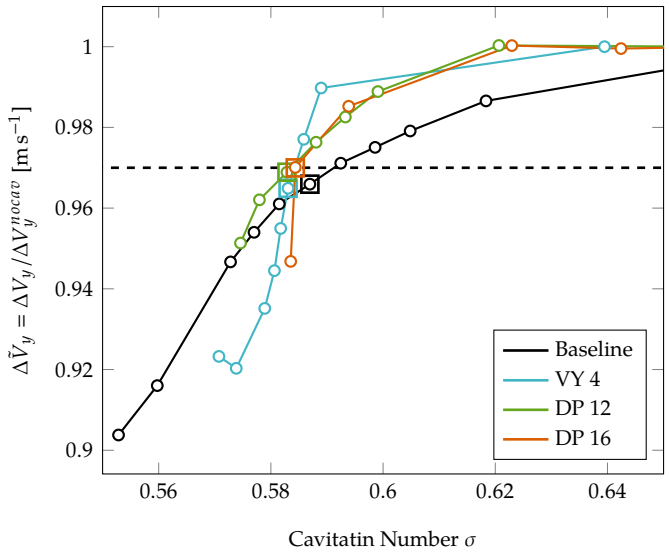

(b) *Shock focused* designs

Figure 6.19: Normalised ΔV_y breakdown. The dashed line corresponds to the 3% drop in output.

Table 6.7: Cavitation numbers for existing solutions closest and superior to the 3% drop.

Design Case	$\sigma_{3\%}$	Design Case	$\sigma_{3\%}$
Baseline	0.587		
VY 3	0.504	VY 8	0.703
VY 4	0.583	DP 12	0.583
VY 7	0.441	DP 16	0.584

plotted at $\sigma_{3\%}$. Both the time averaged values and spread (95% quartile range) are presented. The variability data informs us on the movement of the distributions. A first observation is that

the aft-loaded cases VY 3 and VY 7 are less stable than the other geometries both in terms of pressure and volume fraction (see Figures 6.20a and 6.20c). For both cases, the cavity extends beyond the mid-chord point and is characterised by strong variations in size (see Figure 6.17). Geometry VY 8 is the opposite. At $\sigma_{3\%}$, the cavity is thicker than for VY 3 and VY 7 but shorter and more stable. This illustrates the trade-off relation between suction performance and breakdown stability: small σ range means a static cavity even at the $\sigma_{3\%}$, large σ range produces an unstable cavity even before the 3% breakdown point.

Shock focused case VY 4 also shows a large range in pressure and volume fraction. The fluctuation is much more pronounced than for Baseline, DP 12 and DP 16. The implication is that the high magnitude of the wavy suction surface distribution for VY 4 negatively affects the stability of the cavity. This constitutes a significant advantage for the Δp strategy for shock smoothing: the disturbances on the surface pressure distribution are minimal which prevents the onset of adverse unsteadiness. For the Baseline and *shock focused* cases, the time averaged closure is located at $x/chord = 0.4$. This matches the design condition for VY 4 but not for DP 12 and DP 16 ($x/chord = 0.3$). Here, it was decided to favour the $\sigma_{3\%}$ based comparison so that all blades are on an equal footing in terms of performance. For a full picture, erosion assessment over the entire range would be necessary.

The results of the erosion prediction techniques are presented in Figures 6.21, 6.22 and 6.23 for respectively the Li et al., Mouvanal et al., Peters et al. methods and 6.24 to 6.27 for the four Nohmi et al. expressions. *Tip to tail* and *shock focused* designs are plotted separately to enable focus on the closure region for the latter group. The different approaches mean that the order of magnitude of the computed values are incomparable. Note that for the *Li et al.* criterion, the authors recommend selecting a threshold value representing material resistance. In our case, only the pressure time derivatives larger than $\partial p/\partial t > 10^6$ are recorded.

For the Baseline case, all indicators suggest it yields comparatively high erosion intensity both in terms of amplitude and impacted area. This comes from the combination of significant unsteadiness and large pressure gap $p - p_v$ around cavity closure. The techniques that rely on the time derivatives of α or p i.e. Li et al. (Figure 6.21), and Nohmi et al.'s first, third and fourth indicators (Figures 6.24, 6.26, 6.27) all place the Baseline as the first or second, behind VY 7, most aggressive case. This suggests that most designs reach the target: reducing the erosive aggressiveness of cavitation.

VY 7 is the worst performer. Two highly erosive zones are consistently picked up: at the closure of the suction side cavity around $x/chord = 0.7$ and at the closure of the pressure side cavity at $x/chord = 0.2$. Although the strong aft-loading produces a reduced shock, the

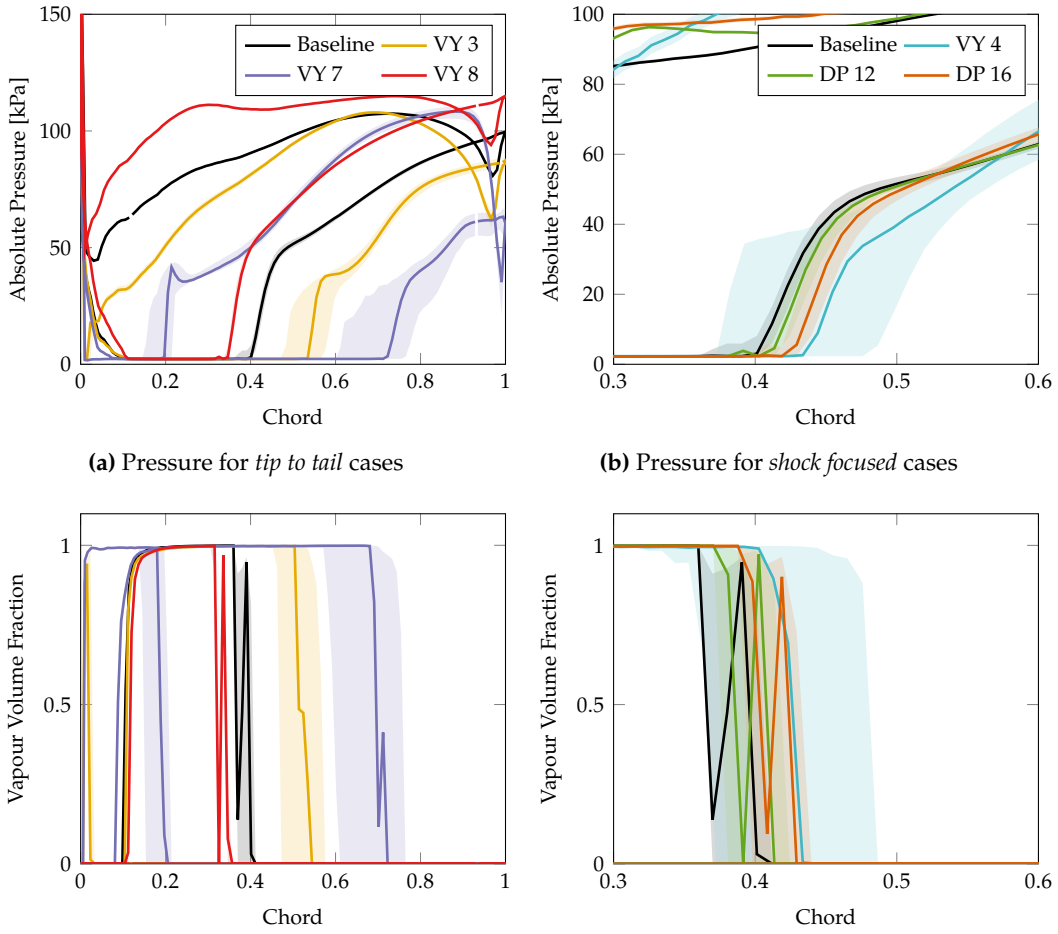

(a) Pressure for *tip to tail* cases

(b) Pressure for *shock focused* cases

(c) Volume fraction for *tip to tail* cases

(d) Volume fraction for *shock focused* cases

Figure 6.20: Unsteady surface pressure and volume fraction at the respective $\sigma_{3\%}$ conditions for each geometry (see Table 6.7). The spread contains 95% of the unsteady data.

weakness of this extreme strategy – on top of the poor hydrodynamic performance – is that cavitation will abruptly transition from stable to violent as soon as a critical point is passed. If one were to run the same analysis at $\sigma_{1\%}$ instead of $\sigma_{3\%}$, VY 7 is likely to cause significantly less damage, as inferred by the data in Figure 6.17. VY 3, the other aft-loaded case, shows a similar two-zone pattern. This time, the upstream pressure side closure is negligible compared to the downstream suction side closure one. Thanks to reduced instability, the erosive potential is below that of VY 7 and Baseline according to all indicators except for Peters et al.'s and Nohmi et al.'s second. The latter two are based on the non-differentiated pressure value and yield higher values because of VY 3's large shock amplitude (see Figure 6.20a).

Geometry VY 8, fore-loaded, is an interesting case because of the strong disagreement in erosion predictions. On one hand, the Li et al., and Nohmi et al.'s first, third and fourth formulations predict low aggressiveness compared to the other cases. On the other, the

Mouvanal et al., Peters et al. and Nohmi et al.'s second techniques portray VY 8 as one of the most erosive configurations. The first group of models are all constructed using time derivative terms. VY 8 being completely stable at $\sigma_{3\%}$ (see Figure 6.20), the resulting aggressiveness is small. The second group of models take the instantaneous pressure instead of its derivative. The high amplitude shock specific to VY 8, therefore, gives rise to amplified erosion metrics. The characteristics of the cavity for case VY 8 at $\sigma_{3\%}$ are thick tangential breadth, short streamwise length, no detachment or shedding and low unsteadiness. Li et al. [35] and Nohmi et al. [62] develop their approach for a single stationary hydrofoil with cavities that are highly mobile and prone to detachment. A fundamental notion for these models is that erosion is caused by the collapse of large cavity structures shed from the surface. As such, the Li et al. and Nohmi et al. (formulations 1,3 and 4) may not be suited to measure the aggressiveness of stable attached cavities where the erosive action is focused in a narrow region.

For the *shock focused* cases, the erosion evaluations are consistent across prediction techniques. There is a clear loser: VY 4, and a clear winner: DP 12. The issue with the former is the length of the affected region rather than the intensity of the damage. This is due to the unsteadiness of the cavity which sweeps across a larger portion of the suction surface as shown in Figure 6.20. For VY 4, the aggressiveness computed by the time derivative techniques is more intense when compared against the other cases than the aggressiveness coming from non differentiated approaches.

The fact that the closure location at $\sigma_{3\%}$ does not match the design location for DP 12 and DP 16 does not appear to be detrimental to their performance. On the contrary, both cases present significant reductions in erosion aggressiveness over the Baseline. Design DP 12 presents by far the largest improvement of all cases: its at-risk region is constituted of small slivers in the vicinity of $x/chord = 0.4$ at intensities that are significantly smaller than Baseline. This assessment is confirmed by all of the adopted prediction techniques with minor differences in relative peak values. This suggests that the wavy pressure distribution contributes to stabilising the cavity (see Figure 6.20) as well as limiting the amplitude of the closure shock. Despite the initial concern brought by the early onset of unsteadiness, these results clearly support the working strategy: smooth the shock to reduce erosion.

6.4 Concluding remarks

A two pronged approach was adopted to assess the performance of the selected designs numerically: steady state and transient. With the steady state analysis, we recovered the

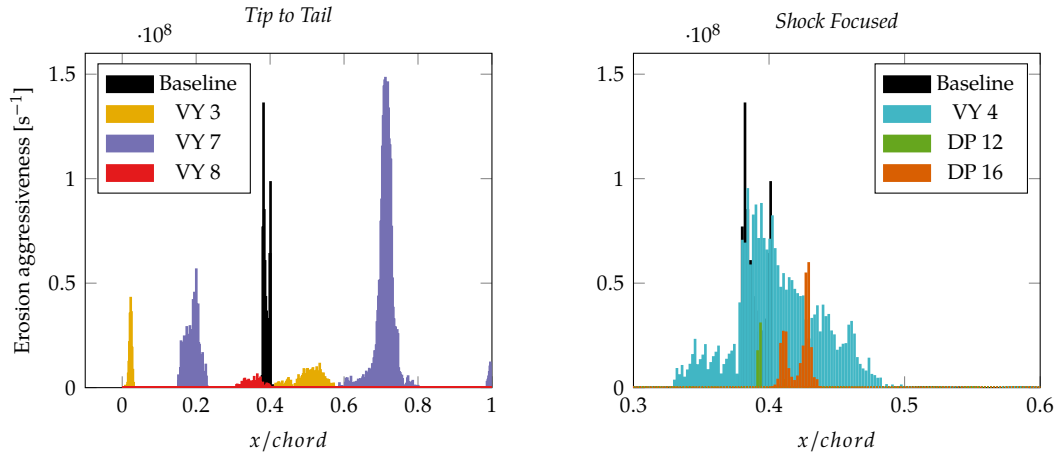

Figure 6.21: Li et al. erosion predictor computed from the time accurate solution data at $\sigma_{3\%}$ (see Table 6.7). The cumulative distributions are normalised over the effective duration of the simulation such that a time independent erosion aggressiveness metric is presented.

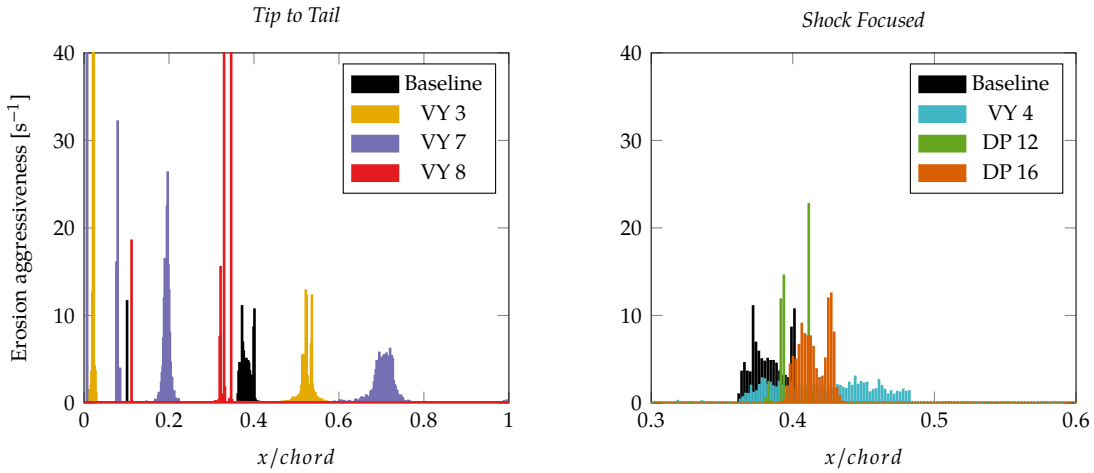

Figure 6.22: Peters et al. erosion predictor computed from the time accurate solution data at $\sigma_{3\%}$ (see Table 6.7). The cumulative distributions are normalised over the effective duration of the simulation such that a time independent erosion aggressiveness metric is presented.

flow attributes specific to each design using a separate commercial solver with a competing cavitation model. Of most importance, was the confirmation that the shock focused design strategy produced blades with weakened pressure jumps. It also highlighted the of loading type on shock amplitude and cavity growth: high amplitude and slow growth for fore-loaded profiles, low amplitude and rapid growth for aft-loaded cases.

With the unsteady analysis, we captured the dynamic behaviour of cavities in order to assess cavitation aggressiveness. Two dynamic regimes were identified: stable fixed length sheet and unstable growing and collapsing sheet. The transition point was found to depend on the global loading type i.e. gradual and post-3% breakdown point ($\sigma_T < \sigma_{3\%}$) for fore-loaded

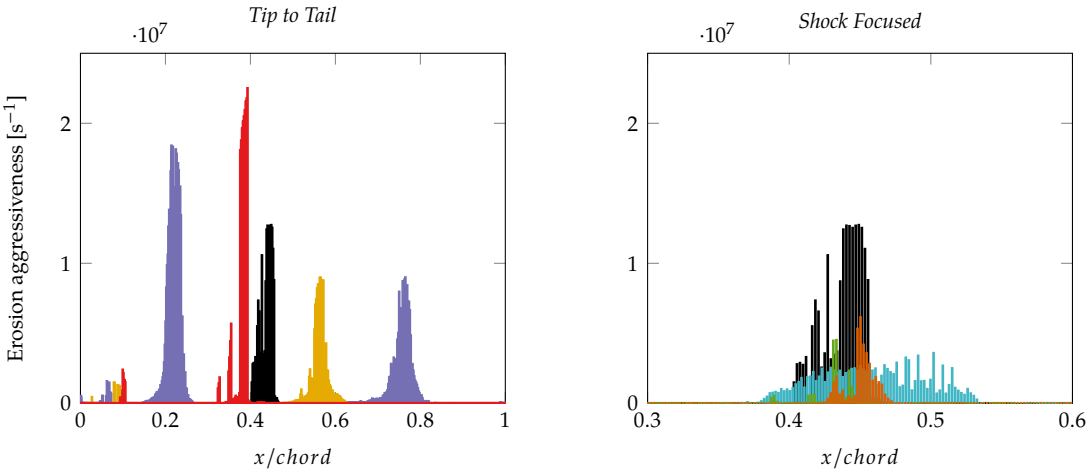

Figure 6.23: Mouvanal et al. erosion predictor computed from the time accurate solution data at $\sigma_{3\%}$ (see Table 6.7). The cumulative distributions are normalised over the effective duration of the simulation such that a time independent erosion aggressiveness metric is presented.

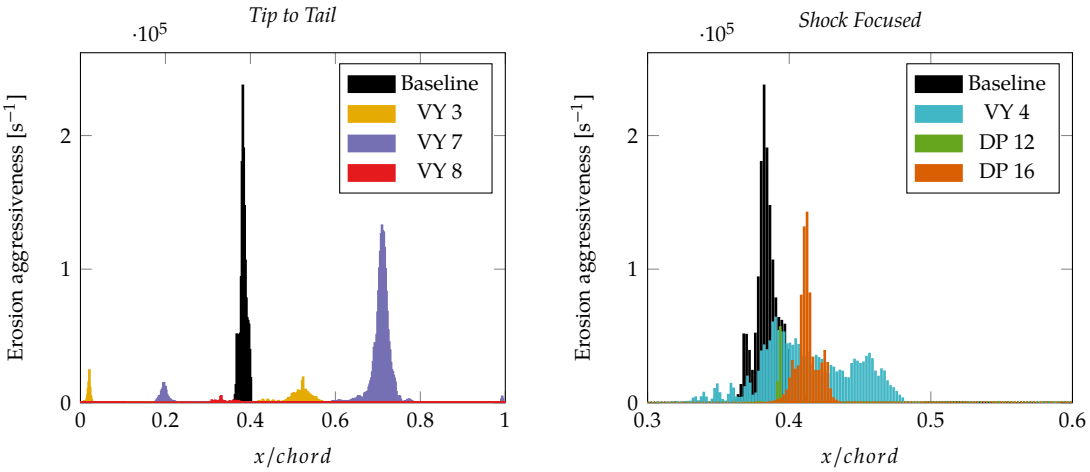

Figure 6.24: Nohmi et al. erosion predictor **Formulation 1**: $\frac{1}{T}\int_0^T \alpha \max\left(\frac{\partial p}{\partial t}, 0\right)$; computed from the time accurate solution data at $\sigma_{3\%}$ (see Table 6.7). The cumulative distributions are normalised over the effective duration of the simulation such that a time independent erosion aggressiveness metric is presented.

cases, abrupt and pre-breakdown if aft-loaded. For the shock focused cases, the study showed that unsteadiness was minimised when the shock location matched the design location.

Using the time-resolved data, we applied the techniques presented in Sections 2.2.2 to indicate erosion aggressiveness at the $\sigma_{3\%}$ condition. The first observation was a significant disparity between the approaches based on the time derivative of pressure and volume fraction, and those constructed from the instantaneous values of the same variables. This discrepancy was particularly visible on fore-loaded case VY 8, which was either at the low erosion end of the spectrum with the time derivative methods or at the high end with the instantaneous

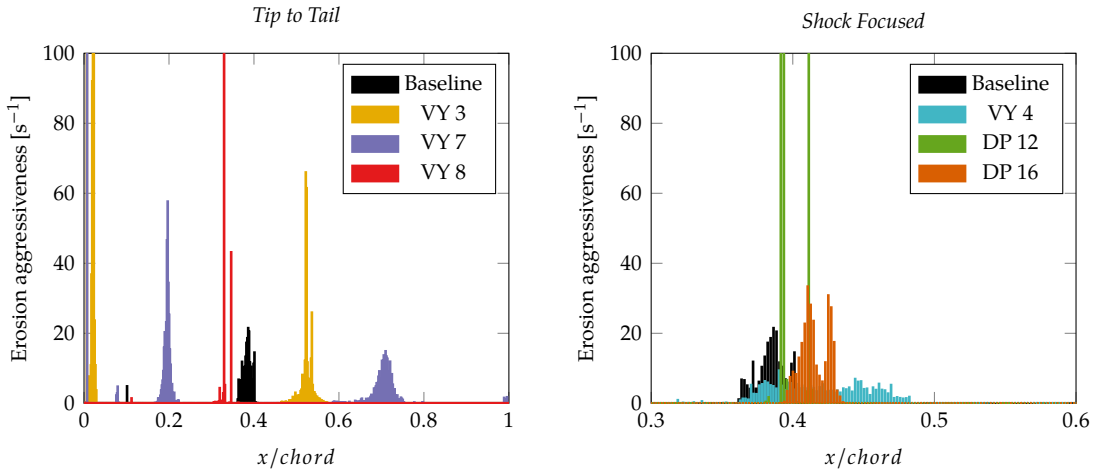

Figure 6.25: Nohmi et al. erosion predictor **Formulation 2**: $\frac{1}{T}\int_0^T \alpha \max\left(p_\infty - p_v, 0\right)$; computed from the time accurate solution data at $\sigma_{3\%}$ (see Table 6.7). The cumulative distributions are normalised over the effective duration of the simulation such that a time independent erosion aggressiveness metric is presented.

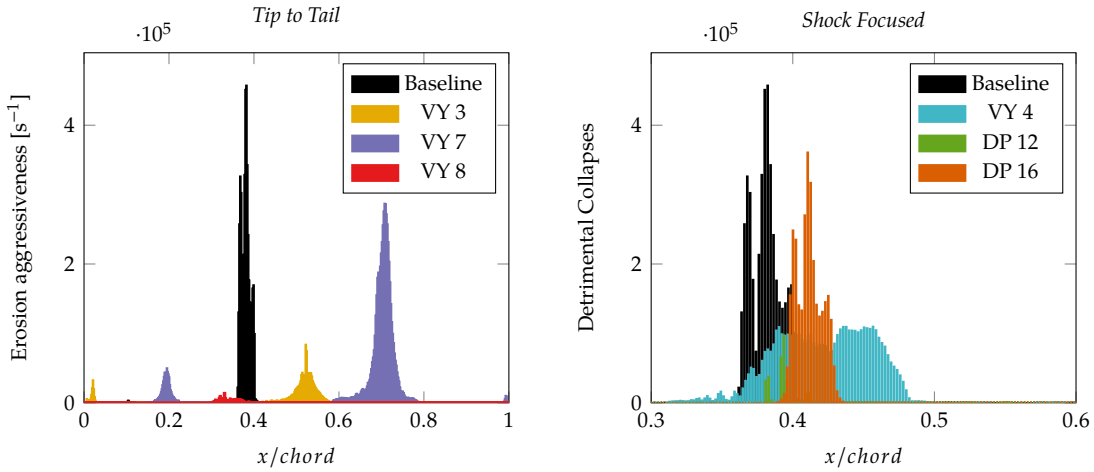

Figure 6.26: Nohmi et al. erosion predictor **Formulation 3**: $\frac{1}{T}\int_0^T p_\infty \max\left(\left|\frac{\partial \alpha}{\partial t}\right|, 0\right)$; computed from the time accurate solution data at $\sigma_{3\%}$ (see Table 6.7). The cumulative distributions are normalised over the effective duration of the simulation such that a time independent erosion aggressiveness metric is presented.

methods.

Results from the erosion prediction techniques indicate that the shock focused designs and ensuing wavy distribution were highly beneficial to the erosive performance. In particular, designs DP 12 and DP 16, with the former consistently ranked least erosive by all tested indicators. This constitutes an important milestone in this research as it provides the fist element of proof supporting the validity of the working hypothesis.

The final stage in this work will consist in replicating the analysis laid out here experimen-

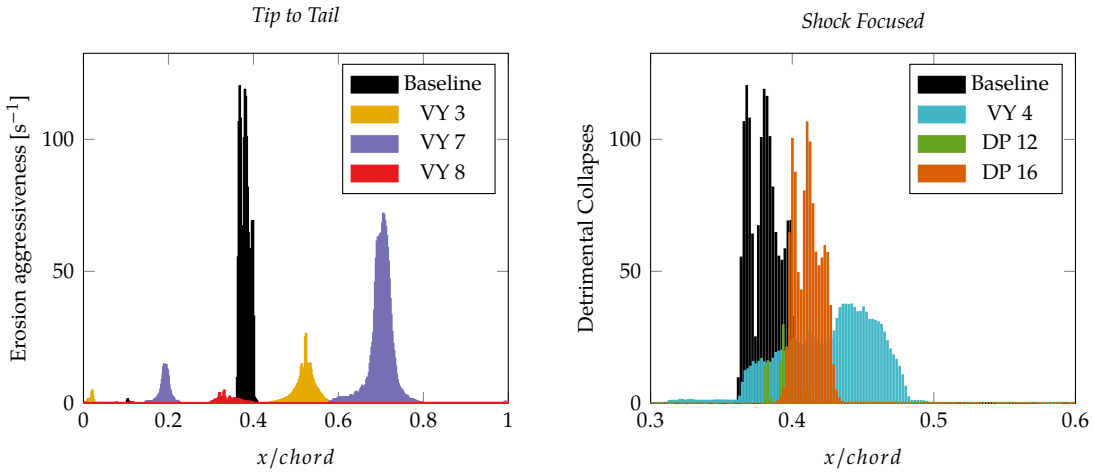

Figure 6.27: Nohmi et al. erosion predictor **Formulation 4**: $\frac{1}{T}\int_0^T \max\left(\left|\frac{\partial \alpha}{\partial t}\right|, 0\right)$; computed from the time accurate solution data at $\sigma_{3\%}$ (see Table 6.7). The cumulative distributions are normalised over the effective duration of the simulation such that a time independent erosion aggressiveness metric is presented.

tally.

7 Experimental Study of Designs

Experimental analysis is essential to verify the benefits of the design strategy laid out in this research. Without it, the representation of cavitation characteristics delivered by numerical methods does not carry sufficient assurance. For cavitation erosion in particular, the novel approaches tested in Section 6.3 are largely theoretical and still lack the necessary reliability. Two independent experimental studies are, therefore, carried out:

1. a cavitation characterisation analysis,

2. an erosion evaluation.

Because of time limitation a sample of the designed geometries is put under inspection. For each of the two experiments, the objectives and procedures are described in detail. Both are carried out in conditions that must replicate the cascade configuration. To that end, a bespoke experimental platform has been developed. Its conception and particular adjustments needed to convert two dimensional flow into three dimensions and to model periodicity realistically are laid out here.

The results from the first experiment serve to show the effect of blade geometry on sheet cavitation characteristics. The data is compared against numerical solutions and aims to demonstrate the capacity to control cavitation and its dynamics through geometry. It also provides valuable information on the accuracy of the two competing cavitation models employed in this work: TE and ZGB. With the second experiment – the erosion assessment – it is the central hypothesis of the work that is challenged. The Baseline geometry is tested against a smoothed shock profile to see whether cavitation erosion aggressiveness is softened. The data

is further utilised as a reference to evaluate the performance of the erosion indicators tested in Section 6.3.

7.1 Experimental Strategy and Objectives

Three geometries are selected for testing: Baseline, VY 3 and DP 12. A complete experimental assessment of all produced designs is not feasible due to limitations in time and material resources. The designed profiles VY 3 and DP 12 are constructed using different design strategies: *tip to tail* for VY 3 with an aft-loaded profile, *shock focused* for DP 12. The selected blades are chosen because they are representative of their particular design strategy and show positive erosion response according to the CFD metrics (see Chapter 6).

With the characterisation experiment, the aim is to measure the flow field around the blades as cavitation increases. It is essentially a reproduction, in experimental conditions, of the numerical runs at descending cavitation numbers. Flow characterisation is achieved in two ways: (i) blade surface pressure measurements, (ii) high speed video recordings of the cavity. If the collected data matches the flow field predicted numerically, the ability to control cavitation using inverse design is demonstrated.

The second experiment seeks to evaluate the erosive response of the geometries. To speed up the test, erosion is measured by painting the blade surfaces and inspecting the worn off regions. The analysis is purely comparative and sets the Baseline geometry against DP 12 to assess the *shock smoothing* strategy. Case VY 3 is left out of this part of the analysis because the development of cavitation occurs at a rate that differs significantly from the other two. The erosion data in visual format is converted into a 2D distribution which is used to diagnose the accuracy of the erosion indicators.

7.2 Rig Development

The difficulty in creating an experimental environment that realistically replicates the cascade flow comes from:

- the 2D to 3D conversion,
- the periodicity of the cascade,
- the need for an adaptable rig to incorporate a variety of geometries.

The first issue is connected to span length and the second to the number of channels N. These must be chosen so that the flow field is only marginally different from the 2D numerical analysis. The features also have to comply to the capabilities of the testing facility. Furthermore, mechanisms need to be put in place to, not only measure, but control the flow. This means that sensing equipment must be installed on the blade surfaces as well as around the cascade to ensure that cavitation number and flow uniformity are as desired. The design choices made during rig development to address these issues are described in detail in the following sections, from sizing to controllability and observability.

7.2.1 Sizing and architecture

The dimensional and flow characteristics of the stationary cascade, as tested numerically, are listed in Table 7.1. For experimental assessment, specific features such as periodicity, which assumes the absence of top and bottom walls, and infinite span length cannot be realistically replicated. This is a systematic issue when comparing 2D analytical or numerical solutions to real flow measurements. To ensure similarity, action has to be taken to suppress three dimensional effects. Here, pitchwise periodicity is approached by stacking a finite number N of channels. N is selected such that boundary layer effects at the walls do not affect the central channels. Here, $N = 6$ is chosen, meaning that the height of the test channel is $6 \times pitch = 0.543\,\mathrm{m}$. The same applies to the spanwise width: the side walls are to be separated by a sufficiently large distance to achieve uniform spanwise flow at the hydrofoil mid-section. To that end, the span is set equal to the axial chord, i.e. $0.136\,\mathrm{m}$.

Table 7.1: Operating conditions and dimensions of the 2D cascade for numerical analysis.

2D cascade configuration	
Inlet velocity	$14.48\,\mathrm{m\,s^{-1}}$
Inflow angle	$46.321°$
Inlet Axial velocity V_x	$10.0\,\mathrm{m\,s^{-1}}$
Inlet Tangential velocity V_y	$10.47\,\mathrm{m\,s^{-1}}$
Axial chord	$0.136\,\mathrm{m}$
Pitch	$9.053 \times 10^{-2}\,\mathrm{m}$
Reynolds number Re	1.97×10^{6}

The flow requirements given in Table 7.1 are combined with the channel span and total height to provide operating conditions for the test section. The volume flow rate is obtained

by multiplying the cross-sectional area and inlet velocity:

$$Q = V_x N(pitch)(span) = 0.738\,\mathrm{m^3\,s^{-1}} \tag{7.1}$$

or $44.257\,\mathrm{m^3\,min^{-1}}$. At this speed and size, the required capacity exceeds the capabilities of the water circuit at our disposal. Rather than calibrating the velocity, which would affect the pressure field, the system is downsized to reduce volume flow rate. Similarity between the original configuration and the scaled setup is maintained as long as the change in turbulent regime is not significant. The axial chord length is scaled down to 0.09 m such that all dimensions are reduced by a factor of 0.6628, meaning that $pitch = 0.06\,\mathrm{m}$ and $span = 0.09\,\mathrm{m}$. The new volume flow rate for the same inflow speed of $14.48\,\mathrm{m\,s^{-1}}$ is $Q_{Scaled} = 19.44\,\mathrm{m^3\,min^{-1}}$, which is well within the acceptable operating range of the test facility. Furthermore, to facilitate construction, the cascade is rotated such that the inflow direction is no longer at $\gamma = 46.321°$ but horizontal. This means that the line connecting the leading edges of each hydrofoil is not vertical but slanted at angle γ. Details of the operating conditions for the scaled cascade are given in Table 7.2; the complete testing platform is shown in Figure 7.1. Comparing the Reynolds number of the scaled configuration to that of the original cascade, it is found that with values of approximately 1.3×10^6 and 2.0×10^6 respectively, both flows are in the same turbulent regime.

Table 7.2: Scaled operating conditions and dimension of the experimental cascade.

Experimental operating conditions	
Inlet velocity	$14.48\,\mathrm{m\,s^{-1}}$
Axial chord	0.09 m
Pitch	0.06 m
Channel number N	6
Span	0.09 m
Cross-sectional area	$3.24 \times 10^{-2}\,\mathrm{m^2}$
Volume flow rate	$19.44\,\mathrm{m^3\,min^{-1}}$
Reynolds number Re	1.3×10^6

To be able to compare the various designs it is imperative that the rig be modular. The test section is made up of three separate parts: the support frame, the blades and the pitchwise walls. The support corresponds to the left side wall (following flow direction). A large grove is hollowed out from the surface to accommodate the blades. Each blade comes as a single

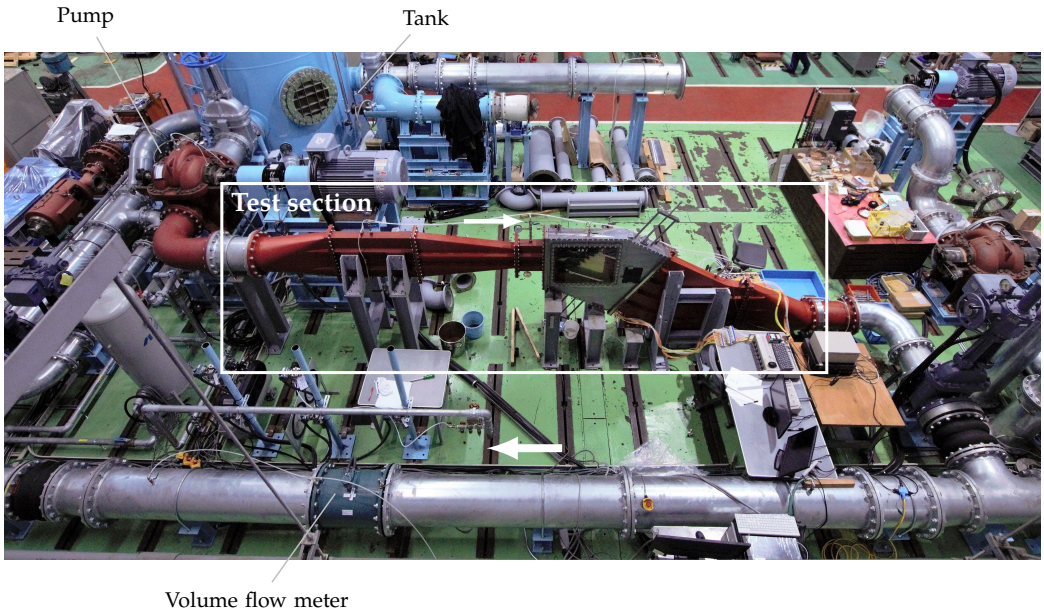

(a) Overhead view of entire water circuit. Circulation is in the clockwise direction.

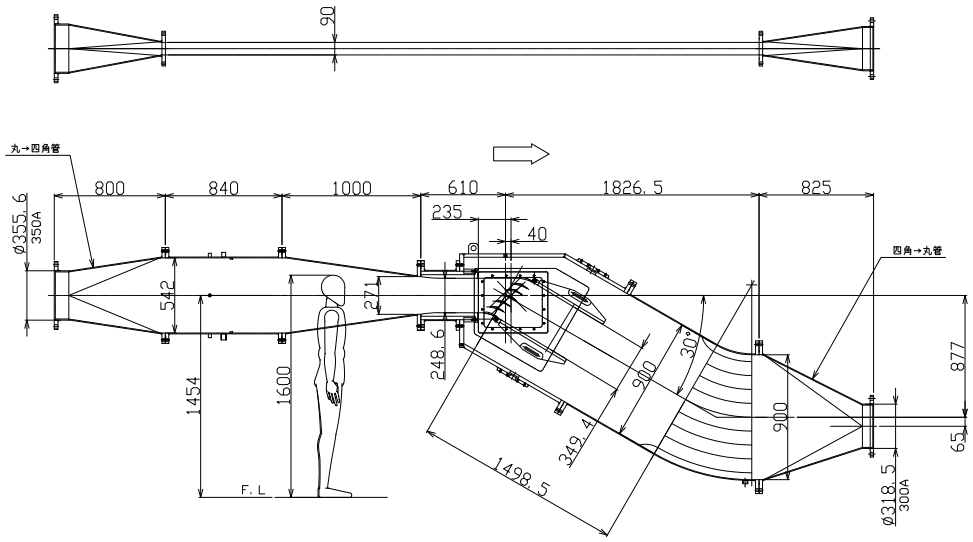

(b) Test section: overhead and side view.

Figure 7.1: Experimental installation for evaluating cascade performance.

separate piece consisting of the extruded profile and the base (see Figure 7.2b). The shape of the base remains the same for all geometries and coincides with the grove in the support wall. The top and bottom cascade walls are also interchangeable and follow the shape of either the suction surface (bottom wall) or pressure surface (top wall). With this setup, the swapping of geometries is done in a straightforward manner by replacing the five bladed elements and pitchwise walls that form the cascade.

Efforts were made during the design stage to mitigate differences in the amount of flow

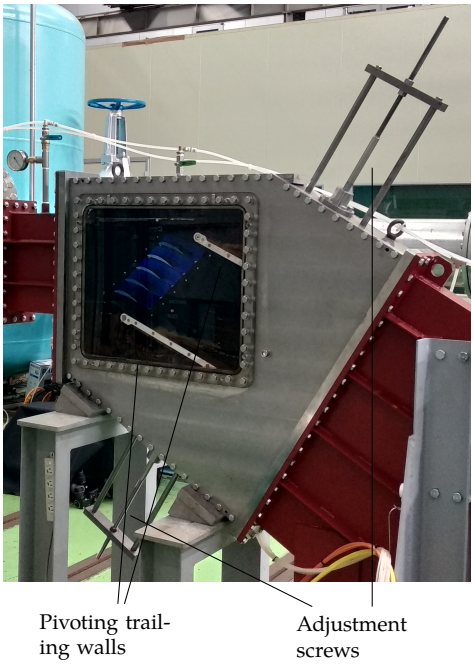

(a) Cascade section

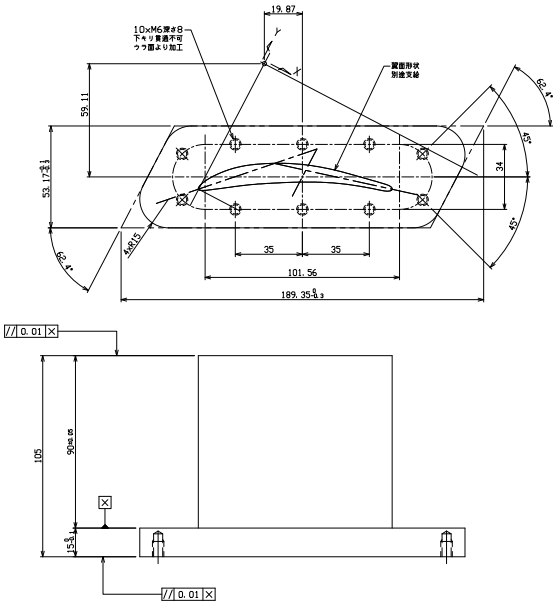

(b) Removable blade element

Figure 7.2: Cascade section (7.2a) with adjustable trailing walls and observation window. Blade element (7.2b) consisting of the base (constant shape) and the foil surfaces which vary with the design.

turning ΔV_y generated by the cascade (see Section 7.12c). Despite the adjustment, it is likely that discrepancies resulting from the limitations of CFD predictions arise in real conditions. If the outflow direction is not aligned with the outlet walls, periodicity breaks down and propagates upstream, affecting blade measurements. To remedy this issue the angle of the trailing walls is adjusted through the connected screws (see Figure 7.2. These can be operated externally so that the periodicity is fine tuned while flow is running.

The cascade assembly is contained within a casing, which connects to the inlet and outlet ducts. A honeycomb structure is fitted into the inlet pipe to enforce a uniform horizontal inflow. The casing is equipped with an observation window at the cascade section through which cavitation and trailing wall angles can be monitored. Because of manufacturing limitations, leakage occurs through the blade tip and window clearance. At low pressure, the leakage flow produces tip vortex cavitation before sheet cavitation starts to appear. To suppress tip leakage, 2 mm thick silicon membranes, cropped to the shape of the profile, are appended to the top of the blade pieces.

7.2.2 Control and Measurement System

The sensing infrastructure serves two purposes: (i) ensuring that the test conditions are met i.e. flow rate at $Q = 19.44\,\mathrm{m^3\,s^{-1}}$, temperature around $T = 20\,°\mathrm{C}$ and inlet pressure chosen to deliver the desired cavitation number, (ii) providing the target flow measurements. For flow rate, measurement is taken downstream of the test section using an electromagnetic flow meter. Its value is adjusted by changing the pump RPM and the opening of the two valves. Fluid temperature is measured at the tank. In our numerical analysis, flow is assumed isothermal at $T = 20\,°\mathrm{C}$. In reality, it tends to heat up with friction, which heightens the vapour pressure p_v and facilitates cavitation. To maintain an acceptable temperature i.e. $T = 20 \pm 2\,°\mathrm{C}$, the system is cooled down intermittently. For flow rate, pump RPM and water temperature the measurement instruments are built into the initial water circuit (see Figure 7.1a).

For pressure, however, the measurement system comes as part of the cascade component. At the inlet, five pressure taps are manufactured into the support wall and placed at the pitchwise centre of channels 2 to 6. These are intended to control periodicity and to pick up inflow pressure (see Figure 7.3a). The same goes for the outlet where six pressure taps are located at regular intervals along the pitch line. It is understood that periodicity is successfully attained when the pressure is uniform across the inlet and the outlet. To record blade surface pressure, nine taps are arranged along the mid-span meridional line on both suction and pressure surfaces (see Figure 7.3b). Blade measurements are only taken for channel 4 where pitchwise wall effects are weakest. The taps are located on the suction side of blade 3 and pressure side of blade 4. It is important to take into account the difference in height between the sensor and the tap because it exerts additional hydrostatic pressure which needs to be taken into account. All pressure taps are connected to a manual switchboard, which selectively channels the water to the *Druck DPI280* absolute pressure sensor.

Sheet cavitation patterns are recorded using high speed imaging. The filming instrument is the *Photron Fastcam SA5* camera. Video data is acquired at frame rates ranging from 1000 to 40 000 fps with focus on channel 4. To avoid light reverberating from the aluminium surfaces and masking the vapour region, a thin layer of black paint is applied to the cascade.

7.3 Cavitating Flow Characterisation Experiment

As previously explained, this first experiment consists of reproducing the cavitation development analysis carried out numerically. It is run for the Baseline, VY 3 and DP 12 geometries.

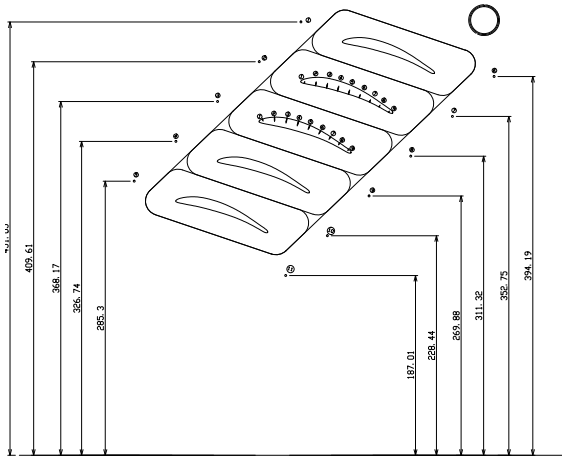

(a) Upstream and downstream side wall taps

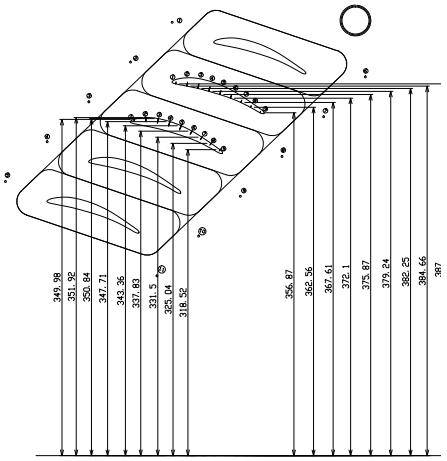

(b) Blade surface taps

Figure 7.3: Placement of pressure taps inside the cascade section used to measure operating conditions and surface pressure. All connect to the pressure sensor through the switchboard.

Flow characterisation is achieved by taking surface pressure measurements and high speed video recordings.

7.3.1 Procedure

The first step after rig assembly consists in starting up the water circuit. Pump rotation is gradually increased until the flow rate $Q = 19.44\,\mathrm{m}^3\,\mathrm{s}^{-1}$ is reached. The experiment is initiated at high inlet pressure without cavitation. For our rig specifications, this is only the case if the valves are partially opened ($\approx$ 20% of opening) and pump RPM is pushed above 1500. After that, the angle of the trailing walls is adjusted to ensure periodicity. The orientation of the top and bottom walls is updated iteratively using the screw system. The pressure values at

the inlet and outlet are continuously recorded to monitor flow uniformity. The angle setting is deemed satisfactory once all readings are within a ±2% margin from average. The trailing wall procedure is repeated every time the cascade geometry is replaced.

Several runs at incrementally decreasing cavitation numbers are carried out. Surface pressures and high speed videos are taken for each. The cavitation number is determined using the pressure reading at the inlet of channel 4 where the surface taps are positioned. It is important to mention that to get the actual static pressure p_{tap} exerted by the fluid flowing through the cascade, the hydrostatic pressure between the tap and sensor has to be subtracted from the reading:

$$p_{tap} = p_{sensor} - \rho g \Delta h \tag{7.2}$$

where Δh is the height difference between the sensor and the tap. This holds true for all pressure measurements. The cavitation number is determined using the definition $\sigma = (p^0_\infty - p_v(T))/(0.5\rho V^2_\infty)$ and is dependent on fluid temperature through $p_v(T)$. The value for the saturation vapour pressure is given by the Tetens equation which works for temperatures above 0 °C [113]

$$p_v = 0.61078 \exp\left(\frac{17.27T}{T + 237.3}\right) \tag{7.3}$$

where T is in °C and p_v in kPa. Cavitation number reduction is achieved by lowering the inlet pressure p_∞. To that end, the pump is slowed down and the valves are expanded to compensate for flow rate loss. The two parameters are subtly balanced until the operating flow rate is recovered at the target cavitation number.

For all pressure measurements, the value is recorded after time has been allowed for sensor stabilisation. The pressure is then acquired over a 10 s window, numerised and assembled into a bespoke table which serves as the raw data source. Simultaneously, high speed recordings are taken through the observation window at 1000, 5000 and 10 000 fps.

Before the experiment is initiated, the water circuit is de-aired. Preliminary runs indeed revealed large amounts of non-condensable air entrained with the liquid flow. The gas is present in the form of visible bubbles as well as dissolved in the water. The issue with pre-existing air bubbles is that they expand more rapidly than vapour bubbles. Sheet cavitation therefore appears at excessively high pressures. The de-airing process consists of creating a vacuum inside the water tank such that absorbed air is sucked out of the liquid. Because of limitations in vacuum pressure and in area of exchange surface, the air content cannot be entirely eliminated. Experimental runs will also inevitably trigger air entrapment through

tank sloshing. To keep air related discrepancies at bay, the de-airing procedure is carried out at regular intervals throughout the experimental analysis.

7.3.2 Results

The outcomes from the characterisation runs are, first, presented independently for each geometry. The following points are addressed systematically:

- non-cavitating surface pressure,
- cavitation inception,
- visual definition of the developing sheet cavity,
- surface pressure at descending cavitation number,
- cavity dynamics.

The idea is to give the reader an account of the experimental testing that is as precise and as comprehensive as possible. Numerical data is presented alongside the experimental results to assess the accuracy of the approaches.

Baseline

A total of eleven runs are carried out for the Baseline geometry at cavitation numbers ranging from $\sigma = 1.167$ to $\sigma = 0.663$. At lower pressures, the size of the cavity exceeds the scope of the numerical investigation as it extends well beyond the mid-chord location. Pressure measurements in non-cavitating conditions are shown in Figure 7.4 and compared against the *In-house* and *Fluent* solutions. Experimental and numerical results are in good agreement. The small negative offset on the suction side comes from slightly high inflow speed. As expected, the trailing edge behaviour is in closer agreement with the Fluent RANS result than with the *In-house* inviscid solution. This preliminary non-cavitating result is important because it demonstrates the capability of the rig: the design choices properly suppress three-dimensional effects such that experimental flow at mid-span accurately replicates the 2D cascade flow.

Measurements in cavitating conditions are shown in Figure 7.5 for three representative cavitation numbers $\sigma = 0.872, 0.732, 0.663$. Image records and pressure readings are presented side by side for completeness.

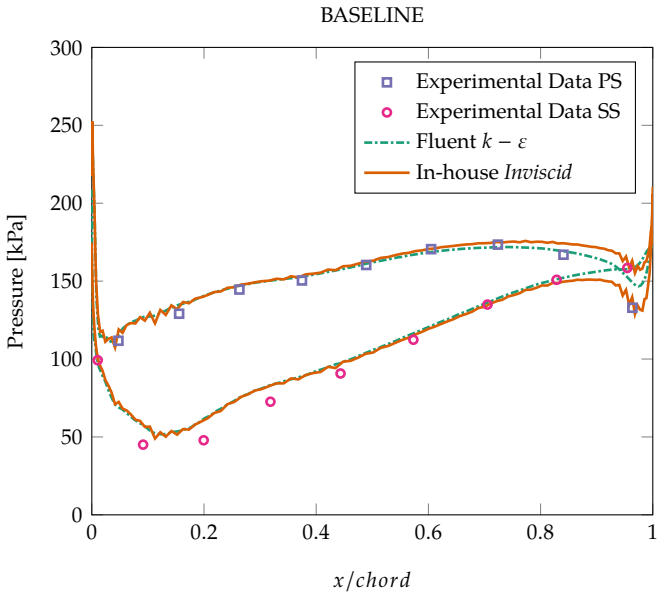

Figure 7.4: Non-cavitating absolute pressure measured and calculated at the blade surfaces for the Baseline case at $\sigma = 1.167$.

Cavitation Inception The vapour sheet is first observed at the high cavitation number $\sigma = 0.872$ (see image data in Figure 7.5a). By contrast, the cavitation inception points for the numerical solutions are at $\sigma = 0.8$ for the TE model and at $\sigma = 0.7$ for the ZGB model. The pressure values measured where cavitation occurs at the second and third pressure taps on the suction side (i.e. $x_2/chord = 0.09$ and $x_3/chord = 0.2$) are respectively $p_2 = 13.2\,\text{kPa}$ and $p_3 = 12.6\,\text{kPa}$. These numbers are significantly higher than $p_v = 2339.2\,\text{Pa}$, which constitutes the phase transition point for the numerical models.

At the inception point $\sigma = 0.872$, the cavity is thin and stable: the closure position does not fluctuate and no shedding is observed. The cavity begins at $x/chord \approx 0.1$ and ends at $x/chord \approx 0.3$. Because of the small pitchwise spread of the vapour sheet, the channel choking effect is weak and the pressure jump measure at closure between taps 3 and 4 is small.

Visual Characterisation At lower cavitation numbers, the vapour sheet continues its downstream progression. It grows in length while the initiation point remains at $x/chord \approx 0.1$. The upstream portion of the vapour sheet appears as a smooth and glassy surface. Towards the closure region, the interface between liquid and vapour is not as well marked: the two independent homogeneous media turn into a heterogeneous mixture characterised by high unsteadiness (see white cavity region in Figure 7.5). The pitchwise width and instability of the bubbly region increases as the cavitation number goes down. At $\sigma = 0.663$, vapour structures can reach the trailing edge region before breaking off as the re-entrant jet clips the cavity. The

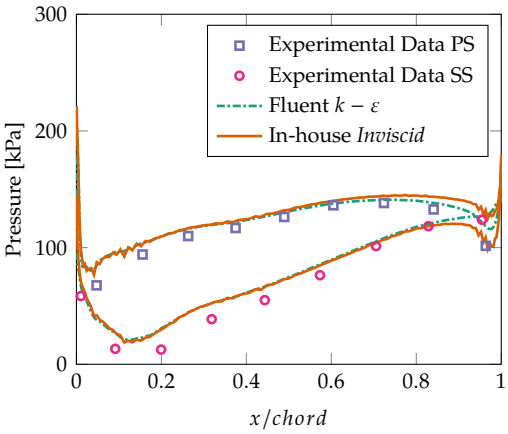

(a) $\sigma = 0.872$

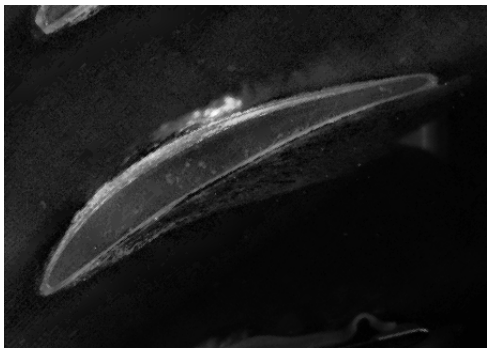

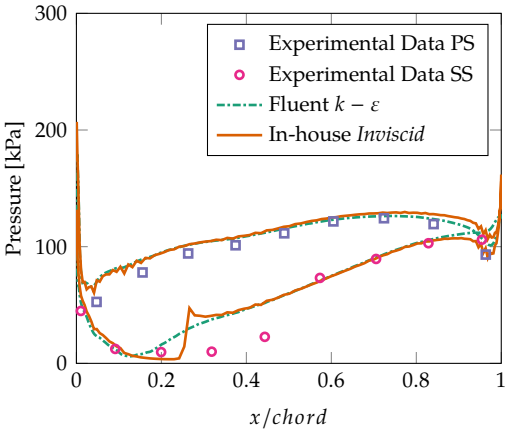

(b) $\sigma = 0.732$

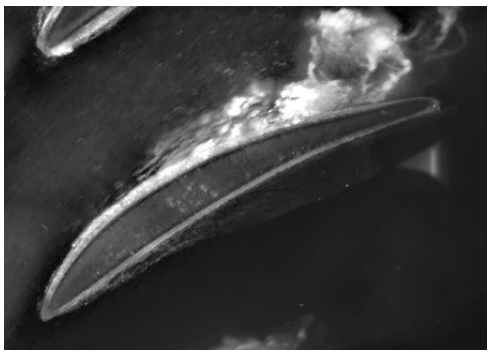

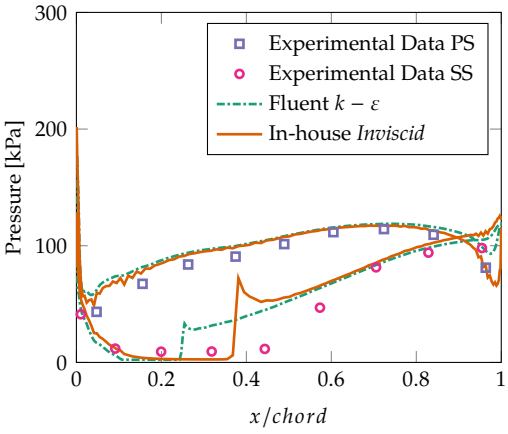

(c) $\sigma = 0.663$

Figure 7.5: Baseline geometry cavity recordings shown side by side with measured and calculated pressure values for decreasing cavitation numbers.

vapour structures shed from the cavity sheet correspond to the hore-shoe type vortex cloud identified from the study of cavitation over the NACA0015 profile.

Surface Pressure On the pressure side, the shape of the distribution is consistent and is in close agreement with the numerical data. The suction surface pressure measurements (see Figure 7.5) show an increase in the sharpness and amplitude of the closure recovery with decreasing cavitation number. Evaluating the precise location and gradient of the closure shock is difficult because of the limited number of pressure taps. Furthermore, the unsteadiness of the cavity means that the closure position fluctuates. Pressure taps are, therefore, covered by both liquid and vapour phases in quick succession. Pressure readings in that scenario were found to oscillate. This applies to, for example, taps number 5 ($x_5/chord = 0.44$) at $\sigma = 0.732$ (see Figure 7.5c) and number 6 ($x_6/chord = 0.57$) at $\sigma = 0.663$ (see Figure 7.5c). For comparison, the position of the cavity closure delivered by the numerical solutions and by the experimental results are plotted in Figure 7.6 for all tested cavitation numbers. The experimental closure location is obtained by examining the suction surface pressure data. Because of the discrete measurement points, the gap between the taps that contain the pressure jump is given as the closure range (e.g $x_5 \leq x_c \leq x_6$ for $\sigma = 0.663$). To complement the range, a spline interpolation of the pressure readings is carried out. It is assumed that the closure corresponds to the point at which the pressure exceeds 12 kPa. Note that because of flow unsteadiness and approximation limitations, the interpolated data is of qualitative value exclusively.

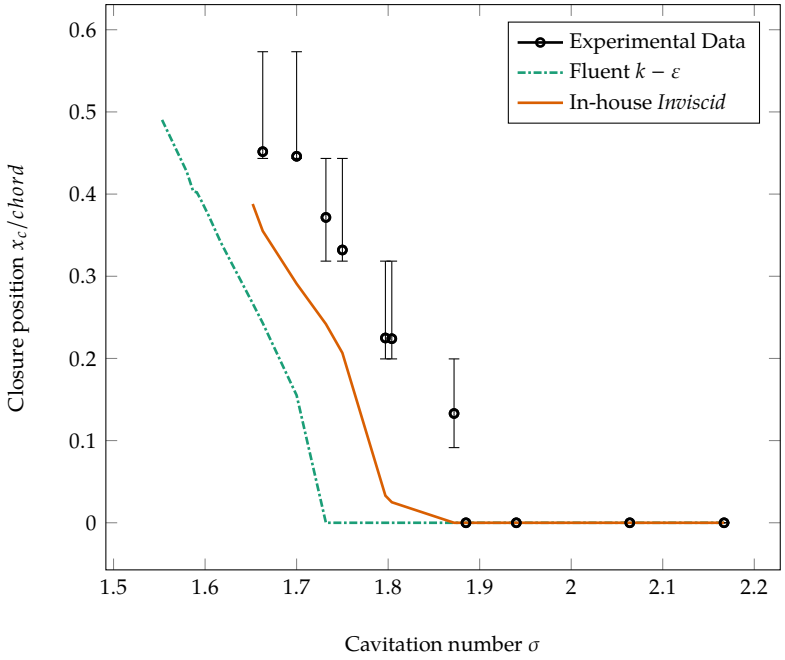

Figure 7.6: Measured and calculated closure shock position for the Baseline geometry. For the experimental data, the error bars correspond to the two tap positions upstream and downstream of the closure, the punctual value comes from the interpolation of the pressure readings and matches the point at which $p > 12$ kPa.

Inside the cavity, the pressure remains substantially higher than the saturation pressure $p_v = 2339.2\,\text{Pa}$ at all cavitation numbers. The discrepancy is either due to measurement limitations or to actual flow physics. In the first case, the offset is an error which comes from the unexpected formation of bubbles in the sensing circuit. When the pressure is low enough to cause cavitation on the suction surface, it also leads to cavitation inside the connection pipes adjoined to the cavitating region. This has a negative effect on sensor response as the presence of bubbles slows down the propagation of pressure waves because of compressibility dampening and phase change absorption. To contain this issue the sensing pipes are connected to a separate high pressure water circuit that serves to expel the bubbles into the main cascade flow. With this add-on, the majority of the vapour is eliminated. Vapour residues, however, remain in proximity to the tap where phase change takes place too rapidly.

Alternatively, it is possible to correlate the cavitating pressure discrepancy to the presence of non-condensable gas in the main cascade flow. Despite the de-airing procedure undertaken before experimental start-up, air is found not only under the form of bubbles of varying sizes, which can be observed as they are convected by the flow, but also as dissolved gas in water. To quantify the dissolved oxygen (DO), measurements are taken before each run and values are found to range from $2.3\,\text{mg}\,\text{L}^{-1}$ to $2.8\,\text{mg}\,\text{L}^{-1}$. In low pressure regions the air bubbles expand and coalesce with other bubbles of the same species or with water vapour to form a visible cavity. The pressure measured in that region is the sum of the partial vapour pressure and partial air pressure. The latter is dependent on the quantity of air in the liquid and on the rate of expansion of the bubble. Because the three fluids may not be at equilibrium, it is difficult to estimate the air pressure value.

Cavity Dynamics Fluctuations in the length of the cavity are observed. The frequency and amplitude of the closure variations depend on the cavitation number. For high numbers, the amplitude in length variation is small. At $\sigma = 0.767$ (see Figure 7.7a), the cavity closure appears to stick to the same chord position. This holds for all cavitation numbers above approximately $\sigma = 0.75$ for the Baseline geometry.

At $\sigma = 0.732$, changes in length are noticeable (see Figure 7.7b). The amplitude remains marginal at less than $0.1 \times chord$. The oscillation cycle occurs at a regular pace with a duration of $5 \times 10^{-3}\,\text{s}$ to $10 \times 10^{-3}\,\text{s}$ or a frequency in the range 100 Hz to 200 Hz. At lower cavitation numbers, the character of the cavity dynamics evolves: the change in length can reach $0.3 \times chord$ and a trail of bubbles is periodically emitted by the cavity. Because of the increase in amplitude, the duration of single oscillatory cycles is prolonged to 20 s to 25 s or a frequency

around 40 Hz to 50 Hz.

These numbers compare well with the time-resolved simulation results, which produced two identifiable dynamic regimes: stable and unstable. The first corresponds to small cavity movements limited to the closure region and occurring at frequencies above 100 Hz (see Section 6.2). The cavitation behaviour observed for $\sigma > 0.70$ matches this characterisation. The second regime is marked by a drop in frequency to values below 30 Hz and by amplitudes in size of the same order as the cavity itself. Although observed variations are not as large as numerically predicted, the second regime applies to cavitation numbers $\sigma < 0.70$.

Performance of Numerical Schemes Because of the offset in cavitating pressure, the similarity between the experimental and numerical results in terms of sheet cavitation prediction is downgraded. Both ZGB and TE cavitation models are constructed on the knowledge that phase change occurs for a saturation vapour pressure $p_v = 2339.2\,\text{Pa}$. Therefore, at the same cavitation number, the numerical solutions deliver a shorter cavity and a reduced pressure jump at closure than the experiment (see Figure 7.5b).

Performance differences also appear between numerical approaches. As described in Section 7.12c, with the ZGB model the sheet cavities are shorter and appear at lower cavitation numbers. Comparison with the experimental data suggests that the TE model provides a more accurate representation of sheet cavitation as the discrepancy is smaller than with the ZGB solution.

The difference in performance can be accounted for by the treatment of the liquid phase and non-condensable gases. The latter is completely ignored in the ZGB cavitation model. The TE EOS, on the other hand, takes into account the air contained inside the cavitating bubbles, through the air mass fraction parameter Y. The effect is an increase in the compressibility of the mixture. Its value is set at $Y = 1 \times 10^{-5}$ for all computations, which matches the order of magnitude of DO in the fluid. The remaining non-negligible offset is explained in part by the fact that Y does not take into account the non-dissolved gases in the form of pre-existing bubbles and by the value of the vapour pressure p_v, which is a determining parameter in the TE EOS.

Design VY 3

For the new designs, the aim of the experimental analysis is to show that the surface pressure distribution matches the numerical predictions and that the changes in cavitating behaviour follow the intended improvements. In the case of geometry VY 3, the *tip to tail* design strategy

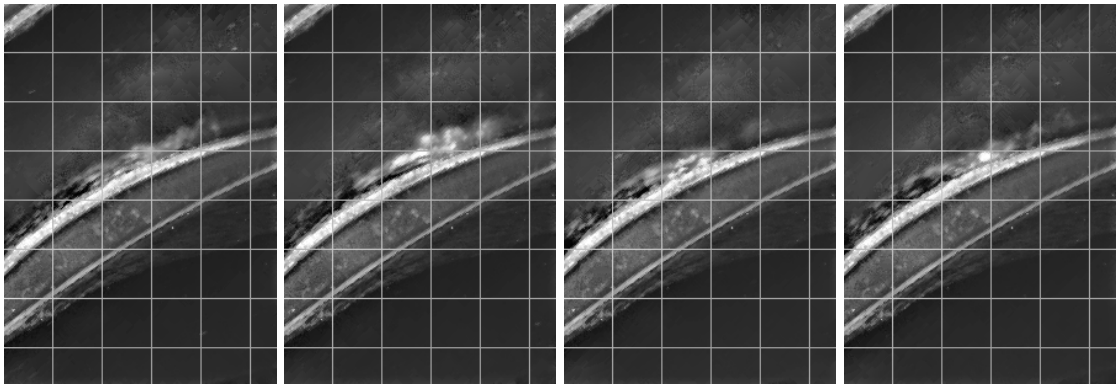

t_0 $t_0 + 5 \times 10^{-3}$ s $t_0 + 10 \times 10^{-3}$ s $t_0 + 15 \times 10^{-3}$ s

(a) $\sigma = 0.767$

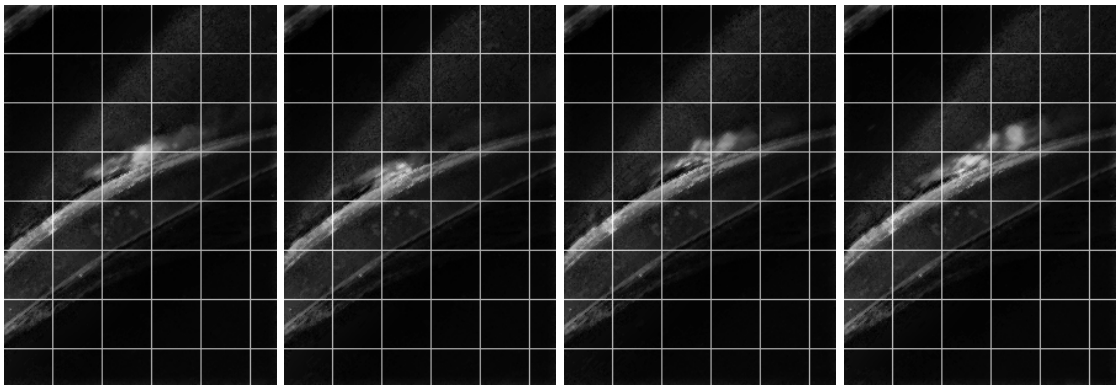

t_0 $t_0 + 5 \times 10^{-3}$ s $t_0 + 10 \times 10^{-3}$ s $t_0 + 15 \times 10^{-3}$ s

(b) $\sigma = 0.732$

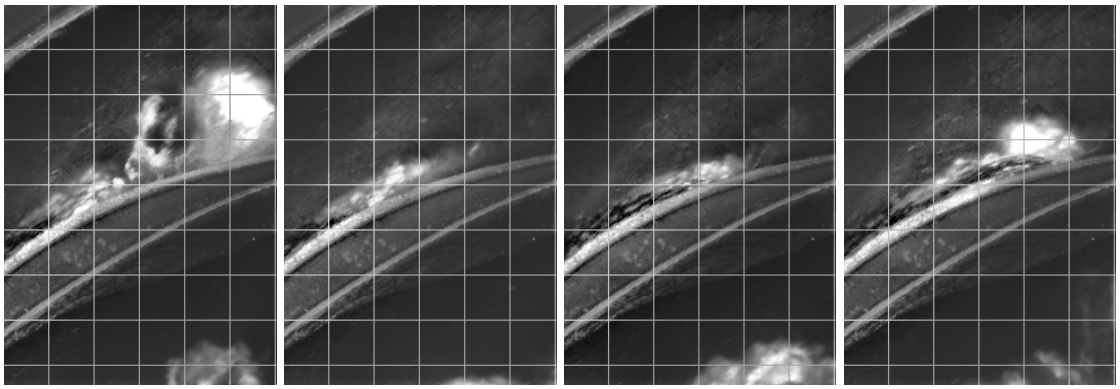

t_0 $t_0 + 5 \times 10^{-3}$ s $t_0 + 10 \times 10^{-3}$ s $t_0 + 15 \times 10^{-3}$ s

(c) $\sigma = 0.663$

Figure 7.7: Baseline geometry cavity variations at decreasing cavitation numbers. Visualisations are single frames of the high speed recording (at 10 000 fps).

was used with an aft-loaded profile. The outcome was a blade with higher curvature in the aft half, which produced a flatter suction surface pressure distribution, delayed cavitation inception and weakened closure shock.

Non-cavitating For VY 3, eleven runs are carried out at cavitation numbers $\sigma = 1.106$ to $\sigma = 0.586$. The non-cavitating pressure distribution is shown in Figure 7.8 at $\sigma = 1.106$. For non-cavitating flow, the agreement between the experimental and numerical data is satisfactory: the loading is stronger in the downstream part of the blade and the gradient of the suction surface remains low until $x/chord = 0.7$.

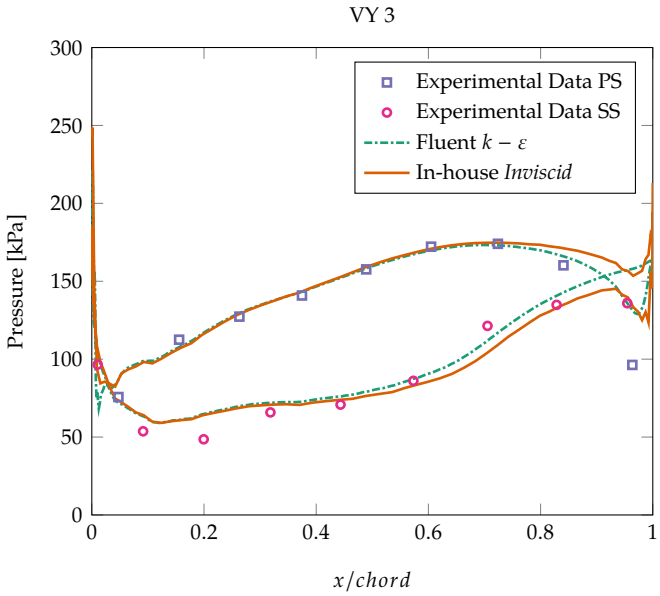

Figure 7.8: Non-cavitating absolute pressure measured and calculated at the blade surfaces for the VY 3 case at $\sigma = 1.106$.

The pressure discrepancy in the region $x/chord = 0.1$ to $x/chord = 0.3$ on the suction side between measurements and computed solutions is due to a high flow rate ($Q = 19.48\,\mathrm{m\,s^{-1}}$ instead of $19.44\,\mathrm{m\,s^{-1}}$). At the trailing edge, the drop on the pressure side is more pronounced in the experimental conditions than predicted numerically. The implication is that boundary layer separation does occur on the suction side, forcing the fluid to accelerate on the pressure side as the effective channel cross-section is narrowed. It is known that $k-\varepsilon$ type turbulence models under-evaluate the strength of separation. Other RANS approaches such as $k-\omega$ SST are more effective at capturing boundary layer phenomena. The unsteady RANS simulations detailed in Section 6.2 were run using the SST model and produce a larger pressure side drop at the trailing edge for case VY 3 (see Figure 6.20a). Nevertheless, the SST amplitude does

not match the measured data, so it is likely that spanwise strain variations affects the position and enhances the strength of boundary layer separation. The effect of trailing edge separation should be secondary when it comes to sheet cavity behaviour but must be taken into account in the performance analysis of VY 3.

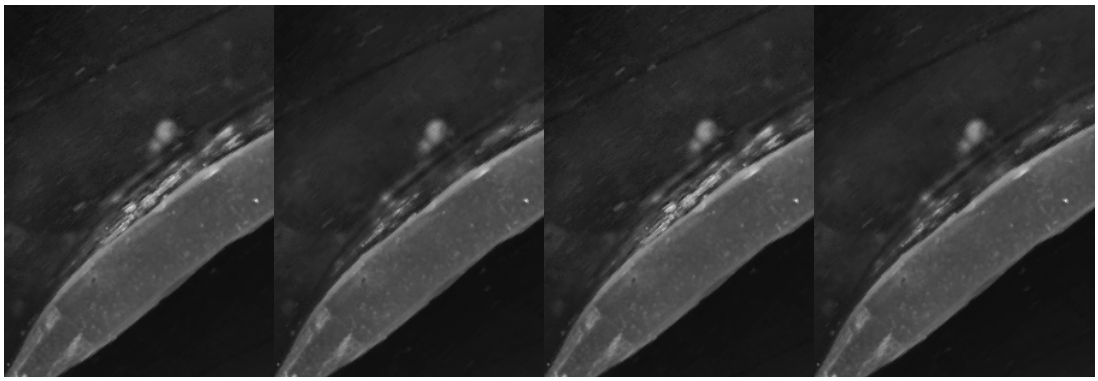

t_0 $t_0 + 5 \times 10^{-3}\,\mathrm{s}$ $t_0 + 10 \times 10^{-3}\,\mathrm{s}$ $t^0 + 15 \times 10^{-3}\,\mathrm{s}$

Figure 7.9: Pulsating cavity for VY 3 at inception conditions $\sigma_i = 0.696$. Pulsation frequency is $f = 100\,\mathrm{Hz}$ to $200\,\mathrm{Hz}$.

Cavitation Inception For VY 3, water vapour appears at $\sigma = 0.696$. It is a considerably lower inception cavitation number than for the Baseline geometry, which started to cavitate at $\sigma = 0.87$. This confirms the expected improvement in suction performance. Numerical simulations predicted a gap in inception points between VY 3 and the Baseline amounting to approximately $\sigma_i^B - \sigma_i^{VY3} = 0.14$ which corresponds to an inflow pressure difference of 14 kPa. With the experimental setup, the difference in inception cavitation number between VY 3 and Baseline is larger with a value at 0.17 (or 18 kPa). The pressure measured in the cavity region (taps 2 and 3) at $\sigma = 0.696$ is $p_2 = 11.9\,\mathrm{kPa}$ and $p_3 = 11.4\,\mathrm{kPa}$ against 13.2 kPa and 12.6 kPa for the Baseline case. As explained in 7.3.2, the cavity pressure is affected by the air dissolved and entrained into the water flow. For the experimental run of geometry VY 3 at $\sigma = 0.696$, de-airing was carried out shortly before so that DO is measured at $c^{VY3} = 2.1\,\mathrm{mg\,L^{-1}}$ instead of $c^{BL} = 2.5\,\mathrm{mg\,L^{-1}}$.

At inception point, the cavity over geometry VY 3's suction side is pulsating rather than stable (see Figure 7.9). Here again, the behaviour is different than the results observed for Baseline. This is due to the character of the suction side distribution in that region: flat for VY 3, convex for Baseline. This means that, for case VY 3, the region where pressure lies below the visible vaporisation threshold is large in the streamwise direction, but that the pressure value is only marginally smaller than the threshold. In this scenario, low amplitude disturbances

in the flow field (e.g. inflow velocity) will periodically raise the pressure above or bring it down below the vaporisation threshold, forcing either the cavity to condense or the liquid to vaporise. Visually, the cavity cycle corresponding to the duration of the growth-collapse-growth fluctuation lasts 5×10^{-3} s to 10×10^{-3} s yielding a frequency $f = 100$ Hz to 200 Hz. When compared against the frequencies obtained from the numerical time resolved solutions (see Figure 6.14 in Section 6.2), it transpires that, at this rate, the small cavity fluctuation matches those caused by turbulent perturbations.

Visual Characterisation Similar to the Baseline geometry, the cavity initiates at $x/chord \approx 0.1$ and extends downstream as the cavitation number goes down. For VY 3, however, the cavity grows in thickness at a lower rate than observed for Baseline. This is clearly visible at $\sigma = 0.616$ (see Figure 7.10b) where, despite reaching $z/chord \approx 0.6$, the width of the vapour layer has only marginally increased from inception $\sigma = 0.696$. In terms of vapour sheet texture, the interface appears smooth and glassy over the majority of the cavity, while the bubbly mixture is limited to the closure region (see Figure 7.10b). Both small width and smooth texture features are attributed to the low gradient pressure distribution over not only the suction surface but the entire upstream section of the channel. With this configuration, the low baroclinic torque reduces vorticity production at the interface between liquid and vapour so the two phases remain independent. The cavity expands in thickness only when it reaches the downstream high gradient region ($x/chord > 0.7$). This is the case for $\sigma = 0.586$ (Figure 7.10c) which produces a cavity that terminates into a thick bubbly mixture.

Surface Pressure On the pressure side, the measurements match the numerically predicted distribution at all cavitation numbers. As explained for the non-cavitating condition result (Section 7.3.2), the discrepancy at the trailing edge is due to a mismatch in location between the numerical and experimental boundary layer separation.

For the suction side measurements, the offset in cavitation closure location between the experimental and numerical results matches the discrepancy found for the Baseline case. Here too, the pressure in the cavity is higher than $p_v = 2339.2$ Pa and sits within the range 10 kPa to 12 kPa. As detailed in Section 7.3.2, the most probable cause is the presence of non-condensable gas in the fluid, which adds to the vapour content in the cavity.

In Figure 7.11, the approximate experimental position of the cavity closure for geometry VY 3 is compared to the Fluent and *In-house* solutions, as well as the Baseline measurements. The improvement in suction performance for VY 3 is made evident. Furthermore, the data

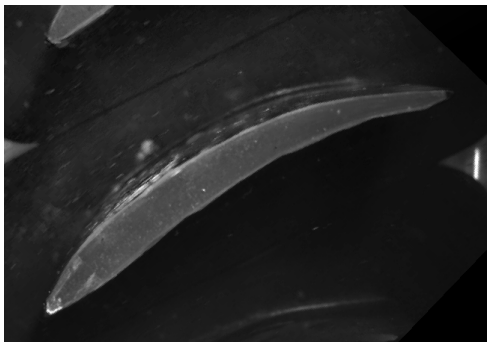

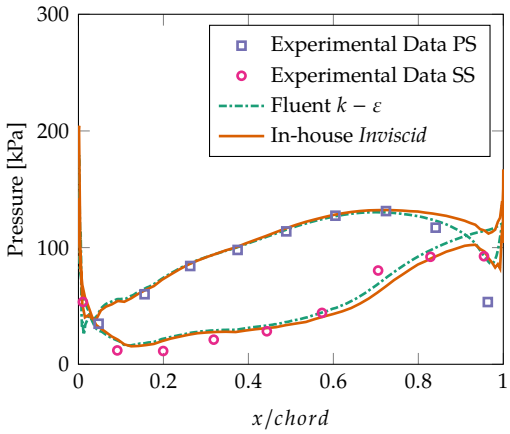

(a) $\sigma = 0.696$

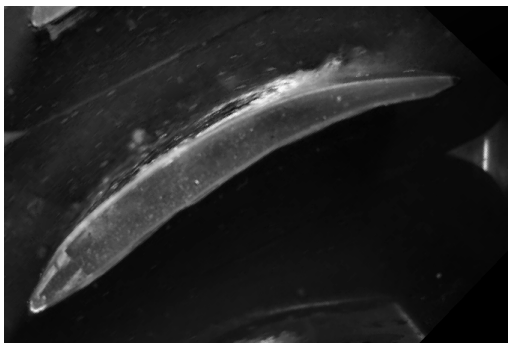

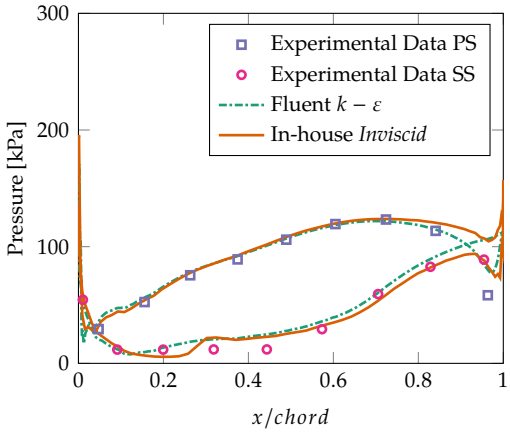

(b) $\sigma = 0.616$

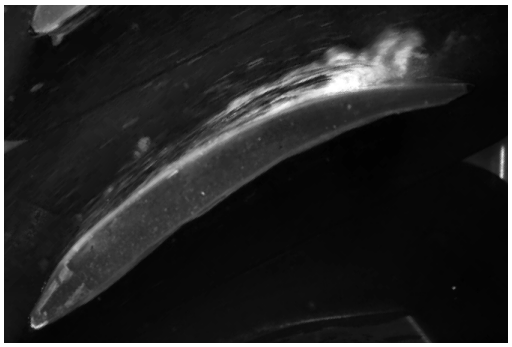

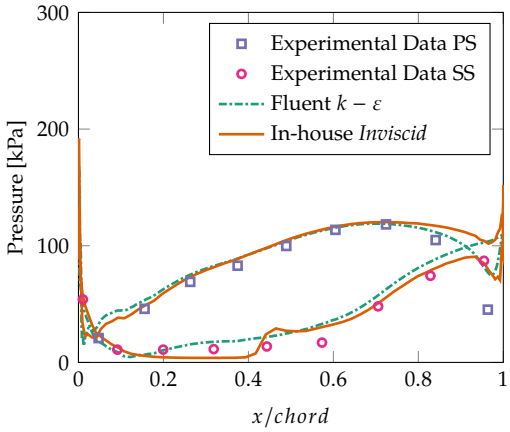

(c) $\sigma = 0.586$

Figure 7.10: VY 3 geometry cavity recordings shown side by side with measured and calculated pressure values for decreasing cavitation numbers.

indicates a clear difference in cavity growth rate. This comes as a natural consequence of VY 3's flat pressure distribution: the zone below the vaporisation pressure threshold propagates with

decreasing cavitation number at a quicker pace than it would for the higher gradient Baseline distribution.

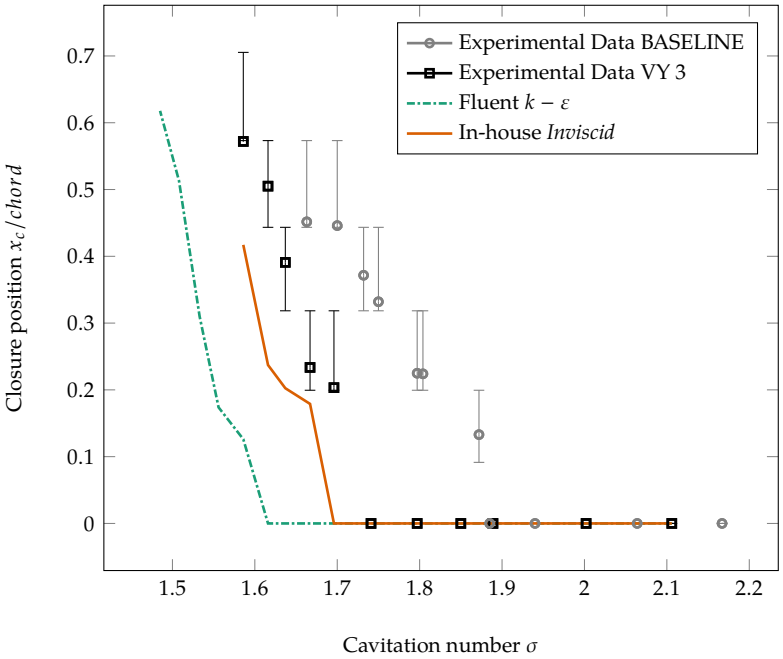

Figure 7.11: Measured and calculated closure shock position for the VY 3 geometry. For the experimental data, the error bars correspond to the two tap positions upstream and downstream of the closure, the punctual value comes from the interpolation of the pressure readings and matches the point at which $p > 12\,\text{kPa}$.

The jump in pressure at closure is estimated by considering the difference between the last tap in the cavity and the next. For VY 3, the jump amplitude is equal to 20 kPa at $\sigma = 0.616$ and 32 kPa at $\sigma = 0.586$. For comparison, the closure jumps measurements for the Baseline case are 56 kPa at $\sigma = 0.700$ and 35 kPa at $\sigma = 0.663$ (where the decrease is due to the averaging of the closure unsteadiness). The substantial reduction in jump amplitude for VY 3 coincides with the expected closure shock performance improvement and demonstrates the feasibility of using the inverse design procedure to control cavitation. Whether the low shock strategy works for softening erosion aggressiveness is answered in Section 7.4.

Cavity Dynamics Fluctuations in cavity size are observed for VY 3 at all cavitation numbers. The variability concerns the closure position, which swings forward and backward along the suction surface. The difference in length between the largest and smallest cavity can be substantial. Down to $\sigma = 0.67$, the vapour sheet can periodically disappear for short time intervals and grow back to $x/chord \approx 0.3$ (see Figure 7.9). At lower cavitation numbers, the cavity is always present and can vary in length by up to two times its smallest size. In

Figure 7.12, snapshots of the cavity closure are shown at regular intervals ($\Delta t = 25 \times 10^{-3}$ s) for cavitation numbers $\sigma = 0.637$, $\sigma = 0.616$ and $\sigma = 0.586$. At $\sigma = 0.637$ the closure position oscillates by less than $0.1 \times chord$. At cavitation numbers $\sigma = 0.616$ and $\sigma = 0.586$, larger variations are observed as the closure moves back and forth by $0.2 \times chord$.

It is difficult to isolate a single clear frequency associated with the cavity fluctuations. By carefully examining the high speed recordings, two tentative dynamic modes are identified. The first, high frequency mode, corresponds to small fluctuations of the closure position. These reduced oscillations last approximately 6×10^{-3} s to 10×10^{-3} s yielding a frequency $f = 100$ Hz to 167 Hz. This high frequency mode is common to all cavitation numbers for the VY 3 geometry and matches the frequency picked up at cavitation inception. The second, lower frequency, fluctuation type is less regular than the first and emerges only at lower cavitation numbers $\sigma < 0.64$. In this case, the variation amplitude of the closure position is wider. The breathing cycle lasts 30×10^{-3} s to 70×10^{-3} s, which corresponds to a frequency in the range $f = 14$ Hz to 30 Hz.

Performance of Numerical Schemes Because of the consistent discrepancy in vaporisation pressure, the difference between numerical solutions and experimental results found for the Baseline case is replicated for VY 3. The accuracy ranking of the cavitation models is maintained as the TE solution delivers a satisfactory closure shock amplitude and a smaller offset in cavity length. By contrast, the discrepancy between the ZGB solution and the experimental findings for case VY 3 is amplified. At $\sigma \approx 0.6$, for example, the ZGB predicted cavity is at its inception point, whereas with the experimental setup it approaches $x/chord = 0.6$ (see Figure 7.11).

In terms of cavity growth, both the ZGB and TE models yield an expansion rate that matches the experimental data. The discrepancy between VY 3 and Baseline was a notable finding of the numerical analysis and is confirmed by the experiment. It is interesting to note that the kink in cavity growth observed for a closure position between $x/chord = 0.2$ and $x/chord = 0.25$ in Figure 7.11 for the experimental profile is also produced, albeit with slight differences in closure position and kink angle, by the numerical models.

Design DP 12

The specificity of case DP 12 comes from the *shock focused* design strategy. At the design cavitation number, it is expected to deliver a low gradient and low amplitude closure recovery. Numerical analysis using the Fluent ZGB solver confirmed the improvement in shock performance at $\sigma = 0.616$, when the cavity closure is located at $x/chord \approx 0.32$. In non-cavitating

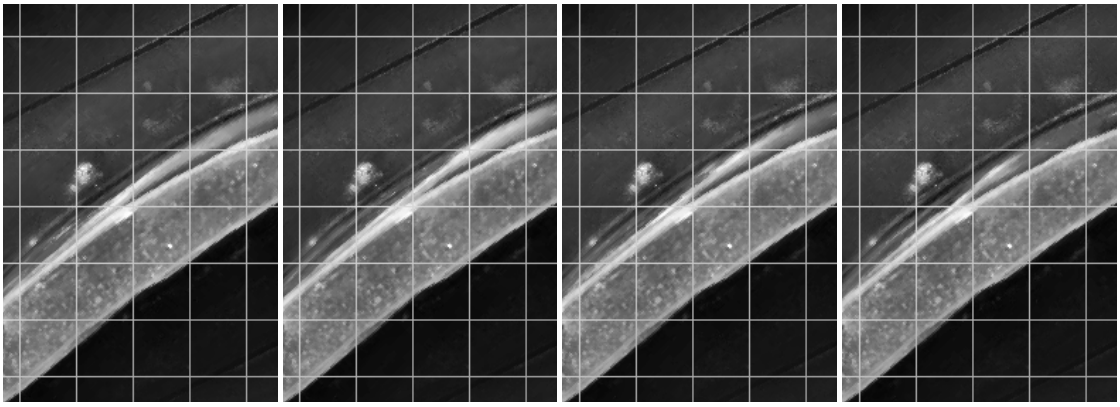

t_0 $t_0 + 25 \times 10^{-3}$ s $t_0 + 50 \times 10^{-3}$ s $t_0 + 75 \times 10^{-3}$ s

(a) $\sigma = 0.637$

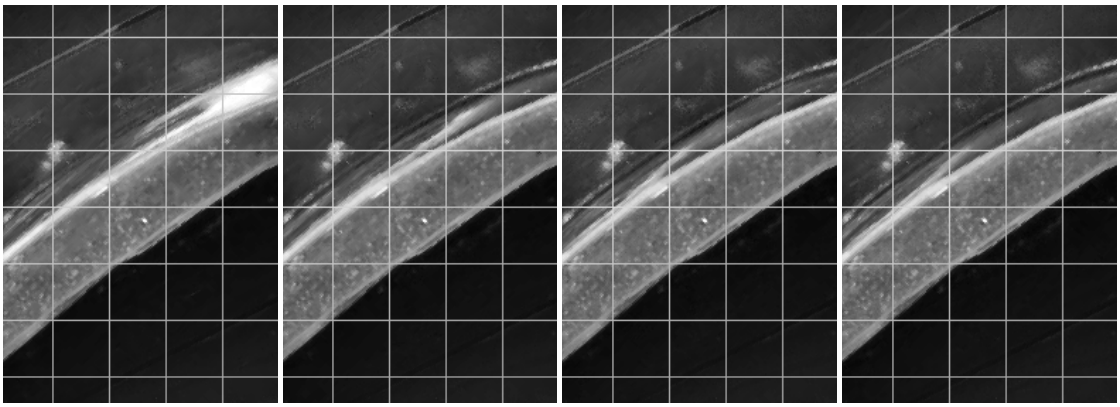

t_0 $t_0 + 25 \times 10^{-3}$ s $t_0 + 50 \times 10^{-3}$ s $t_0 + 75 \times 10^{-3}$ s

(b) $\sigma = 0.616$

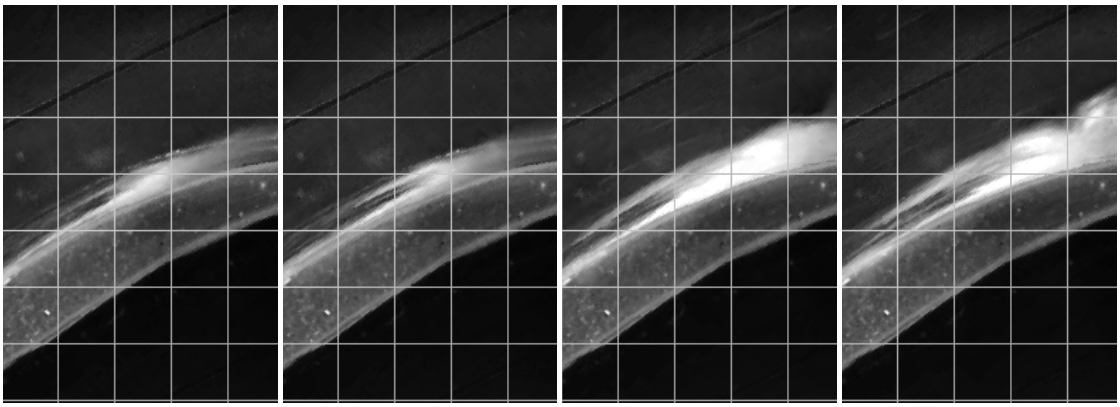

t_0 $t_0 + 25 \times 10^{-3}$ s $t_0 + 50 \times 10^{-3}$ s $t_0 + 75 \times 10^{-3}$ s

(c) $\sigma = 0.586$

Figure 7.12: VY 3 geometry cavity variations at decreasing cavitation numbers. Visualisations are single frames of the high speed recording (at 10 000 fps).

conditions, the pressure distribution is characterised by a wavy profile, with a trough that matches the location of the cavity closure at design conditions. In terms of suction performance, DP 12 is designed to match the Baseline case. Out of the *shock focused* geometries, DP 12 was selected because it gave the best response when analysed using the erosion indicators.

Because DP 12 follows the Baseline suction characteristic, runs are carried out at similar cavitation numbers. Eleven runs are, therefore, executed from $\sigma = 1.145$ down to $\sigma = 0.661$.

Non-cavitating The non-cavitating pressure distribution is presented in Figure 7.13. The measured and numerical pressure distributions are in agreement over the entire surface. Unfortunately, the number of taps is too limited to replicate the gradients of the wavy profile. Nevertheless, the stagnation observed between taps 3 and 4 on the suction side matches the pressure prescribed numerically. At $x/chord = 0.318$, tap number 4 corresponds exactly to the trough in the distribution, which matches the cavity closure location at design.

At the trailing edge, the experimental data matches the *In-house* inviscid solution more than the Fluent $k - \varepsilon$ solution. On the suction side, the last two taps show only a marginal increase in pressure. By comparison, the suction side distribution keeps increasing for the Baseline case. The difference is due to a change in the direction of the camber line at the trailing edge (see Figure 5.22). The high angle being limited to a very small zone, the effect on the cascade output is negligible. The only noticeable result is the low pressure pocket on the suction side where the fluid is marginally accelerated. This feature is being picked up by the *In-house* solver and seems to correspond to the experimental flow field. With the Fluent solver, the effect of the trailing edge geometry variation is mitigated. The implication is that the $k - \varepsilon$ turbulence model is too dissipative in that region and for this configuration.

Cavitation Inception Similarly to the Baseline case, the vapour sheet is visible at $\sigma = 0.877$ (see Figure 7.14a). At this condition, it appears as a thin cavity in a small region from $x/chord = 0.1$ to $x/chord = 0.15$. Impurities on the suction surface aid the initiation of cavitation such that vapour streaks are found emanating from single points on the surface. The cavity is consistently visible and pulses at a rapid frequency $f = 150\,\text{Hz}$ to $200\,\text{Hz}$.

As for the Baseline and VY 3 cases, cavitation inception occurs for higher pressures than numerically predicted ($\sigma = 0.8$ for the TE model and $\sigma = 0.7$ for the ZGB model). For DP 12, the pressure measured inside the cavity is in the range 14 kPa to 16 kPa. It is a higher value than for the Baseline and VY 3 runs. This differences is a consequence of the increased air quantity inside the flow as the DO is measured at $3.3\,\text{mg}\,\text{L}^{-1}$. Because of limitations in time,

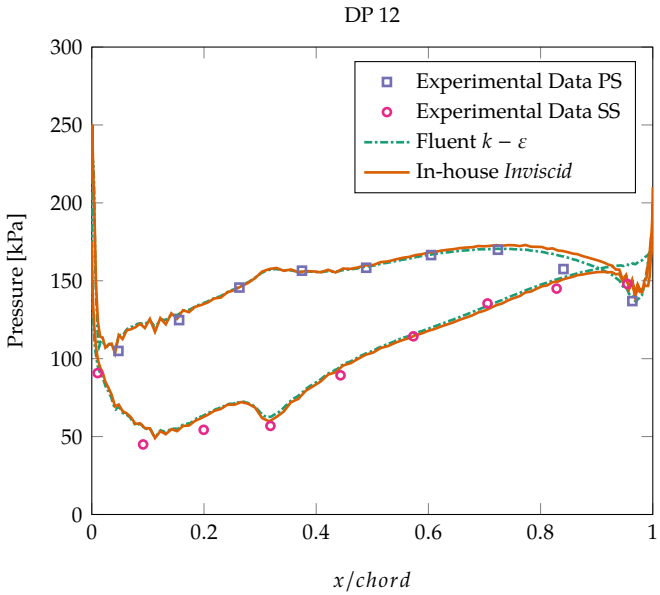

Figure 7.13: Non-cavitating absolute pressure measured and calculated at the blade surfaces for the DP 12 case at $\sigma = 1.145$.

the de-airing procedure could not be carried out between the disassembly of VY 3 and the assembly of the DP 12 cascade.

Visual Characterisation For DP 12, the cavity grows in length by the same increments as the Baseline case, owing to equivalent suction performances. In width, however, the expansion is not as pronounced, as made evident by comparing the two results at $\sigma = 0.732$ (see Figures 7.5b and 7.14b) or at $\sigma = 0.66$ (Figures 7.5c and 7.14c). Most noticeable, is the significant shrinking of the bubbly region. At $\sigma = 0.732$, the DP 12 vapour sheet remains fully attached from initiation point to closure and the smooth glassy texture appears to cover the entire cavity. Even at lower cavitation numbers, the majority of the cavity retains a visibly smooth texture while bubbly flow is limited to the closure and to the downstream region where vapour bubbles are shed. By comparison, the flow around the cavity for the Baseline case turns heterogeneous as early as $\sigma = 0.8$ with vortical structures forcing the cavity to detach.

As explained in Section 7.3.2, the pressure gradient, acting through the baroclinic torque, determines the strength of vorticity in regions characterised by large density differences. Furthermore, single bubble instability is accentuated by large pressure changes. The absence of bubbly flow for the DP 12 experiment, therefore, suggests that the pressure gradient near the cavity closure is substantially reduced, and confirms the shock performance enhancement predicted numerically. This is particularly true at $\sigma = 0.732$ when the cavity closure and the trough of the wavy suction side distribution are aligned. This corresponds to the conditions of

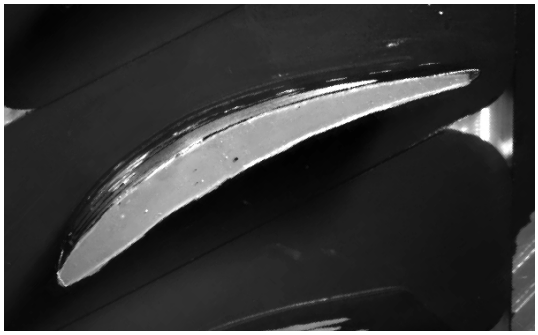

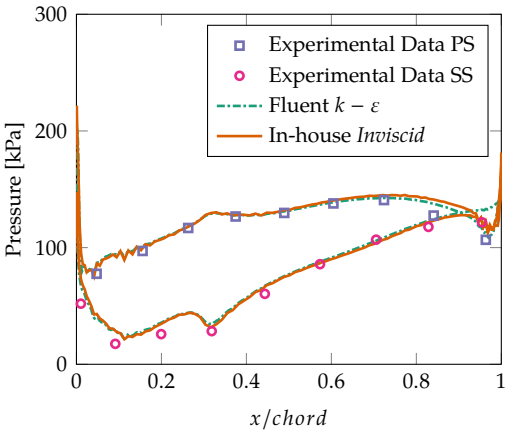

(a) $\sigma = 0.877$

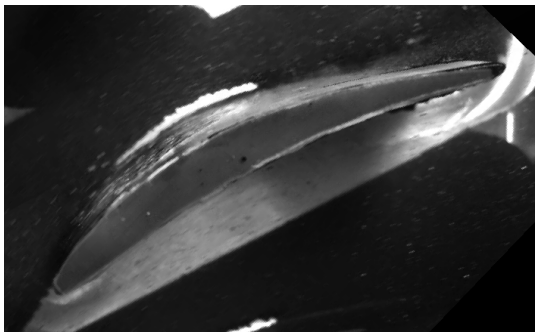

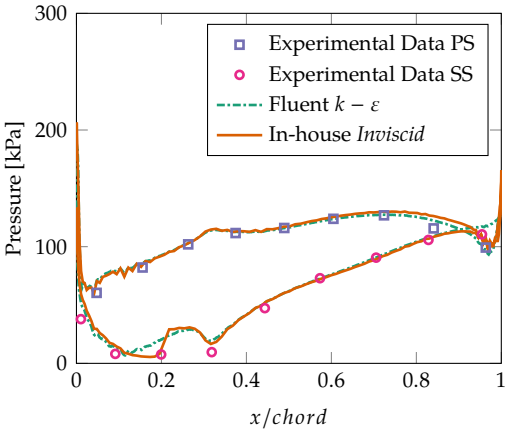

(b) $\sigma = 0.732$

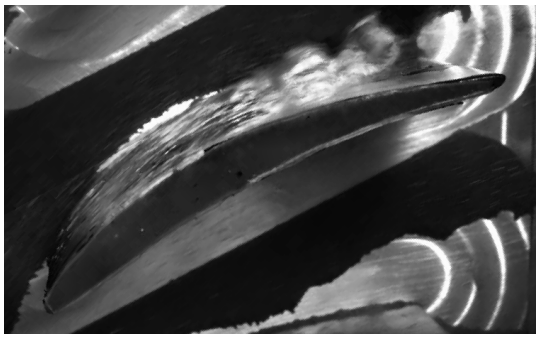

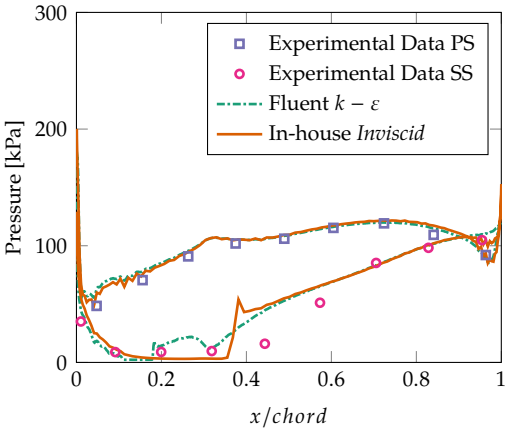

(c) $\sigma = 0.661$

Figure 7.14: DP 12 geometry cavity recordings shown side by side with measured and calculated pressure values for decreasing cavitation numbers.

the design run at which the pressure jump was intentionally smoothed.

At cavitation numbers higher than design condition, the numerical analysis predicts an

amplified pressure jump (see Figure 6.5) meaning that increased cavity thickness and frothing are expected between $0.877 > \sigma > 0.732$. However, experimental runs at $\sigma = 0.752$, $\sigma = 0.775$, $\sigma = 0.799$ and $\sigma = 0.840$ produce a well attached cavity and no bubbly mixture flow. On the other hand, the unsteadiness of the cavity is visibly increased when compared to the Baseline in similar conditions. From this, it is inferred that the upstream part of the wavy distribution affects cavitation stability but does not amplify closure aggressiveness. At lower cavitation numbers ($\sigma < 0.732$), DP 12 still delivers a far smoother and better contained cavity (see Figure 7.14c). This is an interesting observation which suggests that the positive effect of the wavy pressure distribution is carried through to lower cavitation numbers.

Surface Pressure On the pressure side the same comments are made as for all other experimental runs: consistent shape of distribution, agreement with numerical data. It is difficult to experimentally confirm the character of the pressure side wave because of the lack of taps. Nevertheless, the gradients on either side are in agreement with the numerically predicted profile.

On the suction side, tap number 4 consistently coincides with the trough of the wavy distribution as long as it lies outside the cavitating region ($\sigma > 0.7$). This means that the specific wavy distribution of the geometries designed in cavitating conditions is a realistic feature. It is also interesting to observe that the singular profile does not appear to disturb the flow.

Again, the discrepancy in vaporisation pressure reflects in the offset in closure location between experimental and numerical data. One must note, that at $\sigma = 0.732$ (Figure 7.14b), the measurements and *In-house* TE solution appear to match exactly. This is a visualisation error caused by the lack of measurement points between taps 3 and 4 as, by comparing to the corresponding image, the cavity clearly extends continuously from $x/chord = 0.1$ to $x/chord \approx 0.32$.

At $\sigma = 0.732$, the experimental cavity closure is in the same zone as the trough. Numerical analysis demonstrated that the amplitude of the pressure recovery was softened when this alignment was met (see Section 6.1.2). Here, the pressure jump between tap 4 (cavity region) and tap 5 (non-cavitating) is equal to approximately 38 kPa. The experimental data acquired at exactly the same cavitation number for the Baseline case is put to comparison (see Figure 7.5b). In that case, tap number 5 lies in the unsteady cavitation region and is considered to represent the pre-closure pressure. For Baseline, the pressure recovery jump is equal to approximately 50 kPa. The difference is not large but acts in the right direction i.e. lower for DP 12. This metric

must be taken lightly given the extensive chord range covered by the jump instead of the zone immediately following the closure. In that regard, the absence of bubbly flow at cavity closure is a more reliable indication.

The experimental progression of the DP 12 cavity closure is plotted in Figure 7.15 along with the *In-house* TE and Fluent $k-\varepsilon$ results, as well as the Baseline experimental data. As expected, DP 12 and Baseline cases deliver a similar cavity growth profile i.e. equivalent rates and inception points. Discrepancies do, however, appear at lower cavitation numbers $\sigma \leq 0.7$ with the DP 12 closure progression slowing down. This coincides with the trough in the pressure distribution suggesting that one of the effects of the DP 12 kink is to curb the expansion of the cavity. It is likely that the slowing down is temporary and that the Baseline growth rate is recovered at lower cavitation numbers.

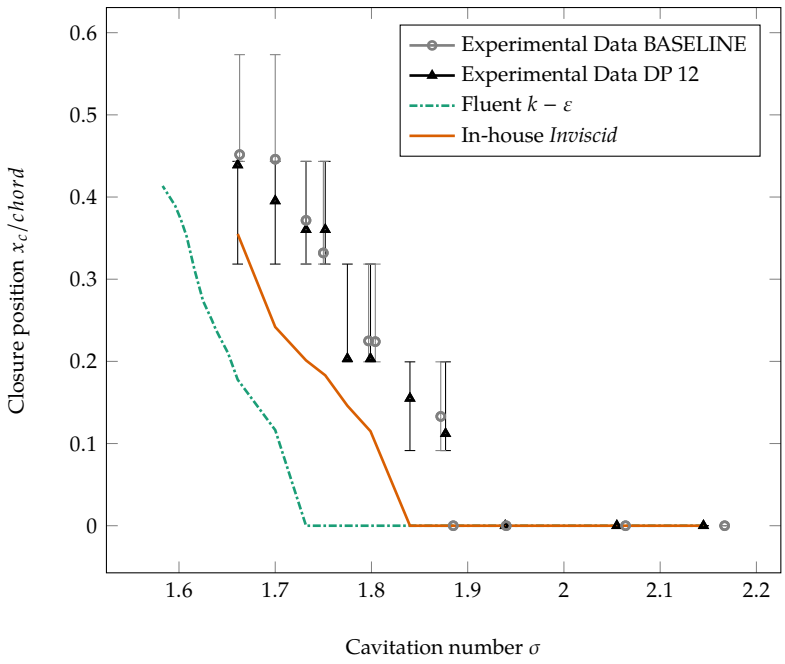

Figure 7.15: Measured and calculated closure shock position for the VY 3 geometry. For the experimental data, the error bars correspond to the two tap positions upstream and downstream of the closure, the punctual value comes from the interpolation of the pressure readings and matches the point at which $p > 12\,\text{kPa}$.

Cavity Dynamics For cavitation numbers higher than design condition ($\sigma > 0.75$), the cavity closure fluctuates at a rapid pace. Growth-collapse-growth cycles last $5 \times 10^{-3}\,\text{s}$ to $10 \times 10^{-3}\,\text{s}$ which corresponds to a frequency $f = 100\,\text{Hz}$ to $200\,\text{Hz}$. At these conditions, the cavity can double in length. As the cavitation number approaches $\sigma = 0.732$, the vapour sheet gains in stability. The amplitude of the fluctuations diminish and the range of frequencies narrows

down. At $\sigma = 0.732$, the closure displacement is less than $0.1 \times chord$ and the oscillation frequency is 125 Hz to 170 Hz.

The reduction in amplitude continues beyond the design cavitation number. At the lowest pressure run ($\sigma = 0.661$), the cavity does not appear to grow or shrink in length (see Figure 7.16c). Instead, changes are observed in the density of bubbles being shed from the frothing closure region. Larger bubble clusters are ejected at irregular intervals which can last 8×10^{-3} s to 20×10^{-3} s or at a frequency 50 Hz to 125 Hz.

It is interesting to note that the cavity stabilises as the cavitation number goes down. For Baseline, by comparison, it is the opposite that occurs. This suggests that the DP 12 features have stabilising attributes which activate when the cavity closure is located in the same region as the trough in the suction surface distribution. A likely explanation is that with the reduction in shock amplitude, the reverse flow in the boundary layer at closure is weakened to such an extent that the cavity is only marginally affected.

Performance of Numerical Schemes DP 12 does not differ from Baseline and VY 3 in terms of numerical prediction performance: both approaches are offset by approximately $\Delta\sigma = 0.07$ (or 7316 Pa) for the *In-house* TE solver and $\Delta\sigma = 0.17$ (or 17 768 Pa) for Fluent with the ZGB model. In terms of cavity growth rate, the numerical solutions match the experimental data. The source of the discrepancy is, as explained for the Baseline and VY 3 results, the air content in the water flow. For details on the mechanism, the reader is referred to Sections 7.3.2 and 7.3.2.

7.4 Erosion Assessment Experiment

With the erosion experiment, the aim is to answer the central question of our research : can cavitation erosion be controlled through blade geometry and does the strategy implemented in this research work. It also serves to evaluate the prediction performance of the numerical erosion techniques tested in Section 6.3. To assess the erosive response of the geometries under cavitating flow, the paint layer approach is put into application. For the flow speeds considered here, it would take close to a hundred hours of operation to obtain detectable material loss for the aluminium cascade. With paint, the intensity and zone of action of cavitation erosion is highlighted much sooner and can be identified by looking at the paint-free patterns.

Given the allocated resources, erosion assessment is carried out for the Baseline and DP 12 cases at a single cavitation number. Geometry VY 3 is discarded at this point in time because it

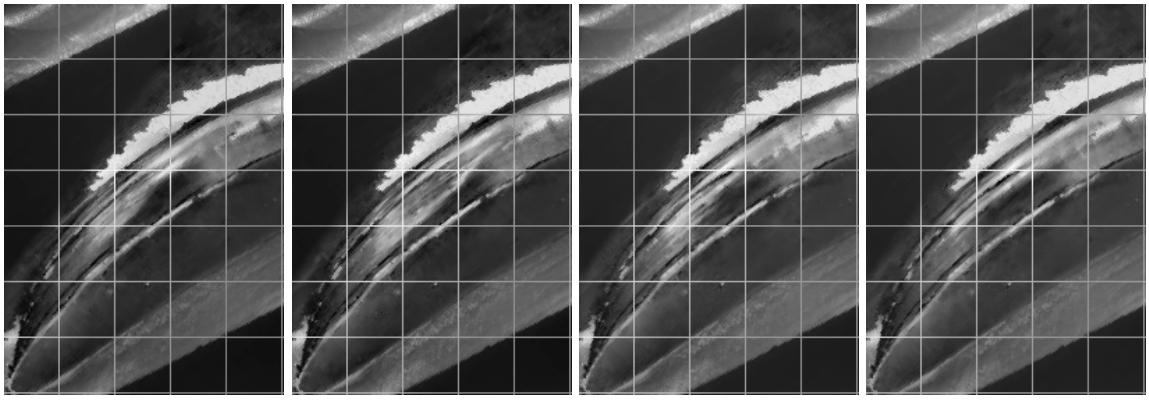

t_0 $t_0 + 10 \times 10^{-3}$ s $t_0 + 20 \times 10^{-3}$ s $t_0 + 30 \times 10^{-3}$ s

(a) $\sigma = 0.775$

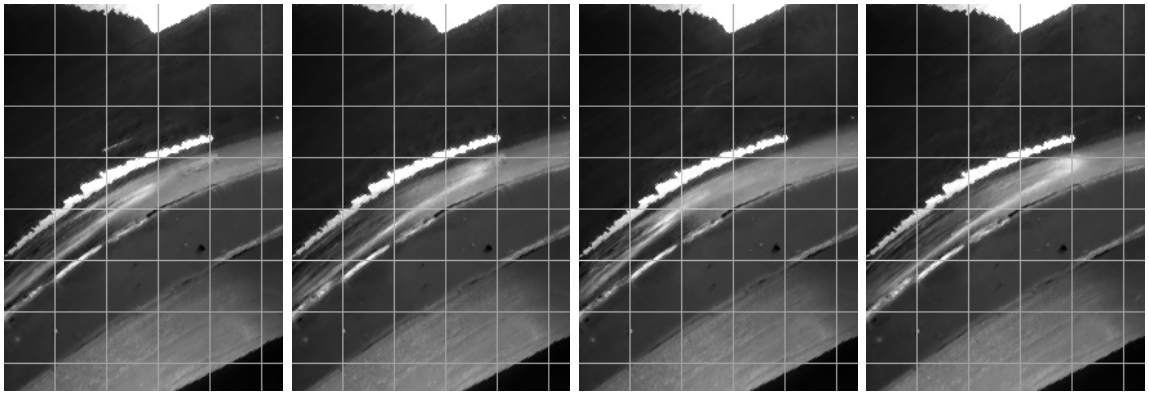

t_0 $t_0 + 10 \times 10^{-3}$ s $t_0 + 20 \times 10^{-3}$ s $t_0 + 30 \times 10^{-3}$ s

(b) $\sigma = 0.732$

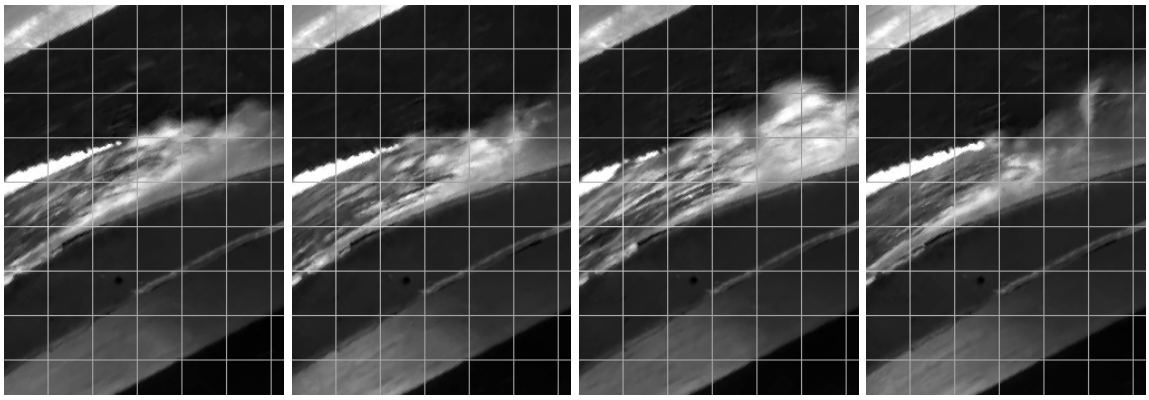

t_0 $t_0 + 10 \times 10^{-3}$ s $t_0 + 20 \times 10^{-3}$ s $t_0 + 30 \times 10^{-3}$ s

(c) $\sigma = 0.661$

Figure 7.16: DP 12 geometry cavity variations at decreasing cavitation numbers. Visualisations are single frames of the high speed recording (at 10 000 fps).

presents a substantially different breakdown or shock growth profile (see Figure 7.11). In Section 6.3, the discrepancy was remedied by considering the cavitation numbers that correspond to a 3% breakdown. With the current experimental platform, the vertical component of velocity at the outlet, V_y^{out}, needed to calculate work output is not accessible, and the number of pressure measurements on the blade surface is too low for lift force calculation. An alternative is to match the cavity length to the solution provided by the numerical computations to deduce the experimental conditions that produce comparable cavitation characteristics. However, given the offset between the predictions and observations, such a procedure would not be reliable. Ideally, for a range of breakdown profiles, erosion should be assessed for the entire range of cavitation numbers from inception to full blade cavity. This constitutes a possible direction for continuation of this research.

Unlike VY 3, the Baseline and DP 12 cases are designed to deliver a similar breakdown profile. Results from the characterisation experiment confirm the closeness of the two cases as portrayed by the cavity growth analysis (see Figure 7.15). The two cases can therefore be run in identical conditions meaning that potential discrepancies in the erosive response are caused by differences in the pressure distribution exclusively.

In the numerical analysis, the 3% breakdown cavitation number is $\sigma_{3\%} = 0.587$ for Baseline and $\sigma_{3\%} = 0.583$ for DP 12. In these conditions the cavity closure is predicted to be positioned at $x/chord = 0.4$ for both cases by Fluent with the ZGB model. For the erosion experiment, the cavitation number is chosen so that the same cavity length is observed. This corresponds to $\sigma^{exp} = 0.73$ and matches the design condition for DP 12 when the position of the cavity closure aligns with the suction side trough. It is, therefore, the ideal operating point to assess the performance improvement delivered by the shock smoothing design strategy.

7.4.1 Procedure

The protocol for erosion assessment by paint application is straightforward. The two centre blades with pressure holes are discarded and replaced by even surface blades. The hydrofoils are spray painted uniformly and assembled into the cascade rig. The same procedure carried out for the cavitation characterisation experiments is used to adjust the valve opening and pump RPM to get the desired cavitation number. The operating conditions are maintained during exposure time. The duration of the erosion test is determined by running a preliminary test and observing the gradual removal of the paint layer. Using the Baseline geometry, it was found that at least 8 hours of cavitation exposure are necessary to produce visible patterns. In total and including the preliminary run, three erosion tests were carried out (see details in

Table 7.3). For the comparative study, 15 hours of exposure was chosen as appropriate.

Table 7.3: Runs details for the erosion experiments.

Experimental run	Geometry	Test conditions
1 (Preliminary)	Baseline	6.4 h at $\sigma = 0.75$, followed by 9 h at $\sigma = 0.73$
2	Baseline	15 h at $\sigma = 0.73$
3	DP 12	15 h at $\sigma = 0.73$

After expossure, images are taken of the suction surface along the central channel where the flow field is well controlled. The image data is processed to provide a one-dimensional distribution of the erosion intensity along the axial direction (in the model coordinate system). The result is compared to : i) the numerical erosion indicators applied to the time-resolved simulations, ii) the experimental erosion distributions obtained for the other tested blade.

7.4.2 Results

As can be seen in Figure 7.18, the eroded zones appear as clusters of paint free specks or as continuous paint-free regions. The density of visible metal determines the intensity of cavitation erosion. For the preliminary test result, several separate regions are picked up. At the leading edge, the erosion is caused by the impact of solid particles carried by the water onto the surface. The particles are metallic dust or detached fragments of the honeycomb structure contained in the inflow pipe. This type of solid to solid erosion is of no interest to this research. Slightly further downstream, a low intensity erosion region is visible. In this case, paint removal is caused by cavitation. However, the origin of cavitation is not the drop in surface pressure but low pressure vortices emanating from particles clinging to the leading edge (see Figure 7.17). As such, this manifestation of erosion is of no value either.

The third larger region located at mid-blade corresponds to the erosion action that is investigated here. Its location matches the sheet cavity closure position at $\sigma = 0.73$ (for the Baseline case). The streamwise spread comes from the movements of the closure. In the spanwise direction, the eroded zone is not uniformly distributed: the surface is intact close to the walls and the density of metal specks is maximum at midspan. This agrees with the spanwise shape of the experimental cavity which disappears at the side walls and flattens between $0.3 \times span$ and $0.7 \times span$. The areas affected by wall effects are eliminated from the study. Instead, the region of analysis is limited in span to the uniform erosion section (see Figure 7.19).

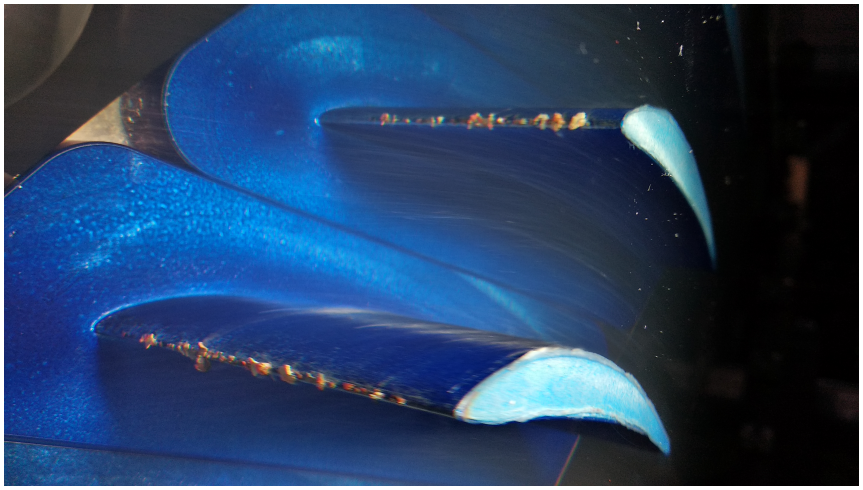

Figure 7.17: Particles clinging to the leading edge of cascade blades cause vortex cavitation which collapses onto the suction surface. The particles are likely to be fragments of the honeycomb channel upstream of the cascade section.

For erosion test number 2 (Baseline for 15 h at $\sigma = 0.73$, see Table 7.3), the main pattern is much sharper (see Figure 7.19). Instead of the large speckled region leading up to the bare aluminium with increasing density, the paint layer goes from being in perfect condition to completely detached in less than $0.1 \times chord$. The fact that, for this test, the geometry is run at a single condition explains the boundedness of the erosion pattern. Here, the preliminary run serves as a trial experiment. The relevant data comes from test number 2.

The RGB image of the suction surface is cropped accordingly and converted to grayscale (see Figure 7.18b or 7.19b). With the colour conversion, each pixel carries a scalar value which determines whether the surface is bare aluminium or paint. In this format, the image turns into to a two-dimensional matrix where each column and row correspond to a fixed streamwise and spanwise coordinate respectively, and each component is a measure of the erosive intensity EI. To get a 2D chordwise distribution, the matrix is collapsed into a vector by calculating the mean for each column and normalising by the span length of the evaluated section. At image acquisition, the blade rests on the side of its base (see Figure 7.2b) meaning that the image's streamwise axis is parallel to the base part wall. To recover a distribution that compares to the pressure and predicted erosion profiles, the data vector is transformed back to the model coordinate system. Because of differences in colour tones at image acquisition, all experimental distributions are normalised by the erosion intensity of the fully eroded surface for test run number 2 on the Baseline geometry i.e. $EI_{max} = 3.6 \times 10^3\ \mathrm{m}^{-1}$.

The resulting distribution for the 15 h Baseline test is shown in Figure 7.20. The principal eroded zone is spread over taps 4 and 5 from $x/chord = 0.3$ to $x/chord = 0.5$, which corresponds to the unsteady downstream part of the cavity. The peak in erosion between

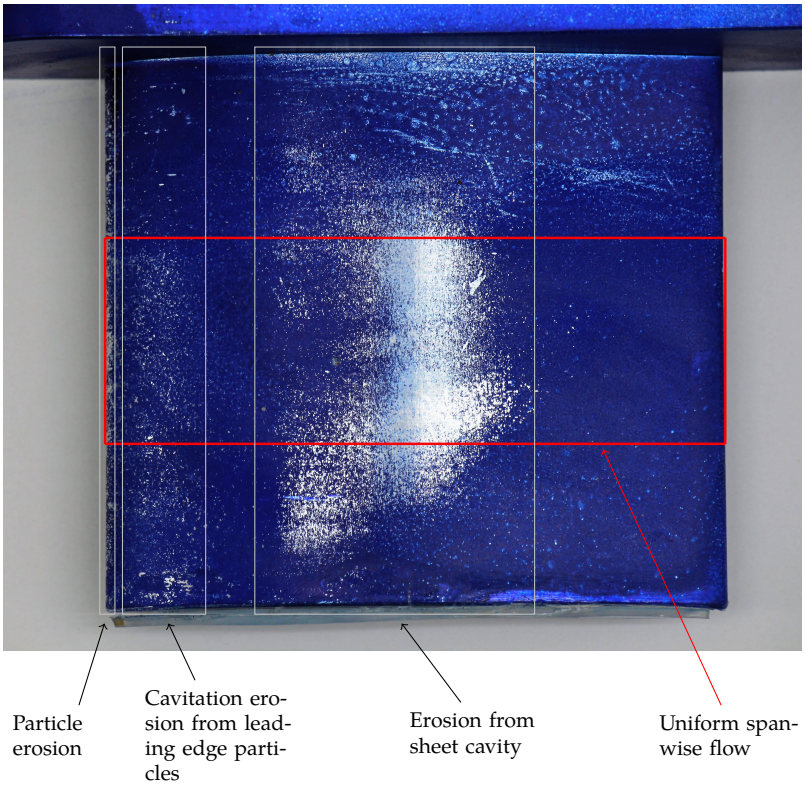

(a) Full suction surface

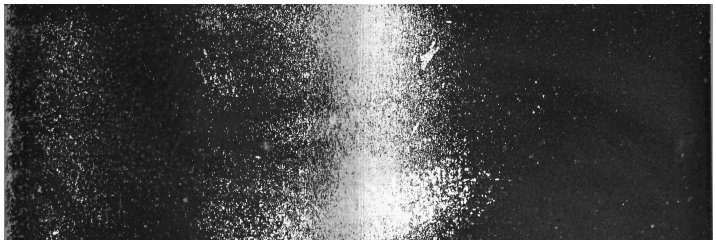

(b) Cropped to uniform spanwise section and converted to gray scale.

Figure 7.18: Paint removal after the preliminary run (number 1 in Table 7.3: 6.4 h at $\sigma = 0.75$ followed by 9 h at $\sigma = 0.73$) with the Baseline geometry. Only the principal erosion region is caused by bubbles collapsing at the sheet cavity closure.

$x/chord = 0.37$ and $x/chord = 0.46$ is located at the final low pressure reading. In this zone the paint layer is fully removed meaning that the maximum capacity of the paint approach for erosion measurement has been surpassed. It is likely that the real erosive intensity exerted between $x/chord = 0.37$ and $x/chord = 0.46$ onto the aluminium surface is not as flat as presented here.

In Figure 7.22, the experimental erosion distribution is compared to the data predicted numerically for the Baseline geometry. Because of the differences in approaches and durations, the data can only be compared on a qualitative basis. The shape and location of the erosion intensity distribution is, therefore, of more importance than the computed values. All results

(a) Full suction surface

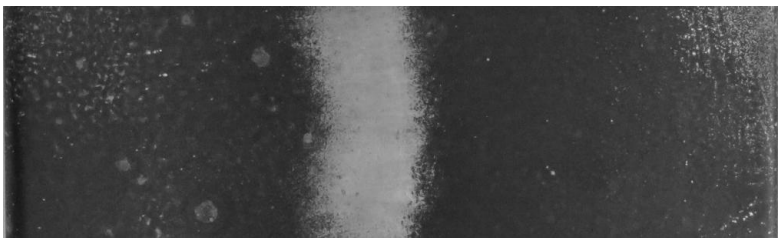

(b) Cropped to uniform spanwise section and converted to gray scale.

Figure 7.19: Paint removal after run 2 (see Table 7.3: 15 h at $\sigma = 0.73$) with the Baseline geometry.

are normalised using the mean value in the eroded region. The reader is reminded that the numerical predictions are obtained from time-resolved simulations with the ZGB cavitation model at $\sigma = 0.587$ for Baseline.

For all erosion indicators, the predicted zone is narrower than observed experimentally. The width of the predicted erosion action is governed by the width of the unsteady cavitating region. At $\sigma^{num} = 0.587$, the time-resolved simulation produced a cavity with smaller variations in length than recorded here. Except for the *Mouvanal* prediction, erosion is predicted to occur between $x/chord = 0.35$ and $x/chord = 0.4$. This corresponds to the zone of highest pressure and volume fraction variation. The *Mouvanal* technique delivers an erosion zone that begins at $x/chord = 0.4$ and ends at $x/chord = 0.46$. The specificity of this approach is that it is not the immediate pressure or volume fraction and their rate of change that is taken into

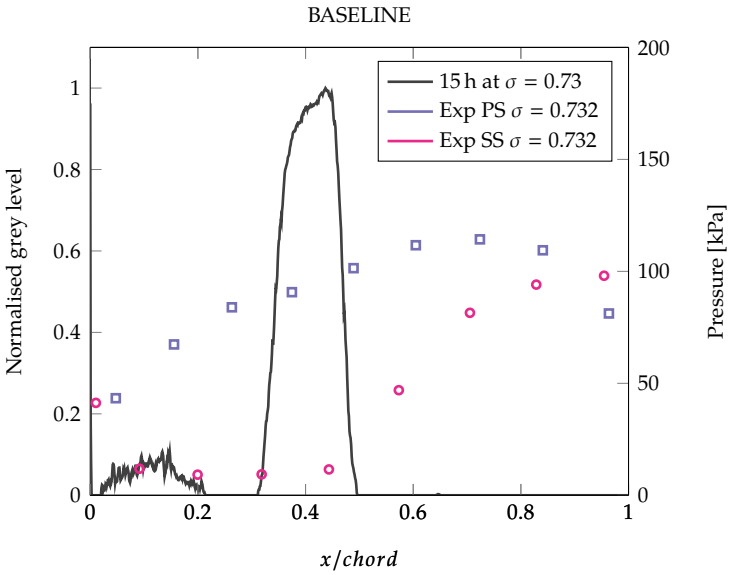

Figure 7.20: Streamwise gray level distribution (spanwise averaged from Figure 7.19b) for the Baseline case compared against the measured surface pressure at $\sigma = 0.732$ ($\sigma = 0.73$ for erosion testing).

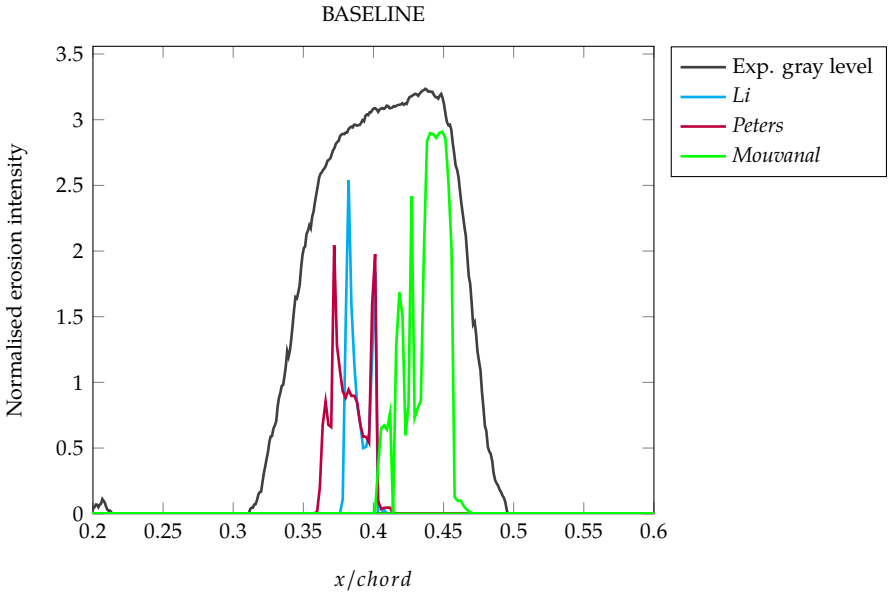

Figure 7.21: Comparison of experimental gray level with computational erosion predictions (see Section 6.3) for the Baseline geometry: Li et al., Peters et al. and Mouvanal et al. indicators. The experimental data is obtained at $\sigma^{exp} = 0.73$, while the computational analysis is carried out at $\sigma^{num} = 0.587$ for the same closure position $x/chord = 0.4$.

consideration, but whether conditions spanning previous time steps are met. This produces a delay in activation of cavitation erosion compared to the other methods.

As far as the shape of the erosion distribution goes, all produce an abrupt peak centred at the closure point rather than the rounded experimental curve. The exception, here again, is the *Mouvanal* approach. Because of the inadequacy of the paint method to evaluate erosive

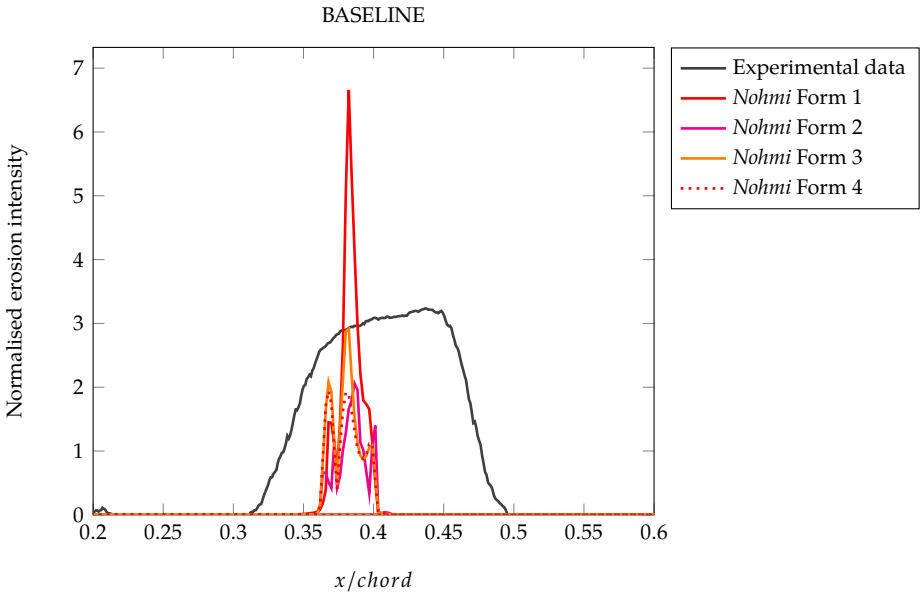

Figure 7.22: Comparison of experimental gray level with computational erosion predictions (see Section 6.3) for the Baseline geometry: Nohmi et al. indicators.

intensity once the layer has been depleted, one can argue that the experimental distribution does not represent the actual pattern. However, when observing the erosion experiment during operation, no such narrow zone showed signs of accelerated progress. Rather, a larger region of about $0.1 \times chord$ got eroded at the same rate as portrayed by the current results.

For DP 12, the erosion test is run at operating conditions identical to Baseline i.e. $\sigma = 0.73$. The suction surface after exposure is shown in Figure 7.23. The erosive action appears less powerful than for the Baseline as the paint layer in the region corresponding to cavity closure is only thinned instead of being peeled off. Indeed, a cluster of punctual impacts are revealed by the lighter colour but no bare aluminium is uncovered. As illustrated by the characterisation experiment, the DP 12 geometry produces softer cavitation: the cavity is better attached and the closure region is more homogeneous. The outcome of the erosion test suggests that the attenuated features of DP 12 cavitation are transmitted to the erosion aggressiveness. This constitutes a positive indication of the capability of our *shock smoothing* design strategy. Naturally, repeated tests are needed to enhance the reliability of the result.

As well as the principal erosion zone, two small lighter regions are visible further upstream and located symmetrically from midspan. Because of side wall effects, the cavity closure is located further upstream and sits on the other side of the smoothing kink. This corresponds to the peak in the wavy distribution where the closure jump is amplified rather than attenuated. As a result, erosion is accentuated at the pre-kink point for DP 12. The implication is that at higher cavitation numbers, when the cavity closure is located in the aforementioned region,

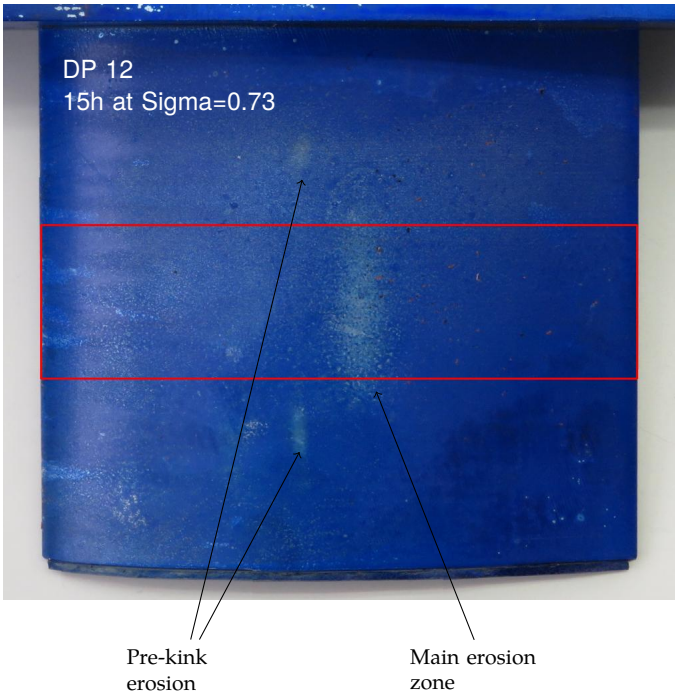

(a) Full suction surface

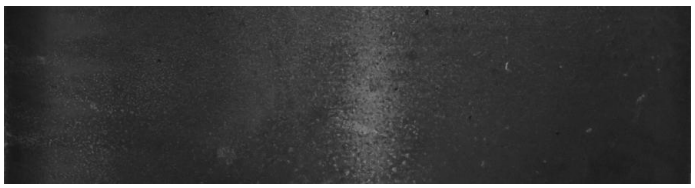

(b) Cropped to uniform spanwise section and converted to gray scale.

Figure 7.23: Paint removal after run 3 (see Table 7.3: 15 h at $\sigma = 0.73$) with the DP 12 geometry.

erosion is likely to be stronger than for the smooth Baseline case. Nevertheless, given the small size of the cavity in that condition, its erosive intensity remains within tolerable bounds. Cavitation assessment over the complete breakdown range is needed to ascertain this effect. On a more compelling note, the presence of the two pre-kink patches supports the correlation between shock amplitude at cavity closure and erosion strength.

The chordwise distribution is presented in Figure 7.24 and compared to the Baseline distribution. The DP 12 erosion patch is shifted downstream of the Baseline one and centred between pressure taps 5 and 6. With the characterisation experiment, it was shown that the Baseline and DP 12 cavity lengths are comparable (see Figure 7.15). At $\sigma = 0.732$ in particular, the DP 12 closure is measured further upstream. However, one must bear in mind that the cavity length data is taken from wide spaced time-averaged pressure readings and that the closure position can intermittently exceed the proposed range. Here, it is advanced that the peculiar suction side pressure distribution is able to either soften or suppress a large number

of collapse events between $x/chord = 0.3$ and $x/chord = 0.42$. The bulk of erosive action is limited to the region from $x/chord = 0.42$ to $x/chord = 0.5$ and kept at low intensity as portrayed in Figure 7.24 because of dampened bubble collapses and lower cavity presence.

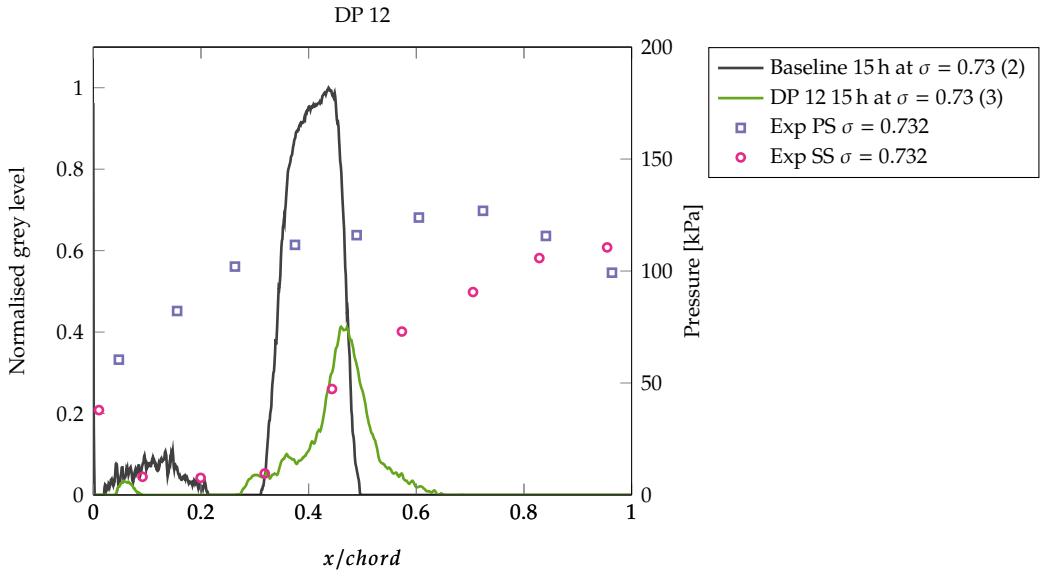

Figure 7.24: Streamwise gray level distribution (spanwise averaged from Figure 7.23b) fro DP 12 compared against the measured surface pressure at $\sigma = 0.732$ ($\sigma = 0.73$ for erosion testing) and the Baseline paint removal result in identical conditions.

In Figures 7.25 and 7.26, the predicted erosion patterns are plotted against the measured distribution. As observed for the Baseline case, the numerical indicators consistently place the erosive peak further upstream than the experimental data. For DP 12, the issue is that the time-resolved computation produces a stable cavity with small closure variations only in a narrow region around $x/chord = 0.4$. The resulting predictions, regardless of the approach, yield a substantially reduced erosive intensity compared to the competing designs. Here, the reader is referred to Figures 6.21 to 6.27 in Section 6.3. The more potent erosion found between $x/chord = 0.42$ and $x/chord = 0.5$ is overlooked. The width of the predicted erosion zone is affected in the same manner: all are spread over a zone of length $\Delta x/chord \approx 0.03$ except for the *Mouvanal* indicator which covers $\Delta x/chord \approx 0.06$.

7.5 Concluding remarks

Two experimental procedures were detailed here. The first consisted in analysing the flow field for three of the geometries in our design set: Baseline, VY 3 and DP 12. Pressure measurements taken in non-cavitating conditions showed good agreement between the numerically predicted

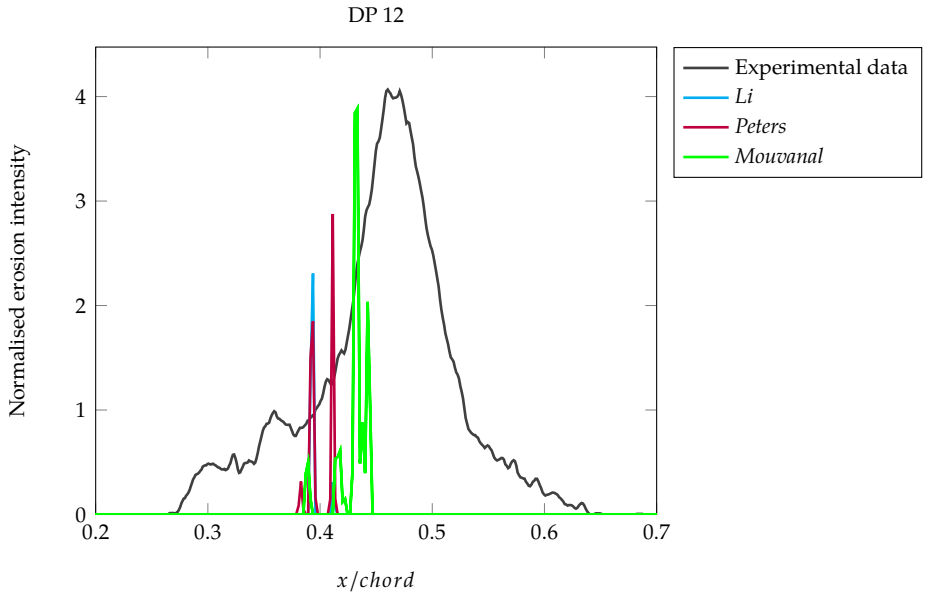

Figure 7.25: Comparison of experimental gray level with computational erosion predictions (see Section 6.3) for the DP 12 geometry: Li et al., Peters et al. and Mouvanal et al. indicators. The experimental data is obtained at $\sigma^{exp} = 0.73$, while the computational analysis is carried out at $\sigma^{num} = 0.583$ for the same closure position $x/chord = 0.4$.

pressure distributions and the experimental ones for all tested cases, giving us proof of the reliability of the experimental rig.

At lower pressures, with the appearance of cavitation, discrepancies arose between experimental and numerical data. In the experiment, cavitation inception occurred at pressures higher than predicted. Furthermore, the pressure measured within the cavity plateaued at 10 kPa instead of the 2 kPa to 3 kPa associated with saturation vapour pressure. This was due to the large quantity of air entrained and dissolved in the liquid flow, responsible for precipitating bubble formation Brennen [1]. At lower cavitation numbers, the discrepancy translated to a consistent downstream offset in closure location between experimental and numerical data.

In terms of the performance of the tested cavitation models, the TE approach appeared superior to the ZGB approach because of its significantly smaller difference with experimental results. This supports the argument that the inclusion of air as a parameter is a non-negligible step in numerical modelling of cavitation.

Similarities between experiments and numerical predictions for cavitating flow were nevertheless picked up, most notably, in the evolution of the dynamic regime. Two fluctuation modes were identified through high speed video capturing: a small amplitude, high frequency oscillation observed from inception, and a large amplitude, low frequency cycle appearing for large ($x/chord > 0.5$) cavities. These matched the two frequency groups detected by the time resolved computational analysis.

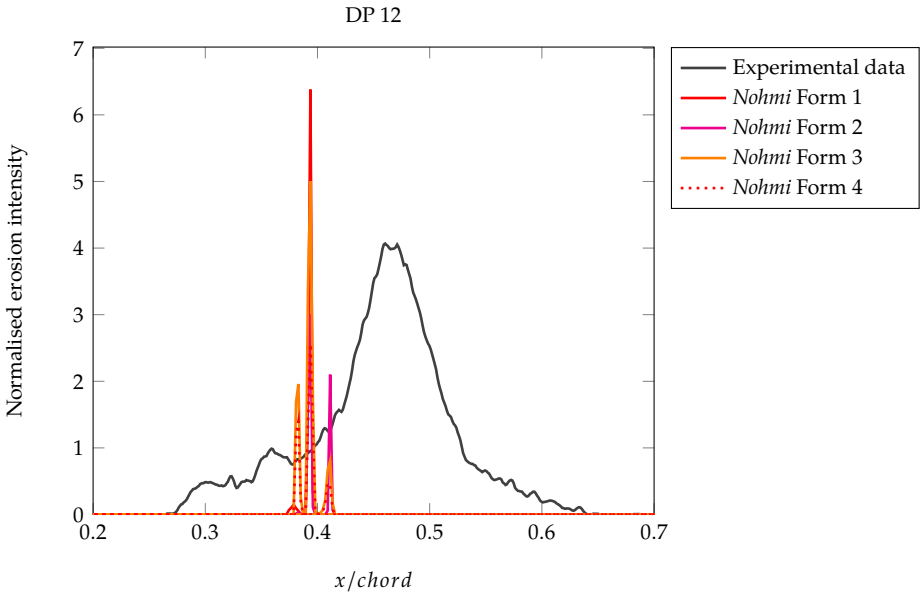

Figure 7.26: Comparison of experimental gray level with computational erosion predictions (see Section 6.3) for the Baseline geometry: Nohmi et al. indicators.

The conclusions drawn from blade-to-blade comparison concurred with those arrived at numerically : (i) the similarity in inception conditions and cavity growth rate for the Baseline and shock focused cases (DP 12 here), (ii) the delay in cavitation inception for aft-loaded geometries (VY 3), (iii) the faster growth of the cavity sheet for aft-loaded cases. The study also revealed a significant difference in the aspect of cavitation between the Baseline and DP 12 case. For identical conditions, the latter produced a thinner and more stable cavity with a substantially smaller amount of bubbly mixture at the closure region.

The second experiment was aimed at measuring the blades' erosive performance. The paint removal approach was adopted and applied to the Baseline and DP 12 cases, thus, providing an evaluation of the shock smoothing strategy. After 15 h of exposure at $\sigma = 0.73$ (or for a closure location of $x/chord \approx 0.4$), comparative analysis revealed a clear disparity in favour of the shock smoothed geometry (DP 12). Instead of the Baseline's fully uncovered surface, the paint layer was only speckled in a contained region.

The eroded surfaces were processed through imaging techniques to provide a streamwise aggressiveness profile, which was compared to the numerically predicted erosion distributions. The numerical approaches match the experimental results in terms of location but consistently under-evaluate the spread of erosion. Out of the tested techniques, it is the Mouvanal et al. indicator that appears to provide the most reliable aggressiveness profile.

8 Conclusion and Future Work

With the increase in rotational speed of turbomachinery systems, cavitation aggressiveness is intensified. The amplified structural damage drastically downgrades the life expectancy of rotating parts. Gains in cost and efficiency brought about by smaller and faster configurations are immediately cancelled out. To overcome this issue and allow the industrial drive for compactness to continue, new solutions are needed to reduce cavitation erosion.

The aim of this research was to demonstrate the effectiveness of controlling cavitation aggressiveness through blade design. The work was based on the assumption that the character of the cavity closure shock could impact the erosive mechanisms of bubble collapse. To test the hypothesis, a 2D cascade inverse design solver for cavitating flow was developed and used to generate a family of geometries with competing shock profiles. These were then assessed numerically and experimentally with erosion performance evaluation as a primary target. The results are summarised in the following sections.

8.1 Inverse Cavitating Flow Solver

The new blades were designed under one guideline: deliver a variety of cavity closure shock characteristics. To that end, the inverse design algorithm for cavitating flow was developed. It constitutes one of the major contributions of this research as it demonstrates the feasibility of designing under cavitating conditions. The solver combines several state-of-the-art numerical techniques which have been adapted to overcome the difficulties associated with predicting cavitating flow, namely its multiphase nature and range in flow regime. The phase change,

firstly, is modelled using the TE equation of state of Nohmi et al. [42], which is a homogeneous barotropic approach. It was selected because of its ability to take into account liquid compressibility and inclusion of entrained air. The fluxing scheme was carefully selected by comparing four approaches: the Jameson et al. [96] central technique with artificial dissipation, the Roe [97] upwind FDS technique, the original AUSM [98] hybrid scheme and its updated version the SLAU [100] scheme. Comparisons of shock capturing and computational effectiveness, put the SLAU approach in front of all the rest.

The preconditioning used to accelerate the computation by clustering eigenvalues combines the conservative formulation of Weiss and Smith [104] and the multidimensional optimisation by Turkel [105]. The development of the multigrid routine was a crucial step. Special treatments were taken from hypersonic flow practices to handle the cavity closure region where the high speed vapour ($M > 10$) and low speed liquid ($M < 0.2$) are separated by the high amplitude shock. Two methods turned out to be essential: the upwind residual smoothing and residual shock weighting. Trial and error selection of the parameters delivered a tenfold improvement in convergence speed.

Two inverse design methods were successfully implemented into the solver: the $\overline{V_y}$ and Δp approaches. The Δp algorithm was clearly shown to be the superior method because of its far greater computational efficiency. It was found that a reinterpretation of the permeable wall boundary condition as a modified reflecting boundary was necessary to ensure stability and convergence.

Together, these algorithmic blocks delivered a robust and fast solver. In pure analysis mode and in identical conditions, it largely outperforms ANSYS Fluent in terms of computational effort, all the while producing the same level of sharpness.

8.2 Designed Geometries

New geometries were designed following two approaches: tip to tail and shock focused modifications. In the first strategy, global changes are imposed on the profile in order to change the overall loading type. Three geometries came out of this: VY 3 (aft-loading), VY 7 (strong aft-loading), VY 8 (fore-loading). The rationale was to use the properties of aft-loaded blades to reduce shock amplitude and those of fore-loaded blades to increase it, and observe the effect on erosion aggressiveness.

The shock focused route consisted in enforcing the low gradient pressure recovery without perturbing the rest of the geometry. With this approach, the idea was to test the working

hypothesis directly in a manner that maintained hydrodynamic performance. Successful runs using both $\overline{V_y}$ and Δp methods produced geometries with a characteristic kink in the camber line. It was shown that the kink drove the shock softening mechanism by imposing a wavy suction side distribution with a second pressure drop. Out of the successful *shock focused* cases, the three best (VY 4, DP 12 and DP 16) were selected by measuring the amplitude of the improved closure shock.

Table 8.1: Summary of selected designs

Design Case	Design strategy		Inverse algorithm		Cavitation number at design σ			Blade channel cells at design	
	Shock focused	Tip to tail	V_y	Δp	0.652	0.680	1.367	64×32	112×32
Selected designs									
VY 3		Aft-loading	•				•	•	
VY 7		Strong aft-loading	•				•	•	
VY 8		Fore-loading	•				•	•	
VY 4	•		•		•			•	
DP 12	•			•		•			•
DP 16	•			•		•			•

8.3 CFD Analysis of Design Set

The performance of the new geometries was assessed numerically first. All seven blades (6 designs and Baseline) were run with ANSYS Fluent using the Zwart et al. [26] cavitation model and RANS turbulence. Both steady state and time resolved analyses were carried out. The aim of the steady state runs was to verify that the flow behaviour targeted at design was also picked up by the RANS solver using a competing cavitation model. The result of the analysis was positive with all expected trends confirmed: aft-loaded designs (cases VY 3 and VY 7) yielded weaker shocks and thinner cavities, fore-loaded design (case VY 8) amplified the shock and cavity thickness, and the shock focused designs (cases VY 4, DP 12 and DP 16) reduced the shock amplitude at design condition without altering the suction performance.

With the time resolved simulations, a more in-depth characterisation of the cavitating flow was generated. The focus was shifted to measuring the unsteadiness of each design. Runs were carried out in non-cavitating conditions first, before gradually descending through the

cavitation number range. Performance metrics such as ΔV_y, lift and drag were quantified in terms of time averages and data spread. Two blade cavitation regimes were identified: stable fixed length sheet and unstable growing and collapsing sheet. It was found that the transition depended on the global loading type. For the fore-loaded case, the transition was gradual and initiated after the 3% breakdown point ($\sigma_T < \sigma_{3\%}$). For the aft-loaded designs, the transition was abrupt and breakdown occurred within the unstable regime. For the shock focused cases, the study showed that unsteadiness was minimised when the shock location matched the design location i.e. when the amplitude of the shock was reduced.

The time-resolved data also served to predict the erosion aggressiveness of each design. To that end, the indicators presented in Sections 2.2.2 and 6.3 were used to produce time averaged aggressiveness distributions. To put blades on an equal footing, the comparison was carried out in the $\sigma_{3\%}$ condition. From the computed results, a dichotomy was shown to exist between the implemented approaches: (i) those based on the time derivative of pressure and volume fraction, (ii) those constructed from the instantaneous values of the same variables. The first group of techniques are mainly driven by the unsteadiness level, while, for the second group, the amplitude of the closure is of primary importance. This discrepancy was particularly visible on fore-loaded case VY 8, which was either at the low erosion end of the spectrum with the time derivative methods or at the high end with the instantaneous methods.

Blade to blade comparison addressed the spread of erosion prone regions and the intensity of the erosion metrics. Results suggested that the shock focused designs and ensuing wavy distribution were highly beneficial to the erosive performance. In particular, designs DP 12 and DP 16, with the former consistently ranked least erosive by all tested indicators. This constituted an important milestone in this research as it provided the fist element of proof supporting the validity of the working hypothesis.

8.4 Experimental Assessment

Following the numerical characterisation, an experimental study was carried out on three of the selected geometries: Baseline, VY 3 (aft-loaded) and DP 12. The study was made possible by constructing an entirely new platform to replicate the cascade configuration with modular capabilities. The initial study consisted in following the procedure used numerically to evaluate erosion growth i.e begin at high σ and gradually descend. The flow field was characterised by surface pressure readings and visual recordings of blade cavitation. Non-cavitating results showed good agreement with the pressure distributions predicted numerically by both the *in-*

house solver and Fluent for all tested cases. This was proof of the reliability of the experimental rig. It also confirmed that the wavy suction side distribution of case DP 12 did not excessively perturb the flow field: the boundary layer remained attached throughout the kink region.

In the experiment, cavitation inception was found to occur at substantially higher pressures than predicted. Furthermore, the pressure measured within the cavity plateaued at 10 kPa instead of the 2 kPa to 3 kPa associated with saturation vapour pressure. The origin of this discrepancy was traced back to the large quantity of air entrained and dissolved in the liquid flow, responsible for precipitating bubble formation. This concurs with the remarks made by Brennen [1] who insists on the dependence of cavitation inception on air presence. At lower cavitation numbers, the discrepancy translated to a consistent downstream offset in closure location between experimental and numerical data. Surface pressure readings were used to compare the prediction performance of the two tested cavitation models, i.e. TE and ZGB, on this new cascade configuration. It was made evident that the TE model carried a significant advantage over the ZGB approach because of its significantly smaller difference with experimental results. This has serious implications on the accuracy of cavitation models, suggesting that the inclusion of air as a parameter is a non-negligible step.

The high speed video capturing confirmed the evolution of the dynamic cavity behaviour picked up by the computational analysis. At high cavitation numbers, unsteadiness was limited to small movements in the closure region. As the cavity grew, changes in size became larger and the duration of each cycle increased. Two fluctuation modes were generally identified: a small amplitude, high frequency oscillation observed from inception, and a large amplitude, low frequency cycle appearing for large ($x/chord > 0.5$) cavities. These matched the two frequency groups detected by the time resolved computational analysis.

Comparing experimental flow characterisation results for the three blades confirmed (i) the similarity in inception conditions and cavity growth rate for the Baseline and shock focused cases (DP 12 here), (ii) the delay in cavitation inception for aft-loaded geometries (VY 3), (iii) the faster growth of the cavity sheet for aft-loaded cases. The study also revealed a significant difference in the aspect of cavitation between the Baseline and DP 12 case. For identical conditions, the latter produced a thinner and more stable cavity. A noteworthy trait was the substantially smaller amount of bubbly mixture at the closure region.

To measure the blades' erosive performance, the paint removal approach was adopted. The inability to identify the 3% breakdown conditions meant that VY 3 had to be eliminated from the erosion analysis. By assessing the Baseline and DP 12 cases, the impact of shock smoothing was directly evaluated. Paint removal results were obtained after 15 h of exposure at $\sigma = 0.73$

(or for a closure location of $x/chord \approx 0.4$). Comparative analysis revealed a clear disparity in favour of the shock smoothed geometry (DP 12). Instead of the Baseline's fully uncovered surface, the paint layer was only speckled in a contained region. By processing images of the eroded surfaces, the results were compared to the predicted erosion distributions.

8.5 Concluding Remarks

Overall, it is safe to say that the objective of this research has been attained. Not only did numerical and experimental evaluations demonstrate the potency of closure shock modification on erosion aggressiveness, this work also lays out an unprecedented and now verified concept for controlling erosion aggressiveness in turbomachinery flows. Through the accomplishment of this research, significant advances in cavitating flow control have been produced and major findings have been brought to light:

- the work contains the first development of an inverse design algorithm capable of generating blades under cavitating conditions,
- it provides new experimentally supported arguments for the necessity of air parametrisation in cavitation models,
- the novel kink feature and associated wavy distribution are presented as products of the shock smoothing design strategy,
- the wavy distribution acts as a cavity stabiliser and prevents vapour detachment from the surface,
- the camber kink and wavy pressure distribution lead to a marked reduction in erosion rate without any negative impact on the rest of the flow field.

8.6 Limitations Due to Simplifications

It is important to go over the simplifications made during the realisation of this work and understand their potential effect on the outcomes laid out here. The points of importance are:

- two-dimensional definition,
- assumption of inviscid flow,
- steady-state based design.

The two-dimensional simplification has been addressed in Chapter 1. It is justified here by considering that cascade flow is similar in nature to flow through axial impellers. In configurations of this type, spanwise variations are negligible compared to those in action in the streamwise direction. One could therefore readily apply the 2D methodology presented in this work to axial flow type impellers by stacking successive spanwise sections. Similar outcomes are expected to result from this procedure.

For mixed flow impellers, radial flow impellers or Francis turbines, however, contributions in the counter-streamwise direction cannot be neglected. Our strategy would therefore need to be enhanced to take into account the additional forces at play. This constitutes one of the major suggestions for further work.

To minimise the complexity of the inverse design solver, the flow was assumed inviscid. In Section 4.5, it was shown that this simplification did not downgrade the reliability of the steady state solution as viscous and RANS forces effected a negligible change on cavity closure location and jump amplitude. For the unsteady phenomena that unfold within cavitating flow and are responsible for erosion one must examine the mechanism at the origin of cavity dynamics. It is best understood by considering the interface between cavity and liquid and the closure point where the pressure equilibrium is lost due to the sudden one-sided increase. Here, the low pressure vapour cannot resist the high pressure liquid water causing a re-entrant jet to force its way upstream into the cavity. This chain of events is governed solely by inertial effects such that viscous contributions can be omitted without loss of accuracy. For the objectives of this work, the assumption of inviscid flow is therefore legitimate and has provided compelling results in cavitation instability or erosion analysis [114, 115, 116].

The fact that the typical closure shock pressure profile, shown in Figure 5.1 for example, is not an indefinitely sustainable configuration leads us to address the assumption of steadiness. In reality, the cavity continuously oscillates at amplitudes that depend on the flow condition as shown in Section 6.2. This is particularly problematic for the shock focused design strategy which assumes that the cavity closure is immobile. A more rigorous approach would consist in operating gradient smoothing through inverse design using the time-averaged pressure as the baseline distribution.

Nevertheless, post-design analysis of shock focused designs VY 4, DP 12 and DP 16 (see Figure 6.5 in Section 6.1.2) reveals that the new designs lead to shock amplitude reduction over a streamwise region rather than a single point. Consequently, the approach remains effective as long as the cavity fluctuations are within a case dependent margin. To eliminate the issue associated with cavity unsteadiness from the rationale of our methodology, one can consider

the potential energy interpretation of cavitation aggressiveness [61] (see Section 2.2.2). It states that the potential power is driven by the variation in the surrounding liquid pressure meaning that one only has to consider the flow features of the liquid phase to determine erosion risk. In essence, our strategy works by imposing a slow pressure increase on the surrounding liquid rather than the cavity itself to reduce the erosive potential of collapsing cavities. Ultimately, the evidence delivered by the erosion experiment is in support of the steady state based design approach.

8.7 Suggestions for Further Work

The advancement of the research presented here can follow two directions. The first focuses on the enhancement of the inverse design solver to increase its applicability and accuracy. The second addresses the performance analyses (both numerical and experimental). Erosion evaluation, in particular, can be further refined to provide a more exhaustive and reliable picture.

8.7.1 Inverse Design Solver Enhancement

Because of feasibility concerns, the scope of the solver was limited to inviscid flow for stationary 2D configurations. It was shown that the inclusion of viscous and turbulent effects did not significantly affect the computed length of the steady state cavity nor the amplitude of the shock (see Section 4.5). However, strong wake effects and boundary layer separation were completely overlooked. This was problematic when comparing the non-cavitating ΔV_y outputs and forced an additional correction step (see Section 5.2.5).

Augmenting the existing code with viscous term discretisation and turbulence modelling would enhance the accuracy of the flow field and reliability of the produced geometries. To achieve this, one can follow the work carried out by Tiow and Zangeneh [80] on transonic cascades which uses the Denton [83] body force approach to take turbulence into account. Alternatively, de Vito et al. [117] and Roidl and Ghaly [118] apply the Bladwin-Lomax algebraic RANS model to a surface distribution based inverse design approach for the former, and a loading type method for the latter. To the author's knowledge, no established inverse method makes use of higher order turbulence models. The issue comes from (i) the risk of boundary layer separation affecting geometry treatment, (ii) the high computational cost of repeatedly calculating blade wall distance.

Furthermore, the two dimensional methodology proves the validity of the concept but

does not constitute, by itself, a usable turbomachinery design tool. That objective requires 3D treatment and a rotating frame formulation of the governing equations. The work by Tiow and Zangeneh[82, 81] or Ray and Zangeneh [119] can be used as reference codes to adapt the existing solver. Of most importance, is the capacity to handle the mixed and radial flow configurations frequently used in pump or turbine (Francis type) installations. With such a code, the cavitation erosion control methodology could be tested on existing impeller, turbine or propeller cases known to suffer from structural damage.

8.7.2 Erosion Aggressiveness Evaluation

The erosion analysis carried out numerically focused on the single 3% breakdown point. This resulted in a restricted characterisation of the erosion performance spectrum. Aggressiveness intensities at higher and lower cavitation numbers were not assessed. An interesting addition would be to track the increase in erosion rate throughout the operating range. Aggressiveness distributions could be integrated over the blade to provide single number metrics for each blade and each condition. This would yield a set of breakdown type curves (similar to Figures 6.4 or 6.17) which depict the case by case erosion increase profiles. The data would be particularly interesting for the shock focused cases which produce a slight increase in shock amplitude at higher cavitation numbers (see Figure 6.5).

Experimental assessment was carried out on the Baseline and DP 12 cases. Out of the design selection, numerous blades remain to be tested. Cases VY 3 and VY 8 would be the next chosen candidates. Comparing the two would decide which of the fore-loaded or aft-loaded configuration works best at reducing erosion aggressiveness. Because of the strong discrepancy in cavity growth profiles, the blades should be evaluated at several cavitation numbers as just described for the numerical erosion analysis. Assessing blade VY 8 experimentally would also serve to determine which group of erosion predictors is most accurate i.e. time derivative or instantaneous value.

The choice of using the paint removal technique for experimental erosion assessment was motivated mainly by limitations in time. The method works for qualitative evaluation and provides a clear demarcation of erosion prone zones. The issue with the paint technique is that measurements hit a saturation point as soon as the layer is fully removed. This was observed for the Baseline assessment (see Figure 7.19). Instead, a direct material erosion method is recommended. These have been used extensively in damage measurement for turbomachinery flows or single hydrofoils. The quantitative erosion intensity is given by the density of surface pits. The measurement is therefore entirely reliable as long as material loss is sufficiently low

to avoid flow field disturbances. The long exposure time can be minimised by applying a layer of softer material [9].

Bibliography

[1] C. E. Brennen. *Hydrodynamics of pumps*, volume 9781107002. 2011.

[2] P. J. McNulty and I. S. Pearsall. Cavitation Inception in Pumps. *Journal of Fluids Engineering*, 104(1):99, 1982.

[3] Johann Friedrich Gulich. *Centrifugal Pumps*. Springer, Heidelberg, second edi edition, 2010.

[4] Francois Avellan. Introduction to cavitation in hydraulic machinery. *6th International Conference on Hydraulic Machinery and Hydrodynamics*, pages 11–22, 2004.

[5] Igor Karassik, Joseph Messina, Paul Cooper, and Charles Heald. *Pump Handbook*. McGraw-Hill, third edit edition, 2004.

[6] R E A Arndt. Cavitation in Fluid Machinery and Hydraulic Structures. *Annual Review of Fluid Mechanics*, 13(1):273–326, 2003.

[7] François Avellan and Philippe Dupont. Cavitation erosion of the hydraulic machines : generation and dynamics of erosive cavities. *Proceedings of the 14th IAHR Symposium on Hydraulic Machinery : Progress within Large and High Specific Energy Units*, 2:725–738, 1988.

[8] W. K. Chan. Correlation between cavitation type and cavitation erosion in centrifugal pumps. *International Journal of Heat and Fluid Flow*, 11(3):269–271, 1990.

[9] Matevž Dular, Bernd Bachert, Bernard Stoffel, and Brane Širok. Relationship between cavitation structures and cavitation damage. *Wear*, 257(11):1176–1184, dec 2004.

[10] Martin Petkovšek and Matevž Dular. Simultaneous observation of cavitation structures and cavitation erosion. *Wear*, 300(1-2):55–64, 2013.

[11] C. E. Brennen. *Cavitation and bubble dynamics*. Oxford University Press, New York, oxford eng edition, 2013.

[12] K-H. Kim, J-P. Franc, A Karimi, K-H. Kim, J-P. Franc, and A Karimi. *Advanced Experimental and Numerical Techniques for Cavitation Erosion Prediction, Series Fluid Mechanics and Its Applications*, volume 106. Springer, fluid mech edition, 2014.

[13] R T Knapp, J W Daily, and F G Hammitt. *Cavitation*. McGraw-Hill, 1970.

[14] Mingxi Wan, Yangzi Qiao, Shanshan Xu, Xiaodong Liu, and Charles C. Church. *Fundamentals of Cavitation*. Springer, fluid mech edition, 2015.

[15] F R Young. *Cavitation*. World Scientific, 1999.

[16] Maria Vittoria D'Agostino, Luca ; Salvetti. *Fluid Dynamics Of Cavitation and Cavitating Turbopumps*. Springer, Pisa, Italy, 2007.

[17] Aljaz Osterman, Matevž Dular, and Brane Sirok. Numerical Simulation of a Near-Wall Bubble Collapse in an Ultrasonic Field. *Journal of Fluid Science and Technology*, 4(1): 210–221, 2009.

[18] P. Koukouvinis, M. Gavaises, O. Supponen, and M. Farhat. Simulation of bubble expansion and collapse in the vicinity of a free surface. *Physics of Fluids*, 28(5), may 2016.

[19] N. A. Hawker and Y. Ventikos. Interaction of a strong shockwave with a gas bubble in a liquid medium: A numerical study. *Journal of Fluid Mechanics*, 701:59–97, jun 2012.

[20] E. Lauer, X. Y. Hu, S. Hickel, and N. A. Adams. Numerical modelling and investigation of symmetric and asymmetric cavitation bubble dynamics. *Computers and Fluids*, 69:1–19, oct 2012.

[21] Y. Chen and S. Heister. A Numerical Treatment for Attached Cavitation. *Journal of Fluids Engineering*, 116(3):613, sep 1994.

[22] Manish Deshpande, Jinzhang Feng, and Charles L. Merkle. Numerical Modeling of the Thermodynamic Effects of Cavitation. *Journal of Fluids Engineering*, 119(2):420, jun 1997.

[23] Chien-Chou Tseng. *Modeling of Turbulent Cavitating Flows*. PhD thesis, The University of Michigan, 2010.

[24] Y. Delannoy and J. L. Kueny. Two-Phase Flow Approach in Unsteady Cavitation Modelling. In *Spring Meeting of the Fluids Engineering Division*, page 6, 1990.

[25] Akihiro Kubota, Hiroharu Kato, and Hajime Yamaguchi. A new modelling of cavitating flows: A numerical study of unsteady cavitation on a hydrofoil section. *Journal of Fluid Mechanics*, 240(3):59–96, 1992.

[26] Philip J Zwart, Andrew G Gerber, and Thabet Belamri. A Two-Phase Flow Model for Predicting Cavitation Dynamics. In *International Conference on Multiphase Flow*, number 152, page 152, 2004.

[27] Ashok K. Singhal, Mahesh M. Athavale, Huiying Li, and Yu Jiang. Mathematical Basis and Validation of the Full Cavitation Model. *Journal of Fluids Engineering*, 124(3):617, 2002.

[28] Mitja Morgut, Enrico Nobile, and Ignacijo Biluš. Comparison of mass transfer models for the numerical prediction of sheet cavitation around a hydrofoil. *International Journal of Multiphase Flow*, 37(6):620–626, 2011.

[29] Antoine Ducoin, Biao Huang, and Yin Lu Young. Numerical modeling of unsteady cavitating flows around a stationary hydrofoil. *International Journal of Rotating Machinery*, 2012:1–17, 2012.

[30] Charles L Merkle, JinZhang Feng, and Phillip E O Buelow. Computational modeling of the dynamics of sheet cavitation. In *3rd International Symposium on Cavitation*, volume 2, pages 47–54, Grenoble, France, 1998.

[31] Jiongyang Wu, Guoyu Wang, and Wei Shyy. Time-dependent turbulent cavitating flow computations with interfacial transport and filter-based models. *International Journal for Numerical Methods in Fluids*, 49(7):739–761, 2005.

[32] Inanc Senocak and Wei Shyy. Interfacial dynamics-based modelling of turbulent cavitating flows, Part-1: Model development and steady-state computations. *International Journal for Numerical Methods in Fluids*, 44(9):975–995, mar 2004.

[33] Robert F. Kunz, David A. Boger, David R. Stinebring, Thomas S. Chyczewski, Jules W. Lindau, Howard J. Gibeling, Sankaran Venkateswaran, and T. R. Govindan. A preconditioned Navier-Stokes method for two-phase flows with application to cavitation prediction. *Computers and Fluids*, 29(8):849–875, 2000.

[34] Inanc Senocak and Wei Shyy. A pressure-based method for turbulent cavitating flow computations. *Journal of Computational Physics*, 176(2):363–383, 2002.

[35] Zi-ru Li, Mathieu Pourquie, and Tom van Terwisga. Assessment of Cavitation Erosion With a URANS Method. *Journal of Fluids Engineering*, 136(4):041101, feb 2013.

[36] R. F. Tangren, C. H. Dodge, and H. S. Seifert. Compressibility effects in two-phase flow. *Journal of Applied Physics*, 20(7):637–645, jul 1949.

[37] A T J Hayward. Compressibility equations for liquids: a comparative study. *British Journal of Applied Physics*, 18(7):965–977, jul 1967.

[38] Eric Goncalves and Regiane Fortes Patella. Numerical simulation of cavitating flows with homogeneous models. *Computers and Fluids*, 38(9):1682–1696, 2009.

[39] O. Le Métayer, J. Massoni, and R. Saurel. Élaboration Des Lois D'État D'Un Liquide Et De Sa Vapeur Pour Les Modèles D'Écoulements Diphasiques. *International Journal of Thermal Sciences*, 43(3):265–276, mar 2004.

[40] Jl Reboud, Olivier Coutier-Delgosha, B Pouffary, and Regiane Fortes-Patella. Numerical simulation of unsteady cavitating flows: some applications and open problems. In *Fifth International Symposium on Cavitation (CAV2003)*, pages 1–10, 2003.

[41] Yuka Iga, Byeong Rog Shin, Toshiaki Ikohagi, Motohiko Nohmi, and Akira Goto. Numerical Study of Sheet Cavitation Breakoff Phenomenon on a Cascade Hydrofoil. *Journal of Fluids Engineering*, 125(4):643, 2003.

[42] Motohiko Nohmi, Akira Goto, Yuka Iga, and Toshiaki Ikohagi. Cavitation CFD in a Centrifugal Pump. In *Fifth International Symposium on Cavitation (CAV2003)*, pages 1–7, Osaka, 2003.

[43] Chisachi Kato. Industry-University Collaborative Project on Numerical Predictions of Cavitating Flows in Hydraulic Machinery - Part 1: Benchmark test on cavitating hydrofoils. In *ASME-JSME-KSME Joint FLuids Engineering Conference*, 2011.

[44] Jeremy Nahon, Mehrdad Zangeneh, Motohiko Nohmi, and Hiroyoshi Watanabe. Comparative Assessment of a Barotropic Model and a Void Fraction Transport Model for Numerically Predicting Steady Sheet Cavitation. In *Proceedings of the 10th International Symposium on Cavitation (CAV2018)*. ASME Press, 2018.

[45] Lord Rayleigh. VIII. On the pressure developed in a liquid during the collapse of a spherical cavity. *The London, Edinburgh, and Dublin Philosophical Magazine and Journal of Science*, 34(200):94–98, aug 1941.

[46] Robert Hickling and M S Plesset. Nonlinear Bubble Dynamics. *The Physics of Fluids*, 7(7), 1964.

[47] Marc Tinguely. *The effect of pressure gradient on the collapse of cavitation bubbles in normal and reduced gravity*. PhD thesis, Ecole Polytechnique Federale de Lausanne, 2013.

[48] François Avellan and Mohamed Farhat. Shock pressure generated by cavitation vortex collapse. *Proceedings of the 3rd international Symposium on Cavitation Noise and Erosion in Fluid System of the ASME Winter Annual Meeting*, pages 119–125, 1989.

[49] Matevž Dular, Bernd Stoffel, and Brane Širok. Development of a cavitation erosion model. *Wear*, 261(5-6):642–655, 2006.

[50] Masahito Shimada, Yoichiro Matsumoto, and Takashi Kobayashi. Dynamics of the Cloud Cavitation and Cavitation Erosion. *Transactions of the Japan Society of Mechanical Engineers Series B*, 65(634):1934–1941, jun 1999.

[51] Andreas Peters, Hemant Sagar, Udo Lantermann, and Ould el Moctar. Numerical modelling and prediction of cavitation erosion. *Wear*, 338-339:189–201, sep 2015.

[52] F. Pereira, F. Avellan, and Ph. Dupont. Prediction of Cavitation Erosion: An Energy Approach. *Journal of Fluids Engineering*, 120(4):719, 2008.

[53] Regiane Fortes Patella and Jean-Luc Reboud. A New Approach to Evaluate the Cavitation Erosion Power. *Journal of Fluids Engineering*, 120(2):335, 1998.

[54] Hiroharu Kato, Akihisa Konno, Masatsugu Maeda, and Hajime Yamaguchi. Possibility of Quantitative Prediction of Cavitation Erosion Without Model Test. *Journal of Fluids Engineering*, 118(3):582, sep 1996.

[55] Naoya Ochiai, Yuka Iga, Motohiko Nohmi, and Toshiaki Ikohagi. Numerical Prediction of Cavitation Erosion Intensity in Cavitating Flows around a Clark Y 11.7% Hydrofoil. *Journal of Fluid Science and Technology*, 5(3):416–431, 2010.

[56] Mohamed Farhat, Francisco Pereira, and François Avellan. Cavitation Erosion Power as a Scaling Factor for Cavitation Erosion of Hydraulic Machines. In *Proceedings of Bubble Noise and Cavitation Erosion in Fluid Systems, ASME Winter Annual Meeting, New Orleans, USA, Nov*, volume 176, page 129. The American Society of Mechanical Engineers, 1993.

[57] Jean Marc Dorey, Eric Laperrousaz, FranÃ§ois Avellan, Philippe Dupont, Raynald Simoneau, and Paul Bourdon. Cavitation Erosion Prediction on Francis Turbines Part 3 : Methodologies of Prediction. In *Proceedings of the18th IAHR Symposium*, pages 564–573, Dordrecht, the Netherlands, 1996.

[58] Milton S. Plesset and Richard B. Chapman. Collapse of an initially spherical vapour cavity in the neighbourhood of a solid boundary. *Journal of Fluid Mechanics*, 47(2):283–290, may 1971.

[59] Andreas Peters, Udo Lantermann, and Ould el Moctar. Numerical prediction of cavitation erosion on a ship propeller in model- and full-scale. *Wear*, 408-409:1–12, aug 2018.

[60] R. Fortes-Patella, J L Reboud, and L Brianconn-Marjollet. A phenomenological and numerical model for scaling the flow agressiveness in cavitation erosion. Technical report, 2004.

[61] F. G. Hammitt. Observations on Cavitation Damage in a Flowing System. *Journal of Basic Engineering*, 85(3):347, sep 1963.

[62] Motohiko Nohmi, Toshiaki Ikohagi, and Yuka Iga. Numerical Prediction Method of Cavitation Erosion. In *ASME Fluids Engineering Conference*, pages 1139–1145, 2009.

[63] Zi Ru Li, Guang Ming Zhang, Wei He, and Tom Van Terwisga. A numerical study of unsteady cavitation on a hydrofoil by les and URANS method. *Journal of Physics: Conference Series*, 656(1):012157, dec 2015.

[64] Sandeep Mouvanal, Dhiman Chatterjee, Shamit Bakshi, Axel Burkhardt, and Volker Mohr. Numerical prediction of potential cavitation erosion in fuel injectors. *International Journal of Multiphase Flow*, 104:113–124, 2018.

[65] H H Anderson. Prediction of Head, Quantity and Efficiency in Pumps - The Area Ratio Principle. In *Performance Prediction of Centrifugal Pumps and Compressors*, pages 201–211. ASME, 1980.

[66] Carl Pfleiderer. *Die Kreiselpumpen für Flüssigkeiten und Gase*. Springer-Verlag, 5te auflag edition, 2012.

[67] M. Zangeneh, A. Goto, and H. Harada. On the role of three-dimensional inverse design methods in turbomachinery shape optimization. *Proceedings of the Institution of Mechanical Engineers, Part C: Journal of Mechanical Engineering*, 213(1):27–42, 1998.

[68] M J Lighthill. A New Method of Two-dimensional Aerodynamic Design. Technical report, Aeronautical Research Council, 1945.

[69] Stanitz and John D. Design of two-dimensional channels with prescribed velocity distributions along the channel walls. Technical report, NACA, Cleveland, OH, 1953.

[70] W. R. Hawthorne, C. Wang, C. S. Tan, and J. E. McCune. Theory of Blade Design for Large Deflections: Part I—Two-Dimensional Cascade. *Journal of Engineering for Gas Turbines and Power*, 106(2):346, apr 1984.

[71] C. S. Tan, W. R. Hawthorne, J. E. McCune, and C. Wang. Theory of Blade Design for Large Deflections: Part II—Annular Cascades. *Journal of Engineering for Gas Turbines and Power*, 106(2):354, 1984.

[72] M. Zangeneh. A compressible three-dimensional design method for radial and mixed flow turbomachinery blades. *International Journal for Numerical Methods in Fluids*, 13(5): 599–624, 1991.

[73] M. Zangeneh, B. Ribi, C. Roduner, M. Schleer, S. S. Hong, F. Pløger, and R. S. Abhari. Investigation of an Inversely Designed Centrifugal Compressor Stage—Part I: Design and Numerical Verification. *Journal of Turbomachinery*, 126(1):73, 2003.

[74] G. Meauzé. An Inverse Time Marching Method for the Definition of Cascade Geometry. *Journal of Engineering for Power*, 104(3):650, 1982.

[75] L. Zannetti. Time-Dependent Method to Solve the Inverse Problem for Internal Flows. *AIAA Journal*, 18(7):754–758, jul 2008.

[76] O. Léonard and R. A. Van den Braembussche. Design Method for Subsonic and Transonic Cascade With Prescribed Mach Number Distribution. In *Journal of Turbomachinery*, volume 114, page 553. ASME, jun 1991.

[77] T. Dang and V. Isgro. Euler-based inverse method for turbomachine blades. I - Two-dimensional cascades. *AIAA Journal*, 33(12):2309–2315, 1995.

[78] A. Demeulenaere, O. Léonard, and R. Van Den Braembussche. A two-dimensional Navier-Stokes inverse solver for compressor and turbine blade design. In *Second European Conference on Turbomachinery - Fluid Dynamics and Thermodynamics*, volume 211, pages 299–307, 1997.

[79] T. Dang, S. Damle, and X. Qiu. Euler-Based Inverse Method for Turbomachine Blades, Part 2: Three-Dimensional Flows. *AIAA Journal*, 38(11):2007–2013, 2000.

[80] W. T. Tiow and M. Zangeneh. A Viscous Transonic Inverse Design Method for Turbomachinery Blades: Part I — 2D Cascades. In *International Gas Turbine Conference and Exhibit*. ASME, jun 1998.

[81] W. T. Tiow and M. Zangeneh. A Three-dimensional Inverse Method Based on Pressure Loading for the Design of Turbomachinery Blades. In *Advances of CFD in Fluid Machinery Design*. Professional Engineering Publishing, 2003.

[82] W. T. Tiow and M. Zangeneh. Application of a three-dimensional viscous transonic inverse method to NASA rotor 67. *Proceedings of the Institution of Mechanical Engineers, Part A: Journal of Power and Energy*, 216(3):243–256, 2002.

[83] J. D. Denton. The Use of a Distributed Body Force to Simulate Viscous Effects in 3D Flow Calculations. In *International Gas Turbine Conference and Exhibit*, page V001T01A058, Duesseldorf, Germany, 1986.

[84] M. Zangeneh, A. Goto, and T. Takemura. Suppression of Secondary Flows in a Mixed-Flow Pump Impeller by Application of Three-Dimensional Inverse Design Method: Part 1—Design and Numerical Validation. *Journal of Turbomachinery*, 118(3):536, 1996.

[85] A. Goto, T. Takemura, and M. Zangeneh. Suppression of Secondary Flows in a Mixed-Flow Pump Impeller by Application of Three-Dimensional Inverse Design Method: Part 2—Experimental Validation. *Journal of Turbomachinery*, 118(3):544, 1996.

[86] A. Goto and M. Zangeneh. Hydrodynamic Design of Pump Diffuser Using Inverse Design Method and CFD. *Journal of Fluids Engineering*, 124(2):319, 2002.

[87] Hidenobu Okamoto and Akira Goto. Suppression of Cavitation in a Francis Turbine Runner by Application of 3D Inverse Design Method. In *Joint U.S.-European Fluids Engineering Division Conference*, pages 851–858. ASME, 2009.

[88] K. Daneshkah and M. Zangeneh. Parametric design of a Francis turbine runner by means of a three-dimensional inverse design method. In *25th IAHR Symposium on Hydraulic Machinery and Systems*, volume 12, page 012058. IOP Publishing, aug 2010.

[89] D. Bonaiuti, M. Zangeneh, R. Aartojarvi, and J. Eriksson. Parametric Design of a Waterjet Pump by Means of Inverse Design, CFD Calculations and Experimental Analyses. *Journal of Fluids Engineering*, 132(3):031104, 2010.

[90] J. F. Gülich. Selection criteria for suction impellers of centrifugal pumps. *World Pumps*, 2001(415):42–46, apr 2001.

[91] Fengrong Yu, Lixiang Zhang, Yun Zeng, and Zhumei Luo. Preliminary discussion for improving cavitating flow around hydrofoil by punching. *Procedia Engineering*, 31:261–266, 2012.

[92] Michael Hofmann, Bernd Stoffel, J. Friedrichs, and G. Kosyna. Similarities and Geometrical Effects on Rotating Cavitation in Two Scaled Centrifugal Pumps. In *Fourth International Symposium on Cavitation, Pasadena, CA USA*, 2001.

[93] Hyosung Sun. Numerical study of hydrofoil geometry effect on cavitating flow. *Journal of Mechanical Science and Technology*, 26(8):2535–2545, 2012.

[94] J. Blazek. *Computational Fluid Dynamics: Principles and Applications*. Elsevier Ltd, first edit edition, 2001.

[95] A T J Hayward. Compressibility equations for liquids: a comparative study. *British Journal of Applied Physics*, 18(7):965–977, jul 1967.

[96] Antony Jameson, Wolfgang Schmidt, and Eli Turkel. Numerical solution of the Euler equations by finite volume methods using Runge Kutta time stepping schemes. In *14th Fluid and Plasma Dynamics Conference*, Palo Alto, CA, USA, 1981. American Institute of Aeronautics and Astronautics.

[97] P. L. Roe. Approximate Riemann solvers, parameter vectors, and difference schemes. *Journal of Computational Physics*, 43(2):357–372, 1981.

[98] Meng Sing Liou and Christopher J. Steffen. A new flux splitting scheme. *Journal of Computational Physics*, 107(1):23–39, 1993.

[99] B van Leer. Fourteenth International Conference on Numerical Methods in Fluid Dynamics. *Lecture Notes In Physics*, 8(February):11–15, 1982.

[100] Eiji Shima and Keiichi Kitamura. Parameter-Free Simple Low-Dissipation AUSM-Family Scheme for All Speeds. *AIAA Journal*, 49(8):1693–1709, 2012.

[101] Arthur Rizzi and Mamoru Inouye. Time-Split Finite-Volume Method for Three-Dimensional Blunt-Body Flow. *AIAA Journal*, 11(11):1478–1485, nov 1973.

[102] Chang-Hsien Tai, Jiann-Hwa Sheu, and Bram van Leer. Optimal multistage schemes for Euler equations with residual smoothing. *AIAA Journal*, 33(6):1008–1016, 1995.

[103] Y. H. Choi and C. L. Merkle. The application of preconditioning in viscous flows. *Journal of Computational Physics*, 105(2):207–223, 1993.

[104] Jonathan M. Weiss and Wayne A. Smith. Preconditioning applied to variable and constant density flows. *AIAA Journal*, 33(11):2050–2057, 1995.

[105] Eli Turkel. Preconditioned methods for solving the incompressible and low speed compressible equations. *Journal of Computational Physics*, 72(2):277–298, 1987.

[106] Achi Brandt. Multi-Level Adaptive Solutions to Boundary-Value Problems. *Mathematics of Computation*, 31(138):333–390, 1977.

[107] A Jameson. Solution of the Euler equations by a Multigrid Method. *Applied Mathematics and Computations*, 13:327–356, 1983.

[108] Achi Brandt. Guide to multigrid development. Technical report, 1982.

[109] F. Grasso and M. Marini. Solutions of hypersonic viscous flows with total variation diminishing multigrid techniques. *Computers and Fluids*, 24(5):571–592, 1995.

[110] J. Blazek, C.-C. Rossow, N. Kroll, and R.C. Swanson. A comparison of several implicit residual smoothing methods in combination with multigrid. In M. Napolitano and F. Sabetta, editors, *Numerical Methods in Fluid Dynamics*, pages 386–390. 1993.

[111] R. Radespiel and R. C. Swanson. Progress with multigrid schemes for hypersonic flow problems. *Journal of Computational Physics*, 116(1):103–122, 1995.

[112] Charles L. Merkle, Philip E. O. Buelow, Sankaran Venkateswaran, and Jennifer Y. Sullivan. Computation of flows with arbitrary equations of state. *AIAA Journal*, 36(4):515–521, 2012.

[113] John Monteith and Mike Unsworth. *Principles of environmental physics: plants, animals, and the atmosphere*. Academic Press, 2013.

[114] Steffen J. Schmidt, Ismail H. Sezal, and Günter H. Schnerr. Compressible Simulation of High-Speed Hydrodynamics with Phase Change. In *European Conference on Computational Fluid Dynamics*, pages 1–20, 2006.

[115] Günter H. Schnerr, Ismail H. Sezal, and Steffen J. Schmidt. Numerical investigation of three-dimensional cloud cavitation with special emphasis on collapse induced shock dynamics. *Physics of Fluids*, 040703(April 2008), 2008.

[116] Michael S. Mihatsch, Steffen J. Schmidt, and Nikolaus A. Adams. Cavitation erosion prediction based on analysis of flow dynamics and impact load spectra. *Physics of Fluids*, 27(10), 2015.

[117] L. de Vito, R. A. Van den Braembussche, and H. Deconinck. A Novel Two-Dimensional Viscous Inverse Design Method for Turbomachinery Blading. In *Journal of Turbomachinery*, volume 125, page 310. ASME, 2003.

[118] Benedikt Roidl and Wahid Ghaly. Redesign of a low speed turbine stage using a new viscous inverse design method. *Journal of Turbomachinery*, 133(1), 2011.

[119] Saurya Ranjan Ray and Mehrdad Zangeneh. A Robust Mixing Plane and Its Application in Three-Dimensional Inverse Design of Transonic Turbine Stages. *Journal of Turbomachinery*, 137(1):1–16, 2014.